Title

Computational Modeling of Multicomponent Disordered Rocksalt Cathodes

Author

Zhong, Peichen

Publication Date

2023

Peer reviewed|Thesis/dissertation

Computational Modeling of Multicomponent Disordered Rocksalt Cathodes

By

Peichen Zhong

A dissertation submitted in partial satisfaction of the

requirements for the degree of

Doctor of Philosophy

in

Engineering – Materials Science and Engineering

in the

Graduate Division

of the

University of California, Berkeley

Committee in charge:

Professor Gerbrand Ceder, Chair
Professor Kristin Persson
Professor Mark Asta
Professor Bryan D. McCloskey

Summer 2023

Computational Modeling of Multicomponent Disordered Rocksalt Cathodes

Peichen Zhong

Abstract

Computational Modeling of Multicomponent Disordered Rocksalt Cathodes

by

Peichen Zhong

Doctor of Philosophy in Engineering – Materials Science and Engineering

University of California, Berkeley

Professor Gerbrand Ceder, Chair

The pursuit of carbon neutrality necessitates improvements in energy storage technologies, with high-performance Li-ion battery cathode materials offering a promising avenue. Modern battery materials can contain many elements with substantial structural complexity, such as configurational disorder that has been shown to be critical for their electrochemical performance. Taking disordered rocksalt cathodes (DRX) as examples, the thesis presents a comprehensive computational modeling study to address the multicomponent complexity through an integrated approach spanning from first-principles calculations to machine learning methods.

The thesis introduces the methodologies required for modeling thermodynamics on lattices from first principles, leveraging density functional theory and lattice models to investigate configurational degrees of freedom. It subsequently demonstrates the application of cluster expansion Monte Carlo simulations to model the short-range order (SRO) in DRXs. The important effect of SRO is demonstrated through the Li-F locking effect in several Mn-based DRXs. A Mg-doping strategy is proposed to increase the capacity by decreasing the amount of Li bound to F. The important role SRO plays in the Li diffusion kinetics is illustrated in several DRX compounds with composition $Li_xMn_{0.4}Nb_{0.3}O_{1.6}F_{0.4}$. By quantifying the percolating Li content in the diffusion network, a strategy of introducing cation deficiency is proposed to tune the SRO and improve the high-rate performance.

Subsequent chapters transition to atomistic modeling with charge information, which is crucial for modeling redox reactions and charge transfer phenomena in cathode materials. Two conceptual approaches – charge-decorated cluster expansion and charge-informed machine learning interatomic potentials – are introduced. The charge-decorated cluster expansion is applied to study the intercalation chemistry with multi-redox reactions in $Li_{1.3-x}Mn_{0.4}Nb_{0.3}O_{1.6}F_{0.4}$, providing a clear demonstration of the Mn and oxygen redox contribution to the redox potential as a function of Li content. The charge-informed interatomic potential is used to study the transition metal migration-induced phase transformation in

$Li_{1.1-x}Mn_{0.8}Ti_{0.1}O_{1.9}F_{0.1}$ via molecular dynamics. An analysis of structural change and SRO is discussed to reveal the effect on the intercalation chemistry.

Lastly, the thesis introduces a novel approach for directly modeling the electrochemical performance of DRX materials. A comprehensive machine learning model (DRXNet) is introduced as a universal end-to-end model with modular design. A graph neural network and embedding networks are used to encode the chemical and electrochemical conditions, including composition, current density, working voltage window, and battery cycle state. The DRXNet is trained on years of experimental discharge voltage profiles and enables an extensive exploratory search across diverse chemical spaces and test conditions, paving the way for identifying novel cathode materials for next-generation batteries.

By integrating the progress achieved in this thesis with recent advances in the fields of computational physics and AI for Science, the thesis proposes general strategies for advancing computational modeling in energy materials design as future directions.

Thesis Advisor: Prof. Gerbrand Ceder
Professor of Materials Science and Engineering
Samsung Distinguished Chair in Nanoscience and Nanotechnology Research

To my beloved wife, Yunshu Shi

Acknowledgments

First and foremost, I express my deepest gratitude to my advisor, Prof. Gerd Ceder. Gerd is one of the most insightful and generous mentors. His valuable suggestions are of immense help throughout my projects and the perceptive criticism keeps me working to make this thesis of some real worth. The discussions with Gerd always leave me enlightened. Gerd Ceder Is All You Need!

I would like to express my sincere gratitude to my qualifying and thesis committee: Prof. Kristin Persson, Prof. Mark Asta, Prof. Bryan D. McCloskey, and Dr. Anubhav Jain. Their insightful suggestions and invaluable guidance have significantly enriched my research and thesis composition.

I am deeply grateful to my colleagues and collaborators, Bowen Deng, Fengyu Xie, Janosh Riebesell, KyuJung Jun, Dr. Luis Barroso-Luque, Dr. Jianping Huang, Dr. Liliang Huang, Dr. Tanjin He, Dr. Tina Chen, Dr. Zijian Cai, Dr. Sunny Gupta, Prof. Raphaële Clément and Prof. Bin Ouyang, for their help in contributing to this challenging journey. Furthermore, my sincere gratitude extends to Prof. Zhengyan Lun, Prof. Nong Artrith and Prof. Chris Bartel for their dedication, knowledge, and guidance.

Throughout my graduate journey, I have had the pleasure of working with different project teams. My sincere appreciation extends to the Statistical Learning and Simulation subgroup, the Cluster Expansion subgroup, the Li-excess and Delta subgroup, and the Halide Solid-State subgroup. I am immensely grateful for the fruitful brainstorming sessions, engaging conversations, and stimulating discussions that happened in the 'Ceder Group Colony' (with Bowen, Fengyu, Shash, Yunyeong, Tanjin, Zhuohan, and Xinye). Additionally, thanks to all members of the Ceder Group for their continuous support and collaborative spirit.

During the Covid-19 pandemic, I had the privilege of founding and organizing the Youth Forum in Science webinar with many young researchers. This platform facilitates fruitful discussion that bridges international academic communication gaps during this challenging time. Many thanks to Yifan, Fei, Yuhao, Liding, Bowen, and Yujie for their invaluable contributions to this initiative's success. I am particularly thankful to my undergraduate advisor, Prof. Zhenhua Qiao, and KouShare for their support.

I wish to express my love and gratitude to my parents; their blessings and teachings have always been my greatest strength. Finally, I extend my heartfelt appreciation to my beloved wife, Yunshu Shi. From our time at USTC to our journey at UC, your love, support, patience, and understanding have been my guiding light through this rigorous journey. My success in achieving this Ph.D. degree would not have been possible without this wonderful soul mate.

Contents

List of Figures

List of Tables

List of Publications

1. **P. Zhong**, T. Chen, L. Barroso-Luque, F. Xie, and G. Ceder*, "An $\ell_0\ell_2$-norm regularized regression model for construction of robust cluster expansion in multicomponent systems", *Phys. Rev. B* **106**, 024203 (2022). (Included in Chapter 2)

2. L. Barroso-Luque*, **P. Zhong**, J. H. Yang, T. Chen, F. Xie, B. Ouyang, and G. Ceder*, "Cluster expansions of multi-component oxides: Formalism and methods", *Phys. Rev. B* **106**, 144202 (2022). (Partially included in Chapter 2)

3. **P. Zhong**†, Z. Cai†, Y. Zhang, R. Giovine, B. Ouyang, G. Zeng, R. J. Clément, Z. Lun* and G. Ceder*, "Increasing Capacity in Disordered Rocksalt Cathodes by Mg Doping", *Chemistry of Materials* **32**, 10728–10736 (2020). (Partially included in Chapter 3)

4. L. Huang†, **P. Zhong**†, Y. Ha, Z. Cai, Y. Byeon, T. Huang, Y. Sun, F. Xie, H. Hau, H. Kim, M. Balasubramanian, B. D. McCloskey, W. Yang, G. Ceder*, "Optimizing Li-Excess Cation-Disordered Rocksalt Cathode Design through Partial Li Deficiency", *Advanced Energy Materials* **13**, 2202345 (2023) (Partially included in Chapter 3)

5. B. Deng, **P. Zhong***, K. Jun, J. Riebesell, K. Han, C. J. Bartel, and G. Ceder*, "CHGNet: Pretrained universal neural network potential for charge-informed atomistic modeling", arXiv:2302.14231. (Partially included in Chapter 4)

6. **P. Zhong**†, F. Xie†, L. Barroso-Luque, L. Huang, and G. Ceder*, "Modeling intercalation chemistry with multi-redox reactions by sparse lattice models in disordered rocksalt cathodes", arXiv:2307.03717. (Included in Chapters 5)

7. **P. Zhong***, B. Deng, T. He and G. Ceder*, "Deep learning of experimental electrochemistry for battery cathodes across diverse compositions", arXiv:2304.04986. (Included in Chapter 6)

8. J. Huang, **P. Zhong**, Y. Ha, D. Kwon, M. J. Crafton, Y. Tian, M. Balasubramanian, B. D. McCloskey, W. Yang and G. Ceder*, "Non-topotactic reactions enable high rate capability in Li-rich cathode materials", *Nature Energy* **6**, 706–714 (2021).

9. J. Huang, **P. Zhong**, Y. Ha, Z. Lun, Y. Tian, M. Balasubramanian, W. Yang, G. Ceder*, "Oxygen vacancy introduction to increase the capacity and voltage retention in Li excess cathode materials", *Small Structures*, **4**, 2200343 (2023).

10. F. Xie, **P. Zhong**, L. Barroso-Luque, B. Ouyang and G. Ceder*, "Semigrand-canonical Monte-Carlo simulation methods for charge-decorated cluster expansions", *Computational Materials Science* **218**, 112000 (2023).

11. L. Barroso-Luque*, J. H. Yang, T. Chen, F. Xie, R. Kam, Z. Jadidi, **P. Zhong** and G. Ceder*, "smol: A Python package for cluster expansions and beyond", *Journal of Open Source Software* **7**, 4504 (2022).

12. Y. Chen, C. J. Bartel, M. Avdeev, Y. Zhang, **P. Zhong**, G. Zeng, Z. Cai, H. Kim, H. Ji*, G. Ceder* "Solid-State Calcium-Ion Diffusion in $Ca_{1.5}Ba_{0.5}Si_5O_3N_6$", *Chemistry of Materials* **34**, 128–139 (2022).

(† equal contribution, * corresponding author)

List of Abbreviations

DRX	Disordered Rocksalt Cathode
SRO	Short-Range Order
DFT	Density Functional Theory
GGA	Generalized Gradient Approximation
PBE	Perdew-Burke-Ernzerhof
SCAN	Strongly-Constrained and Approximately-Normed
MC	Monte Carlo
GCMC	Grand Canonical Monte Carlo
CE	Cluster Expansion
ECI	Effective Cluster Interaction
CS	Compressive Sensing
i.i.d.	Identically Independently Distributed
MIQP	Mixed-Integer Quadratic Programming
CV	Cross Validation
PD	Phase Diagram
GS	Ground State
TM	Transition Metal
HE	High-Entropy
XRD	X-Ray Diffraction
AI	Artificial Intelligence
MD	Molecular Dynamics
AIMD	Ab-Initio Molecular Dynamics
PES	Potential Energy Surface
GP	Gaussian Process
MLIP	Machine-Learning Interatomic Potential
MLP	Multi-Layer Perceptron
NN	Neural Network
GNN	Graph Neural Network
RMSE	Root Mean Square Error
MAE	Mean Abusolute Error
MAD	Mean Abusolute Deviation

Chapter 1

Introduction

1.1 Motivation

The quest for energy exploration and utilization is intrinsically related to the technological advancement of civilization. This intriguing relationship was proposed by Soviet scientist Nikolai Kardashev in 1964 [1]. The Kardashev scale categorizes civilizations into three types.

A Type I civilization (planet level) is able to access all the energy available on its planet and store it for consumption. A Type II civilization (stellar level) can harness the total energy of a star. A Type III civilization (intergalactic level) can directly consume all the energy of its entire host galaxy. The scale was later suggested by Sagan [2] with a definition

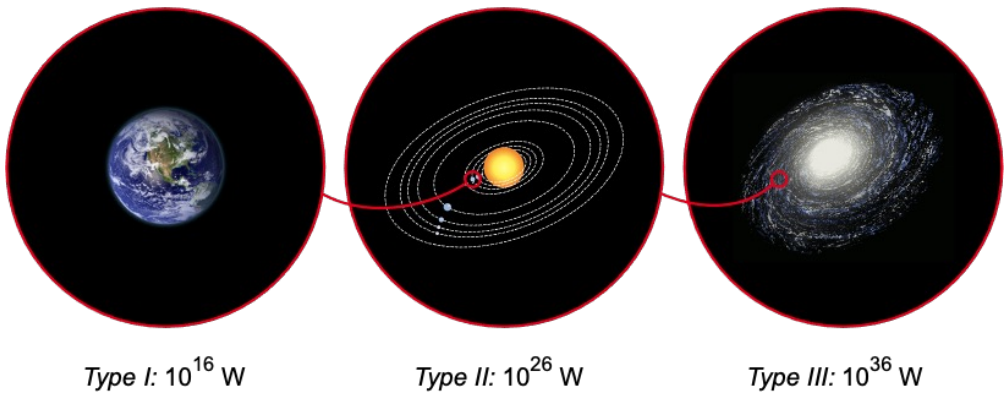

Figure 1.1: Three types of civilizations with energy consumption rate in the Kardashev scale: (1) Type I: Planetary civilization (10^{16} W); (2) Type II: Stellar civilization (10^{26} W); (3) Type III: Intergalactic civilization (10^{36} W).

by interpolating and extrapolating the characteristic values, which produce the formula

$$K(P) = \frac{\log_{10} P - 6}{10}, \tag{1.1}$$

where K is a civilization's Kardashev rating and P is the power it uses (in W).

The current total world's annual energy consumption in 2022 is 604.04 exajoules (167,789 TWh), with 494.05 exajoules (81.8% of total) consumed by oil, natural gas and coal [3]. Our human world is therefore classified as a Type 0.728 civilization on this scale. This signifies that we are less developed and not yet fully utilize the complete energy potential of our planet, especially for the utilization of renewable energies, and far from reaching the status of a Type I civilization. The statistics underscore the significance of research in the field of energy applications. The objective is to advance our understanding of energy conversion, storage, and distribution to move forward on the Kardashev scale. This advancement not only denotes our progression as a civilization but also provides solutions to the pressing energy-related challenges we face today, such as clean energy production, energy efficiency, and environmental sustainability. This compelling motivation drives the research in clean energy that forms the focus of this thesis.

1.2 Li-ion batteries

Looking back to our planet and materials science, the pursuit of efficient and clean energy utilization for a better world necessitates advancements in energy storage technologies. One promising direction is to explore high-performance lithium-ion (Li-ion) batteries. Since the first invention by Sony in 1991 [4], Li-ion batteries have emerged as a cornerstone of modern energy storage, offering portable, high-energy density, and rechargeable power for diverse applications encompassing consumer electronics, electric vehicles, and grid-scale energy storage systems. Fundamental to a Li-ion battery are the cathode, anode, and electrolyte, which collectively enable the efficient storage and release of electrical energy via the charge and discharge processes [5].

Figure 1.2 illustrates the components of a Li-ion battery, which include the cathode, anode, and electrolyte. Both the anode and cathode are intercalation materials, which allows Li to be reversibly inserted/extracted from the host structure. For example, during the charging process, Li-ions are extracted/inserted into the cathode/anode, accompanied by charge transfer via redox reactions. The equilibrium voltage of a battery is defined by the difference in Li chemical potentials between the cathode and anode:

$$V = -\frac{\mu_{\mathrm{Li}}^{\mathrm{cathode}} - \mu_{\mathrm{Li}}^{\mathrm{anode}}}{zF}, \tag{1.2}$$

where z is the charge transferred per ion, F is Faraday's constant, and μ_{Li} is the chemical potential on the cathode and anode, respectively. The anode is typically composed of graphite

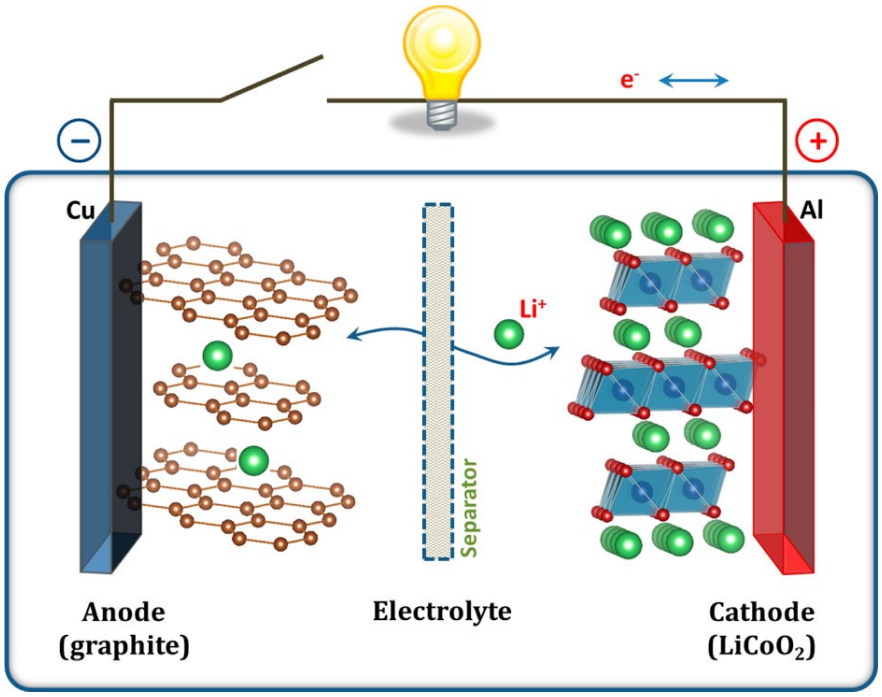

Figure 1.2: Components of a rechargeable Li-ion battery with anode, electrolyte, and cathode. (Ref. [6])

[7] or silicon-based materials [8]. The electrolyte is composed of a Li-salt dissolved in an organic solvent (e.g., $LiPF_6$) or solid-state superionic conductors to facilitate the fast Li-ion transport between the electrodes [9]. And the cathode materials encompass a diverse range of compounds, including layered oxides (e.g., $LiCoO_2$ [10]), spinels (e.g., $LiMn_2O_4$ [11]), and polyanion-based structures (e.g., $LiFePO_4$ [12]).

Despite significant progress in the development of Li-ion batteries, the design of advanced cathode materials remains a crucial bottleneck in achieving higher energy densities, higher charging rates, and long-term cycle retention. The challenges in cathode design are multifaceted, encompassing issues such as structural stability, voltage fade, capacity retention, and thermal stability. Moreover, the increasing demand for sustainable and cost-effective materials necessitates the exploration of alternative and earth-abundant elements (e.g., Mn-based cathode materials) [13].

1.3 Disordered rocksalt cathodes

Disordered rocksalt cathode (DRX) materials have emerged as a promising alternative to conventional layered cathodes, such as Ni–Mn–Co and Ni–Co–Al (NMCA) type cathodes.

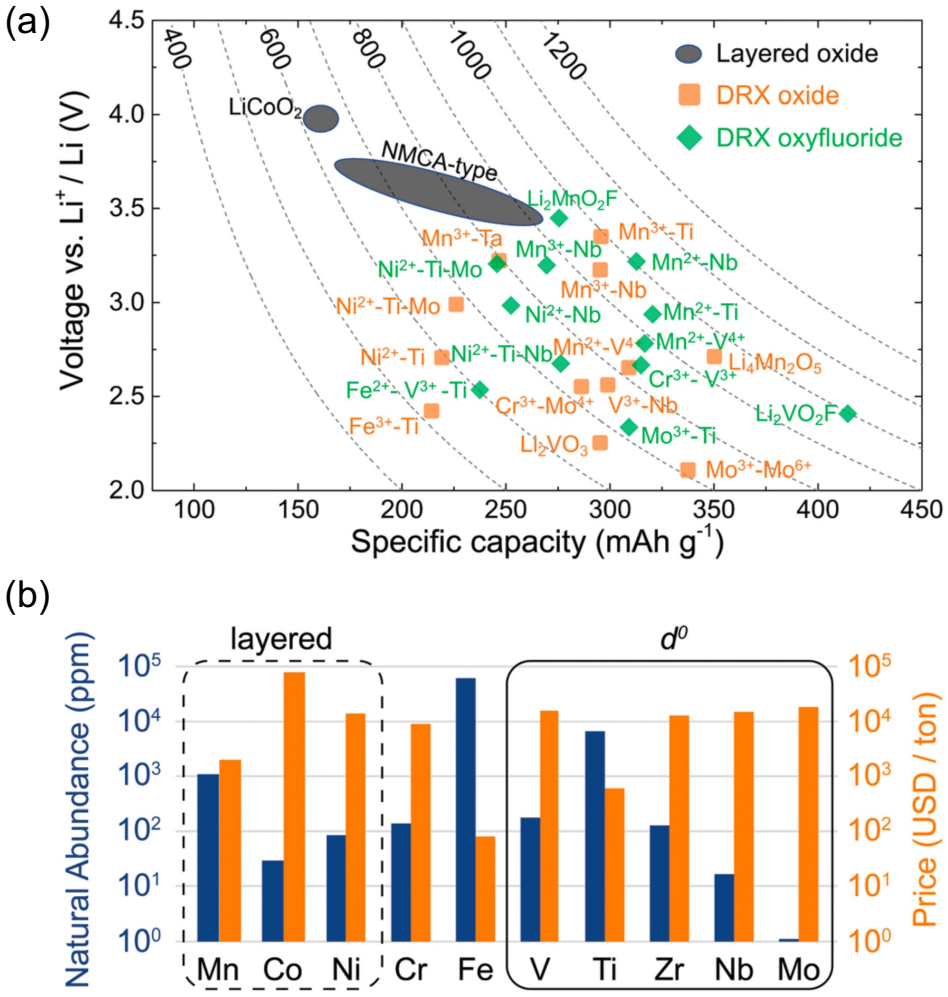

Figure 1.3: (a) Average discharge potential (Voltage vs. Li^+/Li) and gravimetric capacity (mAh/g) of selected layered and DRX cathodes. Contour lines represent the gravimetric energy density (Wh/kg). NMCA = NMC: Li(Ni,Mn,Co)O_2 and NCA: Li(Ni,Co,Al)O_2. (b) Natural abundance (blue bars) and price (orange bars) of selected $3d$ and $4d$ transition metal elements found in disordered lithium transition metal oxide cathodes (on a log scale). (Ref. [14])

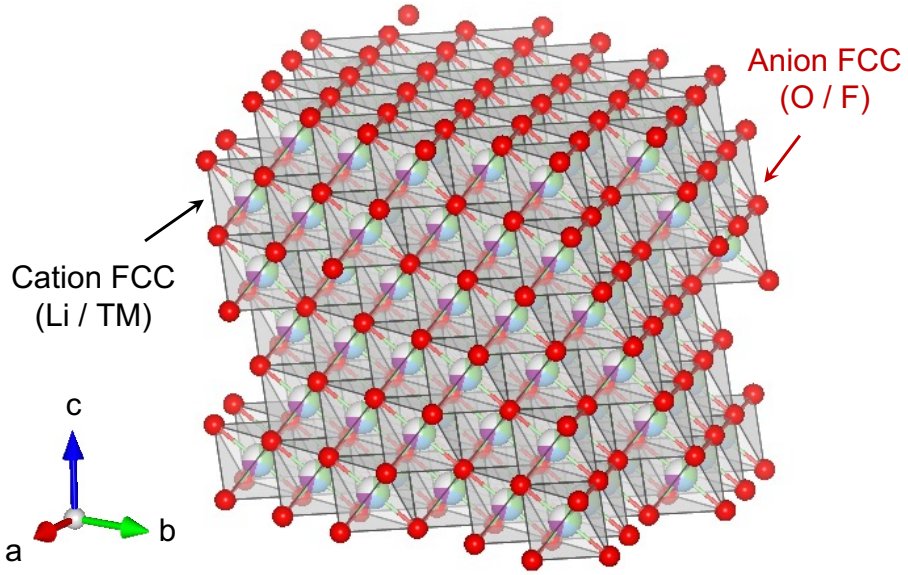

Figure 1.4: The disordered rocksalt structure composed of cation FCC (occupied by Li/TM) and anion FCC (occupied by O/F).

The high cost of Ni and Co in NMC-type cathodes limits the large-scale expansion of Li-ion batteries, whereas DRX cathodes can enable scaling of Li-ion energy storage to several TWh/year production due to their earth-abundant precursors [14]. These materials feature a nearly unlimited compositional design space and a more complex structure-property relationship than conventional layered cathodes. Figure 1.3(a) presents the average voltage and specific capacity of reported DRX compounds as compared to the NMCA-type cathodes. Figure 1.3(b) demonstrates the natural abundance and price per ton of $3d$ and $4d$ transition metals that are typically considered in cathode design. The high price of Ni and Co highlights the advantages of DRX, which can be composed of non-precious elements such as Mn and Ti.

Since the absence of long-range cation order, DRX materials are characterized by a random distribution of cation species within a rocksalt lattice. As shown in Fig. 1.4, the cation FCC sublattice can be occupied by Li and different transition metals, and the anion FCC sublattice can be occupied by oxygen and fluorine. A typical DRX cathode ($Li_{1+x}M'_aM''_bO_{2-y}F_y$) is composed of three major components: (1) the redox-active species M', which provides electron redox; (2) the inert high-valent TM M", which charge compensates for the Li excess and stabilizes disordered structures [15]; (3) fluorine, which can improve the cyclability and allows more Li excess to be accommodated without losing TM redox by lowering the cation valence [16].

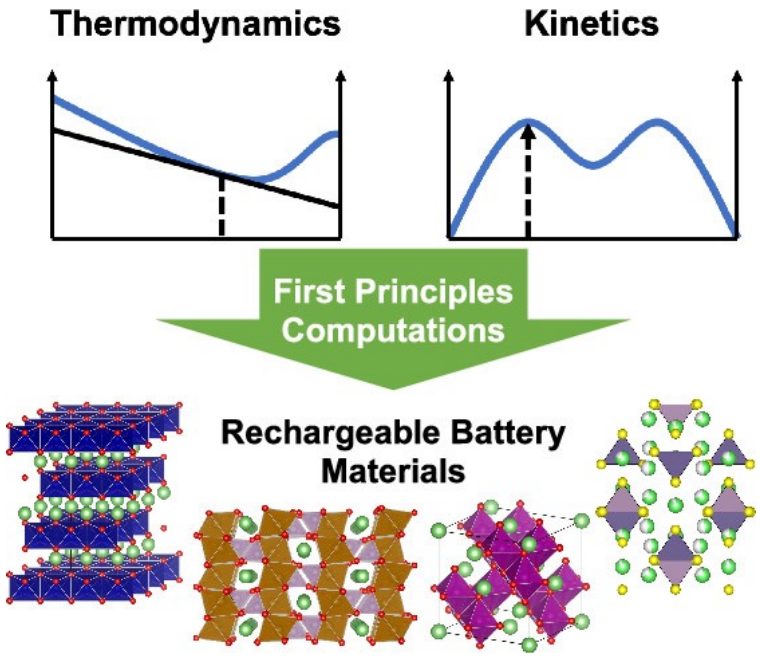

Figure 1.5: Theory and computational modeling of rechargeable Li-ion battery materials. (Ref. [24])

Despite the absence of long-range cation order, interactions between species can also generate short-range ordering (SRO), which critically affects electrochemical performance in various DRX compounds [17]. The wide variety of chemical environments for Li and TMs provided by SRO and chemistry offers new opportunities for improving cathode performance, such as enhancing cyclability through fluorine/vacancy doping of the anion sublattice [18, 19], boosting rate capability by engineering cation SRO [20], and achieving zero-strain cathodes for solid-state batteries [21–23].

1.4 Challenges in modeling complex oxides

In order to push the boundaries of Li-ion battery performance, especially the DRX materials, a deeper understanding of the fundamental mechanisms governing cathode behavior is essential. This includes the investigation of novel crystal structures with degrees of disorder and partial disorder [25–27], compositional tuning [28], and advanced characterization tools (e.g., pair-distribution function analysis [29], spherical-aberration-corrected transmission electron microscopy [30], solid-state nuclear magnetic resonance spectroscopy [31]).

Particularly, the integration of computational modeling from first-principles calculations has demonstrated substantial efficacy in studying and designing rechargeable Li-ion bat-

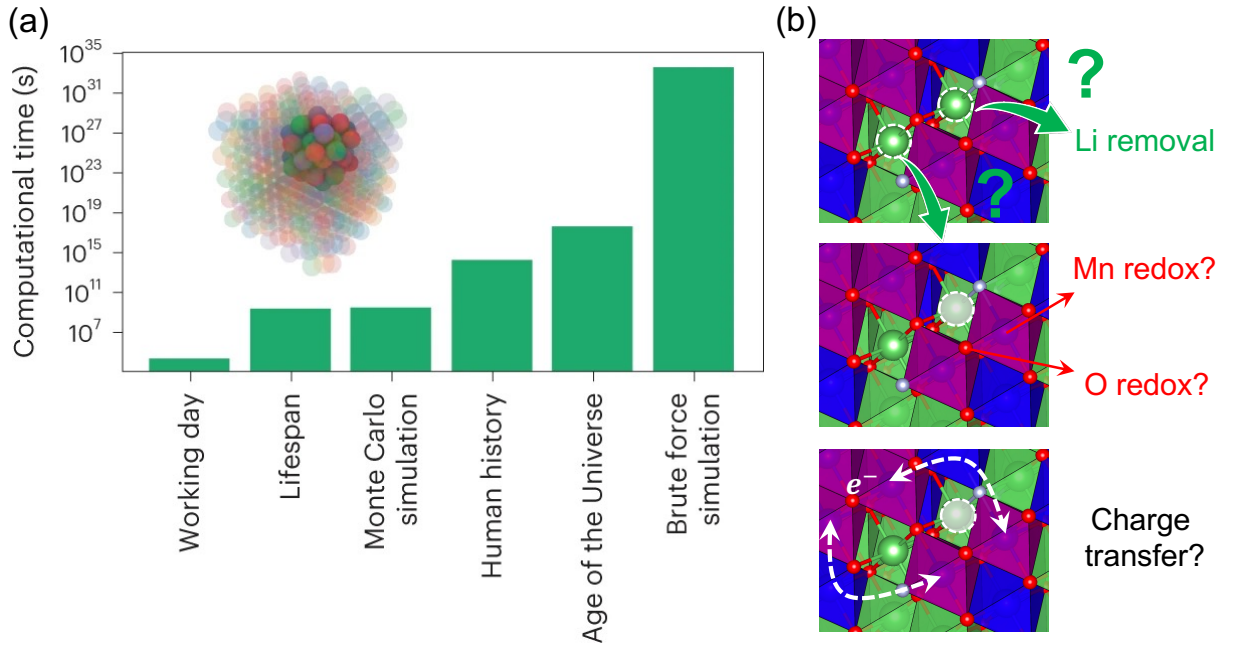

Figure 1.6: (a) The estimated time required given by Ferrari et al. [32] to sample all the possible configurations in the first three neighbor shells (see inset) of a quinary alloy ('brute force') or to perform a million Monte Carlo steps with DFT, compared to the length of a working day, the average human lifetime, the whole span of human history and the age of the Universe. For the DFT calculations, it is assumed a typical time of 1 h for each configuration. (Ref. [32]) (b) Illustration of various local configurations in DRX materials with heterovalence in modeling Li intercalation chemistry.

tery materials. This powerful approach greatly facilitates the understanding of fundamental mechanisms and accelerates materials optimization. Starting from fundamental thermodynamics and kinetics, the theoretical relationships for key battery properties, such as voltage, capacity, ion diffusivity, and other electrochemically relevant quantities, can be accurately formulated and computed using a variety of computational techniques as overviewed by Van der Ven et al. [24]. Insights derived from these developments have been instrumental in advancing the application to DRX materials. Noteworthy achievements include the elucidation of unlocking Li capacity limits through nudged elastic band calculations and percolation models [25], the understanding of how different short-range order distributions impact kinetic properties via cluster expansion from first-principles calculations [17] and the study of fluorine dopability via phase diagram calculations [16].

Since DRX materials are categorized as multicomponent complex oxides, the challenges lie in that the computational modeling needs to capture the complexes of the configurational

degrees of freedom correlated with the chemistries. Ferrari et al. [32] presents an estimated time required to sample configurations in the first three neighbor shells of a quinary alloy with brute force using DFT evaluations via a brute force way or Monte Carlo. The time is compared to the length of a working day, the average human lifetime, the whole span of human history, and the age of the Universe. The exponentially increased computational cost clearly discourages the direct application of DFT to study multicomponent materials.

As types of TM oxides, DRX materials also exhibit complex electronic structures and strong correlation effects that need to be addressed computationally. One approach is to use density functional theory (DFT) with the Hubbard U correction [33] or employ meta-generalized gradient approximation (meta-GGA) functionals [34]. These methods are designed to address the electron delocalization effects and provide a more precise description of the exchange-correlation effects.

Moreover, one of the most critical properties of batteries is the voltage resulting from redox reactions, which characterizes intercalation chemistry and is strongly correlated with the electronic structures of TM oxides. As demonstrated in Fig. 1.6(b), the intercalation chemistry involves energy evaluations of configurations between Li, vacancy, and oxidized species, which is related to the determination of Li removal, TM-redox or O-redox, and charge transfer effects. The coupling between these electronic degrees of freedom and configurational orderings substantially complicates the computational approaches. It is worth noting that these computational challenges are also of significant concern for optimizing cathode materials from an industry perspective [35]. Therefore, accurate, predictive, and robust computational approaches are highly desired for both scientific understanding of fundamental mechanisms and the acceleration of advanced battery manufacturing.

1.5 Overview of the thesis

This thesis aims to deepen understanding of DRX materials by advancing simulation and statistical/machine learning techniques. By integrating cutting-edge methods, it strives to lay the foundation for a new era of materials discovery and optimization for energy storage applications. The thesis is structured as follows:

- In Chapter 2, the thesis begins by introducing the fundamentals of computational thermodynamics and the essential tools for *ab-initio* modeling, which include DFT calculations, statistical mechanics in lattices, and Monte Carlo simulations. It emphasizes discussing the mathematical foundations of cluster expansion methods and exploring approaches for developing robust, accurate, and predictive models by using sparse regression with $\ell_0\ell_2$-norm regularization.
- In Chapter 3, the thesis introduces the application of cluster expansion Monte Carlo to investigate the short-range order effects on the electrochemical performance of DRX

materials. Examples include (1) using Mg-doping to resolve the Li-F locking effect to increase capacity and (2) improving Li transport kinetics through partial Li deficiency.

- In Chapter 4 and 5, the thesis introduces advanced computational methodologies for ionic materials with charge information: charge-decorated cluster expansions and charge-informed machine-learning interatomic potentials. The discussion focuses on how to model configurational thermodynamics coupled with electronic degrees of freedom and model transition metal migration with atomic charge correlation.
- In Chapter 6, the application of deep learning techniques for predicting experimental discharge voltage profiles using DRXNet is discussed. DRXNet is a universal model trained on a wide range of chemistries and experimental test conditions, which provides a data-driven approach to accelerate the discovery and identification of novel cathode materials.
- In Chapter 7, conclusions of this thesis and an outlook on future directions are discussed.

Chapter 2

Thermodynamics on lattices from first principles

2.1 Introduction

The cornerstone of computational thermodynamics is first-principles calculation, for example, Density Functional Theory (DFT), a quantum mechanical method used to investigate the electronic structure (primarily the ground state) of many-body systems. DFT provides a practical approach for studying systems with many electrons while maintaining a tractable computational cost; it is instrumental in predicting properties such as formation energy, density of states, band structure, etc. In addition to DFT, statistical mechanics plays a crucial role in the analysis of systems with substantial configurational disorder. For example, Monte Carlo simulations with lattice models are statistical mechanical tools that offer insights into energy sampling, free energy integration, and materials' phase transitions by simulating configurations on lattices, which enables the exploration of materials' macroscopic properties based on their microscopic distributions.

In Chapter 2, the fundamentals of DFT and statistical mechanics in lattices will be introduced. Specifically, this chapter discusses the mathematical formulation and development of the cluster expansion method, a powerful tool used to study the configurational thermodynamics of alloy systems and disordered solid-state materials.

2.1.1 Quantum mechanics of electrons

In quantum mechanics, the many-body Schrodinger Equation for interacting electrons is

$$\left[\sum_i \left(-\frac{\hbar}{2m_e}\nabla_i^2 + V_{\text{ext}}\right) + \frac{e^2}{2}\sum_{i,j}\frac{1}{|\boldsymbol{r}_i - \boldsymbol{r}_j|}\right]\Psi_n(\boldsymbol{r}_1, \boldsymbol{r}_2, ...) = E_n\Psi_n(\boldsymbol{r}_1, \boldsymbol{r}_2, ...), \qquad (2.1)$$

where $\Psi_n(\boldsymbol{r}_1, \boldsymbol{r}_2, ...)$ is a many-body wavefunction. The V_{ext} is the external potential, e.g., taking Bohn-Oppenheimer approximation, is the interaction between electron and atomic nuclei $V_{\text{ext}}(\boldsymbol{r}) = \sum_A e^2 Z_A / |\boldsymbol{r} - \boldsymbol{R}_A|$. However, direct solving the many-body wavefunction is an intractable problem in solids. As an approximation, the Hartree-Fock method is introduced to include the electron exchange effect. The ground-state many-body wavefunction is approximated as a Slater determinate to represent the anti-symmetrical nature of electrons:

$$\Psi(\boldsymbol{r}_1, \ldots, \boldsymbol{r}_N) = \frac{1}{\sqrt{N!}} \begin{vmatrix} \phi_1(\boldsymbol{r}_1, \sigma_1) & \cdots & \phi_1(\boldsymbol{r}_N, \sigma_N) \\ \vdots & \ddots & \vdots \\ \phi_N(\boldsymbol{r}_1, \sigma_1) & \cdots & \phi_N(\boldsymbol{r}_N, \sigma_N) \end{vmatrix}, \tag{2.2}$$

where $\phi_i(\boldsymbol{r}_j, \sigma_j)$ are single particle orbits, each of which is a product of the position function $\psi_i^\sigma(\boldsymbol{r}_j)$ and spinel variable $\alpha_i(\sigma_j)$ [36]. For simplicity, taking that the Hamiltonian is diagonal in the spin basis, the expected value of energy is obtained by integrating

$$\begin{aligned} E &= \langle \Psi | \hat{H} | \Psi \rangle \\ &= \sum_i \int \psi_i^{\sigma *}(\boldsymbol{r}) \left(-\frac{\hbar}{2m_e} \nabla^2 + V_{\text{ext}} \right) \psi_i^\sigma(\boldsymbol{r}) d\boldsymbol{r} \\ &+ \frac{1}{2} \sum_{i,j,\sigma_i,\sigma_j} \int \psi_i^{\sigma_i *}(\boldsymbol{r}) \psi_j^{\sigma_j *}(\boldsymbol{r}') \frac{e^2}{|\boldsymbol{r} - \boldsymbol{r}'|} \psi_i^{\sigma_i}(\boldsymbol{r}) \psi_j^{\sigma_j}(\boldsymbol{r}') d\boldsymbol{r} d\boldsymbol{r}' \\ &- \frac{1}{2} \sum_{i,j,\sigma} \int \psi_i^{\sigma *}(\boldsymbol{r}) \psi_j^{\sigma *}(\boldsymbol{r}') \frac{e^2}{|\boldsymbol{r} - \boldsymbol{r}'|} \psi_j^\sigma(\boldsymbol{r}) \psi_i^\sigma(\boldsymbol{r}') d\boldsymbol{r} d\boldsymbol{r}', \end{aligned} \tag{2.3}$$

Taking the variational principle

$$E_0 \leq \frac{\langle \Psi | \hat{H} | \Psi \rangle}{\langle \Psi | \Psi \rangle} \;\Rightarrow\; \delta \left(\langle \Psi | H | \Psi \rangle - E_0 \langle \Psi | \Psi \rangle \right) = 0, \tag{2.4}$$

for each orbit ψ_i^σ, the Hartree (Columb) term $\hat{J}(\boldsymbol{r})$ and exchange term $\hat{K}(\boldsymbol{r})$ is obtained

$$\begin{aligned} \hat{J}(\boldsymbol{r}) \psi_i^\sigma(\boldsymbol{r}) &= \sum_{j,\sigma_j} \int \frac{\psi_j^{\sigma_j *}(\boldsymbol{r}') \psi_j^{\sigma_j}(\boldsymbol{r}')}{|\boldsymbol{r} - \boldsymbol{r}'|} d\boldsymbol{r}' \psi_i^\sigma(\boldsymbol{r}) \\ \hat{K}(\boldsymbol{r}) \psi_i^\sigma(\boldsymbol{r}) &= \sum_{j,\sigma} \int \frac{\psi_j^{\sigma *}(\boldsymbol{r}) \psi_i^\sigma(\boldsymbol{r}')}{|\boldsymbol{r} - \boldsymbol{r}'|} d\boldsymbol{r}' \psi_j^\sigma(\boldsymbol{r}) \end{aligned} \tag{2.5}$$

The exchange term $\hat{K}(\boldsymbol{r})$ is summed over all orbitals $\{j\}$ of the same spin σ, including the self-term $j = i$. Since the $\hat{K}(\boldsymbol{r})$ stands for non-local effect, it cannot be represented by electron density $n(\boldsymbol{r}) = \psi_j^{\sigma_j *}(\boldsymbol{r}) \psi_j^{\sigma_j}(\boldsymbol{r})$ solely.

2.1.2 Density Functional Theory

While the Hartree-Fock method offers a way to address the exchange effect in many-body quantum systems, it remains computationally intensive to solve Ψ variationally. An alternative approach is Density Functional Theory (DFT), which addresses the properties of many-electron systems in terms of spacial functionals of the electron density. DFT strikes a balance between computational efficiency and accuracy, establishing itself as a pivotal tool in the field of computational quantum mechanics, particularly for solid-state systems. The theoretical foundation of DFT is grounded in the Hohenberg-Kohn theorems, which furnish a rigorous framework for the treatment of many-body quantum systems [36].

Theorem 1 (First Hohenberg-Kohn theorem) *For any systems of interacting particles in an external potential $V_{ext}(\boldsymbol{r})$, the potential $V_{ext}(\boldsymbol{r})$ is uniquely determined, except for a constant shift, by the ground state particle density $n_0(\boldsymbol{r})$.*

Theorem 2 (Second Hohenberg-Kohn theorem) *The ground-state energy, E_0, is a functional of the electron density, $n(\boldsymbol{r})$, and the exact ground-state density, $n_0(\boldsymbol{r})$, minimizes this functional. Mathematically, if $n(\boldsymbol{r})$ is any density that satisfies the particle number constraint, i.e.,*

$$\int n(\boldsymbol{r})d\boldsymbol{r} = N, \tag{2.6}$$

where N is the number of electrons, and

$$E[n_0(\boldsymbol{r})] \leq E[n(\boldsymbol{r})], \tag{2.7}$$

with equality if and only if $n(\boldsymbol{r}) = n_0(\boldsymbol{r})$.

While the Hohenberg-Kohn theorems establish the foundation for DFT, they do not provide an explicit form of the energy functional. Kohn and Sham proposed a practical scheme to approximate by rewriting the multi-body problem discussed earlier as a system of non–interacting single–orbital $\{\phi_i(\boldsymbol{r})\}$ problems [38]. Briefly, the Kohn–Sham energy functional is given by

$$E[n] = T_s[n] + U_H[n] + V_{\text{ext}}[n] + E_{xc}[n], \tag{2.8}$$

where $T_s[n]$ is the single-particle-like kinetic energy

$$T_s[n] = -\frac{\hbar^2}{2m_e}\sum_i \int \phi_i^*(\boldsymbol{r})\nabla^2\phi_i(\boldsymbol{r}) = T_s[\{\phi_i(\boldsymbol{r})\}]d\boldsymbol{r}, \tag{2.9}$$

and $U_H[n]$ is the Hartree energy

$$U_H[n] = \frac{e^2}{2}\int \frac{n(\boldsymbol{r})n(\boldsymbol{r}')}{|\boldsymbol{r}-\boldsymbol{r}'|}d\boldsymbol{r}d\boldsymbol{r}'. \tag{2.10}$$

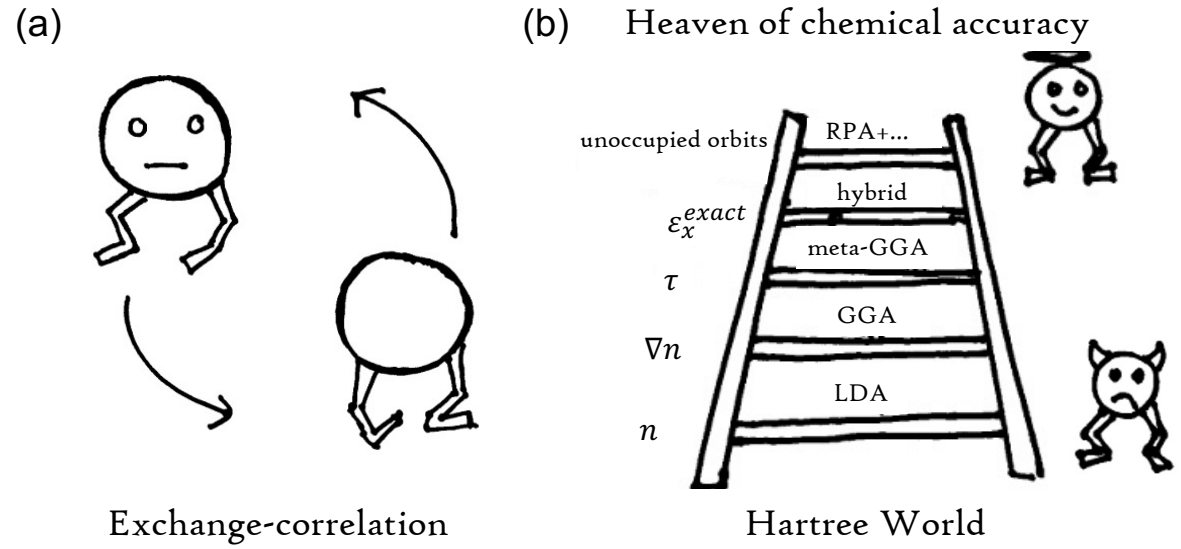

Figure 2.1: (a) Illustration of electron exchange effect. (b) The Jacob's ladder of DFT approximations from Hartree approximation to exact quantum accuracy of many-body systems. (Ref. [37]).

The exchange-correlation energy $E_{xc}[n]$ is captured as the energy associated with electron exchange and correlation. The correlation energy arises from the interactions between electrons beyond treating their motion in a static potential background. The minimization of the energy functional gives

$$\delta\left(E[n]-\varepsilon_i\int n(\boldsymbol{r})d\boldsymbol{r}\right)=0,\ \delta n(\boldsymbol{r})=\delta\phi_i^*(\boldsymbol{r})\phi_i(\boldsymbol{r}) \tag{2.11}$$

and the Kohn–Sham Equation

$$\left[-\frac{\hbar^2}{2m_e}\nabla^2+V_{\text{eff}}(\boldsymbol{r})\right]\phi_i(\boldsymbol{r})=\varepsilon_i\phi_i(\boldsymbol{r}), \tag{2.12}$$

where the effective potential is given by

$$V_{\text{eff}}(\boldsymbol{r})=V_{\text{ext}}(\boldsymbol{r})+e^2\int\frac{n(\boldsymbol{r}')}{|\boldsymbol{r}-\boldsymbol{r}'|}d\boldsymbol{r}'+\frac{\delta E_{xc}[n]}{\delta n(\boldsymbol{r})}. \tag{2.13}$$

One difficulty in the Kohn—Sham scheme is the approximation of the exchange-correlation energy. The simplest approach is the local density approximation (LDA):

$$E_{xc}^{\text{LDA}}[n]=\int\varepsilon_{xc}[n(\boldsymbol{r})]n(\boldsymbol{r})d(\boldsymbol{r}), \tag{2.14}$$

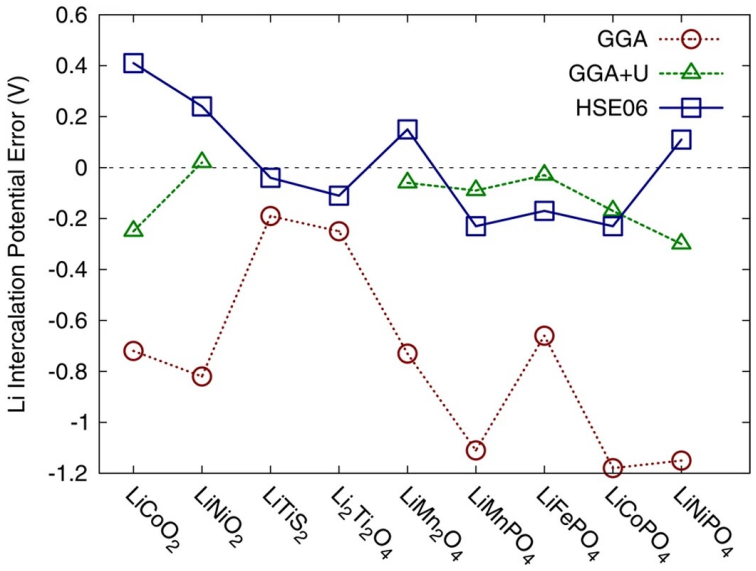

Figure 2.2: Comparison of the errors in intercalation voltages calculated with GGA (red circles), GGA+U (green triangles), and the HSE hybrid functional (blue squares). (Ref. [40])

where the ε_{xc} equals the exchange-correlation energy per electron of a homogeneous electron gas, therefore ε_{xc} is local and neglects the inhomogeneous effects around $\boldsymbol{r}$. The Generalized Gradient Approximation (GGA) improves LDA by taking into account for the gradient of the electron density:

$$E_{xc}^{\mathrm{GGA}}[n] = \int \varepsilon_{xc}[n(\boldsymbol{r}), \nabla n(\boldsymbol{r})] n(\boldsymbol{r}) d(\boldsymbol{r}), \tag{2.15}$$

where the functional $\varepsilon_{xc}[n(\boldsymbol{r}), \nabla n(\boldsymbol{r})]$ can be chosen by satisfying various limiting behaviors or through the empirical fitting, such as the PBE (Perdew-Burke-Ernzerhof) functional [39].

LDA/GGA+U

Early DFT calculations for battery materials primarily relied on either the LDA [38] or the GGA [39]. However, these approaches led to a systematic underestimation of experimentally measured voltages in ordered Li-TM oxides by up to 1.5 V (out of $\sim$ 4 V) [41]. The failure of DFT in predicting the voltages of Li-TM oxides can be attributed to the self-interaction problem. This issue arises because LDA and GGA functionals treat each electron as if it were in a mean field created by all the other electrons, including the electron's Coulombic interaction with itself. Consequently, this results in a spurious delocalization of electrons, leading to significant errors in strongly-correlated systems [42].

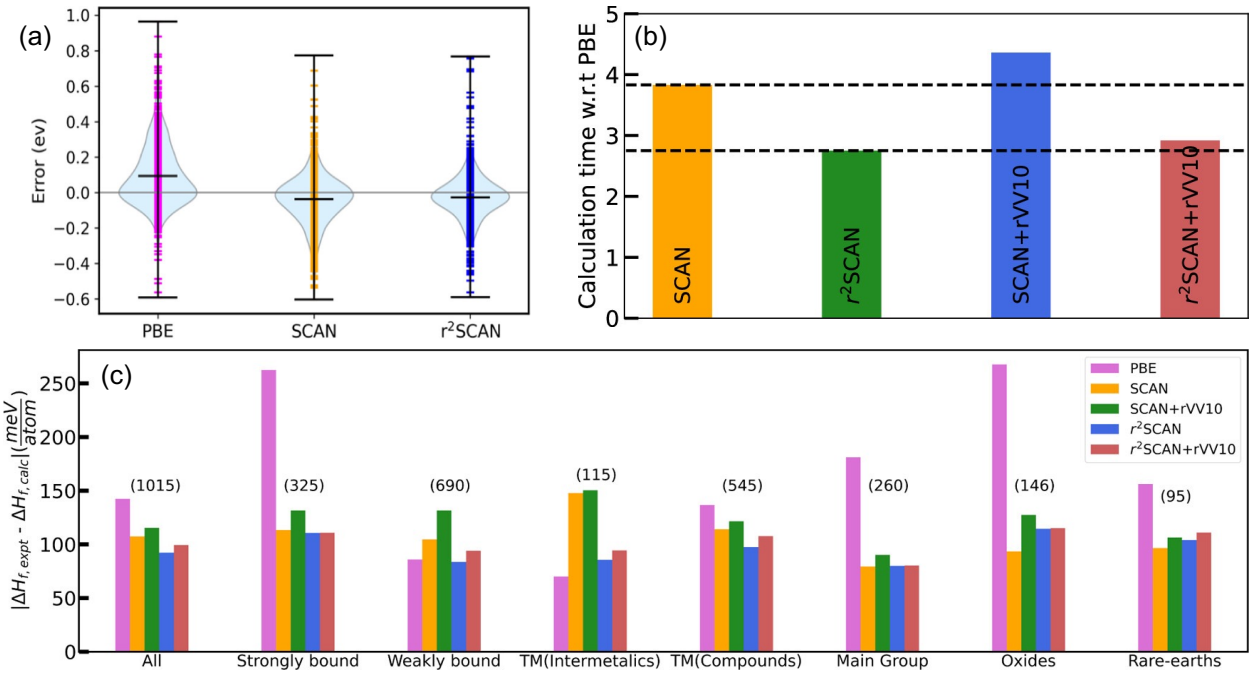

Figure 2.3: (a) Error distributions of PBE, SCAN, and r^{2}SCAN calculated formation energy in comparison to the values of experimental formation enthalpies. (b) Average calculation time for all functionals considered here relative to that of PBE. (c) Comparison of mean absolute errors for PBE, SCAN, SCAN+rVV10, r^{2}SCAN, and r^{2}SCAN+rVV10 with respect to experimental values for formation enthalpies of solids. (Ref. [47])

The GGA+U method offers a practical solution to correct the self-interaction error [33, 41–43]. It introduces a penalty term for partial on-site occupations inspired by the Hubbard model ($H_{\text{onsite}} = U \sum_i n_{i\uparrow} n_{i\downarrow}$), favoring disproportionation into fully occupied and empty states. Such an effort results in significantly reduced prediction error on the voltages, which is evidenced in Fig. 2.2. The prediction errors of DFT calculations with several functionals are presented, where the red circles represent GGA, green triangles represent GGA+U, and blue squares represent the HSE hybrid functional). The magnitude of the $+U$ correction is controlled by a system-specific parameter, which can either be determined self-consistently from linear response theory [42, 44, 45] or by fitting to reference band structures or formation energies [33, 41]. Another approach is to include the exact exchange term (Hatree-Fock method) into the exchange-correlation functional, e.g., hybrid functional [46]. Although the hybrid functional offers an improved description of electron-electron interactions, its substantial computational resource requirements limit its applicability for large-scale energy evaluations in DRX materials.

Meta-GGA: SCAN and r^{2}SCAN

Although LDA/GGA+U partially resolves the systematic errors associated with electron self-interaction, the $+U$ value remains system-specific and has limited transferability. In principle, higher levels of theory, such as meta-GGA DFT functionals, can capture medium-range dispersion interactions and should exhibit smaller self-interaction errors than GGA without $+U$ corrections by introducing the kinetic term $\nabla^2 n$ and satisfying all known constraints on an exchange-correlation functional

$$E_{xc}^{\text{meta-GGA}}[n] = \int \varepsilon_{xc}[n(\boldsymbol{r}), \nabla n(\boldsymbol{r}), \nabla^2 n(\boldsymbol{r})] n(\boldsymbol{r}) d(\boldsymbol{r}). \tag{2.16}$$

Sun et al. [34] addressed the challenge of generality by developing the strongly constrained and appropriately normed (SCAN) functional. This nonempirical meta-GGA functional has been shown to be substantially more accurate than PBE for predicting lattice constants and ground-state structures of solids [48]. Furthermore, the r^{2}SCAN revision of SCAN has demonstrated better numerical stability and high general accuracy. Figure 2.3(a) displays the error distribution of calculated formation energies compared to experimental values for formation enthalpies in 1,015 solid compounds using PBE, SCAN, and r^{2}SCAN functionals. Figure 2.3(b) illustrates the computational time relative to PBE, and Figure 2.3(c) presents the mean absolute error (MAE) by partitioning the 1,015 compounds into various subsets. The numbers in parentheses above each set of bars indicate the number of compounds in that subset, as reported in the benchmark tests by Kothakonda et al. [47].

In this thesis, SCAN/r^{2}SCAN-DFT is used for the calculations of DRX systems with vacancies, as the introduction of vacancy is coupled with charge transfer effects and requires a nonempirical, accurate description of the electronic structures. SCAN/r^{2}SCAN is believed to better capture cation-anion hybridization and Li-coordination [48, 49].

2.2 Statistical mechanics on lattices

In statistical mechanics, each microstate s possesses an associated energy E_s. The enthalpy for microstate s is defined as $H_s = E_s + PV$, where pressure P (intensive variable) and volume V (extensive variable) represent a pair of conjugate variables. In solid-state systems, the volume change is considered negligible for our discussion of configurational problems, implying $H_s \approx E_s$. The probability in the microstate s is given by

$$P_s = \frac{\exp(-E_s/k_B T)}{Z},\ Z = \sum_s \exp(-E_s/k_B T), \tag{2.17}$$

where k_B is the Boltzmann constant and Z is the canonical partition function of (N, V, T) ensemble. The average energy is a weighted summation of all possible microstates

$$\langle E \rangle = \sum_s P_s E_s. \tag{2.18}$$

Treating the partition function as a generating function of E_s, the average and variance of energy can be expressed in a more natural way [50]:

$$\langle E\rangle = -\frac{\partial \ln Z}{\partial \beta},\ \langle E^2\rangle - \langle E\rangle^2 = \frac{\partial^2 \ln Z}{\partial \beta^2}, \tag{2.19}$$

where $\beta = 1/k_B T$, $\langle E\rangle$ is the first-order cumulant (mean), and $\sigma^2(E) = \langle E^2\rangle - \langle E\rangle^2$ is the second-order cumulant (variance) of $\ln Z$ (cumulant generating function). The free energy can be expressed as

$$F = -\frac{1}{\beta}\ln Z. \tag{2.20}$$

Nonetheless, providing a detailed description of the partition function proves challenging, as it necessitates knowledge of the energy spectrum for all relevant excitations. At finite temperatures, various excited states are possible, including vibrations around equilibrium sites, intra-atomic excitations, and substitutional excitations [51]. Among these, only the substitutional excitation contributes to configurational rearrangement, and the solid generally experiences a large number of vibrations before such a thermal fluctuation results in a configurational rearrangement. These observations imply that the partition function in solids with configurational disorder can be expressed as

$$Z = \sum_{\boldsymbol{\sigma}} \sum_{s\in\boldsymbol{\sigma}} \exp(-\beta E_s), \tag{2.21}$$

where the second summation $\sum_{s\in\boldsymbol{\sigma}}$ includes all the vibrational and electronic states associated with the configuration $\boldsymbol{\sigma}$. By introducing the configurational-dependent free energy function

$$F(\boldsymbol{\sigma}) = -\frac{1}{\beta}\ln\left(\sum_{s\in\boldsymbol{\sigma}} \exp(-\beta E_s)\right), \tag{2.22}$$

the partition function can be written as a generating function of $F(\boldsymbol{\sigma})$

$$Z(\beta) = \sum_{\boldsymbol{\sigma}} \exp\left(-\beta F(\boldsymbol{\sigma})\right). \tag{2.23}$$

The configurational dependent free energy function can be written as $F(\boldsymbol{\sigma}) = E_{\mathrm{GS}}(\boldsymbol{\sigma}) + F_{\mathrm{ex}}$, where $E_{\mathrm{GS}}(\boldsymbol{\sigma})$ is the ground state energy and F_{ex} includes excitations from vibrational (and electronic) degrees of freedom. Prior research indicates that this approximation only affects the order-disorder transition temperature quantitatively but does not change the phase diagram's topology [52–54]. Consequently, it can be inferred that the coarse-grained partition function detailed in Eq. (2.23) is equivalent to the partition function for a lattice model [51]. Although some early studies assumed the electronic degrees of freedom to be ergodic as well and can be coarse-grained into $\{\boldsymbol{\sigma}\}$ in several metallic systems [55–57], however, as discussed in Chapter 4 and 5, the electronic degrees of freedom cannot be effectively coarse-grained for many ionic materials and must be explicitly included in the

orbits of the lattice model [58]. In this thesis, vibrational degrees of freedom are neglected from our discussion.

For systems that can exchange component numbers by interacting with external environments (e.g., intercalation process of Li-ions when a voltage is applied), the grand-canonical ensemble (μ, V, T) is more useful for discussion. The grand partition function is a generating function of $Z(\beta, N)$

$$\Xi(\mu, \beta) = \sum_N \exp(\beta\mu N) \cdot Z(\beta, N). \tag{2.24}$$

The average and variance of the number of components are

$$\langle N \rangle = \frac{\partial \ln \Xi}{\partial(\beta\mu)},\ \langle N^2 \rangle - \langle N \rangle^2 = \frac{\partial^2 \ln \Xi}{\partial(\beta\mu)^2}. \tag{2.25}$$

And the average and variance of the grand canonical energy are

$$\langle \Lambda \rangle = -\frac{\partial \ln \Xi}{\partial \beta},\ \langle \Lambda^2 \rangle - \langle \Lambda \rangle^2 = \frac{\partial^2 \ln \Xi}{\partial \beta^2}, \tag{2.26}$$

where $\Lambda = E - \mu N$.

2.2.1 Monte Carlo simulations

In lattice systems with multiple components, enumerating all the possible configurations is an intractable NP-hard problem. Monte Carlo (MC) simulation is a natural choice to efficiently sample the high-dimensional configurational space. A key aspect in MC simulations is to ensure that the system reaches equilibrium following the Detailed Balance Condition.

Theorem 3 (Detailed Balance Condition) *Consider a system with transitions between states i, j according to a Markov process. The transition rate from state i to state j is denoted by W_{ij}. The probability for the system to be in state i is P_i. At equilibrium, for every pair of states i and j, the following relation holds:*

$$P_i W_{ij} = P_j W_{ji} \tag{2.27}$$

The Detailed Balance Condition plays a fundamental role in formulating MC algorithms. The Metropolis-Hastings algorithm, in particular, is a widely used technique for sampling probability distributions. It was initially developed by Metropolis et al. [59] and later generalized by Hastings [60]. This algorithm is often applied to systems with a large number of microstates. An outline of the Metropolis-Hastings algorithm applied to a canonical MC in a lattice system with the spin-flip method is presented below:

1. Initialize the system with a specific configuration $\boldsymbol{\sigma}_i$ and calculate its energy $E(\boldsymbol{\sigma}_i)$.

2. Randomly select site i and j, propose a new configuration σ_{i+1} by exchanging the spin variables (i.e., occupied atom) of site i and j.

3. Compute the energy difference $\Delta E = E(\boldsymbol{\sigma}_{i+1}) - E(\boldsymbol{\sigma}_i)$ and the transition probability $P = \min\left\{1, \exp\left(-\frac{\Delta E}{k_B T}\right)\right\}$, where k_B is Boltzmann constant and T is the temperature.

4. Generate a random number r, uniformly distributed between 0 and 1.

5. If $r < P$, accept the proposed configuration and set $\boldsymbol{\sigma}_{i+1}$ as the current state. Otherwise, reject the proposed configuration and retain $\boldsymbol{\sigma}_i$ as the current state for the next iteration.

In canonical MC, the transition rate W_{ij} equals W_{ji} since states i and j share the same composition. In grand-canonical MC, the transition rate W_{ij} is composition-dependent and needs to be precomputed into a table for quick identification of all events that need to be updated, which is called table-exchange method [61, 62]. MC simulations typically require numerous energy evaluations (on the order of millions of steps), highlighting the need for a reduced but efficient Hamiltonian with *ab-initio* accuracy.

2.3 Cluster expansion method

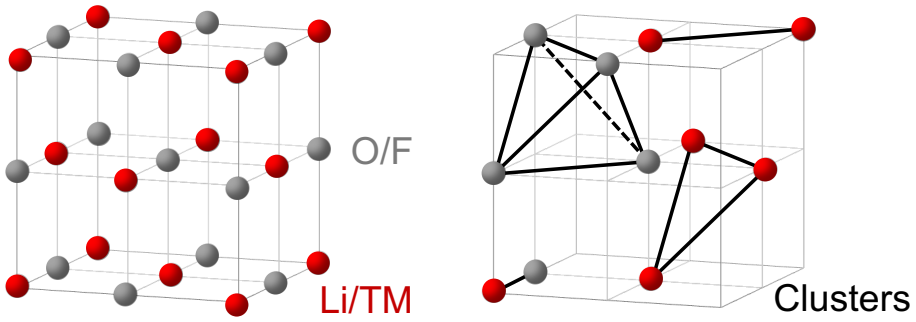

Figure 2.4: The cation sites in a rocksalt lattice are labeled in red and can be occupied by Li^+ and transition metals (TM) in DRX. The anion sites are labeled in gray and can be occupied by O^{2-} and F^-. Some examples of n-body ($n = 2, 3, 4$) clusters are included to represent the intra- and inter-sublattice interactions.

The cluster expansion (CE) method is one approach to the effective Hamiltonian from *ab-initio* calculations [63–65]. The CE expands any property (e.g., formation energy) in terms of the distribution of atoms on a set of predefined sites, which has been well developed to describe such configurational energetics for metallic alloys [66, 67], as well as for ionic

systems [68, 69]. When the quantity being expanded is the energy, the expansion coefficients are referred to as Effective Cluster Interactions (ECI). For example, in a multicomponent system, the energy is expanded as

$$E(\boldsymbol{\sigma}) = \sum_{\beta} m_\beta J_\beta \left\langle \Phi_{\boldsymbol{\alpha}\in\beta} \right\rangle_\beta , \ \Phi_{\boldsymbol{\alpha}} = \prod_{i=1}^{N} \phi_{\alpha_i}(\sigma_i). \tag{2.28}$$

A configuration $\boldsymbol{\sigma}$ represents a specific occupancy on all the sites of the system, where σ_i describes which species sits on the i-th site of the structure. The site basis function $\phi_{\alpha_i}(\sigma_i)$ transforms the occupancy variable σ_i into a scalar value. There are typically as many (non-constant) cluster basis functions as possible occupancies on a site minus one. The cluster basis function label $\boldsymbol{\alpha} = (\alpha_1, \alpha_2, \alpha_3, \ldots)$ indicates a group of sites, each with a specific basis function on it, where each entry α_i labels the corresponding site basis function ϕ_{α_i}. Thus, the cluster basis function $\Phi_{\boldsymbol{\alpha}} = \prod_{i=1}^{N} \phi_{\alpha_i}(\sigma_i)$ can be obtained by taking the product of site basis functions. The detailed formalism of cluster expansion can be found in Ref. [63].

Basis function transformation

For example, the cation sublattice of a $LiMnO_2$ rocksalt oxide is a binary system where Li and Mn share the octahedral interstitial of the FCC anion framework. In such a system, Li can be encoded by $\sigma^{\mathrm{Li}} = 0$ and Mn by $\sigma^{\mathrm{Mn}} = 1$. The parameter α_i takes a value from $[0, 1, ...M-1]$, where M is the number of allowed species defined on the sublattice (e.g., $M = 2$ for Li-Mn). While many forms of site basis function can be used [66, 70, 71], a sinusoid basis function is applied here to transform the occupancy variable $(\sigma^{\mathrm{Li}}, \sigma^{\mathrm{Mn}})$ into a value [72], where

$$\phi_j(\sigma_i) = \begin{cases} 1 & \text{if } j = 0 \\ -\cos\left(\frac{\pi(j+1)\sigma_i}{M}\right) & \text{if } j \text{ is odd} \\ -\sin\left(\frac{\pi j \sigma_i}{M}\right) & \text{if } j \text{ is even} \end{cases} . \tag{2.29}$$

The j indicates α_i in Eq. (2.28) and can take a value of 0 or 1. Thus, we have $\phi_{j=0} \equiv 1$, $\phi_{j=1}(\sigma^{\mathrm{Li}} = 0) = -1$, and $\phi_{j=1}(\sigma^{\mathrm{Mn}} = 1) = 1$. This situation corresponds to the spin variables used in a generalized Ising model [51, 73]. For systems with species number $M > 2$, the basis functions take values beyond those of spin variables $\{-1, 1\}$ typically used in binary CE. Some examples of other types of site-basis functions also developed for the CE method are the Chebyshev polynomials [66]

$$\phi_j(\sigma_i) = \begin{cases} \sum_{k=0}^{j/2} c_k \sigma_i^{2k} & \text{if } j \text{ is even} \\ \sum_{k=0}^{(j-1)/2} c_k \sigma_i^{2k+1} & \text{if } j \text{ is odd} \end{cases} , \tag{2.30}$$

where the coefficients c_k are chosen so that the basis is orthonormal. The indicator (point delta function) basis function [70]

$$\phi_j(\sigma_i) = \begin{cases} 1 & \text{if } j = 0 \\ \mathbf{1}_{\sigma_j}(\sigma_i) & \text{if } j > 0 \end{cases}, \tag{2.31}$$

where $\mathbf{1}_{\sigma_j}(\sigma_i)$ are singleton indicator functions ($\mathbf{1}_{\sigma_j}(\sigma_i) = 1$ if $\sigma_i = \sigma_j$ and 0 otherwise).

Correlation function and feature matrix

The correlation function $\langle \Phi_{\boldsymbol{\alpha} \in \beta} \rangle_\beta$ is computed as a normalized quantity with respect to the crystallographic primitive cell

$$E(\boldsymbol{\sigma}) = \sum_\beta m_\beta J_\beta \langle \Phi_{\boldsymbol{\alpha} \in \beta} \rangle_\beta , \ \langle \Phi_{\boldsymbol{\alpha}}(\boldsymbol{\sigma}) \rangle_\beta = \frac{1}{N_{\boldsymbol{\sigma}} m_\beta} \sum_{\boldsymbol{\alpha} \in \beta} \Phi_{\boldsymbol{\alpha}}(\boldsymbol{\sigma}), \tag{2.32}$$

where β is an orbit representing all symmetrically equivalent cluster basis functions $\boldsymbol{\alpha}$, m_β is the corresponding multiplicity, $N_{\boldsymbol{\sigma}}$ is the size of the supercell of configuration $\boldsymbol{\sigma}$ for the normalization, and J_β is the effective cluster interaction (ECI). The CE energy is linearly dependent on the ECIs $\boldsymbol{J}$ when the configuration $\boldsymbol{\sigma}$ is given

$$E_{\text{CE}}(\boldsymbol{\sigma}) = \boldsymbol{\Pi}(\boldsymbol{\sigma}) \cdot \boldsymbol{J}, \tag{2.33}$$

where $\boldsymbol{\Pi}(\boldsymbol{\sigma}) = [\mathbf{1}, \langle \Phi \rangle_{\beta_1}, \langle \Phi \rangle_{\beta_2}, ...]$ is a row vector of correlation functions and $\boldsymbol{J}$ is the column vector of ECIs.

2.3.1 Parameterizing Effective Cluster Interactions (ECIs)

Given a set of input occupancy configurations S, the set of correlation vectors forms a feature matrix $\boldsymbol{\Pi}_S = [\boldsymbol{\Pi}_1, \boldsymbol{\Pi}_2, ...]$, and the corresponding DFT energies are used to construct the target vector $\boldsymbol{E}_{\text{DFT},S}$. Determining the ECIs is an inverse problem of Eq. (2.33), also called linear regression. Generally, the problem can be solved by minimizing the cost function

$$\min_{\boldsymbol{J}} \ ||\boldsymbol{E}_{\text{DFT},S} - \boldsymbol{\Pi}_S \boldsymbol{J}||_2^2 + \rho(\boldsymbol{J}), \tag{2.34}$$

where $\rho(\boldsymbol{J})$ is the regularization of ECIs $\boldsymbol{J}$ to avoid over-fitting. The selection of the regularization function $\rho(\boldsymbol{J})$ plays a crucial role in determining the reliability of ECIs, which will be explored in depth in Section 2.4.

Figure 2.6(b) presents a brief illustration of how to construct a CE Hamiltonian iteratively. In practice, the CE model is initially fitted on a small set of DFT calculations, where the DFT-relaxed structures are refined to the crystallographic sites (i.e., Wyckoff positions) as predefined by the CE (illustrated in Fig. 2.6(a)). This procedure can be accomplished by

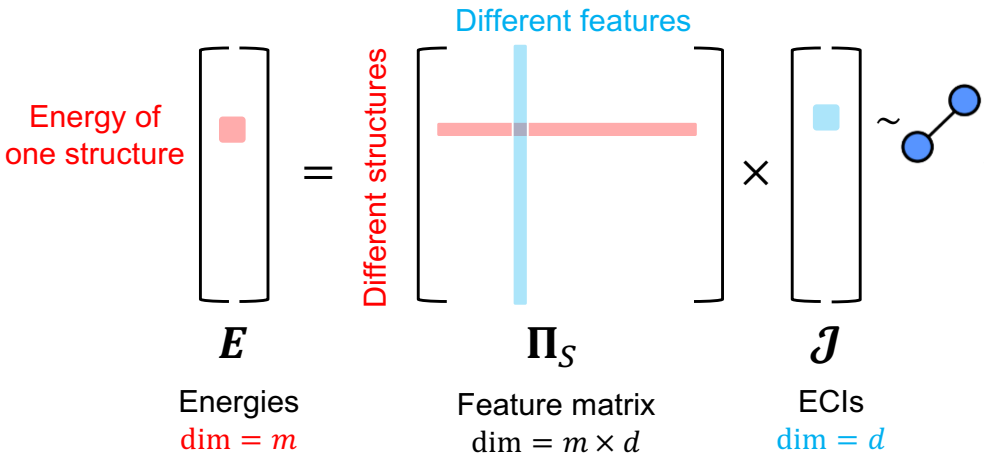

Figure 2.5: Illustration of the linear relation between energies, feature matrix, and ECIs.

the crystallographic matching algorithm such as `StructureMatcher` in the `pymatgen` library [74]. Subsequently, a basic CE is fitted, which can be utilized in a Monte Carlo simulation to generate new structures. DFT calculations are then applied to a subset of the Monte Carlo-derived structures, and an updated CE is fitted. This procedure is executed iteratively until the model converges, as evidenced by a consistently low and stable cross-validation error and accurate reproduction of DFT ground states, among other factors. In such a process, it is always desirable to achieve fewer training iterations, as DFT calculations are costly in terms of CPU time. On the other hand, fewer structures may also result in a worse fitting due to insufficient sampling of the configuration space, which addresses the importance of structure selection for training data generation.

2.3.2 Structure selection

Obtaining representative training structures through sampling is crucial for creating effective CE models. Ideally, such sampling encompasses all pertinent regions within the configuration space, ensuring that CE predictions are interpolative rather than extrapolative. However, comprehensively covering vast configuration spaces is typically infeasible. Structure sampling techniques generally rely on the relationship between the number of structures m and the number of correlation functions d employed for fitting a CE model. Depending on this relationship (i.e., the shape of the feature matrix $\mathbf{\Pi}_S$), the linear system in Eq. (2.34) can be classified as either an overdetermined ($m > d$) or an underdetermined ($m < d$) problem. The choice of structure sampling methods and their underlying mathematical rationale vary accordingly.

The theoretical properties and practical stability of regression primarily hinge on the

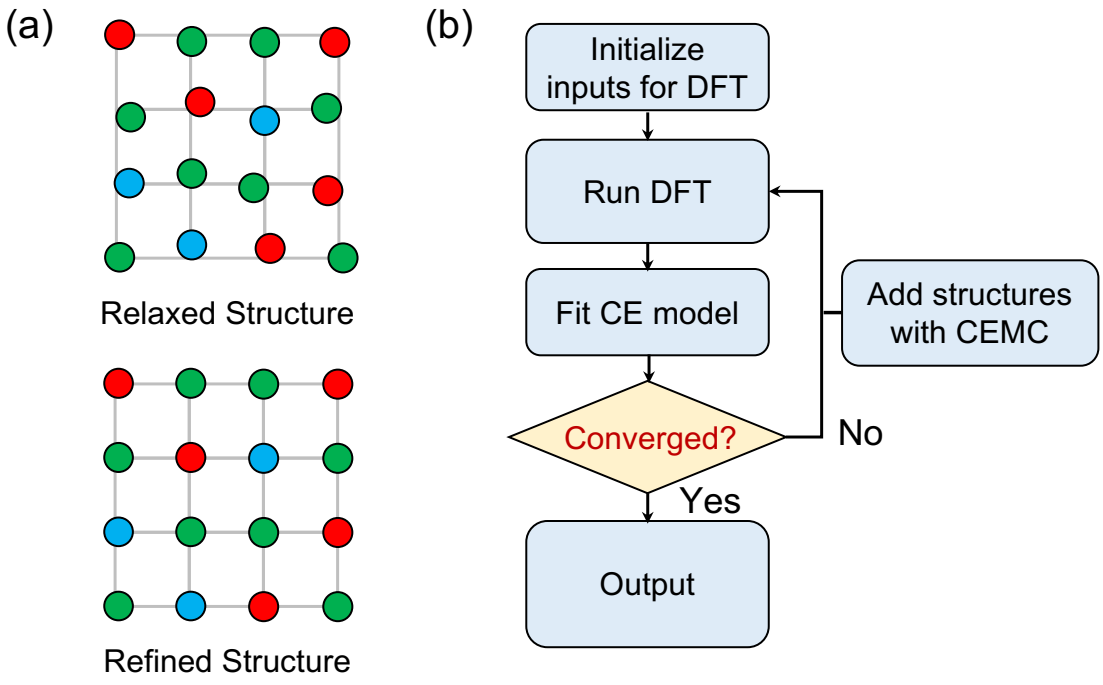

Figure 2.6: (a) Schematics of an input structure (DFT-relaxed) and a refined structure. The refined structure is represented by the sites of the relaxed structure mapped to the locations of the sites of the rigid lattice. The different colors represent multiple species on the lattice. (b) The general flowchart of constructing a CE model, including initialization of input structures, DFT calculations, fitting and convergence check, and cluster expansion Monte Carlo (CEMC) for sampling.

feature matrix $\mathbf{\Pi}_S$ having full rank, $\text{rank}(\mathbf{\Pi}) = \min\{m, d\}$. In other words, the rank equals the number of columns in the overdetermined case ($m > d$) and the number of rows in the underdetermined case ($m < d$). Two scenarios and their relevance to structure sampling will be discussed.

Overdetermined linear system

In the overdetermined case, a full-rank matrix consists of linearly independent sampled values for each correlation function. For any finite set of samples, intrinsic linear dependencies and inadequate sampling may contribute to rank deficiencies in $\mathbf{\Pi}_S$. Rank deficiency can be further exacerbated by configurations with energies inaccessible to first-principle calculations (i.e., in overdetermined cases, although $m > d$, the $\text{rank}(\mathbf{\Pi})$ can be smaller than d. In such situations, the $\text{rank}(\mathbf{\Pi}_S)$ can be increased by incorporating more structures to encompass a broader range of correlation values, and/or adding supplementary correlation

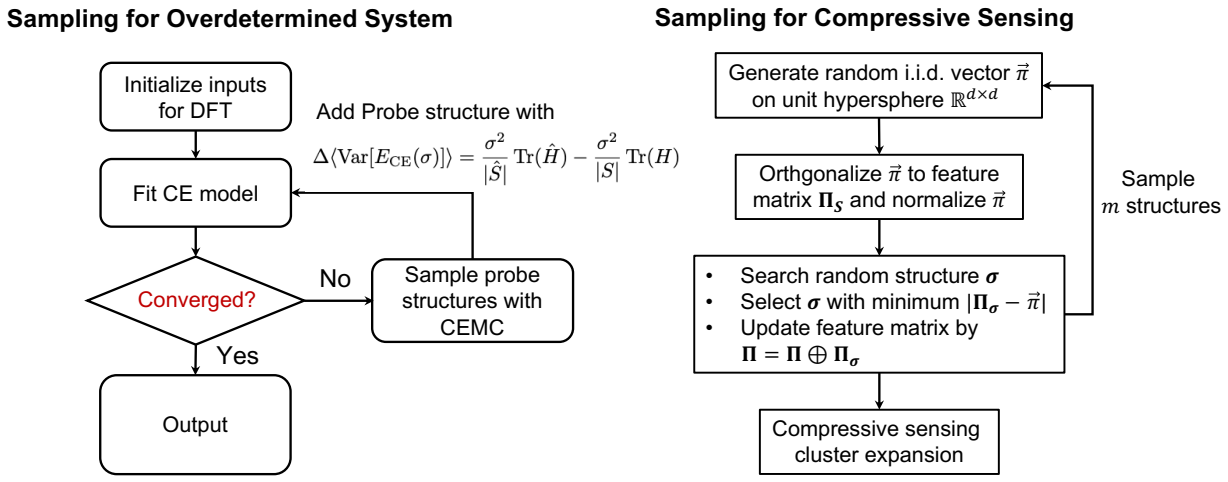

Figure 2.7: (a) Sampling procedure for overdetermined problems, including initialization of inputs for DFT calculations, fits of CE models, convergence checks, and addition of probe (additional) structures [69]. The probe structures are selected by maximizing the reduction of leverage score (uncertainty) between the previous set S and the new set $\hat{S}$. (b) Sampling procedure for the compressive sensing cluster expansion. In such a procedure, structures are selected by selecting correlation vectors $\Pi_{\boldsymbol{\sigma}}$ that most closely align with uniformly random vectors over the hyper-sphere $\vec{\pi}$ [75]. (Ref. [63])

functions that introduce new linearly independent features. The focus of structure sampling should be on improving the predictions and variances for a fitted CE for any acceptable estimates of ECI. To simplify our analysis of prediction variance, it is assumed that a fitted CE model is fitted with an overdetermined, full-rank feature matrix and captures the real target energy as follows,

$$E_{\mathrm{DFT}}(\boldsymbol{\sigma}) = \mathbf{\Pi}_{\boldsymbol{\sigma}} \cdot \boldsymbol{J} + \varepsilon, \tag{2.35}$$

where ε is a random error from $\mathcal{N}(0, s^2)$. Under the assumptions above, the variance of the predicted energy by a CE fitted with least squares regression can be expressed as

$$\mathrm{Var}[E_{\mathrm{CE}}(\boldsymbol{\sigma})] = s^2 \mathbf{\Pi}_{\boldsymbol{\sigma}}{}^T (\mathbf{\Pi}^T \mathbf{\Pi})^{-1} \mathbf{\Pi}_{\boldsymbol{\sigma}}, \tag{2.36}$$

where s^2 represents the variance from intrinsic noise in the DFT calculations for a given population of structures, and $\mathbf{\Pi}_{\boldsymbol{\sigma}}$ is the correlation vector for the particular occupancy $\boldsymbol{\sigma}$ used in prediction [69, 76, 77]. The expression above can be adjusted for penalized regression models under a Bayesian interpretation [78]. According to Eq. (2.36), the average variance

for predicted energies is given as

$$\langle \mathrm{Var}[E_{\mathrm{CE}}(\boldsymbol{\sigma})] \rangle = \frac{\sigma^2}{|S|} \sum_{\boldsymbol{\sigma} \in S} \boldsymbol{\Pi}_{\boldsymbol{\sigma}}{}^T (\boldsymbol{\Pi}^T \boldsymbol{\Pi})^{-1} \boldsymbol{\Pi}_{\boldsymbol{\sigma}}$$
$$= \frac{\sigma^2}{|S|} \mathrm{Tr}(H), \tag{2.37}$$

where $|S|$ is the number of training structures. $H = \boldsymbol{\Pi}^T (\boldsymbol{\Pi}^T \boldsymbol{\Pi})^{-1} \boldsymbol{\Pi}$ is the so-called hat matrix [79]. The diagonal elements H_{ii} are the predicted variances for a particular structure, which are also known in the statistics literature as leverage scores. The leverage score ranks the uncertainty of the corresponding probe occupancy $\boldsymbol{\sigma}$ into high-leverage or low-leverage points according to regression diagnostics [80]. A handful of methods for structure sampling have been proposed that seek to minimize the average leverage score, or equivalently maximize the reduction in average predicted variance, for each additional structure included [69, 76, 77]. These methods can lead to improved robustness and accuracy in CE fits.

Underdetermined linear system

In the underdetermined linear regression case ($m < d$), obtaining a full-rank correlation matrix is much more straightforward. An underdetermined system has full rank when all correlation vectors (rows of $\boldsymbol{\Pi}$ are linearly independent), as opposed to linearly independent correlation functions. In this case, maximizing the $\mathrm{rank}(\boldsymbol{\Pi}) \leq m$ necessitates obtaining m structures with linearly independent correlation vectors.

Given the larger number of unknowns compared to samples, sampling and regression for an underdetermined CE system are effectively addressed within the Compressive Sensing (CS) framework. Prior research indicates that a CS approach to cluster expansions can yield accurate and sparse ECI solutions using a relatively small number of DFT measurements compared to the number of correlation functions ($m \ll d$) [71, 75]. The rigorous solution of CS requires an ℓ_0-norm regularization of $\boldsymbol{J}$, but computing the $||\boldsymbol{J}||_0$ in the cost function is challenging due to its NP-hard nature. In the CS paradigm, the ℓ_0-norm can be transformed to an ℓ_1-norm when the feature matrix $\boldsymbol{\Pi}_S$ satisfies the restricted isometry property (RIP) condition [81].

Theorem 4 (Restricted Isometry Property) *Let $\boldsymbol{A}$ be an $m \times d$ matrix. The matrix $\boldsymbol{A}$ is said to satisfy the Restricted Isometry Property (RIP) of order k with constant $\delta_k \in (0, 1)$ if for all k-sparse vectors $\boldsymbol{x} \in \mathbb{R}^d$, the following inequality holds:*

$$(1 - \delta_k)||\boldsymbol{x}||_2^2 \leq ||\boldsymbol{A}\boldsymbol{x}||_2^2 \leq (1 + \delta_k)||\boldsymbol{x}||_2^2. \tag{2.38}$$

To satisfy the RIP in compressive sensing, a key quantity is a coherency between the sensing (measurement) basis Φ and the representation basis Ψ.

$$\nu(\Phi, \Psi) = \sqrt{N} \max_{j,k} |\langle \phi_j, \psi_k \rangle|. \tag{2.39}$$

The probability of correct recovery from M measurements exceeds $1-\delta$ if the number of measurements satisfies $M \geq C\nu(\Phi,\Psi)^2 S\ln(N/\delta)$, where C is a constant and S is the number of non-zero elements. In the context of CE, the representation basis are formed by the symmetry distinct orbits β, and the measurements are formed by the configurations $\{\boldsymbol{\sigma}\}$. For the representation Φ, the Kroenecker δ's hold $\phi_{\beta_g}(\beta_f)=\delta_{fg}$, where β_f and β_g represent different orbits. For the measurements Ψ, the basis function is the normalized correlation function, i.e., $\psi_{\boldsymbol{\sigma}}(\beta_f)=\Pi_{\beta_f}(\boldsymbol{\sigma})/\sqrt{\sum_\beta \Pi_\beta(\boldsymbol{\sigma})^2}$. And the coherence is given by the maximum scalar product of Φ and Ψ

$$\nu(\Phi,\Psi)=\sqrt{N}\max_{\boldsymbol{\sigma},\beta}\frac{|\Pi_{\beta_f}(\boldsymbol{\sigma})|}{\sqrt{\sum_\beta \Pi_\beta^2(\boldsymbol{\sigma})^2}}. \tag{2.40}$$

Nelson et al. [75] proposed generating a training set where each row is an identically independently distributed (i.i.d.) random vector. As illustrated in Fig. 2.7, during each iteration, an i.i.d. random vector $\vec{\pi}$ is sampled from a hyper-sphere and normalized to the current feature matrix $\boldsymbol{\Pi}_S$. The random structure with the closest distance to the normalized $\vec{\pi}$ is then added to the training set for DFT evaluation. However, in many practical cases, the configurations in training set S are correlated because structures are not randomly sampled but are mostly part of an ensemble of configurations with low energy, especially in ionic materials. Such correlations fail to satisfy the i.i.d. condition. Moreover, generating structures from a specific correlation vector is also an NP-hard problem. Although the strict compressive sensing cluster expansion is not easy to construct in practice, it is still feasible to obtain accurate and well-converged CE models by also relying on the appropriate use of structured sparsity regularization [71, 82].

In practical usage, one can separate the structure selection into two stages: (1) for the underdetermined linear system, structures are selected to construct a feature matrix with a low coherency; (2) once the number of structures is sufficient enough to reach the overdetermined region, the additional structure can be added by minimizing the variance according to Eq. (2.36).

2.4 Sparse regression with $\ell_0\ell_2$-norm regularization

In this part, the discussion focuses on how to obtain an optimized ECIs solution given by a training set with feature matrix $\boldsymbol{\Pi}_S$. Generally, the norm-regularized regression problem can be conceptualized as minimizing the cost function

$$\min_{\boldsymbol{J}}\ ||\boldsymbol{E}_{\mathrm{DFT},S}-\boldsymbol{\Pi}_S\boldsymbol{J}||_2^2+\mu||\boldsymbol{J}||_p\ ,\ ||\boldsymbol{x}||_p=\left(\sum_i |x_i|^p\right)^{\frac{1}{p}}, \tag{2.41}$$

where the p-norm of $\boldsymbol{J}$ is added to regularize the fit and suppress over-fitting, and μ controls the degree of regularization. Figure 2.8 shows the comparison of ℓ_2, ℓ_1 and ℓ_0-norm regular-

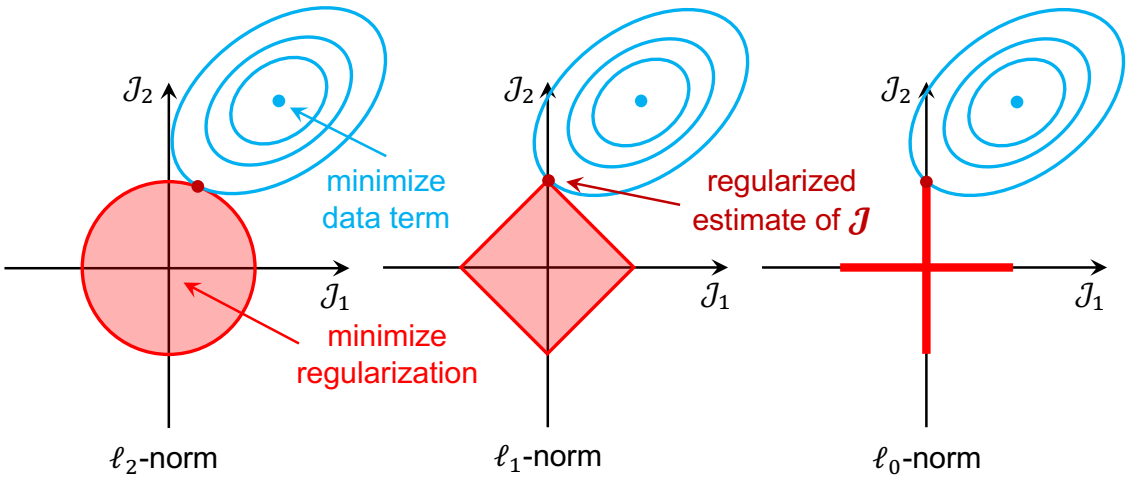

Figure 2.8: Illustration of ℓ_2, ℓ_1 and ℓ_0-norm regularization in a two-parameter space $\boldsymbol{J} = (J_1, J_2)$. The blue circles represent the contours of the data term $||\boldsymbol{E}_{\text{DFT},S} - \boldsymbol{\Pi}_S \boldsymbol{J}||_2^2$ in cost function. The red regions represent the constraints of parameters (e.g., $J_1^2 + J_2^2 \leq s$ for ℓ_2-norm, $|J_1| + |J_2| \leq s$ for ℓ_1-norm). The dark red point is the intersection of the data term and the regularization of parameters, which jointly determines the estimation of $\boldsymbol{J}$. (Ref. [83])

ization in a two-parameter space $\boldsymbol{J} = (J_1, J_2)$. The blue circles are the contours of the data term error $||\boldsymbol{E}_{\text{DFT},S} - \boldsymbol{\Pi}_S \boldsymbol{J}||_2^2$. The red regions represent the regularization constraints on the parameters ($||\boldsymbol{J}||_p \leq s$), which can be transformed to a Lagrangian form in Eq. (2.41).

Theorem 5 (Lagrange multiplier) *Let $f(\boldsymbol{x})$ be a loss function that needs to be minimized, and let $g_j(\boldsymbol{x})$ and $h_k(\boldsymbol{x})$ be the inequality and equality constraints, respectively, such that:*

$$g_j(\boldsymbol{x}) \leq 0, \quad j = 1, \ldots, p, \quad h_k(\boldsymbol{x}) = 0, \quad k = 1, \ldots, q. \tag{2.42}$$

The Lagrangian form of the optimization problem with these boundary constraints can be written as:

$$\mathcal{L}(\boldsymbol{x}, \boldsymbol{\lambda}, \boldsymbol{\mu}) = f(\boldsymbol{x}) + \sum_{j=1}^{p} \lambda_j g_j(\boldsymbol{x}) + \sum_{k=1}^{q} \mu_k h_k(\boldsymbol{x}), \tag{2.43}$$

where $\boldsymbol{\lambda} = (\lambda_1, \ldots, \lambda_p)$ and $\boldsymbol{\mu} = (\mu_1, \ldots, \mu_q)$ are the Lagrange multipliers associated with the inequality and equality constraints, respectively.

The dark red point is the regularized estimation of $\boldsymbol{J}$, which is the intersection between the data error term and the regularization term. The ℓ_1-norm tends to generate sparser solutions compared with the ℓ_2-norm because the intersection is likely to be located on the

axis. The ℓ_0-norm counts the non-zero elements of $\boldsymbol{J}$, where the intersection is exactly located on the axis and thus the ℓ_0-norm imposes an exact sparsity constraint on $\boldsymbol{J}$.

Conventionally, ℓ_2-norm (*ridge regression*, $p = 2$) regularization can be applied when the problem is overdetermined. The ℓ_2-norm regularized regression reduces the over-fitting caused by intrinsic noise in the training data. This can be achieved solely by introducing the ℓ_2 regularization function and additionally using the mixed-basis expansion [84, 85]. Bayesian approaches have also been successfully applied to estimate the ECIs with a prior distribution in several binary systems [78, 86, 87].

However, in most multicomponent systems, the problem is underdetermined as the number of ECIs increases combinatorially with the number of species, scaling approximately as $\prod_k (M_k - 1)^{n_k}$, where M_k is the number of species on the k-th sublattice, and n_k is the number of cluster sites in the same sublattice k. The explosion in the number of basis functions when many species can occupy a site makes it difficult to predefine which cluster basis functions contribute to the expansion for high dimensional multicomponent systems (i.e., which cluster basis function has a non-zero element in the solution of $\boldsymbol{J}$). Hence, a sparse solver for ECIs incorporating feature selection is necessary. Although the ℓ_1-norm regularized regression exhibits some feature selection capabilities, as demonstrated in subsequent sections, its performance is inferior to that of the ℓ_0-norm with structural sparsity.

In the subsequent sections, an $\ell_0\ell_2$-norm regularization approach incorporating hierarchy constraints to develop more robust and predictive CE models is discussed. First, the $\ell_0\ell_2$ penalty term and hierarchy constraints are introduced within the context of mixed-integer quadratic programming (MIQP). Second, the sparsity and convergence rate of ECIs are compared and discussed with those of the conventional ℓ_1 method in the Li–Mn–V–Ti–O–F disordered rocksalt system. Finally, it is demonstrated that an $\ell_0\ell_2$-regularized CE better reproduces the correct physical interactions compared to the ℓ_1-CE, in terms of computed phase diagrams, voltage profiles, and related physical quantities in the Li–Mn–Ti–O system.

2.4.1 The ℓ_0-norm regularization

In Eq. (2.41), $p = 0$ manifests itself as a pseudo-norm that counts the number of non-zero elements of $\boldsymbol{J}$:

$$||\boldsymbol{J}||_0 = \sum_i \mathrm{Ind}(J_i),\ \mathrm{Ind}(J_i) = \begin{cases} 0, J_i = 0 \\ 1, J_i \neq 0 \end{cases} \tag{2.44}$$

Adding the ℓ_0 term into the cost function directly penalizes the number of non-zero ECIs, yielding better sparseness in its solution. However, optimizing a cost function with an ℓ_0 term is an NP-hard problem and is difficult to present in a direct way [81, 88]. Previously, Huang et al. [89] has approached the problem by rewriting ℓ_0 optimization as a mixed-integer

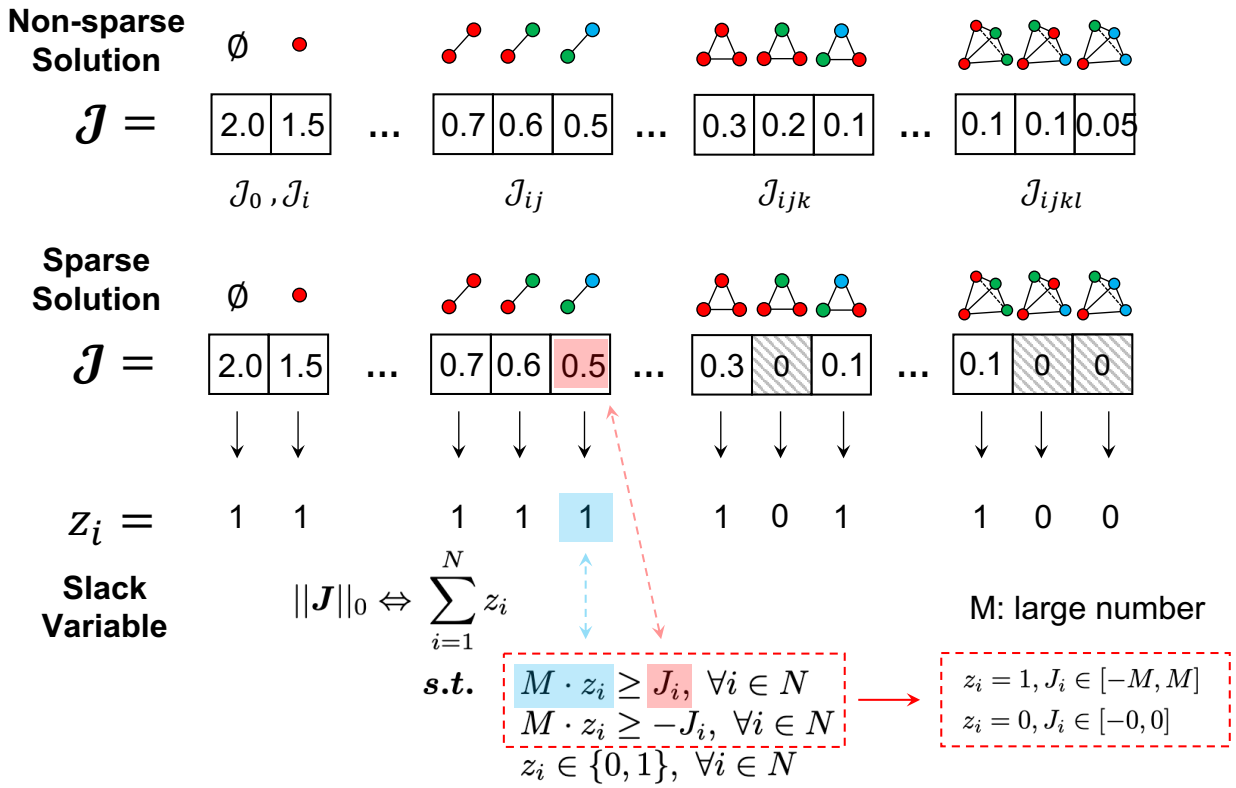

Figure 2.9: Illustration of converting the ℓ_0-norm regularization into integer programming with boundary conditions. The slack variables can take the value of 0 or 1, indicating whether the corresponding ECI is zero or non-zero. The ECI values depicted in the plot are arbitrary and serve only illustrative purposes.

programming problem, such that

$$\begin{aligned} \min ||\boldsymbol{J}||_0 \quad \Leftrightarrow \quad \min \ & \sum_{c \in \boldsymbol{C}} z_{0,c} \\ \boldsymbol{s.t.} \quad & M z_{0,c} \geq J_c, \ \forall c \in \boldsymbol{C} \\ & M z_{0,c} \geq -J_c, \ \forall c \in \boldsymbol{C} \\ & z_{0,c} \in \{0,1\}, \ \forall c \in \boldsymbol{C} \end{aligned} \tag{2.45}$$

where M is a sufficiently large number (larger than the maximum possible absolute value of any ECI), and $z_{0,c}$ is a slack variable (binary integer) indicating whether the ECI of orbit c is zero or not. J_c is constrained to 0 when the slack variable $z_{0,c} = 0$ (inactive) and to $[-M, M]$ when $z_{0,c} = 1$ (active) as illustrated in Fig. 2.9. In practice, it is shown that one can at least obtain a sparseness-improved near-optimal solution within a reasonable CPU time cutoff using a high-performance software package such as `cvxopt` or `gurobi` [90].

2.4.2 Hierarchy constraints

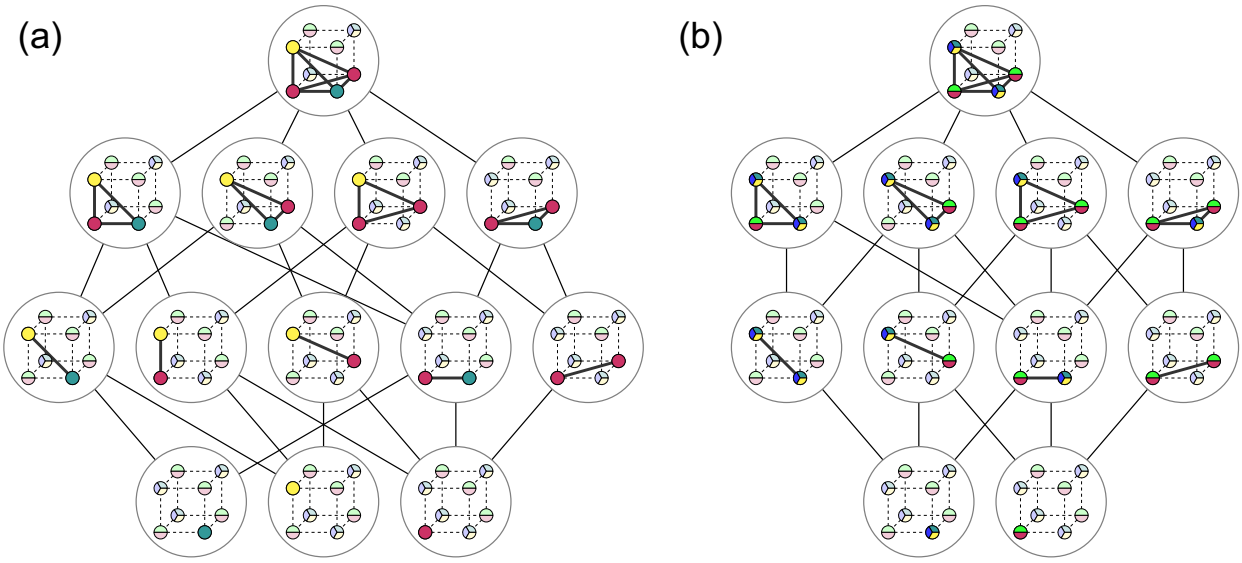

Figure 2.10: Schematic illustrations of hierarchically constrained sparsity for a rocksalt structure. The site coloring in the images represents non-constant site functions. In the illustration there are two types of site spaces, one with 4 allowed species (3 non-constant site functions); and another with 3 allowed species (2 non-constant site functions). (a) Hierarchical relations for a specific quadruplet correlation function and all its possible factors. (b) Hierarchical relations between groups of correlation functions acting over the same orbits of quadruplet clusters and all correlation function groups acting over the orbits of sub-clusters of the quadruplet cluster. (Ref. [63])

In a CE, clusters are usually enumerated in an iterative, low-to-high order (i.e., from singlets to pairs, triplets, quadruplets, and so on). Practically, the CE is truncated to a maximum of n (e.g., quadruplet clusters with $n = 4$ are a typical limit), ignoring the higher-order interactions to control the model complexity. To differentiate the cluster orbits by different significance, one of the basic assumptions of CE is based on the premise that n-body cluster interactions become less important to the configurational energy (or other scalar properties) as n becomes larger. This assumption means that the majority of the fitted property can be described by the lower-order interactions and that the higher-order interactions serve as the fine-tuning part of the fitting.

Such a physically inspired concept can be introduced in the form of hierarchy constraints, as has been done successfully in some previous studies [76, 91, 92]. The hierarchy constraint manifests itself as $J_b \neq 0$ if and only if $J_a \neq 0$ ($a \subset b$), where a and b are a lower- and higher-order cluster function orbit, respectively, and b contains all the site bases of a as a

subset. In the MIQP representation, the hierarchy relationship can be easily expressed as a constraint between slack variables:

$$z_{0,b} \leq z_{0,a}, \ a \subset b. \tag{2.46}$$

This treatment was first proposed by Huang et al. [89], where it was used in the $\ell_0\ell_1$-norm regularization paradigm; however, it may encounter the pseudo-activeness as described in the following content.

2.4.3 The ℓ_2-norm regularization

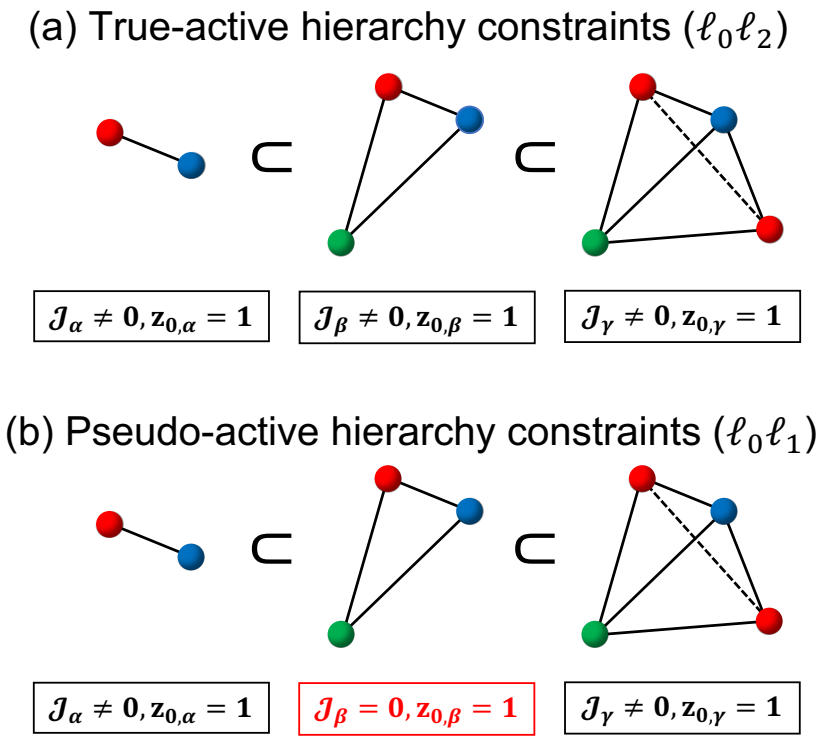

Figure 2.11: Illustration of hierarchy relations ($\alpha \subset \beta \subset \gamma$) between pair, triplet, and quadruplet orbit. The different colors on the cluster sites represent the decorating species for a given site-basis function. The equation in red shows a pseudo-active hierarchy constraint that may appear in ℓ_1 and its derivative methods. (Ref. [83])

It is proposed that combining ℓ_2-norm and ℓ_0-norm regularization can impose true hierarchy constraints, unlike the $\ell_0\ell_1$-norm. It is to be noted that the inequality between slack variables does not necessarily impose the hierarchy relation ($J_b \neq 0$, iff $J_a \neq 0$). This is because the hierarchy constraints are defined on the magnitude of ECIs J_a and J_b, while

the slack variables $z_{0,b}, z_{0,a}$ are intermediate to represent the presence or exclusion of the variables.

When implementing the hierarchy constraints in $\ell_0\ell_1$-norm regularization, pseudo-active behavior can manifest itself when a $J = 0$, but its slack variable $z_0 = 1$ within the MIQP paradigm. J can be regularized to zero, which is still a valid solution between $[-M, M]$, even with $z_0 = 1$. This is caused by the fact that the ℓ_1-norm has feature-selection properties that intrinsically produce a sparse solution [93]. This pseudo-activeness can introduce excessive sparseness to the solution and break the hierarchy constraints. Figure 2.11 presents an example of pseudo-activeness in $\ell_0\ell_1$-norm regularization. The excessive sparseness is introduced to the orbit β with $J_\beta = 0$, while all orbits α, β, γ has active slack variables $z_0 = 1$. The higher-order orbit γ is erroneously activated while $J_\beta = 0$. To avoid such a situation and ensure proper function with ℓ_0 under hierarchy constraints, a norm with no feature-selection properties is required. The ℓ_2-norm is a natural choice.

With the introduction of the $\ell_0\ell_2$-norm and hierarchy constraints, the final ECI optimization problem can be written as

$$\begin{aligned} \min_{\boldsymbol{J}} \;& \boldsymbol{J}^T \boldsymbol{\Pi}_S^T \boldsymbol{\Pi}_S \boldsymbol{J}^T - 2\boldsymbol{E}_{\mathrm{DFT}}^T \boldsymbol{\Pi}_S \boldsymbol{J} + \mu_0 \sum_{c \in \boldsymbol{C}} z_{0,c} + \mu_2 ||\boldsymbol{J}||_2^2 \\ \textbf{\textit{s.t.}} \;& M z_{0,c} \geq J_c, \; \forall c \in \boldsymbol{C} \\ & M z_{0,c} \geq -J_c, \; \forall c \in \boldsymbol{C} \\ & z_{0,b} \leq z_{0,a}, \; \forall a \subset b, \; \{a, b\} \in \boldsymbol{C} \\ & z_{0,c} \in \{0, 1\}, \; \forall c \in \boldsymbol{C}, \end{aligned} \tag{2.47}$$

where $||\boldsymbol{J}||_2^2 = \boldsymbol{J}^T \boldsymbol{J}$ penalizes the magnitude of ECIs, thus avoiding over-fitting by regularizing sampling noise while the ℓ_0-term $\sum_c z_{0,c}$ optimizes the sparseness. The hierarchy constraints ensure correct containment relationships by manifesting lower-order ECIs first to reduce redundancy.

2.4.4 Robustness and convergence of the $\ell_0\ell_2$-norm regularized regresssion

The convergence of the CE when the $\ell_0\ell_2$-norm and hierarchy constraints are enforced was tested on the configurational disorder in the LiF–MnO–$LiVO_2$–Li_2TiO_3 composition space. The CE model contains pair interactions up to 7.1 Å, triplets up to 4.0 Å, and quadruplets up to 4.0 Å based on a lattice parameter $a = 3$ Å for the primitive cell. Figure 2.4(a) presents the rocksalt framework of a DRX structure. The framework contains a cation sublattice (red) and anion sublattice (gray), where the cation sites can be occupied by Li and transition metals (TM, including Mn^{2+}, V^{3+}, Ti^{4+} in this example) and the anion sites can be occupied by O^{2-} and F^-. A species indicator where the site basis function reads $\phi_j(\sigma_i) = \delta_{i,j}$ was used [70]. The electrostatic energy (Ewald energy E_0/ε_r) is included to capture long-range electrostatic interactions [16, 94] (see Section 4.2 for detailed statements). In total, 162 ECIs

(including the constant term J_0) are predefined in the CE Hamiltonian. For this system, DFT calculations were performed with VASP using the projector-augmented wave method[95, 96], a plane-wave basis set with an energy cutoff equal to 520 eV, and a reciprocal space discretization of 25 k-points per Å^{-1}. All calculations were converged to 10^{-6} eV in total energy for electronic loops and 0.02 eV/Å in interatomic forces for ionic loops. The Perdew-Burke-Ernzerhof (PBE) generalized gradient approximation exchange-correlation functional [39] with rotationally averaged Hubbard U correction (GGA+U) was used to compensate for the self-interaction error on all transition-metal atoms except titanium [33] (3.9 eV for Mn and 3.1 eV for V). After DFT evaluation, the dimension of the feature matrix $\mathbf{\Pi}_{\mathrm{DFT},S}$ is 487 × 162. The performance of the $\ell_0\ell_2$-CE is compared with the ℓ_1-CE. Two major improvements are emphasized in the $\ell_0\ell_2$-CE.

Sparseness vs. cross-validation error

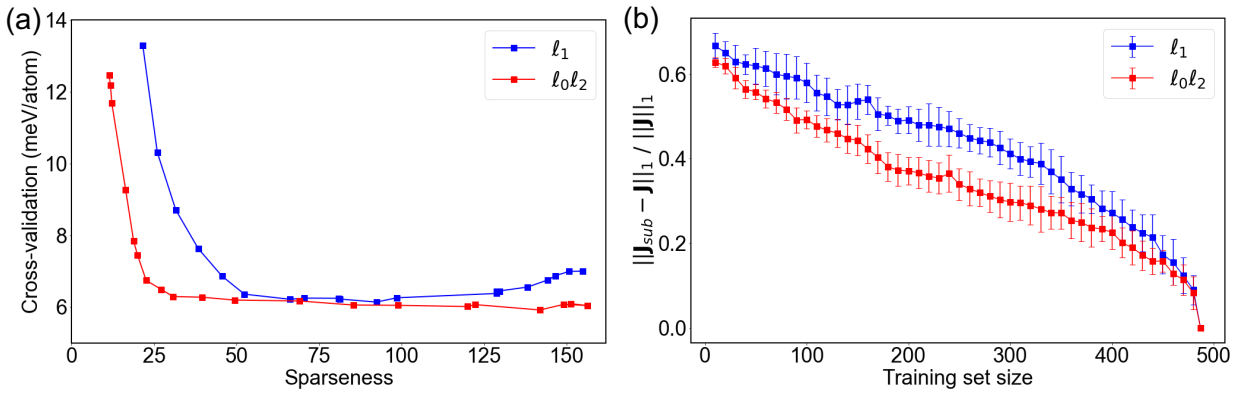

Figure 2.12: (a) Cross-validation error (meV/atom) of the ℓ_1-CE and the $\ell_0\ell_2$-CE. The sparseness is the number of non-zero ECIs in the fit ($||\boldsymbol{J}||_0$). The curves are generated by varying hyperparameters μ_0, μ_1, and μ_2 in regularization. (b) ECIs convergence test vs. training set size. $\boldsymbol{J}$ is the ECIs fitted with full training data, and $\boldsymbol{J}_{sub}$ is the ECIs fitted with a subset of the corresponding size. (Ref. [83])

Cross-validation (CV) error vs. model complexity is a general metric used to evaluate the robustness of a CE model. The optimal trade-off between under-fitting and over-fitting can be found with a CV test, where the optimal model is fitted with the regularization hyper-parameter μ that minimizes the CV error. In our test, a k-fold CV error is used,

$$\mathrm{CV} = \sqrt{\frac{1}{k}\sum_{j=1}^{k}\mathrm{MSE}_j}, \;\; \mathrm{MSE} = \frac{1}{N}\sum_{i=1}^{N}(E^i_{\mathrm{DFT}} - E^i_{\mathrm{CE}})^2, \tag{2.48}$$

where CV is the cross-validation error averaged over k splits of the validation dataset, and MSE is the mean-squared-error of each validation dataset. Here, N is the size of the valida-

tion dataset, and $k = 5$ is the number of folds. In our tests, the regularization hyperparameter μ is selected from the logarithm space between $[10^{-6}, 10^{-1}]$. The sparseness is defined as the number of non-zero elements of the solution ($||\boldsymbol{J}||_0$) and represents the model complexity.

The CV error versus sparseness is presented in Fig. 2.12(a) for an ℓ_1 and $\ell_0\ell_2$-norm regularized CE. For the $\ell_0\ell_2$-CE, the CV error remains low as the sparseness varies between 25 and 150 ECIs. In this regime, the $\ell_0\ell_2$-CE shows no sign of over-fitting as the CV error remains near the global minimum around 6 meV/atom. The ℓ_1-CE shows a similar optimal CV error as that of $\ell_0\ell_2$-CE near this *minimum plateau* regime from 50 to 100 in sparseness. However, as the model complexity changes, the CV error increases at both low and high sparsity, indicating that the ℓ_1-CE is less robust against the choice of model complexity. Therefore, it is concluded that the $\ell_0\ell_2$-CE can reach low CV error with a lower complexity, which is empirically believed to result in models that better reproduce physics. A more sparse CE can increase the computational speed of energy evaluations and is also less sensitive to model complexity change as compared with the ℓ_1-CE.

Convergence of ECIs with a subset of training data

The second point to be emphasized is that the $\ell_0\ell_2$-CE converges to its most accurate solution faster than the ℓ_1-CE, which lowers the risk of obtaining an over-fitted result when the configuration space is under-sampled. This is an important improvement in the practical use of CE constructions. To test this hypothesis and mimic the iterative sampling process, a numerical experiment based on a finished DFT dataset (with 487 structures in total) was designed. Then, the quality of fits performed on subsets of training data of increasing size was evaluated and subsequently compared the subset-fitted ECIs $\boldsymbol{J}_{sub}$ with the full-set result. In such a comparison, the ground-truth (full set) solution is set as follows: (1) For the ℓ_1-CE, the regularization parameter μ_1 is chosen at the minimum CV error according to Fig. 2.12(a). This solution has 99 non-zero ECIs when all 487 training structures are used in the fitting. (2) For the $\ell_0\ell_2$-CE, to compare the convergence rate under a similar degree of model complexity, hyperparameters are selected such that the ℓ_1-CE and $\ell_0\ell_2$-CE have similar sparsity. The resulting $\ell_0\ell_2$-CE has 92 non-zero ECIs with all 487 training structures included according to Fig. 2.12(a).

After setting the hyperparameters for both models, the normalized absolute difference $||\boldsymbol{J}_{sub} - \boldsymbol{J}||_1/||\boldsymbol{J}||_1$ between the ℓ_1-CE (blue line) and $\ell_0\ell_2$-CE (red line) was compared in Fig. 2.12(b). For each subset size, ten randomly selected subsets with the same size were evaluated and averaged. The solid square represents the average, and the error bar represents the standard deviation resulting from different subsets. Figure 2.12(b) indicates that the ℓ_1-CE demonstrates a higher deviation from the ground-truth solution and converges more slowly to it than the $\ell_0\ell_2$-CE as the training set is increased. This result unambiguously demonstrates the robustness of $\ell_0\ell_2$-CE to work with small input data sets.

2.4.5 ECIs with improved physics

From a general perspective of machine learning, the predictions of energies are made by fitting statistical models on a group of data points. The statistical models can predict the absolute energy with high accuracy by minimizing the cost function, which is constructed by the difference between the prediction and observation of the training data. However, in materials science, relative energy quantities are of greater significance than the absolute one (such as energy above the hull, phase diagram, and the derivatives of formation energy with respect to the compositional variables). Bartel et al. [97] critically examined several ML models for energetics prediction and found that while the models predict the formation energy (ΔH_f) of materials well, they failed to predict the relative phase stability. Such a dilemma indicates that the prediction error (CV or RMSE) is not the only thing one should consider when constructing a statistical model for the energy.

To demonstrate that the $\ell_0\ell_2$-CE also leads to a more physically informed solution, a multicomponent system is studied: Li–Mn–Ti–O oxide in an FCC rocksalt framework, with Li^{+}–Mn^{2+}–Mn^{3+}–Mn^{4+}–Ti^{4+}–vacancy disorder on the octahedral cation sites and Li^{+}-Mn^{2+}–Mn^{3+}–vacancy disorder on the interstitial tetrahedral sites. The Li–Mn–Ti–O composition space contains a number of battery-relevant systems [17]. These battery systems are charged and discharged by adding or removing lithium (i.e., lithiation or delithiation) and a charge-compensating electron, which reduces or oxidizes a transition metal. As a result, an important physical property to correctly model in the Li–Mn–Ti–O system is the energetics of Li in octahedral vs. tetrahedral sites. One significant battery-relevant system in which the effects of Li local environment preference are especially presented is the $LiMn_2O_4$ spinel. When fully lithiated to $Li_2Mn_2O_4$, Li-ions occupy octahedral sites while the Li-ions occupy tetrahedral sites for compositions $Li_xMn_2O_4$ when $x \leq 1$.

CE models for Li-Mn-Ti-O systems

The CE was generated with pair interactions up to 7.1 Å, triplet interactions up to 4.0 Å, and quadruplet interactions up to 3.0 Å based on a primitive cell of the rocksalt structure with lattice parameter $a = 3$ Å. A sinusoid site basis as shown in Fig. 2.29 was used. In total, 1475 ECIs (including the constant term J_0) were predefined in the CE Hamiltonian. The dimension of the feature matrix is 1137×1475. Because of the high compositional dimensionality, the possible number of ECIs within the interaction cutoffs is large. In addition, there are some constraints on the occupancies in the Li–Mn–Ti–O system, such as (1) the total number of Li, transition metals, and vacancies is fixed between octahedral and tetrahedral cation sublattice; (2) the net charge of the system must be neutral, etc. These relations and the inability to sample all possible configurations with DFT reduce the rank of the feature matrix below the dimension ($\text{rank}(\mathbf{\Pi}_S) = 557$), which indicates that a sparse solution is required.

From the test results in Fig. 2.12, it is noticed that when the sparseness varies, the

variation of the CV error is smaller when the CE is regularized with the $\ell_0\ell_2$-norm than with the ℓ_1-norm. This result indicates that $\ell_0\ell_2$ has a hyperparameter space that is larger and more tunable, whereas the ℓ_1-CE is more deterministic with a small range of optimal μ_1 obtained by minimizing the CV error. Motivated by this observation, the selection of ECIs for the Li–Mn–Ti–O system was completed as follows.

The regularization strength μ_1 in the ℓ_1-CE was selected from the stable plateau region when minimizing the CV error in *lasso* (e.g., the μ_1 associated with points between sparseness of 50 to 100 in Fig. 2.12). For the $\ell_0\ell_2$-norm, the μ_2 was selected from the stable plateau region by minimizing the CV error in *ridge regression*, similar to what is done for ℓ_1-CE. After obtaining the optimal μ_2, the solution for $\ell_0\ell_2$-CE was further determined by searching μ_0 for a solution with the proper sparseness (at least $||\boldsymbol{J}||_0 < \text{rank}(\boldsymbol{\Pi}_S)$, $\mu_1, \mu_2, \mu_0 \in [10^{-6}, 10^{-1}]$). For both ℓ_1-CE and $\ell_0\ell_2$-CE, several models with low CV error were tested for their ability to well reproduce physical properties, such as minimal violation of DFT ground states in the phase diagram, voltage profile comparison against DFT, as well as the Li-site energy difference between tetrahedral and octahedral occupancy. The best-performing models for both ℓ_1 and $\ell_0\ell_2$ are presented in Fig. 2.13, respectively.

Ground-state phase diagrams

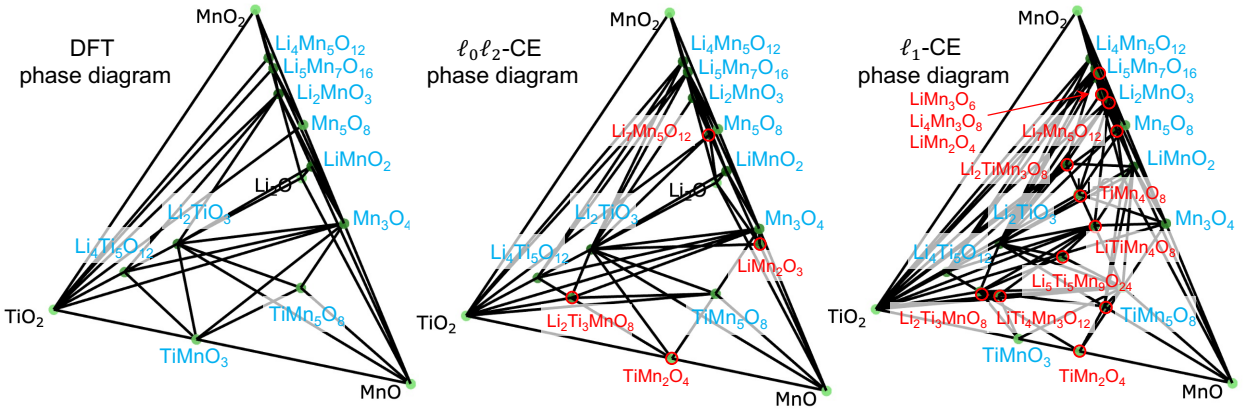

Figure 2.13: Phase diagram generated with DFT, $\ell_0\ell_2$-CE, and ℓ_1-CE. The DFT ground states are labeled in blue text. The incorrectly predicted ground states are labeled with red circles and text. (Ref. [83])

Figure 2.13 presents a comparison of ground-state phase diagrams with the ℓ_1-CE predictions, $\ell_0\ell_2$-CE predictions, and DFT calculations. The phase diagrams were generated with in-sample training data (all 1137 structures evaluated with DFT) for both DFT and CE models. The DFT phase diagram is taken as the ground truth. In formation-energy prediction, the phase diagram is a key quantity that directly demonstrates the correct physics

near the ground states. As the ground states are formed variationally, they are particularly discerning towards spurious ECIs, as the non-physical noisy interactions often create new ground states leading one to miss the true ground states. Thus, a well-reproduced phase diagram is desirable for a CE model. In our tests, the ℓ_1-CE creates 12 new ground states, indicating that the correct physics in terms of cluster interactions is not well captured. However, the $\ell_0\ell_2$-CE preserves most of the DFT ground states, with only four spurious "ground states" in the $\ell_0\ell_2$-CE phase diagram.

Voltage profiles & Li-site energy

To further evaluate the performance of the $\ell_0\ell_2$-CE and ℓ_1-CE, two additional tests are introduced to ensure that the CE models accurately represent the physics of Li octahedral and tetrahedral site preferences. Specifically, it is compared how well the CE model reproduces: (1) energy differences between the Li in the tetrahedral and octahedral sites in layered MnO_2 and spinel MnO_2 frameworks and (2) a simplified spinel voltage profile against the DFT ground truths. The simplified spinel voltage profile includes the fully lithiated rocksalt-like $Li_2Mn_2O_4$, the spinel $LiMn_2O_4$, the commonly seen $Li_{0.5}Mn_2O_4$ ordering, and the fully delithiated Mn_2O_4 and is calculated by taking the average voltage between each set of adjacent orderings. The average voltage is calculated using DFT and the following equation:

$$\bar{V}(x_1, x_2) \approx -\frac{E_{\mathrm{Li}_{x_1}\mathrm{Mn_2O_4}} - E_{\mathrm{Li}_{x_2}\mathrm{Mn_2O_4}} - (x_1 - x_2)E_{\mathrm{Li}}}{F(x_1 - x_2)}, \tag{2.49}$$

where x_1 and x_2 are adjacent Li contents with $x_1 > x_2$, E_{Li} is the DFT energy of bcc Li metal, and F is the Faraday constant [98].

The improvement in the physics of the predictions associated with applying the $\ell_0\ell_2$-norm with hierarchy constraints is further demonstrated by the voltage profile and Li-occupancy energy. In Fig. 2.14(a), the voltage profiles generated by prediction using the ℓ_1-CE and $\ell_0\ell_2$-CE (blue lines) are compared with those from DFT (orange lines), taken as the ground truth. One can see that the ℓ_1-CE incorrectly predicts the voltage plateau between $x = 0.5$ to 1 in the $Li_xMn_2O_4$ spinel-like structure such that the $x = 0.5$ configuration is no longer stable (the voltage between $x = 0.5$ and $x = 1.0$ is higher than that between $x = 0.0$ and $x = 0.5$). In contrast, the $\ell_0\ell_2$-CE matches very well with the DFT-generated voltage profiles. The erroneous predictions of the ℓ_1-CE are further confirmed by the Li-occupancy energy. In Fig. 2.14(b), the energy difference between Li in octahedral and tetrahedral occupancy was evaluated in the layered-MnO_2 and spinel-MnO_2 frameworks. The absolute error compared with DFT is 0.52 eV (layered) and 0.18 eV (spinel) for the ℓ_1-CE, whereas that for the $\ell_0\ell_2$-CE is 0.09 eV (layered) and 0.09 eV (spinel), respectively. A significant reduction of prediction error is observed with the $\ell_0\ell_2$-norm regularized CE.

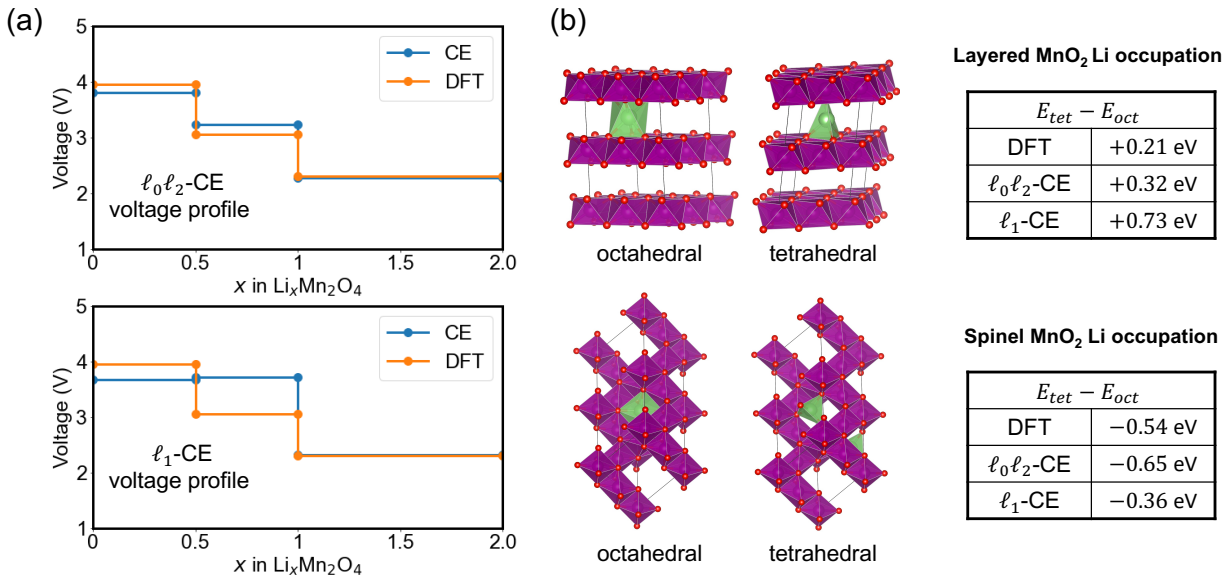

Figure 2.14: (a) The simplified spinel voltage profile (blue line) generated by ℓ_1-CE and $\ell_0\ell_2$-CE for spinel orderings in $Li_xMn_2O_4$ is compared with the DFT ground-truths (orange line). (b) Energy difference of Li occupation in octahedral and tetrahedral sites in layered MnO_2 (upper) and spinel MnO_2 framework (lower). (Ref. [83])

Discussion of MIQP for $\ell_0\ell_2$-norm regularization

To obtain a model that represents the physics of a system well, the relative difference of energies between configurations is of greater significance than the absolute ones. In ordinary least-squares fitting, the cost function only focuses on the global averaged error of the training set, which leads to over-fitting. Adding regularization of the ECIs can alleviate this issue by constraining the optimization space of parameters, but our results show that not all regularization creates physically meaningful solutions. It is beneficial to include the physically inspired constraints into the design of the cost function, such as adding hierarchy constraints with $\ell_0\ell_2$-norm implementation. The $\ell_0\ell_2$-CE can improve the physical meaning of the solution and break the correlation between coupled clusters, which is achieved by directly penalizing the number of non-zero ECIs for feature selection and enforcing hierarchy relations between ECIs via the slack variables in the MIQP paradigm.

In two complex oxide systems, it is shown that the $\ell_0\ell_2$-CE with hierarchy constraints outperforms the conventional ℓ_1-CE in terms of sparseness against CV error, convergence rate with a subset of training data, and some critical physical quantities in Li intercalation materials. More generally, the optimization of the ECIs is not deterministic within a single method, and the successful construction of a CE model typically relies on two aspects: (1)

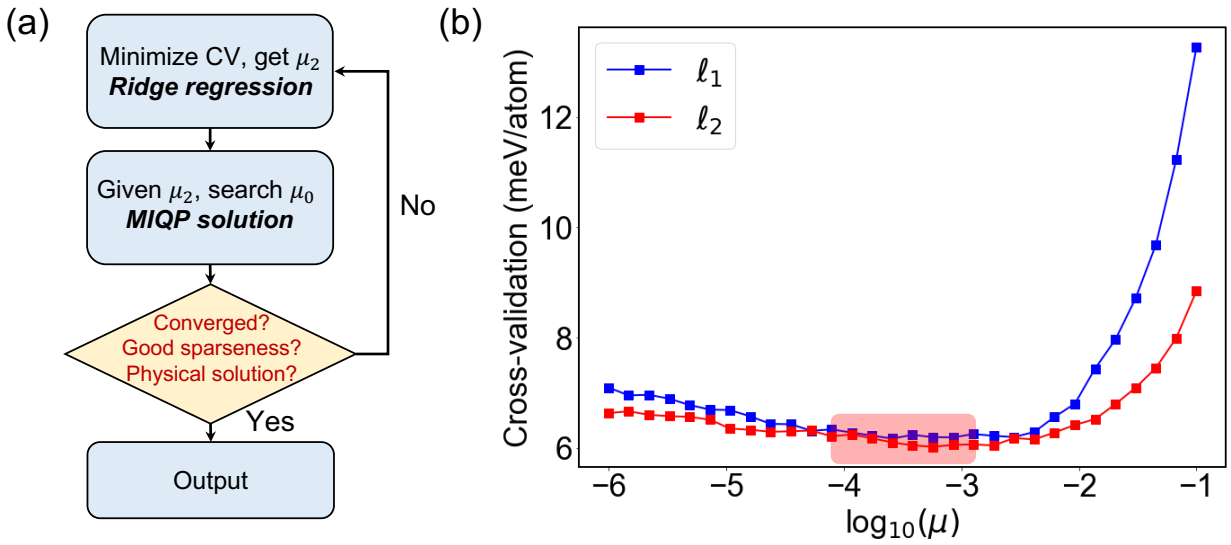

Figure 2.15: (a) The procedure to obtain an $\ell_0\ell_2$-norm regularized solution, including finding the μ_2 by minimizing the CV error in ridge regression, sparseness engineering with ℓ_0 using MIQP, and terminating if the solution is converged with good sparseness, as well as good-reproduction-relevant physical properties. (b) The CV error vs. regularization strength for both pure ℓ_1-norm and ℓ_2-norm, depicted using the Li-Mn-V-Ti-O-F system as an example. A suitable choice for the regularization strength is identified from the plateau in the region with low CV error, which is then used for further MIQP optimization.

choosing a valid interaction space by truncating the clusters or orbits and (2) applying a proper optimization algorithm to obtain the ECIs. The results in this paper show that for the second step, the $\ell_0\ell_2$-norm method is the superior choice for a robust and physical solution compared to the conventional ℓ_1 method.

One limitation of the $\ell_0\ell_2$-norm method within the MIQP paradigm that has been observed is its computational efficiency. As solving the ℓ_0-norm is an NP-hard problem, more computational time is required to solve the MIQP when more predefined ECIs are included. The $\ell_0\ell_2$-CE works well for relatively small or well-predefined systems ($\dim(\mathbf{\Pi}_S) \leq 2000$). Therefore, the most applicable way to use $\ell_0\ell_2$-norm regularized CE with hierarchy constraints is likely to be as follows: (1) define a CE within a relatively small cutoff and truncate to quadruplet or quintuplet clusters at most (ideally staying within $\dim(\mathbf{\Pi}_S) \leq 2000$) and (2) follow the procedure described in Fig. 2.15(a) and (b) to determine the optimal hyperparameter to obtain the ECIs. However, it is noted that $\dim(\mathbf{\Pi}_S) \leq 2000$ applies to virtually all known published CE.

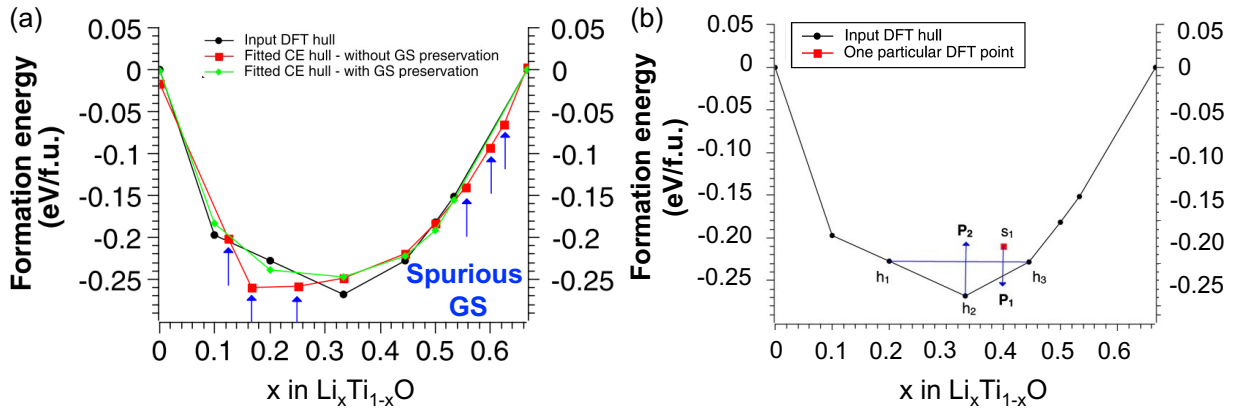

Figure 2.16: (a) Formation energy convex hull in $\mathrm{Li}_x\mathrm{Ti}_{1-x}\mathrm{O}$ system predicted by DFT (black), CE without GS preservation (red) and CE with GS preservation (green). Blue arrows label the spurious GS. (b) The conditions for GS preservation. (Ref. [99])

2.4.6 Ground state preservation method

While the $\ell_0\ell_2$-CE estimates the ECIs that are reasonably consistent with the physics near the ground states (GS), it does not strictly enforce the preservation of these ground states (i.e., phase stability). Figure 2.16(a) shows three cases of the formation energy convex hull of the $\mathrm{Li}_x\mathrm{Ti}_{1-x}\mathrm{O}$ system. The black line represents the ground truth from DFT calculations. The red line represents the convex hull predicted by CE without GS preservation, generating many spurious GS. To address the exact preservation of ground states, GS preservation can be further introduced by adding inequality constraints on the energies to optimize ECIs. As shown in Fig. 2.16, two types of inequalities need to be satisfied to ensure GS preservation. Let H be a set of GS, (1) a meta-stable configuration's energy is higher than the convex hull (any linear combination of $\{\boldsymbol{\sigma}_h, h \in H\}$); (2) a stable configuration's energy is lower than any linear combination of other stable configurations $\{\boldsymbol{\sigma}_h, h \in H \backslash h\}$). These conditions are formalized mathematically by Huang et al. [99]:

$$\begin{aligned} \boldsymbol{\Pi}(\boldsymbol{\sigma}_s)\boldsymbol{J} &\geq \sum_{i \in H} x_i \cdot \boldsymbol{\Pi}(\boldsymbol{\sigma}_i)\boldsymbol{J} + \varepsilon, \ \forall\ \boldsymbol{\sigma}_s \notin H, \\ \boldsymbol{\Pi}(\boldsymbol{\sigma}_h)\boldsymbol{J} &\leq \sum_{i \in H \backslash h} x_i \cdot \boldsymbol{\Pi}(\boldsymbol{\sigma}_i)\boldsymbol{J} - \varepsilon, \ \forall\ \boldsymbol{\sigma}_h \in H. \end{aligned} \tag{2.50}$$

where $\boldsymbol{\sigma}_i$ represents the meta-stable configuration, $\boldsymbol{\sigma}_h$ represents the meta-stable configuration (on the DFT energy convex hull), and x_i is the fraction of stable composition that $\boldsymbol{\sigma}_i$ can decompose into. The ε is a tolerance value for numerical stability (e.g., $\varepsilon = 0.001$). Eq. (2.50) can be straightforwardly formulated with MIQP as boundary conditions in mathe-

matical programming. As such, the corrected convex hull of $Li_xTi_{1-x}O$ system is shown in the green line in Fig. 2.16, where no spurious GS is predicted.

2.5 Conclusion

Chapter 2 lays out the broad methodology employed for analyzing thermodynamics in lattices from first-principles calculations. The chapter initiates with the quantum mechanics of many-electron systems and subsequently introduces the formalism of DFT. Given that the disordered rocksalt cathodes are complex oxides with substantial configurational disorder, investigating the statistical mechanics in lattices is of great significance. This can be approached via Monte Carlo simulation, which typically involves millions of energy evaluations for equilibrium sampling. Such a high amount of calculations necessitates an effective Hamiltonian to approximate DFT calculation with *ab-initio* accuracy.

Further, the chapter delves into the mathematical formulation and development of the cluster expansion method for practical applications. In particular, $\ell_0\ell_2$-norm regularization and structural hierarchy constraints are introduced into linear regression, thereby facilitating the construction of robust cluster expansions. The approach is implemented through mixed integer quadratic programming (MIQP). The ℓ_2-norm regularization serves to mitigate intrinsic data noise, while the ℓ_0-norm is employed to penalize the number of non-zero elements and incorporate the hierarchical relationship between clusters. As such, sparseness and cluster hierarchy can be well optimized to obtain a robust, converged set of effective cluster interactions with improved physical meaning. It is demonstrated that the effectiveness of $\ell_0\ell_2$-norm regularization in two high-component disordered rocksalt cathode material systems, where several metrics are compared, including the cross-validation error, convergence speed, and the reproduction of phase diagrams, voltage profiles, and Li-occupancy energies with those of the conventional ℓ_1-norm regularized cluster expansion models.

The chapter culminates with a general discussion on the development of robust, accurate, and predictive lattice models for battery materials modeling, including some other highlighted features (e.g., CE with ground-state preservation in phase diagram). This chapter thereby provides the theoretical foundation for the investigation of configurational disorder in disordered rocksalt cathode materials, which will be discussed in-depth in the following chapters.

Chapter 3

Short-range order in disordered rocksalt cathodes

3.1 Introduction

For the design of cathode materials, Li diffusion is a critical factor in determining its electrochemical performance. For rocksalt-type Li cathode, the Li diffusion occurs through an intermediate tetrahedral site (T_d, denoted as t) between two octahedral sites (O_h, denoted as o) as illustrated in Fig. 3.1, which is referred to as *o-t-o* diffusion. In layered $LiTMO_2$, the T_d sites are coordinated by either $LiTM_3$ clusters (3-TM channels, not contributing to diffusion) or Li_3TM clusters (1-TM channels, facilitating Li migration). The *o-t-o* diffusion solely takes the 1-TM channel as intralayer diffusion within the Li slab. Van der Ven et al. [100] computed the Li migration barriers for hops between adjacent octahedral sites in $LiTiS_2$ (depicted in Fig. 3.1(b)), revealing that the Li hop mechanism is primarily mediated by neighboring vacancy clusters: (1) the single vacancy hop leads to strong Coulombic interactions between Li in the activated T_d site and Li in the face-sharing O_h site; whereas (2) the divacancy hop lacks such repulsion, resulting in a lower Li diffusion barrier compared to hops into isolated vacancies.

The local environment of the T_d site significantly influences the diffusion energy barrier. In disordered rocksalt cathodes (DRX), it ranges from 0-TM to 4-TM. The 2/3/4-TM channel does not contribute to Li diffusion due to the substantial electrostatic interaction between Li in the activated T_d site and the TM in face-sharing octahedra, while the 1-TM channel allows limited Li diffusion, and only the 0-TM channel offers a low-barrier-energy pathway for facile diffusion. The calculated *o-t-o* migration barriers of 0-TM and 1-TM channels given by Lee et al. [25] with a divacancy diffusion mechanism in disordered $LiCrO_2$ and Li_2MoO_3 are presented in Fig. 3.2. For typical tetrahedral heights in a rocksalt structure, the 0-TM channel displays a barrier energy of approximately 300 meV, and the 1-TM channel exhibits around 500 meV. Furthermore, unlike the layered structure with well-defined intralayer dif-

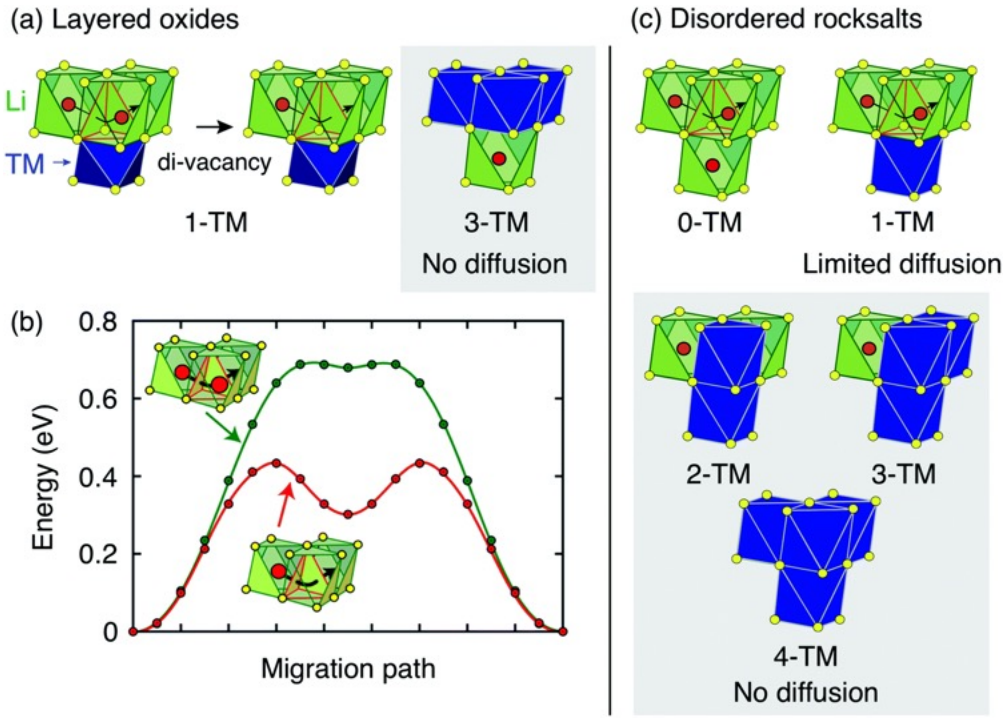

Figure 3.1: (a) Layered Li_xTMO_2 compounds exhibit 1-TM and 3-TM T_d sites, corresponding to Li_3M and LiM_3 clusters. (b) Li migration barriers for hops between neighboring O_h sites in layered Li_xMO_2 are meditated by neighboring vacancy clusters. The barrier for hops into single vacancy (green) is significantly larger than for di-vacancy hops (red line). (c) Cation-disorder results in all types of tetrahedral clusters. In this case, 0-TM channels (and with limited 1-TM channels) contribute to Li diffusion. (Ref. [14])

fusion (Li slab), facile Li diffusion requires that the 0-TM channels be connected over a long-range, i.e., a percolating 0-TM Li network. Lee et al. [25] discovered that a certain amount of Li-excess is necessary to enable such Li percolation ($x > 0.09$ in $Li_{1+x}TM_{1-x}O_2$ in the fully random limit), which explains why the stoichiometric DRX $LiTMO_2$ found in the early 1990s primarily exhibited poor electrochemical performance with limited capacity and rate capability [101], whereas the disordered $Li_{1.211}Mo_{0.467}Cr_{0.3}O_2$ identified in Ref. [25] demonstrated a significant charge/discharge capacity with Li-excess.

The diffusion of Li in various ordered and partially disordered rocksalts can be examined using a similar approach. Urban et al. [102] calculated the critical Li concentrations (x_c) necessary for 0-TM Li percolation in layered (α-$NaFeO_2$), spinel-like (LT-$LiCoO_2$), and γ-$LiFeO_2$ ordering, as depicted by black contour lines in Fig. 3.3. The x-axis represents the degree of Li-excess, while the y-axis signifies the level of cation mixing (0% for ordered structures and 100% for disordered structures in the random limit). The color map displays

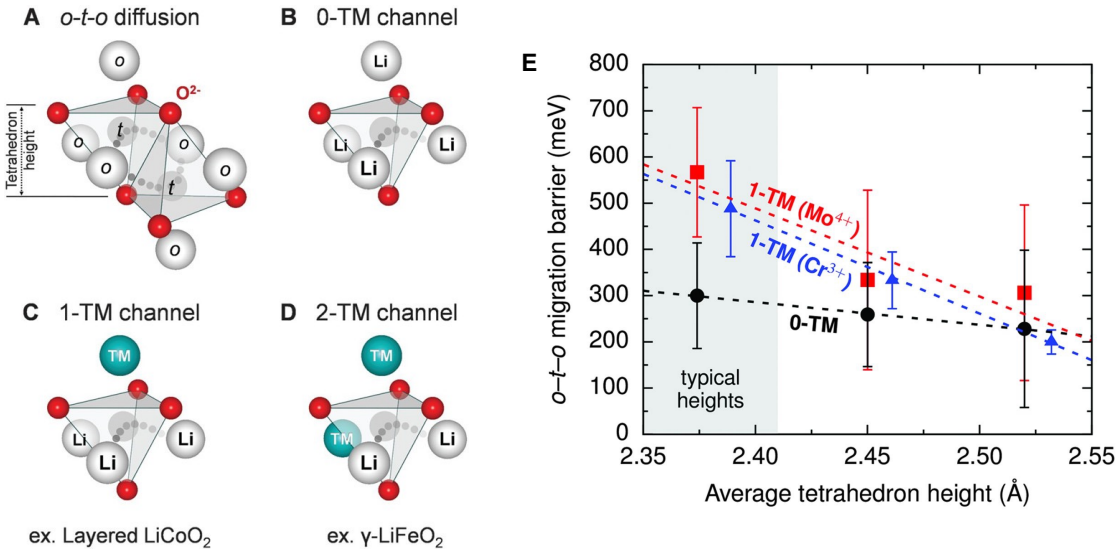

Figure 3.2: (a) Local environments for an *o*–*t*–*o* Li hop in $LiTMO_2$ oxides: two tetrahedral paths connect each pair of neighboring octahedral sites. The activated state in T_d can share faces with no octahedral TM (0-TM channel), one TM (1-TM channel), or two TM (2-TM channel). Calculated Li migration barriers along 1-TM channels for Mo^{4+} (red line) and Cr^{3+} (blue line), and 0-TM channels (black line) as a function of the average tetrahedron height. The error bars denote standard deviation, and the shaded area highlights typical tetrahedron heights of disordered materials (Ref. [25])

the available Li content per f.u., with the red region indicating non-percolating stoichiometry. The outcomes reveal that the lack of reversible Li^+ intercalation in the γ-$LiFeO_2$ structure is attributed to the presence of only 2-TM tetrahedral environments [17], necessitating a substantial Li-excess ($x_c > 1.3$). The spinel-type ordering results in segregation into 0-TM, 2-TM, and 4-TM environments, wherein the connected 0-TM facilitates easy Li^+ diffusion [26] ($x_c > 0.8$).

The determination of cation ordering in practical cases depends on the thermodynamic equilibrium states of the compositions. In thermodynamic equilibrium, the atomic structure is governed by internal energy and entropy. The long-range order (LRO) describes the atomic structure exhibiting periodic repetition throughout the material, which is commonly found at low temperatures, while it tends to diminish at elevated temperatures and goes along with a phase transition. In contrast, the correlations between atoms may still exist across finite spatial extents (e.g., several neighboring shells), and the atomic configuration may retain certain non-random characteristics and exhibit short-range order (SRO).

Ferrari et al. [32] presents an introductory example of configurations of a two-dimensional binary alloy at low-, medium-, and high temperatures, where the interactions between

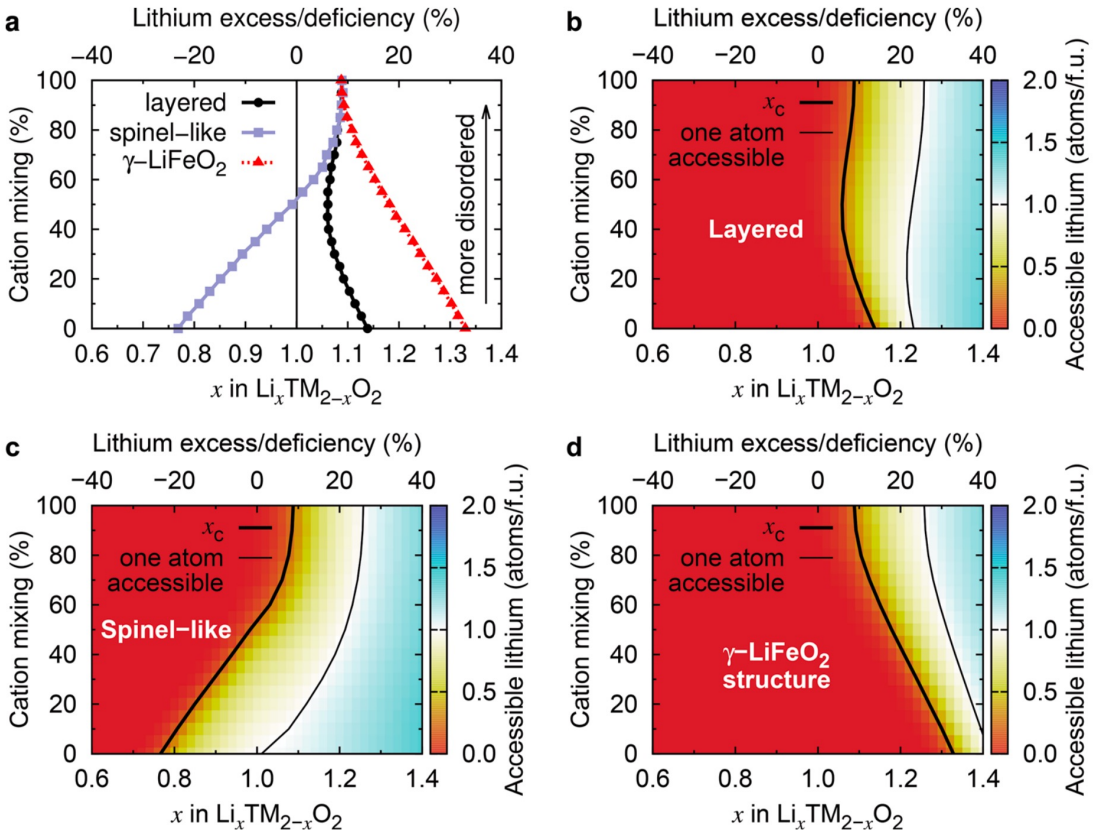

Figure 3.3: Critical Li concentrations (x_c) for 0-TM Li percolation and the accessible Li content via 0-TM channels as a function of Li content and degree of cation mixing in $Li_xTM_{2-x}O_2$ with layered (α-$NaFeO_2$), spinel-like (LT-$LiCoO_2$), and γ-$LiFeO_2$ structures. Thick black contour lines indicate structure-specific x_c values. (Ref. [102])

opposite-type pairs are attractive (see Fig. 3.4). The purple and green shaded areas represent LRO and SRO, respectively. Figure 3.4(d) presents the temperature dependence of the LRO and SRO parameters, indicating that the LRO disappears rapidly after the critical temperature T_{crit} (order-disorder transition), while the SRO decays much more slowly, even at significantly higher temperatures. SRO is particularly important in understanding the properties of DRX materials, as it captures the subtle correlations between atoms on a local scale and affects the available Li content thermodynamically and kinetically (e.g., percolating Li in 0-TM channels).

This chapter delves into the computational modeling of SRO in DRX materials, introducing two main groups of SRO: (1) cation-anion SRO and (2) cation-cation SRO. The thermodynamic (Li-F locking effect) and kinetic effect (formation of 0-TM channel) will be

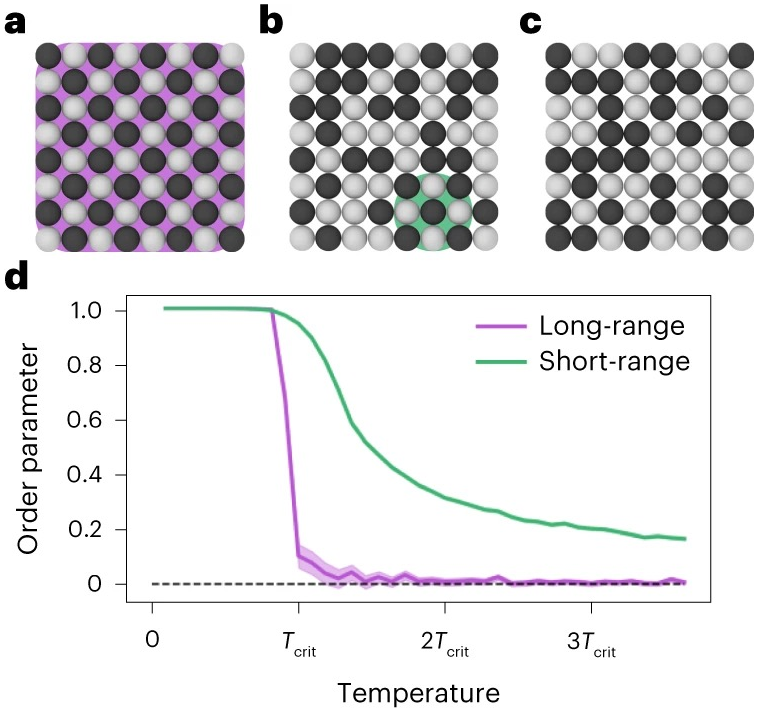

Figure 3.4: Illustration of short-range ordering (SRO) and long-range ordering (LRO) in a binary alloy system. (Ref. [32])

discussed in the following sections.

3.2 Equilibrium thermodynamics with SRO

As discussed above, a sufficient amount of Li-excess is always desired to create 0-TM channels that can be long-range connected and enable percolation. However, the higher Li content in DRX cathodes results in a decrease in available transition metal (TM) redox and increased reliance on oxygen redox, which is detrimental to long-term capacity retention [103–106]. Hence, a key objective in DRX cathode design is to maximize the TM redox capacity while maintaining a high level of Li excess. The substitution of the labile oxygen with species with lower valence (e.g., fluorine or oxygen vacancy) improves the capacity by increasing the redox-active TM content or by lowering the TM valence [107–110]. For example, the Ni^{2+} content in $Li_{1.15}Ni_{0.375}Ti_{0.375}Mo_{0.1}O_2$ can increase from 0.375 to 0.45 when 0.15 O is substituted with F, which was shown to reduce the oxygen loss by 73% [111]. In Li_2MnO_2F, the Mn valence is lowered to +3, which significantly increases the reversible capacity from the Mn redox reservoir relative to that for Li_2MnO_3 [112]. In $Li_5Mn_3O_{6.5}$, the incorporation of oxygen vacancies leads to a substantial increase in the theoretical Mn

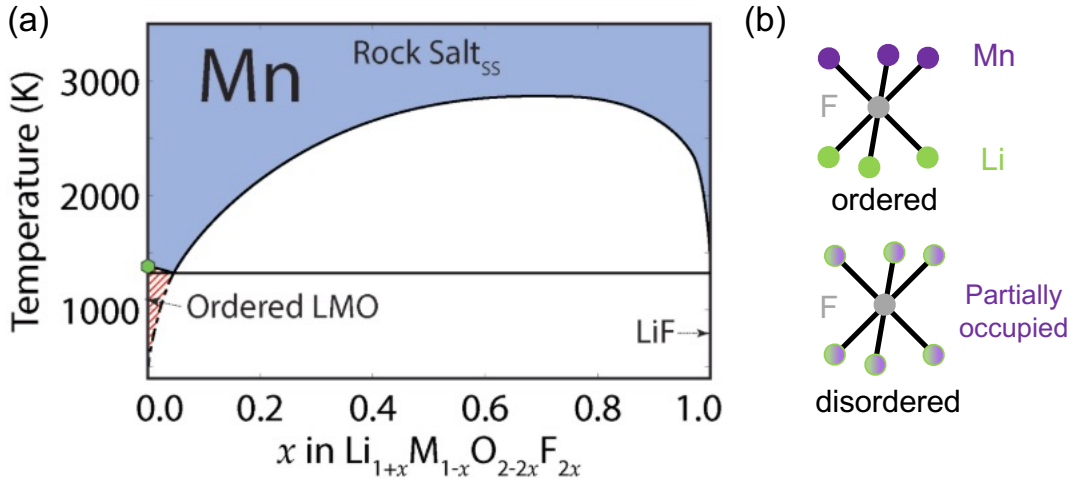

Figure 3.5: (a) Phase diagram of $LiMnO_2$–LiF system derived from cluster expansion Monte Carlo simulations [16]. (b) Schematic illustration of F local environment in ordered (layered) and disordered structure. The partial occupancy of the cation sites provides the possibility of a Li-rich bonding environment to accommodate fluorine.

redox capacity (353 mAh/g) compared to cation-disordered $Li_5Mn_3O_8$. Oxygen vacancies are twice as effective in reducing the metal valence compared to fluorine substitution, and they significantly enhance cyclability by decreasing the reliance on oxygen redox, which delivers a reversible capacity above 270 mAh/g for 25 cycles with negligible voltage fade (0.02 V) [19]. While there are numerous strategies to improve long-term capacity retention through elemental substitution, the fluorination effect, as an example, is used to discuss equilibrium thermodynamics modeling with cluster expansion methods and DFT calculations in this section.

Fluorination of DRX

The introduction of fluorination to Li-TM oxides is not a trivial process, as the bonding energy of F with TM is typically higher than that of Li. In a layered $LiTMO_2$ structure, the anion is always surrounded by three TM and three Li atoms, as shown in Fig. 3.5(b). Such a local environment makes fluorine substitution energetically unfavorable (the 3 TM and 3 Li surrounding F make the local charge non-balanced), therefore making the fluorine solubility in a layered $LiTMO_2$ phase extremely low. It becomes thermodynamically favorable in disordered rocksalt phases due to the Li-rich anion local environment having a statistically higher occurrence. Using DFT and cluster expansion Monte Carlo, Richards et al. [16] demonstrated that the solubility of F in $LiMnO_2$-LiF, for instance, can reach up to 30% above T = 2000 K as shown in Fig. 3.5(a). Such solubility can be achieved through mechano-chemical ball-milling experiments as reported in [112, 113].

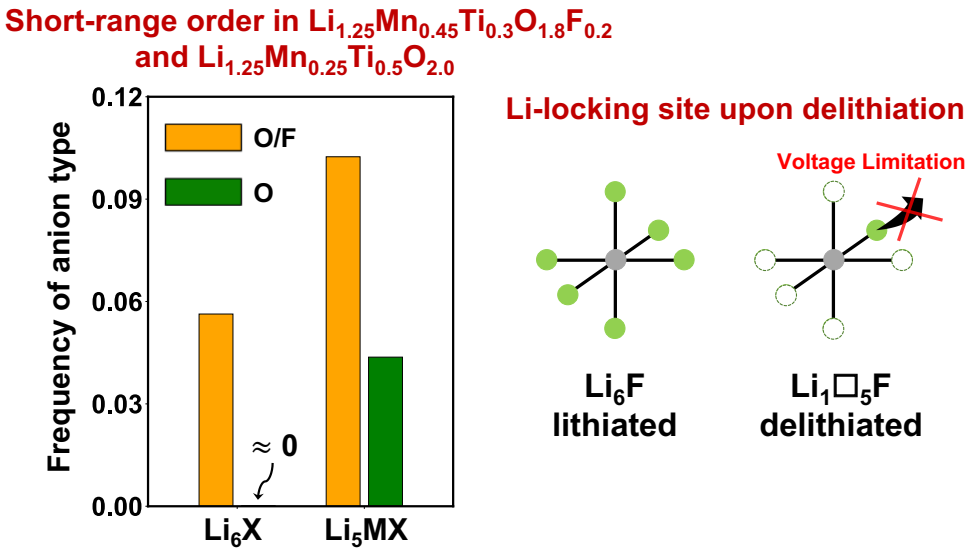

Figure 3.6: Schematic illustration of Li-rich local environment around anion and its statistical occurrence in disordered rocksalt structure. Two cation configurations are illustrated here (Li_6X and Li_5MX (X=anion)). The orange and green bars represent the fluorinated and unfluorinated composition of $Li_{1.25}Mn_{0.45}Ti_{0.3}O_{1.8}F_{0.2}$ and $Li_{1.25}Mn_{0.25}Ti_{0.5}O_{2.0}$, respectively. (Ref. [114])

The bonding preference between Li and F also generates SRO in DRX structures. The effect of Li-F SRO has been discussed from several perspectives in previous research. Using DFT and solid-state nuclear magnetic resonance (NMR) spectroscopy, Clément et al. [31] demonstrated the existence of Li-F SRO and its coupling to unusual modes of nickel redox in DRX cathodes. Mozhzhukhina et al. [115] confirmed the existence of Li-F SRO by Raman spectroscopy. Lun et al. [113] argued that the degree of fluorination has a significant impact on cathode material design by improving the Li percolating network and thus achieving faster ionic diffusion. In addition, Ouyang et al. [116] recently showed that fluorination could substantially affect SRO and, at sufficiently high concentrations, is beneficial to Li-ion transport.

Li-F locking effect

Although fluorination brings several performance improvements to DRX materials, Li-F SRO also has some negative effects on the capacity and energy density of DRX cathodes. One problem is the Li-F "locking effect". This effect manifests itself as a high voltage required to extract all Li-ions from the Li-rich environment that coordinates with F as shown in Fig. 3.6. Using DFT calculations, Kitchaev et al. [117] reported that the voltage is greater than 5.0

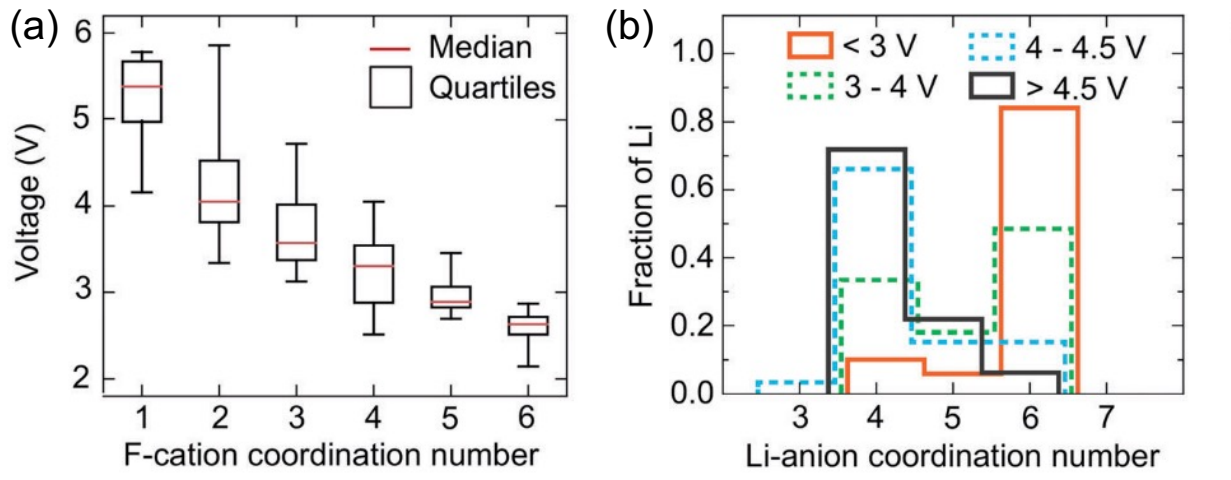

Figure 3.7: Electrochemical accessibility of Li in $Li_{1.171}Mn_{0.343}V_{0.486}O_{1.8}F_{0.2}$ DRX. Distribution of F–cation (a) and Li–anion (b) environments by coordination number, among simulated partially charged structures derived from the pristine structure, according to the voltage at which they appear. (Ref. [117])

V to extract the Li from a fluorine coordination shell and make the fluorine uncoordinated (see Fig. 2.49). The voltage is well above the typical electrolyte stability limit, which means a fraction of Li is "locked" to fluorine and cannot be extracted.

To illustrate the significance of the Li locking effect in oxyfluorides, Fig. 3.6 shows the frequency with which Li_6X and Li_5MX (X=anion) environments are found in $Li_{1.25}Mn_{0.45}Ti_{0.3}O_{1.8}F_{0.2}$ and $Li_{1.25}Mn_{0.25}Ti_{0.5}O_{2.0}$. These results were obtained by averaging over structures obtained from Monte Carlo simulations at T = 1273 K, using a cluster expansion Hamiltonian parameterized by DFT. In Fig. 3.6, the orange and green bars represent the oxyfluoride and pure oxide compounds, respectively. The frequency with which these two types of anion environments occur in oxyfluorides is much higher than in pure oxides; in particular, the presence of Li_6X is almost never found in the oxide but occurs frequently in the oxyfluoride. At least one Li-ion is impossible to be extracted from the Li_6F environment, which limits "extractable lithium" capacity. Thus, to achieve higher capacity and energy density, one of the key factors is to reduce the number of "locked" lithium ions around fluorine in DRX materials.

3.3 Resolve Li-F locking effect by Mg-doping

3.3.1 Computational modeling

Screening cation elements

An initial screening of metals is used to find the metal that prefers to bond with F. The M-F bonding energy is calculated from the formation enthalpy per F atom, $\Delta H_f/y$, of the metal fluoride MF_y. The values of $\Delta H_f/y$, where ΔH_f is obtained from the Materials Project [118], are shown in Fig. 3.8. As a baseline, the bonding energy of Li per F is -3.18 eV. No other element has stronger bonding with F than Li. The fluorides of the {Sc, Y} and {B, Al, Ga} groups have less negative enthalpy than the {Be, Mg, Ca} group. Thus, only group-II elements have comparable interaction with F to Li.

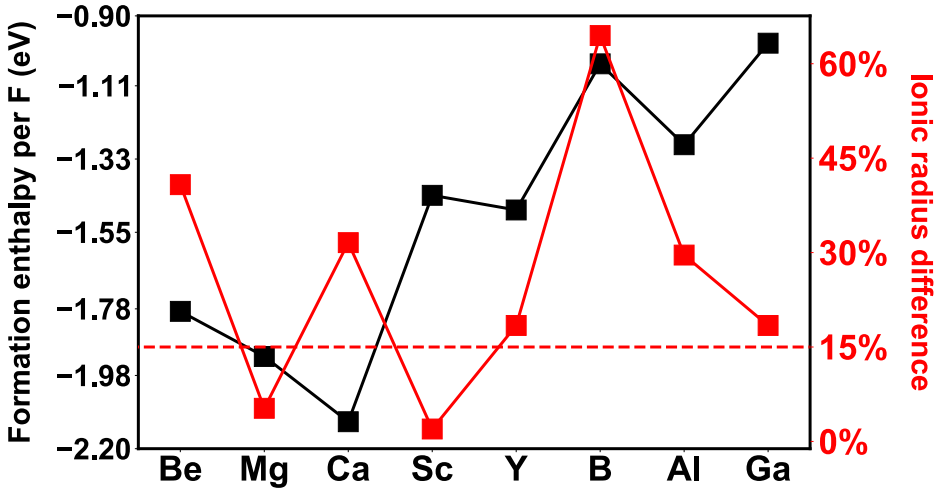

Figure 3.8: Screening of main group elements on bonding preference with F and ionic size difference with Li. The black and red lines represent formation enthalpy per F and the percentage of ionic radius difference with Li-ion, respectively. The dashed red line corresponds to a 15% radius difference. (Ref. [114])

Another criterion is the ability to accommodate the dopant in the disordered rocksalt structure. Empirically, the Hume-Rothery rule predicts that species with similar electronegativity form a solid solution when their atomic radii differ by no more than 15% [119]. Even though this criterion is determined for metallic alloys, it is adopted here to determine whether a candidate element might be substituted in the cation-disordered phase. In Fig. 3.8, the red squares represent the percentage of ionic radii difference with Li^+, and the red dashed line represents 15% difference [120]. Only Mg^{2+} and Sc^{3+} satisfy this criterion, although Y^{3+}

and Ga^{3+} are only slightly above the 15% line. Incorporating both the radius information and energetic preferences suggests that Mg^{2+} is a suitable cation.

DFT calculations

The DFT calculations were performed with VASP using the projector-augmented wave method [95, 96], a plane-wave basis set with an energy cutoff equal to 520 eV, and a reciprocal space discretization of 25 k-points per $Å^{-1}$. All calculations were converged to 10^{-6} eV in total energy for electronic loops and 0.02 eV/Å in interatomic forces for ionic loops. The GGA+U is used to compensate for the self-interaction error on all transition metal atoms except titanium (3.9 eV for Mn and 1.5 eV for Nb) [33].

Cluster expansion Monte Carlo

To evaluate the equilibrium ordering of multicomponent DRX compounds, a cluster expansion (CE) Hamiltonian was constructed in the configurational space LiF–MgO–$LiMnO_2$, LiF–MgO–$LiMnO_2$–Li_3NbO_4, and LiF–$LiMnO_2$–Li_2TiO_3 on a rocksalt lattice. As in the LiF–$LiMnO_2$–Li_2TiO_3 system, the anion FCC lattice comprises O^{2-} and F^-, while the lattice of octahedral cation is composed of Li^+, Mn^{3+}, and Ti^{4+}/Nb^{5+}. The cluster expansion models were fitted consisting of pair interactions up to 7.1 Å, triplet interactions up to 4.0 Å and quadruplet interactions up to 4.0 Å based on a primitive cell of the rocksalt structure with lattice parameter a = 3 Å. Effective cluster interactions (ECIs) were obtained from ℓ_1-norm regularized linear regressions with the best regularization parameter selected to minimize the cross-validation (CV) score [75, 76], as the ℓ_1-norm regularized CE works well for these systems without basis function explosion. The root-mean-squared CV errors were converged to below 8 meV/atom.

Monte Carlo simulations on these cluster expansion Hamiltonians were performed in a canonical ensemble using Metropolis-Hastings sampling on a $8 \times 8 \times 10$ supercell (1,280 atoms) of the primitive unit cell of the rocksalt structure. All the statistical quantities were obtained from 1,000 sampled structures of the equilibrium ensemble. Percolation analysis was completed on these sampled structures using the `dribble` package [121].

Li-F SRO analysis

To characterize in more detail how Mg addition affects cation ordering and Li-F SRO in DRX materials, two compounds are investigated computationally, $Li_{1.25}Mn_{0.45}$ $Ti_{0.3}O_{1.8}F_{0.2}$ (LMTF) and $Li_{1.25}Mg_{0.1}Mn_{0.45}Nb_{0.2}O_{1.8}F_{0.2}$ (LMMNF) with identical Li-excess, redox-active TM and fluorination content. Canonical cluster expansion Monte Carlo (CEMC) simulation was applied at 1,000 °C to simulate the as-synthesized samples. The frequency of different cation configurations around F and their percolation properties were averaged over 1,000 structures sampled from the equilibrium ensemble.

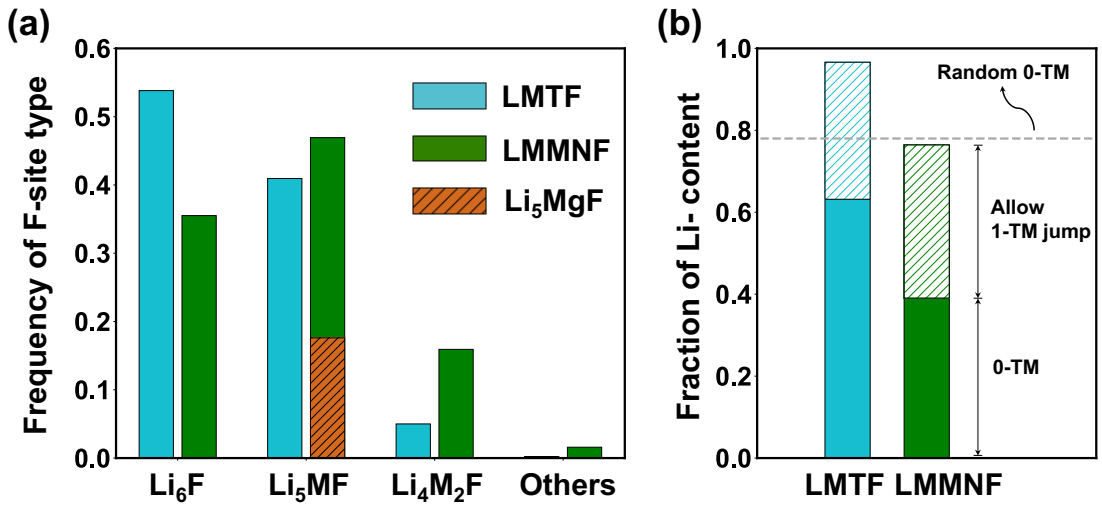

Figure 3.9: (a) Frequency of different types of fluorine environments averaged over 1000 sampled structures from the equilibrium ensemble. LMTF/LMMNF is represented by the blue/green bar, respectively. The brown dashed bar represents the $LiMg_5F$ environment in LMMNF. (b) Percolation analysis of LMTF and LMMNF. The solid bar represents percolating Li-content in the 0-TM percolating network, and the dashed bar (1-TM) represents additional percolating Li-content when one jump through a 1-TM barrier into the 0-TM network is included. (Ref. [114])

Figure 3.9(a) shows the frequency with which several types of cation environments around F occur. The Li_6F and Li_5MF environments dominate both LMTF and LMMNF. In LMTF, without Mg-doping, over 50% of F ions are surrounded by six Li-ions. However, the peak of the distribution shifts to Li_5MF in LMMNF, and the Li_6F frequency is lowered to 35%. In particular, the $LiMg_5F$ environment, shown as the brown dashed bar, makes up around 37% of the Li_5MF environments. This finding indicates that modifying the DRX composition with Mg can effectively reduce the number of Li_6F environments and render Li-ions more accessible.

It is noted that LMTF and LMMNF also differ in their d^0 charge compensating element. Although Ti^{4+} and Nb^{5+} are both electrochemical inactive, they can affect atomic ordering and thus the percolating Li-content of DRX cathodes [15, 122]. To rule out that the capacity improvement of LMMNF is caused by the change in charge compensator, the fraction of Li content in the percolating network of each compound is plotted in Figure 3.9(b). The gray dashed line indicates that a percolating Li content of approximately 78% is achieved when the cations are randomly arranged. The solid bar represents the fraction of Li content in the 0-TM network, and the dashed bar represents the Li that can reach the 0-TM network

with a single 1-TM hop. LMTF has a higher fraction of Li content in both the 0-TM and 1-TM networks, as compared to LMMNF. These results are consistent with percolation predictions in previous work [17] on Li-TM oxides. Thus, the larger fraction of accessible Li ions in LMMNF more likely originates from the fact that Mg displaces Li from the F-bonded position than from the percolating Li content. Compared with LMTF, Mg-doped LMMNF has a much lower frequency of Li_6F environments, leading us to predict a higher achievable electrochemical capacity for LMMNF than for LMTF.

3.3.2 Experimental verification

Synthesis

LMTF and LMMNF were synthesized through a solid-state reaction, using Li_2CO_3, Mn_2O_3, TiO_2, Nb_2O_5, MgF_2, and LiF as precursors. The precursor mixture was pelletized and sintered at 600 °C for 2 hours in an Ar atmosphere to decompose the carbonates, followed by calcination at 1000 °C for 4 hours in Ar. Rietveld refinement revealed simple disordered rocksalt structures (space group: Fm-3m) with lattice parameters of 4.1560 Å for LMTF and 4.1790 Å for LMMNF. The increase in lattice parameter is expected when transitioning from LMTF to LMMNF, as the only change involves substituting Ti^{4+} (74.5 pm) with Mg^{2+} (86 pm) and Nb^{5+} (78 pm). The coin cells were prepared with LMTF and LMMNF as cathode materials and Li-metal as anode materials for electrochemical tests.

Electrochemistry

Figure 3.10 presents the electrochemical properties of LMTF and LMMNF using galvanostatic cycling between 1.5 – 4.8 V at 20 mA/g and room temperature. The blue dashed lines represent the theoretical capacity based on $Mn^{3+/4+}$ redox in each sample. LMTF delivered a first charge capacity of 337 mAh/g and a discharge capacity of 279 mAh/g (899 Wh/kg). LMMNF delivers a similar initial charge capacity of 332 mAh/g but a larger discharge capacity of 290 mAh/g (905 Wh/kg). Charging extracted 1.01 Li and 1.08 Li per formula unit (f.u.) from LMTF and LMMNF, respectively. The locked Li content decreases by about 29% from 0.24 per f.u. in LMTF to 0.17 per f.u. in LMMNF with the substitution of Ti by Mg and Nb, as shown in Fig. 3.10c. To verify that this improvement is not caused by the change in the chemistry of the charge-compensating element, $Li_{1.25}Mn_{0.6}Nb_{0.15}O_{1.8}F_{0.2}$ (LMNF) was synthesized and compared with LMMNF. LMNF exhibits a lower initial charge capacity of 293 mAh/g as compared to LMMNF (see Fig. 3.10(d)), and the amount of non-extractable Li at the top of the charge is increased to 0.28 per f.u. in un-substituted LMNF. Therefore, from the experimental perspective, the decrease of locked Li is not caused by the change of high-valent charge compensators. For a more detailed characterization and electrochemical performance of LMTF and LMMNF, please refer to Ref. [114].

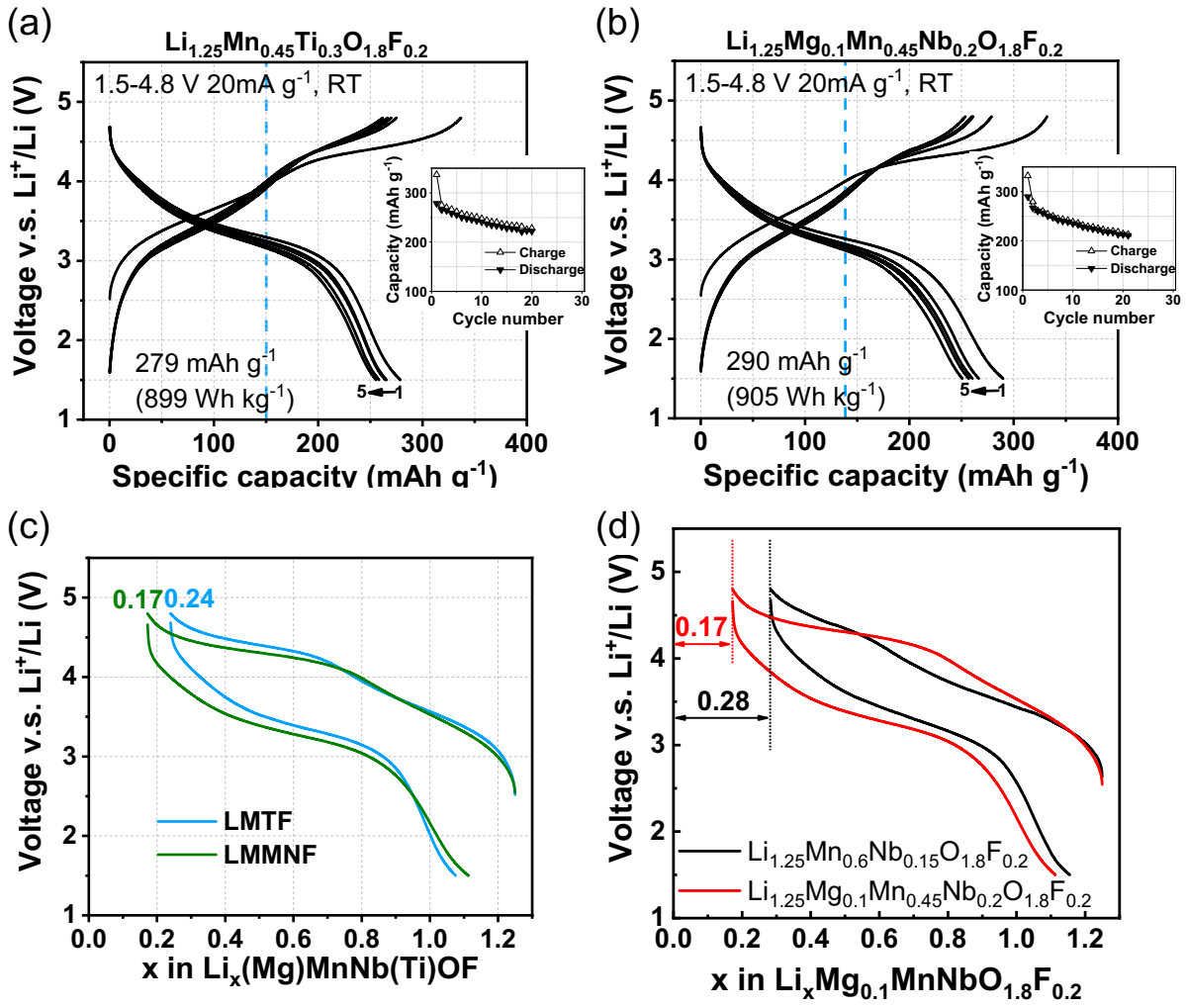

Figure 3.10: Voltage profiles of the first 5 cycles and capacity retention of (a) LMTF and (b) LMMNF within voltage window of 1.5 – 4.8V at 20 mA/g at room temperature. The initial charge and discharge capacity and energy density are shown in the figure. (c) Direct comparison of extractable Li ions in LMTF and LMMNF in the electrochemical test. The amount of remaining Li content is 0.17/0.24 per f.u. at the top of charge for LMTF/LMMNF, respectively. (d) Direct comparison of extractable Li ions in LMMNF and LMNF (non-Mg-doped) in the electrochemical test. (Ref. [114])

3.3.3 Discussion on Mg-doping strategy

To further illustrate the validity of the Mg-doping strategy and critically examine the Mg-doping effect without the effect of different d^0 TM charge compensators, several DRX systems based on composition $Li_{1.333}Mn_{0.667}O_{1.333}F_{0.667}$ (LMF) were further studied [112, 113], which delivers a first charge and discharge capacity of 276 mAh/g and 267 mAh/g (see Fig. 3.11), respectively. The LMF shows lower capacity but better capacity retention than the related disordered Li_2MnO_3 [123], which is consistent with our understanding of the role that F plays: its locking effect reduces capacity, but it also mitigates the irreversible oxygen redox process and reduces oxygen loss, which improves cycling.

Mg can be introduced in a variety of ways into DRX compounds depending on how charge compensation is achieved. Using the Li-Mn-O-F system as an example, it is shown that this degree of freedom can be used to tune the initial capacity versus cyclability. In the previous examples of LMTF and LMMNF, Mg was incorporated by substituting Ti with a charge-equivalent combination of Mg and Nb. Other strategies would be to (1) substitute Mn with Mg, leading to a higher Mn valence and constant Li-excess level; (2) substitute Li with Mg, leading to a lower Mn valence and Li-excess level. To test both strategies, $Li_{1.333}Mg_{0.1}Mn_{0.567}O_{1.333}F_{0.667}$ (ms-LMF) and $Li_{1.233}Mg_{0.1}Mn_{0.667}O_{1.333}F_{0.667}$ (ls-LMF) were prepared by mechanochemical ball-milling. The notation ms-LMF refers to the sample where Mn was substituted by Mg, and the notation ls-LMF refers to the sample where Li was substituted by Mg.

As the Li-excess content remains high in ms-LMF, Mg can free the locked Li to achieve a larger capacity. In agreement with this prediction, ms-LMF exhibits an initial charge (and discharge) capacity of 305 mAh/g (and 309 mAh/g), which is larger than for LMF (see Fig. 3.11(c)). Through this substitution strategy, a specific discharge energy of 1001 Wh kg^{-1} can be achieved. With more capacity contribution from anionic redox, a slightly lower capacity of 252 mAh/g is retained (81.6% of the initial capacity) compared to that of LMF (226 mAh/g, 84.3%) over 30 cycles (Fig. 3.12(d)). In contrast, a lower capacity is expected in ls-LMF as it lowers the Li-excess level. Indeed, it delivers initial charge and discharge capacities of 271 mAh/g and 260 mAh/g (a specific energy of 806 Wh kg^{-1}), respectively (Fig. 3.11(b)). However, the capacity retention of ls-LMF is improved over LMF (248 mAh/g after 30 cycles, 91.5% of the initial capacity), presumably as a result of the theoretical TM capacity that is gained from Mn by lowering its valence in the as-synthesized sample, leading to less oxygen redox.

These results show the two different Mg substitution strategies in fluorinated Li-excess DRX materials, each serving a different purpose: Mg can either substitute for the TM to free some locked Li, resulting in a higher initial capacity with reasonable capacity retention, or Mg can substitute for Li and lower the TM valence, which increases the theoretical TM capacity and results in improved capacity retention. In both cases, the amount of non-extractable Li is lower than that of undoped LMF. This trade-off can be influenced by the

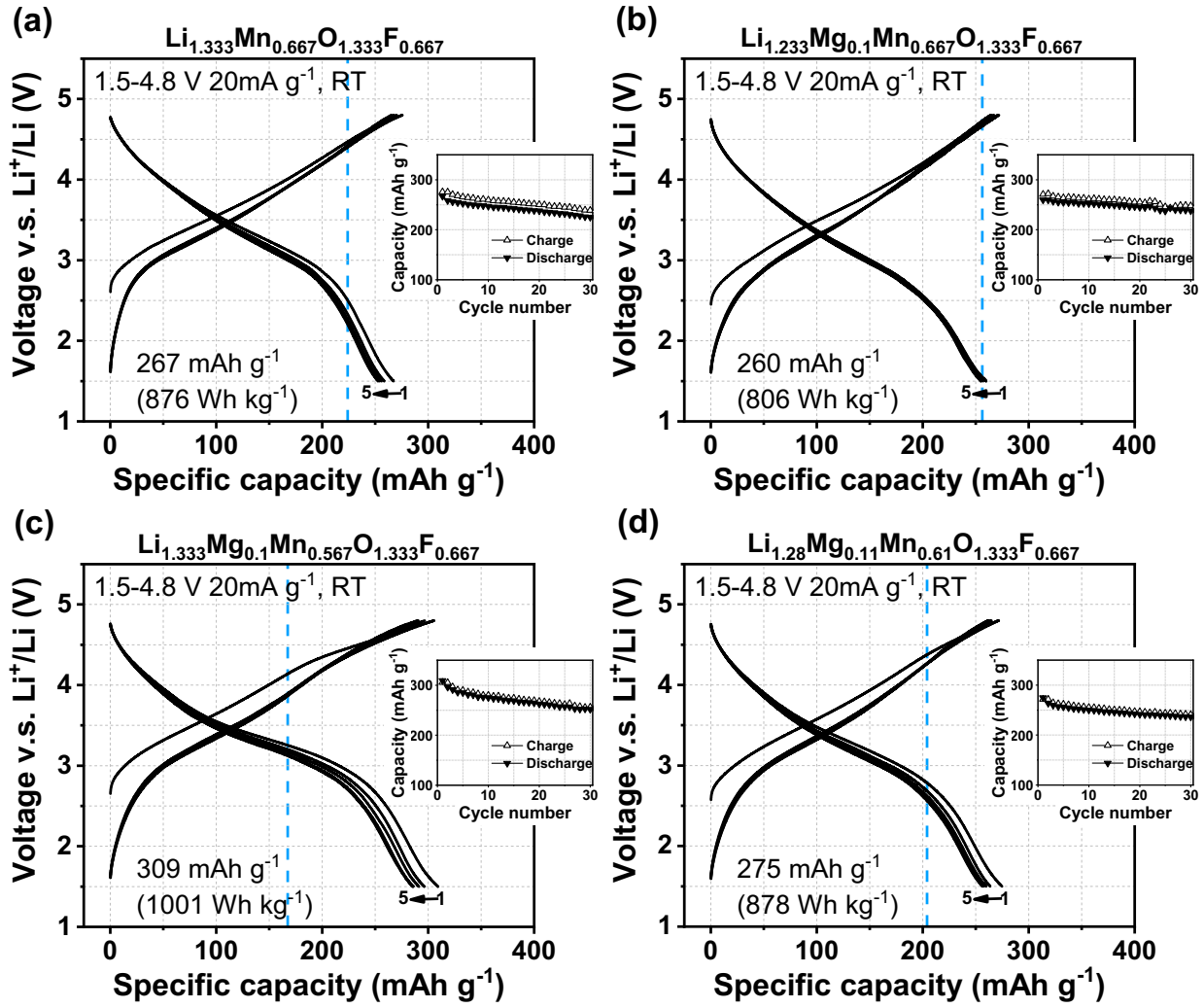

Figure 3.11: Voltage profiles of (a) LMF, (b) ls-LMF, (c) ms-LMF, and (d) LMMF within voltage window of 1.5 – 4.8V at 20 mA/g at room temperature. (Ref. [114])

fluorination level as shown by Lun et al. [113] as a high F content enables one to combine high TM redox capacity with high Li excess. The comparison of cyclability after 30 cycles is shown in Fig. 3.12(b) and Fig. 3.12(d).

Computational analysis of Mg-doping effect in Li-Mn-O-F DRXs

The co-substitution of Li and Mn by Mg is also considered. The voltage profiles of $Li_{1.28}Mg_{0.11}Mn_{0.61}O_{1.333}F_{0.667}$ (LMMF) cycled between 1.5 V and 4.8 V are presented in Fig. 3.11(d). LMMF delivers the first charge and discharge capacities of 272 mAh/g and 275

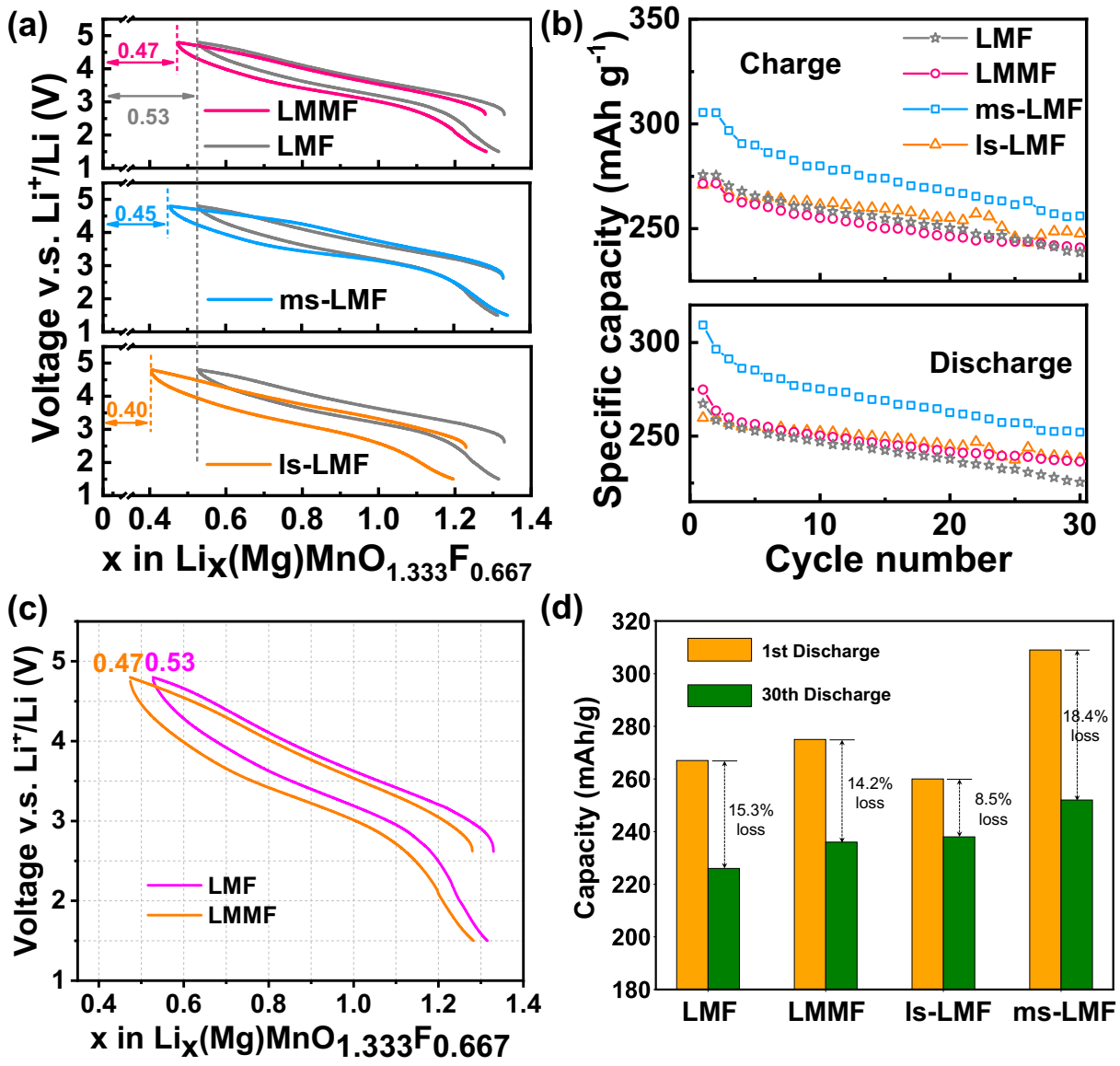

Figure 3.12: (a) Voltage profiles and remaining Li per formula unit (f.u.) for LMF, LMMF, ms-LMF, and ls-LMF within a voltage window of 1.5 – 4.8 V at 20 mA/g at room temperature. Gray curves represent the first cycle voltage profile of LMF for comparison. (b) Cyclability of all Li–(Mg)-Mn–O–F compounds. (c) Direct comparison of remaining Li per f.u. for LMF and LMMF, with short-range order analyzed computationally. (d) Discharge capacity of the 1st cycle and the 30th cycle for the four compounds. (Ref. [114])

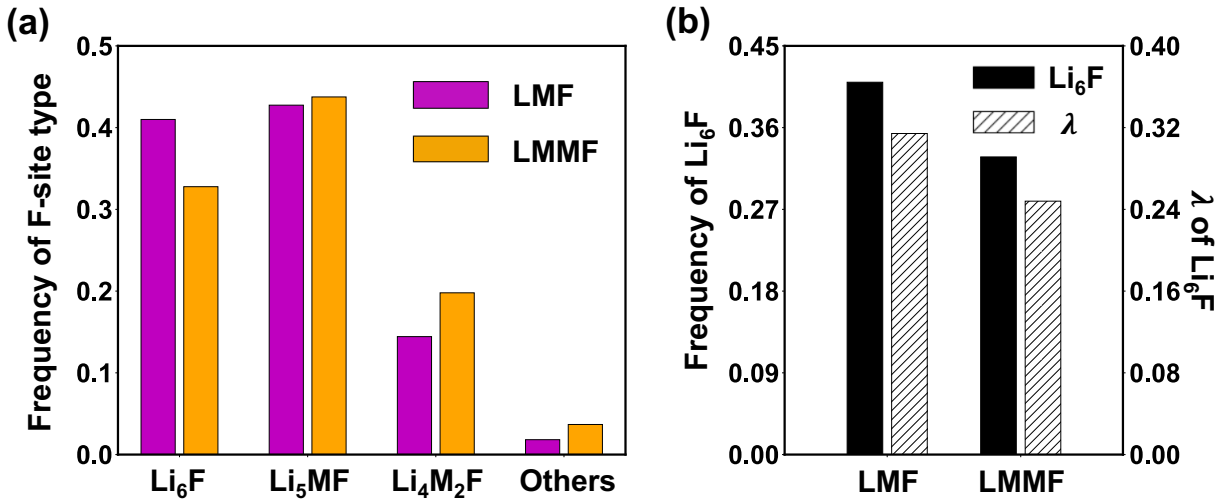

Figure 3.13: (a) Frequency of different types of fluorine environments averaged 1000 sampled structures from cluster expansion Monte Carlo simulation. (b) Frequency and normalized short-range order parameter λ of Li_6F environment of LMF and LMMF. (Ref. [114])

mAh/g, respectively. Over 30 cycles, a capacity of 236 mAh/g is retained (85.8% of the initial capacity). The capacity retention of LMMF is intermediate between that of ls-LMF and ms-LMF. Although slightly less charge capacity is delivered compared with LMF (276 mAh/g), the amount of non-extractable Li at the top of the charge state decreases from 0.53 Li per f.u. for LMF to 0.47 Li per f.u. for LMMF as shown in Fig. 3.12(b).

To relate the performance of the co-substituted sample to its structure, a CEMC simulation with temperature $T = 1750°C$ as a heuristic limit of the mechanical ball-milling condition was run [124]. The transition metals in LMF and LMMF are Mn^{3+} and thus present a similar chemical environment and do not require charge transfer in Monte Carlo simulation. As shown in Fig. 3.13(a), the frequency of the Li_6F configuration is approximately 10% lower in LMMF than in LMF, whereas the frequency of the Li_5MF configuration is quite similar in both compounds. The reduced amount of locked Li in Li_6F indicates that Li ions have been displaced to other non-locking sites and can thus be effectively extracted within the working voltage window. Considering that the Li-excess amount is different in LMF and LMMF, a normalized short-range order parameter is introduced λ to measure the occurrence of Li_6F configuration in the solid solution:

$$\lambda = \frac{P_{calc}(\mathrm{Li_6F}) - P_{rand}(\mathrm{Li_6F})}{P_{max}(\mathrm{Li_6F}) - P_{rand}(\mathrm{Li_6F})}, \tag{3.1}$$

where P_{calc}, P_{rand} represent the calculated and fully random frequency of the Li_6F configuration. P_{max} is the max probability for Li_6F that can be achieved for the given Li and F

Table 3.1: Design principles of Mg-doping in Mn-based DRX materials. The notations of all compositions chosen in this study are listed. In each case, the compositional design objective is briefly described in the Note.

Notation	Composition	Note
LMTF	$Li_{1.25}Mn_{0.45}Ti_{0.3}O_{1.8}F_{0.2}$	solid-state synthesis, low F content,
LMMNF	$Li_{1.25}Mg_{0.1}Mn_{0.45}Nb_{0.2}O_{1.8}F_{0.2}$	$Ti_{0.3}$ to $Mg_{0.1}Nb_{0.2}$ by charge balanced substitution
LMF	$Li_{1.333}Mn_{0.667}O_{1.333}F_{0.667}$	ball-milling synthesis, high F content,
ls-LMF	$Li_{1.233}Mg_{0.1}Mn_{0.667}O_{1.333}F_{0.667}$	Li to Mg substitution, O redox ↓, retention ↑
ms-LMF	$Li_{1.333}Mg_{0.1}Mn_{0.567}O_{1.333}F_{0.667}$	Mn to Mg substitution, extractable Li ↑, capacity ↑
LMMF	$Li_{1.28}Mg_{0.11}Mn_{0.61}O_{1.333}F_{0.667}$	mixed substitution, all Mn^{3+}, non-extractable Li ↓

content. For all of our samples, $P_{max} = 1$. In Fig. 3.13(b), the black solid bar represents the direct frequency of the Li_6F configuration, and the dashed bar represents the normalized SRO parameter λ. The frequency by which the Li_6F configuration occurs decreases from 0.41 for LMF to 0.32 for LMMF, and the corresponding SRO parameter λ decreases from 0.35 to 0.28, respectively. Both experimental and computational results confirm that the co-substitution of Li/TM with Mg reduces the amount of locked Li.

Summary of fluorination and Mg-doping

Fluorine substitution in DRX materials has proven to be beneficial, as it stabilizes compounds with oxygen redox and generally leads to better capacity retention in many systems [18, 26]. The strategy of fluorination is not fully optimized. While Li-excess is needed for percolation, not all Li near F can be extracted, which has motivated the strategy of displacing some Li by adding other metal cations, such as Mg.

Through computational investigation, Mg has been identified as one of the few elements with an appropriate binding strength to F that can displace Li. Replacing $Ti_{0.3}$ in LMTF with $Mg_{0.1}Nb_{0.2}$ in LMMNF reduces non-extractable Li content by about 30% despite reducing percolation. There are other strategies to compensate for the introduction of Mg in DRX materials, such as substituting Li or TM with Mg, which can be used to tune capacity or capacity retention. Substituting Li results in better capacity retention due to reduced TM average charge valence and less irreversible oxygen redox while substituting TM increases capacity by maintaining Li-excess levels and reducing Li-F locking.

Introducing Mg-doping to unlock Li from the Li_6F configuration in DRX oxyfluorides has proven beneficial, with energy densities of 905 and 1001 Wh/kg in LMMNF (solid-state synthesis approach) and ms-LMF (mechanochemical ball-milling approach), respectively. This study demonstrates the successful computational prediction and experimental realization of Mg-doped disordered oxyfluoride cathodes with improved electrochemical performance. Mg^{2+}, with its similar ionic radius to Li^+ and strong bonding preference to F, is a suitable candidate for resolving the Li-F locking effect and increasing the achievable capacity of DRX

materials.

3.4 Transport kinetics with SRO

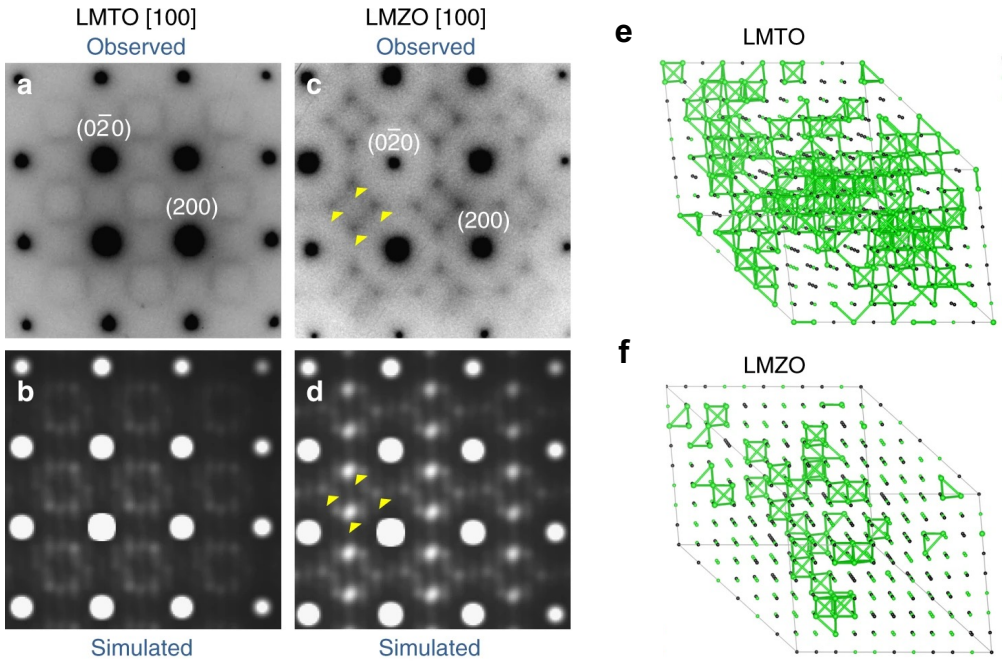

Figure 3.14: Elecron diffraction (ED) patterns of LMTO (a) and LMZO (c) along the zone axis [100]. The round spots are indexed to the Fm–3m space group, while the diffuse scattering patterns nearby are attributed to SRO. Several intensity maxima in the diffuse scattering patterns are highlighted with yellow arrows in LMZO. Simulation of ED patterns for LMTO (b) and LMZO (d) along the same zone axis shows good agreement with experimental observation. Representative MC structures for (e) LMTO and (f) LMZO. Li ions are labeled with green spheres and 0-TM-connected Li sites are bridged with green bonds. (Ref. [17])

In previous sections, the cation-anion SRO and its effect on rocksalt structures are discussed. The interaction strength between cation and anion species, being nearest neighbors, is typically strong, which consequently influences the equilibrium thermodynamic properties such as synthesizability and voltages. In the following sections, the impact of cation SRO on Li transport kinetics will be discussed.

As pointed out in the introduction, a percolating 0-TM network is required throughout the structure to realize bulk-scale Li transport [25]. Percolation is controlled by the amount of 0-TM environments and their arrangement, both of which are influenced by the cation

SRO. Unlike in ordered compounds, remarkable variations in local environments can exist within DRX, influenced by composition [116], annealing time [125], the number of metal cations [28], and even local transition metal migration [126]. As revealed by Ji et al. [17], the cation SRO demonstrates a deviation from fully random cation ordering, which has a significant influence on the electrochemical performance. The cation SRO is important in determining the Li transport kinetics by modifying the percolating network via connected 0-TM channels. It is found that $Li_{1.2}Mn_{0.4}Ti_{0.4}O_{2.0}$ (LMTO) and $Li_{1.2}Mn_{0.4}Zr_{0.4}O_{2.0}$ (LMZO) have almost similar chemistry (e.g., both are Mn^{3+}-based redox, both have Ti^{4+} and Zr^{4+} as an electrochemical inert element but only differ in ionic radius). However, experimental results reveal that LMTO delivers a substantial first-cycle capacity of approximately 260 mAh/g (0.79 Li per formula unit), while LMZO offers a limited capacity with only 0.52 Li per formula unit. This striking difference between the two systems suggests the presence of hidden structural and chemical ordering that governs Li transport in such cation-disordered oxides.

Electron diffraction analysis demonstrates that LMTO and LMZO exhibit distinctly different diffraction patterns. As depicted in Fig. 3.14(a)-(d), the round spots are indexed to the Fm-3m space group (disordered rocksalt), while the nearby diffuse scattering patterns are attributed to SRO. Several intensity maxima in the diffuse scattering patterns of LMZO are highlighted with yellow arrows, in contrast to the ring-like diffusion scattering patterns observed in LMTO. Simulated electron diffraction patterns for LMTO and LMZO along the same zone axis are shown in Fig. 3.14(b) and (d), exhibiting good agreement with experimental observations. Figure 3.14(e) displays representative structures for LMTO and LMZO obtained from cluster expansion Monte Carlo simulations, where Li-ions are marked with green dots, and 0-TM connected Li sites are linked with green bonds. A significant reduction in the number of 0-TM channels within the bulk structures can be observed in LMZO, which aligns with the experimentally observed decrease in extractable Li content.

Ji et al. [17] provides further insights into the formation of SRO in various TMs. Figure 3.15(a) illustrates the accessible Li content (percolation Li content) as a function of the average TM ionic radius for DRXs containing trivalent redox-active TMs. In Fig. 3.15(b), the accessible Li content is plotted against the divalent TM ionic radius for DRXs containing divalent redox-active TMs and various d^0 stabilizers (Ti^{4+}, Nb^{5+}, Mo^{6+}). The results reveal that both an increase in the ionic radius and a decrease in the valence of d^0 TM stabilizers lead to a reduction in the accessible Li content.

It is found that cation SRO in DRX materials is influenced by both charge balance and ionic radius differences. High-valent TMs tend to mix with Li^+ in order to maintain local electroneutrality, thereby reducing 0-TM formation. This effect is due to the charge balance between high-valent TMs (e.g., Mn^{3+}, Ti^{4+}, Nb^{5+}) and Li^+ in DRXs, which discourages Li segregation into Li_4 tetrahedra. On the other hand, the size mismatch between Li^+ and TM cations contributes to Li segregation by minimizing strain, thus promoting 0-TM formation. The interplay between these two effects is best exemplified by the case of LMTO and LMZO.

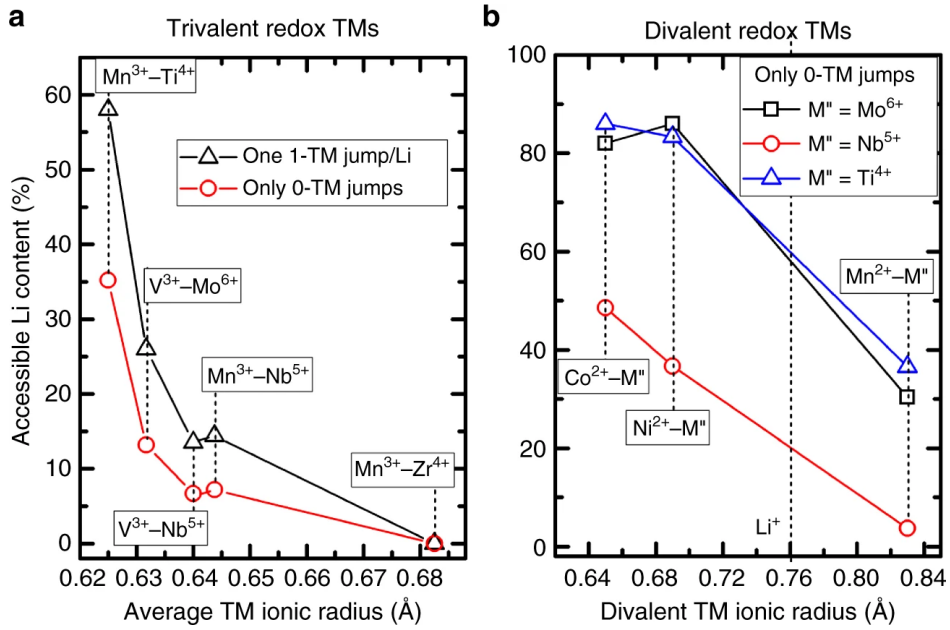

Figure 3.15: (a) Accessible Li content plotted as a function of the average TM ionic radius for DRXs containing trivalent redox-active TMs, considering only 0-TM jumps (red) or allowing a single 1-TM jump to reach the 0-TM percolating network. (b) Accessible Li content plotted as a function of the divalent TM ionic radius for DRXs containing divalent redox-active TMs and various stabilizers, considering only 0-TM jumps. The Li^+ ionic radius is indicated at 0.76Å. All listed compositions exhibit the same Li-excess level of 20%. (Ref. [17])

Despite having the same valence, Zr^{4+} displays a stronger net attraction to Li^+ compared to Ti^{4+}. This phenomenon can be attributed to the difference in ionic radii between Ti^{4+} (0.605 Å) and Li^+ (0.76 Å), which leads to Li^+ segregation away from the smaller Ti^{4+} cation in order to minimize strain. In contrast, the size of Zr^{4+} (0.72 Å) is closer to that of Li^+, causing electrostatic interactions to dominate over the size effect. This results in a maximal separation between high-valent Zr^{4+} and local ordering between Zr^{4+} and Li^+.

3.5 Optimize Li transport by partial Li deficiency

Based on the observations of SRO effects, this section presents another approach to modulating SRO to improve Li transport kinetics. Using Mn-based DRX as a proof-of-concept, materials with nominally the same chemistry can be simply controlled by introducing Li deficiency during synthesis. Consequently, this novel approach can therefore be used to enhance the capacity and rate performance of a DRX without the need to change the transition metal content.

3.5.1 SRO with Li vacancy & Mn^{2+} to Mn^{3+} substitution

The low cost and abundance of Mn, coupled with the excellent thermal stability of the Mn^{4+} charged state, make Mn-based DRX materials promising candidates for cathode applications [113]. A common challenge faced by researchers when designing Mn-based DRX materials is deciding between Mn^{2+} and Mn^{3+} in the as-synthesized state. Theoretically, Mn^{2+} offers a higher transition metal capacity as it provides double electron redox, reducing reliance on oxygen redox [107]. However, Mn^{2+} (0.83 Å), being closer in size to Li^+ (0.76 Å) than Mn^{3+} (0.65 Å), tends to mix more with Li^+, leading to fewer 0-TM channels and consequently lower rate performance. Ideally, it would be desirable to synthesize DRX materials with Mn^{3+} for good rate performance while still utilizing Mn^{2+}/Mn^{3+} redox for high capacity. In this work, it is demonstrated that this can be achieved by synthesizing the material in a partially delithiated state, where the vacancy sites in the as-synthesized Mn^{3+}-based DRX are refilled with Li^+ after the initial discharge process. Specifically, a series of Mn-Nb-based DRX materials were investigated: $Li_{1.3}Mn^{2+}_{0.4}Nb_{0.3}O_{1.6}F_{0.4}$ (L13MNOF), $Li_{1.1}Mn^{2+}_{0.2}Mn^{3+}_{0.2}Nb_{0.3}O_{1.6}F_{0.4}$ (L11MNOF), and $Li_{0.9}Mn^{3+}_{0.4}Nb_{0.3}O_{1.6}F_{0.4}$ (L09MNOF). It is found that substituting Mn^{2+} with Mn^{3+} by incorporating cation vacancies improves both the discharge capacity and rate performance. The rationale for these improvements is discussed in the following parts.

3.5.2 Computational modeling

DFT calculations

The DFT calculations were performed with VASP using the projector-augmented wave method [95, 96], a plane-wave basis set with an energy cutoff equal to 520 eV, and a reciprocal space discretization of 25 k-points per $Å^{-1}$. All calculations were converged to 10^{-6} eV in total energy for electronic loops and 0.02 eV/Å in interatomic forces for ionic loops. The regularized strongly constrained and appropriately normed meta-GGA exchange-correlation functional (r^2SCAN) was used [127], which is believed to better capture cation-anion hybridization and Li-coordination and would improve the accuracy of the energetics when cation vacancies are introduced into the rocksalt [47]. r^2SCAN functional has better computational efficiency performance than the earlier version of SCAN [128].

Cluster expansion Monte Carlo

A cluster-expansion Hamiltonian was generated in the chemical space of Li^+–Mn^{2+}–Mn^{3+}–Nb^{5+}–vacancy–O^{2-}–F^-, with pair interactions up to 7.1 Å, triplet interactions up to 4.0 Å, and quadruplet interactions up to 4.0 Å based on a primitive cell of the rocksalt structure with lattice parameter $a = 3$ Å. In total, 281 ECIs (including the constant term J_0) were defined, and the CE Hamiltonian was fitted with 1206 different structures. As the CE Hamiltonian was defined on a high-dimensional multicomponent system, the ECIs were fitted using the appropriate method to address the complexity-induced over-fitting [63]. The ECIs

were determined with the optimal sparseness and cross-validation error (< 7 meV/atom) with an $\ell_0\ell_2$-norm regularized regression [83].

To simulate atomic orderings at equilibrium, canonical Monte Carlo simulation with the Metropolis-Hastings algorithm was used. Overall, 1,000 representative structures (960 atoms per structure) were sampled from the equilibrium ensemble. The percolating Li content and the different types of tetrahedra clusters were analyzed in these representative structures using the `dribble` package [121].

Computational SRO analysis

Since Mn^{2+}-Nb^{5+}-based DRX systems exhibit SRO that leads to less favorable Li percolation than their Mn^{3+}-Nb^{5+}-based counterparts [17, 116]. The argument put forward is that synthesizing Mn^{3+}-Nb^{5+}-based DRX in a partially delithiated state could allow utilization of Mn^{2+}/Mn^{3+} redox while maintaining the superior SRO from Mn^{3+}. To achieve a more quantitative understanding of the percolation properties of L13MNOF, L11MNOF, and L09MNOF, *ab-initio* cluster-expansion Monte Carlo (CEMC) was implemented to investigate their SRO and percolating Li content. The atomic orderings of the as-synthesized compounds with different concentrations of cation vacancies ($Li_{1.3/1.1/0.9}Mn_{0.4}Nb_{0.3}O_{1.6}F_{0.4}$) were simulated by using canonical CEMC at T = 2023 K. This simulation temperature was calibrated for the ball-milling synthesis condition from the previously reported Li–Mn–O–F DRX system [117]. For percolation purposes, lithium and vacancies were considered equivalent since the latter can be occupied by Li in the discharge.

As shown in Fig. 3.16(a), the amount of Li sites that are part of the percolating clusters increases in the order of L13MNOF (75%) < L11MNOF (80%) < L09MNOF (87%), confirming that the presence of cation vacancies and Mn^{3+} in the synthesis of L11MNOF and L09MNOF improves their SRO and thus Li diffusion kinetics. It is noted that for L09MNOF, the simulation temperature (T = 2023 K) and composition put the system in a part of the phase diagram where phase separation is occurring (see Fig. 3.16(c)). Therefore, even though a higher percolating Li content is predicted for L09MNOF in the Monte Carlo simulation, the increased percolating Li content comes from the Li-rich phase rather than from the desirable disordered phase. This result also indicates that the concentration of cation vacancies that can be achieved in high-temperature synthesis is limited. The phase behavior of these simulated compounds is consistent with the experimental observation, as L13MNOF and L11MNOF can be synthesized as single-phase DRX compounds while an obvious impurity phase exists in the as-synthesized L09MNOF.

The SRO within L13MNOF and L11MNOF is further evaluated by comparing the occurrence (f_{calc}) of different tetrahedral clusters (0/1/2-TM channels) with respect to their frequency (f_{rand}) in the random limit $(f_{calc} - f_{rand})\,/f_{rand}$ (see Fig. 3.16(b)). As mentioned above, the cation SRO in DRX systems is found to be affected by two major factors: the local charge balance and the ionic radius of the cations [14, 17]. These insights can be used

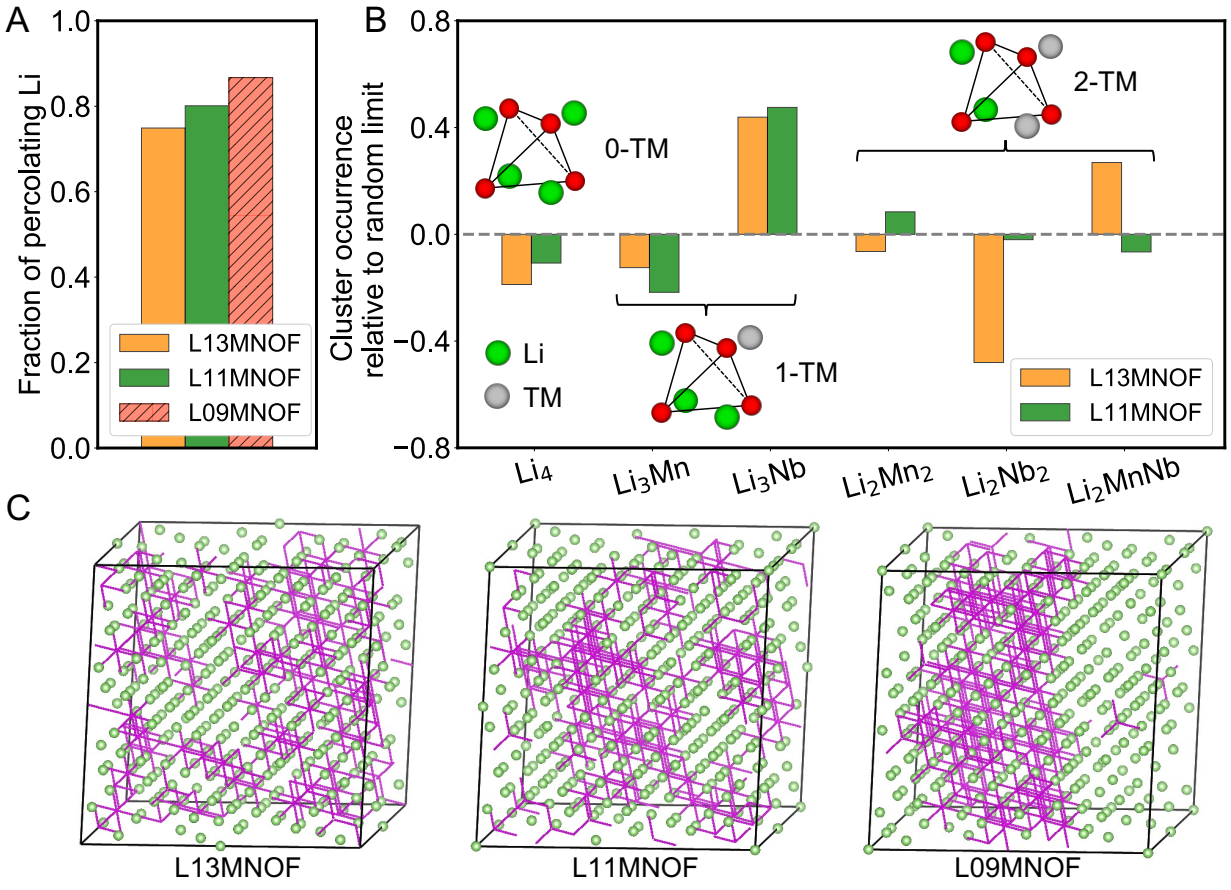

Figure 3.16: (a) Fraction of percolating Li content in L13MNOF (orange), L11MNOF (green), and L09MNOF (red dashed). The dashed bar indicates that the state of L09MNOF is non-disordered at the simulation temperature T = 2023 K. (b) Occurrence of various tetrahedral clusters (0-TM, 1-TM, and 2-TM) in cation-disordered L13MNOF (orange) and L11MNOF (green) as compared to the random limit. (c) Illustration of simulated structures for L13MNOF, L11MNOF, and L09MNOF. The green ball represents the Li atom, and the magenta line represents the distribution of the bond between Mn and its nearest anion. (Ref. [20])

to rationalize the effect of cation vacancies. Because the cation vacancy has a lower charge than the Li-ion, there is a higher tendency for a cation vacancy to mix with a high-valent cation (Nb^{5+}) so as to maintain local charge balance. For example, assuming all four anions (Fig.3.16(b) inset) on a tetrahedron to be O^{2-}, the average charge of the anions is -2. The cluster Li_2Nb_2 has an average charge of $(1 \times 2 + 5 \times 2)/4 = +3$, which is highly charge unbalanced. Therefore, its occurrence should be minimal in L13MNOF (the lowest orange bar of L13MNOF in Fig. 3.16(b)). However, the average charge of the Vac_2Nb_2 cluster is $(0 \times 2 + 5 \times 2)/4 = +2.5$, which is closer to the charge balance than L13MNOF. As a result, the Vac_2Nb_2 forms with higher frequency than Li_2Nb_2. The size effect of a vacancy versus a Li-ion is more difficult to gauge, but their incorporation will induce distortion and strain to neighboring sites. In DRX compounds, the energy penalty to accommodate such lattice distortion is significantly lower for d^0 TM cations (e.g., Nb^{5+}) than for those with partially filled d-orbitals (e.g., d^5 for Mn^{2+} and d^4 for Mn^{3+}) [15]. On this basis, one would also expect the Vac_2Nb_2 cluster formation to be energetically more favored than the Li_2Nb_2 one. Taken together, both local charge balance and lattice distortion promote the formation of Vac-Nb clusters. On the other hand, due to the larger lattice mismatch of Li with Mn^{3+} than with Mn^{2+}, there is a higher tendency for Mn^{3+} to segregate from Li, which increases 0-TM channels and decreases Mn-containing 1-TM and 2-TM channels: the total occurrence of Mn-containing 2-TM (Li_2Mn_2 and Li_2MnNb) and 1-TM (Li_3Mn) channels is lower in L11MNOF (42%) than L13MNOF (48%) (see Fig. 3.16(b)). Indeed, such Vac-Nb gathering and Li-Mn separation becomes even more significant in the CEMC-simulated L09MNOF compound, where the compound decomposes into (1) Li-Vac-Nb-rich and (2) Mn-rich regions with a majority of Nb atoms ($\sim$ 80%) and vacancies ($\sim$ 95%) located in region (1). Although region (1) has excellent Li percolation, it lacks Mn redox and is not useful as a cathode material, which may explain why the impure L09MNOF compound performs slightly worse than L11MNOF. Therefore, to fully utilize the superior SRO enabled by cation vacancies while keeping sufficient TM redox, a single-phase disordered structure must be maintained, which in turn requires that an appropriate amount of cation vacancies be introduced (e.g., 10% of vacancies in L11MNOF).

3.5.3 Experimental results

Synthesis and characterization

A mechanochemical ball-milling method was employed to synthesize cation-disordered $Li_{1.3}Mn^{2+}_{0.4}Nb_{0.3}O_{1.6}F_{0.4}$ (L13MNOF), $Li_{1.1}Mn^{2+}_{0.2}Mn^{3+}_{0.2}Nb_{0.3}O_{1.6}F_{0.4}$ (L11MNOF), and $Li_{0.9}Mn^{3+}_{0.4}Nb_{0.3}O_{1.6}F_{0.4}$ (L09MNOF) [107, 113]. The X-ray diffractions (XRD) of L13MNOF and L11MNOF compounds can be indexed to a DRX structure without obvious impurity peaks (see Fig. 3.17). The Rietveld refinement results indicate that L13MNOF has a larger lattice parameter (4.2261 Å) than L11MNOF (4.2110 Å), consistent with the larger ionic radius of Mn^{2+} (0.83 Å) than Mn^{3+} (0.65 Å) [120]. For L09MNOF, several Mn_2O_3 peaks appeared in the XRD pattern in addition to the DRX phase. Therefore, Mn_2O_3 was included as an

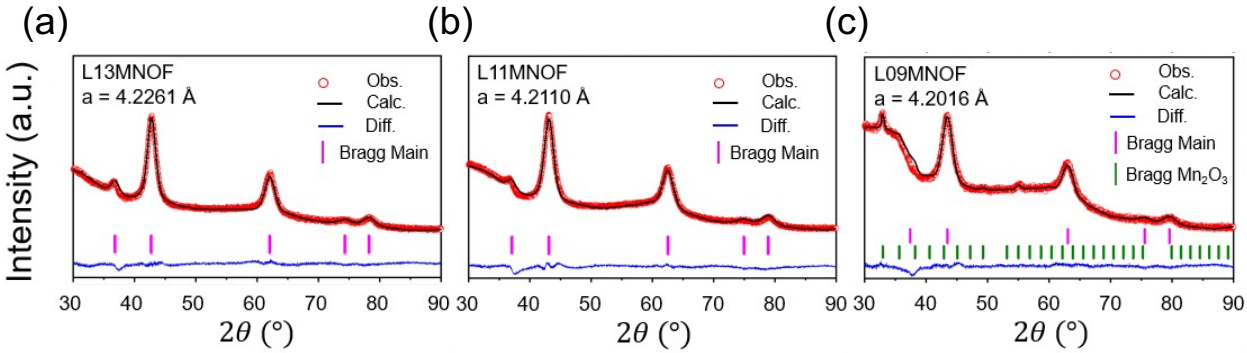

Figure 3.17: XRD patterns and refinement results for (a) L13MNOF, (b) L11MNOF, and (c) L09MNOF, where a is the refined lattice constant, and the Bragg positions are indicated by vertical magenta and olive bars. Obs., Calc., Diff. represent the observed pattern, calculated pattern, and the difference between the observed and calculated patterns, respectively. (Ref. [20])

impurity phase in the refinement for L09MNOF, in addition to a simple rocksalt structural model. The compound was refined to contain 4.5% Mn_2O_3 and 95.5% DRX phase. The synthesizability is consistent with the CEMC simulation, where phase segregation (inaccessible homogeneous distribution) is observed for L09MNOF.

Electrochemistry

The electrochemical performance of the Li-Mn-Nb-O-F compounds was tested in galvanostatic mode at room temperature (Fig. 3.18). The open circuit voltage of as-synthesized samples increases in the order of L13MNOF < L11MNOF < L09MNOF, consistent with their increased Mn valence. When cycled between 1.5 and 5 V at a current density of 20 mA/g, the first-cycle charge capacity decreased in the order of L13MNOF (334 mAh/g) > L11MNOF (280 mAh/g) > L09MNOF (218 mAh/g), consistent with their decreasing theoretical Li capacities. Interestingly, upon discharge, L13MNOF delivered the lowest capacity among the three compounds: 258 mAh/g (810 Wh/kg) for L13MNOF, 283 mAh/g (885 Wh/kg) for L11MNOF, and 272 mAh/g (832 Wh/kg) for L09MNOF. The effect of cation vacancies on improved Li transport is further corroborated by the superior rate performance of L11MNOF and L09MNOF (Fig. 3.18(d) and (f)). For example, upon increasing the current density from 20 to 1000 mA/g, the discharge capacity for L13MNOF decreased from 258 to 113 mAh/g, corresponding to a 56.2% capacity loss at the high rate. In contrast, the capacity loss was reduced to 50.4% for L09MNOF and to 43.1% for L11MNOF, and a large discharge capacity of 161 mAh/g continued to be delivered at 1000 mA/g for L11MNOF. Note that these three compounds can be essentially regarded as three different states of a single material under a topotactic transformation, which in principle would not give rise

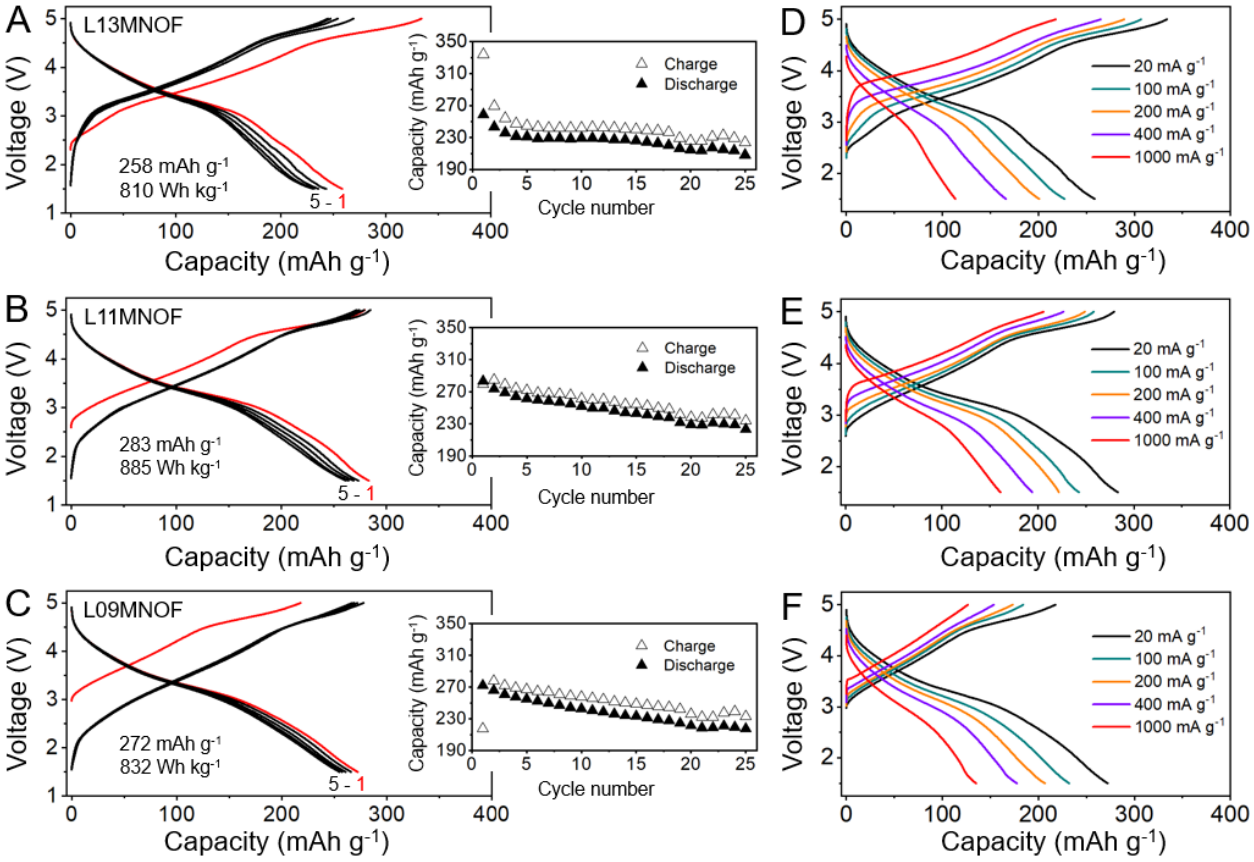

Figure 3.18: Voltage profiles of (a) L13MNOF, (b) L11MNOF, and (c) L09MNOF within the voltage window of 1.5 – 5 V at 20 mA/g and room temperature. The voltage profiles of cycle 1 are plotted in red, and the rest are plotted in black. The corresponding capacity-retention plots for each compound over 25 cycles are shown as insets. First-cycle voltage profiles of (d) L13MNOF, (e) L11MNOF, and (f) L09MNOF at different current densities. (Ref. [20])

to observable differences in overall performance. Therefore, the electrochemical test results strongly suggest that introducing cation vacancies during the synthesis modifies the local chemical ordering within the compound, improving its percolation properties.

In summary, using a combination of *ab-initio* and experimental investigations, it is confirmed that partial Li deficiency strategy results in both Mn^{2+}/Mn^{3+} redox and excellent Li percolation due to the presence of Mn^{3+}, therefore delivering increased discharge capacity and rate performance. The vacancy concentration needs to be appropriately controlled as extensive vacancy doping (e.g., 20% vacancies in $Li_{0.9}Mn^{3+}_{0.4}Nb_{0.3}O_{1.6}F_{0.4}$) creates phase separation between a Li-Nb-rich phase and Mn-rich phase, which impairs the cathode performance. This work extends the DRX design space to non-stoichiometric compounds, providing additional opportunities to optimize their performance.

3.6 Conclusion

Chapter 3 discusses the application of *ab-initio* modeling, facilitated by cluster expansion methods, to simulate the SRO distribution in DRX materials. It is demonstrated that cluster expansion could effectively model configurational disorder by incorporating pair, triplet, and quadruplet interactions between inter- and intra-sublattices in oxides. This approach enabled us to obtain effective cluster interactions and accurately reproduce thermodynamic properties through Monte Carlo simulations.

Applying cluster expansion in simulating SRO offers profound insights into the fundamental understanding of DRX materials. For instance, in the first example, Li-F SRO stems from the strong attraction between Li and F, displaying a locking effect that limits the number of extractable Li within a specific voltage range. This thermodynamically controlled effect can be mitigated by introducing Mg-doping, which presents the possibility of increasing capacity and enhancing the electrochemical performance by increasing the amount of extractable Li. In the second example, cation-SRO and its impact on Li transport kinetic are discussed by analyzing the percolating Li content in the connected 0-TM diffusion networks. It is demonstrated that a novel approach to modulate cation-SRO by introducing partial Li deficiency, resulting in both Mn^{2+}/Mn^{3+} redox and excellent Li percolation in the presence of Mn^{3+}.

These examples highlight the importance of understanding the relationship between local structural orderings and electrochemical performance. Since DRX materials exhibit long-range randomness but possess SRO, statistical modeling is required to accurately sample the thermodynamical quantities. Cluster expansion Monte Carlo provides a natural way for sampling configurations. And the insights obtained from these simulations (e.g., percolating Li content, the specific amount of clusters, etc) are crucial in guiding the design of DRX materials and optimizing existing ones for next-generation energy storage applications.

Chapter 4

Atomistic modeling with charge information – Methodology

4.1 Introduction

In Chapter 2 and Chapter 3, the principles of the cluster expansion method and its application in modeling short-range order within DRX materials are discussed. Within this context, canonical MC simulations are used to sample the equilibrium states of atomic orderings, where the DRX compounds are conceptualized as alloy systems without considering the charge transfer between ions. However, many essential phenomena (e.g., charging/discharging) are correlated with the charge transfer effect in cathode materials. A more comprehensive understanding of these materials mandates an examination of the electronic degrees of freedom.

This chapter is dedicated to addressing methodological advancements that incorporate charge information into the atomistic modeling framework. Specifically, two key methodological approaches will be discussed: (1) charge-decorated cluster expansion and (2) charge-informed interatomic potentials. These methodologies enable a more holistic representation of the DRX materials by considering the interplay between atomic arrangements and charge distributions. Through these multifaceted approaches, one can achieve a more accurate understanding of the structural and electrochemical properties of DRX materials.

4.2 Charge-decorated cluster expansion

Similar to the definition in Eq. (2.28), the internal energy in multicomponent ionic systems can be expressed through the cluster expansion method as

$$E(\boldsymbol{\sigma}) = \sum_{\beta} m_{\beta} J_{\beta} \left\langle \Phi_{\boldsymbol{\alpha} \in \beta} \right\rangle_{\beta} + \frac{E_0}{\varepsilon_r}. \tag{4.1}$$

In this equation, E_0 represents the unscreened electrostatic energy, and $1/\varepsilon_r$ is treated as one of the ECIs with the constraint $1/\varepsilon_r \geq 0$. The inclusion of this additional term is crucial for capturing not only the short-range interactions but also the long-range interactions [94].

4.2.1 Inclusion of long-range electrostatic energy

The unscreened electrostatic energy (Ewald energy E_0) is computed with decorated charges $\{q_i\}$ in a structure via

$$\begin{aligned} E_0 &= E^S + E^L - E^{\text{self}} \\ &= \frac{1}{2}\sum_{\boldsymbol{n}}\sum_{i,j=1}^{N}\frac{q_i q_j}{|\boldsymbol{r}_i - \boldsymbol{r}_j + \boldsymbol{n}L|}\text{erfc}\left(\frac{|\boldsymbol{r}_i - \boldsymbol{r}_j + \boldsymbol{n}L|}{\sqrt{2}\sigma}\right) \\ &\quad + \frac{1}{2V\varepsilon_0}\sum_{\boldsymbol{k}\neq 0}\sum_{i,j=1}^{N}\frac{q_i q_j}{k^2}e^{i\boldsymbol{k}\cdot(\boldsymbol{r}_i - \boldsymbol{r}_j)}e^{-\sigma^2 k^2/2} - \frac{1}{4\pi\varepsilon_0}\frac{1}{\sqrt{2\pi}\sigma}\sum_{i}^{N} q_i^2, \end{aligned} \tag{4.2}$$

where E^S, E^L, and E^{self} represent the short-range, long-range, and self-interaction terms, respectively. The unscreened electrostatic energy E_0 can be computed efficiently and with high accuracy using the Ewald summation method [129] or the fast multipole method [130].

Why need to include long-range electrostatic energy?

Despite some early studies revealed that the systems with long-range interactions can be well-represented and converged by a CE with only considering short-range interactions, as long as the sampling space stays in a certain low-energy domain [131]. The situation may complicate when constructing CE with many species. As the feature dimension of the CE grows combinatorially with the number of components, the DFT samplings can hardly fully cover the predefined ECIs space. The out-of-distribution configurations can be easily reached in MC simulation with a CE only fitted on certain low-energy structures. To partially prevent this, including the long-range electrostatic energy can impose physicality. This effect is illustrated by the example in the following.

Inaccessible configurations and out-of-distribution

When fitting a CE model of a complex ionic material, there will usually exist configurations that cannot be reached due to convergence issues in DFT calculations. There are two main categories of configurations that can be inaccessible to DFT: geometrical inaccessibility and charge-valence inaccessibility. (1) Geometrical inaccessibility occurs when the DFT-relaxed structures drift far from their original lattice sites and cannot be correctly mapped. For example, anion drift destroys the FCC anion framework of a rocksalt. Although the initial configuration may have been in the rock-salt configuration space, the resulting

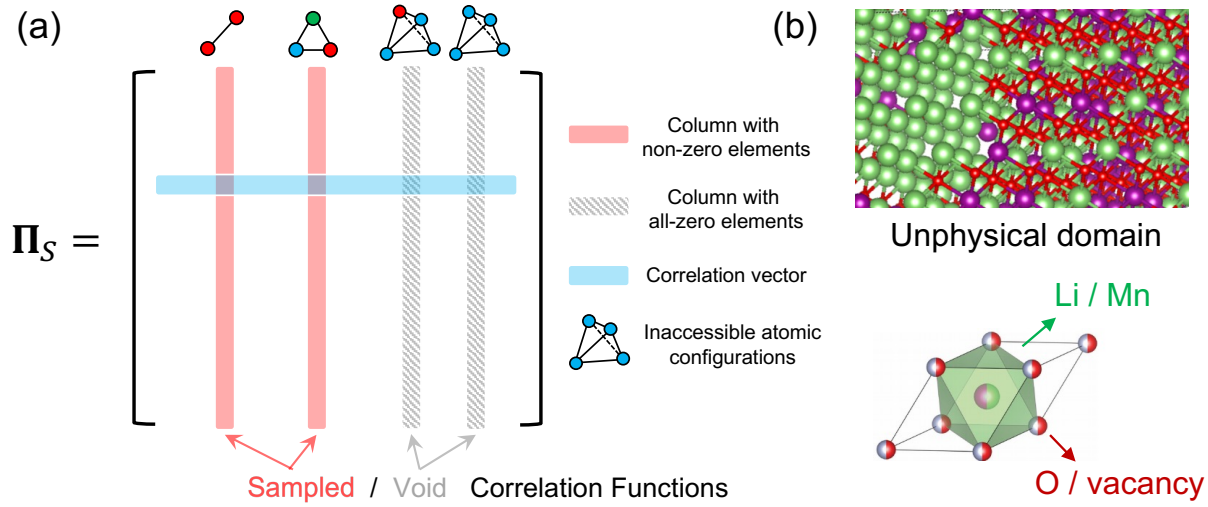

Figure 4.1: (b) Illustration of feature matrix $\mathbf{\Pi}_S$ with inaccessible (non-sampled) configurations using an indicator basis. The red columns represent the correlation functions that are covered by DFT calculations, while the gray (shaded) columns represent the inaccessible atomic configurations. (e.g., the blue sites are occupied by high-valent transition metals such as Nb^{5+}, Mo^{6+}, which have strong repulsion in one tetrahedron and cannot be well evaluated via DFT. And the blue row represents the correlation vector of one specific structure (Ref. [63]). (c) Simulated unphysical domain from a CE Hamiltonian without the inclusion of electrostatic energy, such a trial CE is based on the DRX systems where cation can be occupied by Li/Mn and the anion sites can be occupied by O/vacancy (Ref. [19]).

relaxed structure no longer is. This becomes a very notable problem when considering configurations with a large number of vacancies. (2) Charge-valence inaccessibility happens when the DFT-relaxed configuration can be appropriately mapped back to a lattice model with oxidation-assigned ionic species; however, charge transfer prevents specific oxidation states for particular configurations of the predefined lattice model. This happens mostly in transition metal oxides when the valence of the transition metal cannot be well assigned and results in non-charge-balanced configurations. This can also result from internal charge transfer in very high electrostatic energy configurations.

The efficiency of structure sampling is thus reduced depending on how many physically inaccessible states occur in the sampled training configurations. For example, as shown in Fig. 4.1(a), the blue sites in the cluster figures are occupied by high-valent transition metal (e.g., Nb^{5+}, Mo^{6+}), which have strong repulsion in a single tetrahedron. Such features cannot be appropriately computed by DFT calculations. The effect on sampling is most clear when using an indicator basis since this will result in a void correlation function in the feature matrix $\mathbf{\Pi}_S$. The void correlation function manifests itself as a column with

all elements equal to zero. This happens since no information has been obtained for those particular configurations, such that this correlation function is rendered uninformative and should be removed prior to fitting. Such inaccessibility can lead to issues with configuration sampling in Monte Carlo simulations due to the lack of information regarding the ECIs associated with inaccessible high-energy configurations. This problem becomes evident when a configuration exhibiting inaccessible features is situated close to a low-energy configuration in the configuration space, i.e., only a few Monte Carlo steps away. Such a configuration may be accepted since its energy is inaccurately predicted, thereby resulting in the incorrect sampling of unfavorable configurations in Monte Carlo simulations, which can skew ensemble statistics and calculated thermodynamic properties.

An illustrative example of an extreme case for unphysical configurations is provided by the MC simulations of Li-Mn DRX using a trial CE. In this system, the cation sites can be occupied by Li/Mn, while anion sites can be occupied by either oxygen or vacancy [19]. The simulated ground state, as shown in Fig. 4.1(b), exhibits phase segregation for Li and vacancies, implying a preference for forming a metallic Li phase over rocksalt oxides. This is clearly an incorrect result and likely stems from an over-fitted CE model. As these configurations are neither included in the training set nor can they be obtained from DFT calculations, a practical solution to this out-of-distribution issue is to incorporate the electrostatic energy.

Alternatively, in a charge-decorated CE model, the valences of Li and the vacancy are assigned as +1 and 0, respectively. The segregation of Li and vacancies results in high charge polarization and, consequently, high electrostatic energy. During MC simulations, even if the CE is not explicitly fitted on such configurations, the electrostatic energy can deter the sampling from entering such domains, i.e., preventing reaching the out-of-distribution configurations and thereby enhancing the robustness and physicality of the simulation results. The inclusion of electrostatics has been shown to yield reasonable simulated configurations and insightful short-range order analysis, as demonstrated in Ref. [19].

Other approaches regarding inaccessible and electrostatics

Apart from the approach with electrostatic energy, there are other general flavors to enhance the sampling and avoid inaccessible configurations. Two approaches are suggested that are useful to deal with the issue. (1) First, the ECI can be regularized with more importance given to those corresponding to lower-degree clusters (such as pair-wise interactions). This can be achieved by using hierarchy constraints as detailed in Chapter 2. These fitting strategies are effective when the configuration energy can be well depicted by correlations of clusters with small support. Therefore, void or under-sampled correlation functions for clusters with larger support will contribute minimally to the total energy. (2) If the resulting CE model still under-predicts the energy of configurations that are likely to be high energy, rejection of these configurations can be easily achieved in MC. The rejection can be done by including a cluster indicator function of the orbit β associated with such inaccessible atomic configurations. The probability evaluated in Monte Carlo that guarantees the rejection of

inaccessible configurations is,

$$P(\boldsymbol{\sigma}) \propto \exp\left(-\frac{E_{\mathrm{CE}}(\boldsymbol{\sigma}) + \sum_{\beta\in\mathrm{void}} M \cdot \mathbf{1}_\beta}{k_B T}\right), \tag{4.3}$$

where E_{CE} is the CE energy evaluated with actual ECIs, M is a large positive number, and $\mathbf{1}_\beta$ is the indicating function of orbit β. Since the cluster indicator function will only be nonzero when the specific inaccessible cluster configuration is present, all other configurations that do not include such configuration will not be affected. This approach requires practitioners to detect the inaccessible configurations in the first place explicitly.

Additionally, such a rejection flavor is further adopted for the grand-canonical MC simulations with charge-decorated CEs. Xie et al. [61] introduced the square-charge bias method that allows the system to temporarily drift away from charge neutrality, with a penalized Hamiltonian on the square of unbalanced net charge

$$P(\boldsymbol{\sigma}) \propto \exp\left(-\frac{E_{\mathrm{CE}}(\boldsymbol{\sigma}) - \sum_s \mu_s n_s + \lambda k_B T C(\boldsymbol{\sigma})^2}{k_B T}\right), \tag{4.4}$$

where $C(\boldsymbol{\sigma})$ is the net charge, λ is the hyperparameter for penalization, and $E_{\mathrm{CE}}(\boldsymbol{\sigma}) - \sum_s \mu_s n_s$ is the grand canonical energy. The square-charge bias method is particularly useful in the grand canonical simulation of ionic materials with many components, especially when the single excitation energy is too high to be achieved at low temperatures with the conventional table-exchange method [61].

4.2.2 Charge decoration with magnetic moments

To compute the electrostatic energy, a valence state q_i needs to be assigned for each atom, which necessitates the determination of the atomic charge state. Additionally, the importance of an ion's valence derives from the fact that it can engage in very different bonding with its environment depending on its electron count. For example, according to crystal field theory, valence electron d-filling of the TM-oxygen states is one factor controlling whether a TM ion prefers tetrahedral or octahedral coordination. High spin Mn^{4+} is a non-bonding spherical ion that almost always resides in octahedral coordination by oxygen atoms, whereas Mn^{3+} is a Jahn–Teller active ion that radically distorts its environment, and Mn^{2+} is an ion that strongly prefers tetrahedral coordination [132]. Such strong chemical interaction variability across different valence states exists for almost all transition metal ions and requires the specification of an ion beyond its chemical identity.

Several methods can be used to represent charge information, ranging from simplistic oxidation state labels to intricate wave functions derived from quantum mechanics. Walsh et al. [133] overviewed several approaches for partitioning electron density between atomic centers to determine the oxidation states of atoms using the case of the CdO system. Figure 4.2(a) introduces the simple approach using geometric charge partitioning based on the

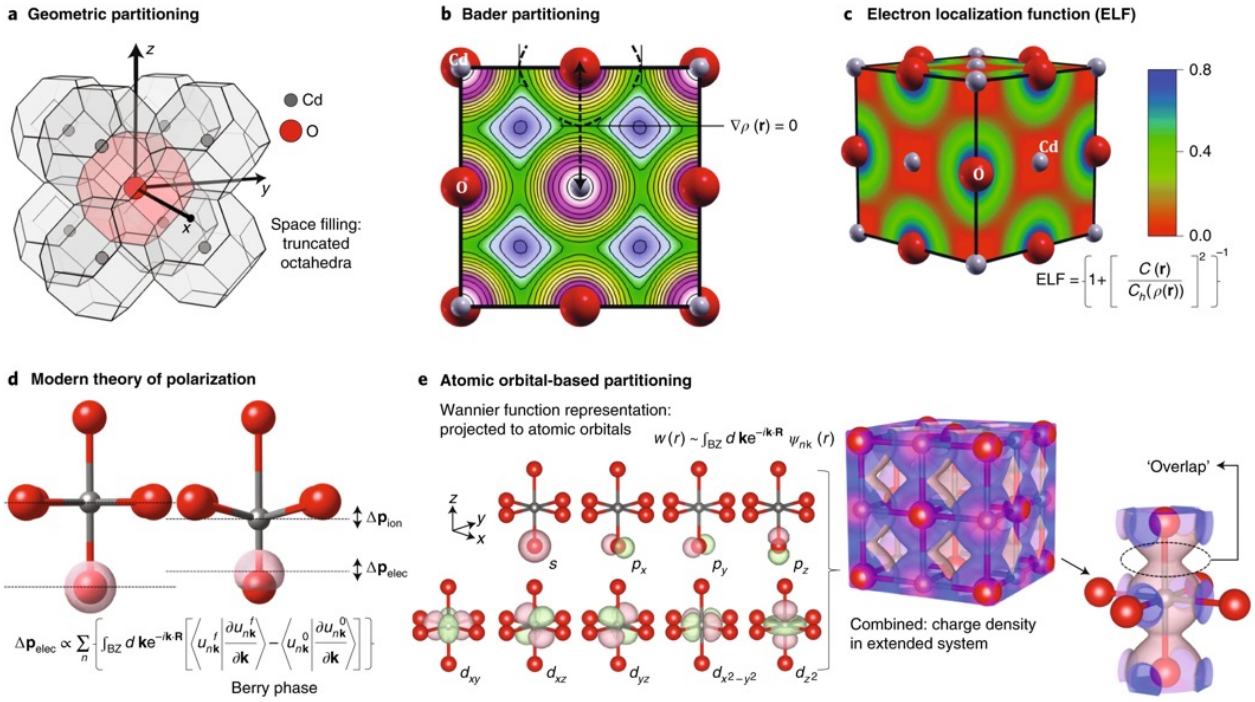

Figure 4.2: Examples of charge density partition in CdO system overviewed by Walsh et al. [133]: (a) Geometric partitioning based on space-filling for a Wigner–Seitz polyhedral decomposition of CdO. (b) Topological analysis of the electron density $\rho(r)$ using Bader's charge. (c) Analysis of electron pair probability distribution as determined using the electron localization function (ELF). (d) Changes in electric polarization $\Delta\rho$ from topological analysis of the electron distribution using the Berry phase formalism. (e) Projection of extended electronic wavefunctions onto localized orbitals (Wannier functions) that combine to reproduce the full electron density of the crystal (Ref. [133])

Wigner–Seitz polyhedral. Figure 4.2(b) illustrates a topological analysis of the electron density $\rho(r)$ in a rocksalt CdO structure through Bader's 'atoms in molecules' approach, highlighting the partitioning of electron density based on zero-flux surfaces [134]. Figure 4.2(c) delves into the analysis of the electron pair probability distribution using the electron localization function (ELF). The ELF is calculated via the Kohn-Sham orbitals $\{\phi_i\}$ and charge densities ρ [135], which have values between 0 and 1 (one corresponds to perfect localization). Alternatively, changes in electric polarization $\Delta\rho(r)$ derived from a topological analysis of electron distribution using the Berry phase formalism can be used for representation (Fig. 4.2(d)). And Figure 4.2(e) highlights the projection of extended electronic wavefunctions onto localized orbitals (Wannier functions) [136]. The approaches such as using Bader's charge [137], incorporating maximally localized Wannier functions for long-range electrostatic interactions [138], and neural network prediction of MLWF have been reported

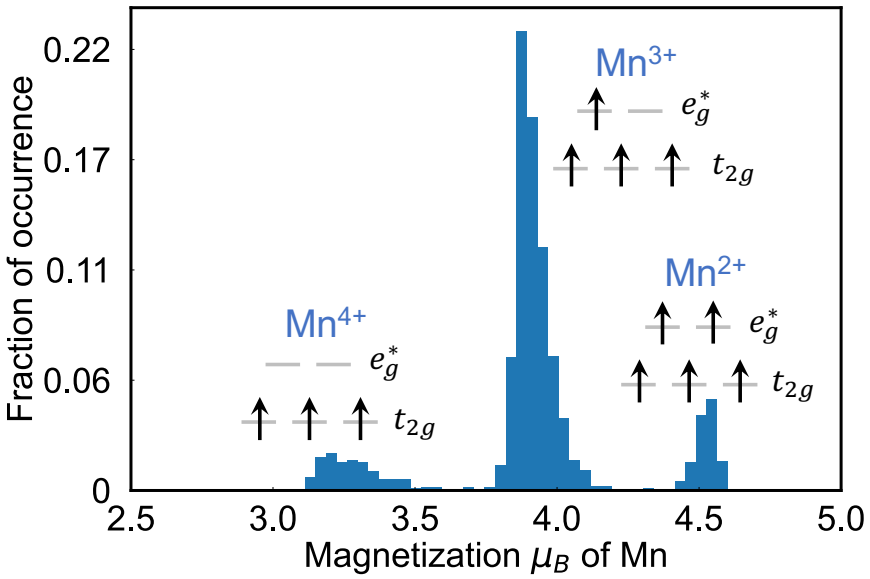

Figure 4.3: The magnetization distribution of Mn calculated with GGA+U in the system of $Li_{1.2}Mn_{0.6}Nb_{0.2}O_{2.0}$. (Ref. [63])

in previous research associated with the charge-information representation [139].

Nonetheless, when evaluating the formal valence of transition metal ions, particularly those with d-orbital transitions, directly using the charge density from DFT is favorable. This is because the density remains unchanged across various valence states due to hybridization with neighboring anions. This is elegantly discussed by Wolverton and Zunger [140] for Li_xCoO_2, where the charge density around Co in CoO_2 and $LiCoO_2$ is surprisingly similar, as described by the authors:

> *This self-regulating response [141, 142] (minimizing the effect of external perturbations via rehybridization) is characteristic of systems having localized d states that communicate with a covalent manifold.*

Therefore, a more reliable method is to assign a formal charge based on the magnetic moment for a given metal site, which can be derived from the sum of s, p, and d- local orbital contributions or from the individual d-orbital contribution. This local contribution can be obtained by integrating the difference between spin-up and spin-down magnetic moments surrounding each atom. Figure 4.3 displays the magnetization distribution of Mn calculated with GGA+U in a DRX system with composition $Li_{1.2}Mn_{0.6}Nb_{0.2}O_{2.0}$. From the histogram,

one can estimate the boundary for $Mn^{4+/3+}$ and $Mn^{3+/2+}$ classification to be $3.6\mu_B$ and $4.2\mu_B$ and use the charge-decorated species to construct the CE Hamiltonian with multi-component basis functions as described in Chapter 2.

Since the *d*-electron occupancy is most relevant to capture the local bonding environment of a TM (e.g., its size, coordination preference, any tendency for Jahn–Teller distortion), the charge decoration on TM based on the magnetic moment is important to project the interactions into cluster expansion basis functions accurately.

4.3 Charge-informed interatomic potential

Although charge-decorated cluster expansion offers an ideal toolkit to understand the equilibrium thermodynamics of ionic materials, it is not capable of modeling the dynamics when the degrees of freedom are continuous in space rather than the coarse-grained lattice. The computational modeling of kinetic properties, such as ion migrations, phase transformation, and chemical reactions, is highly desired for the study of computation materials science. For example, large-scale molecular dynamics (MD) are essential for the computational design of solid-state materials [143]. Although *ab-initio* molecular dynamics (AIMD) with DFT can provide high-fidelity results, they are computationally expensive, especially when the AIMD is implemented with spin-polarized DFT, which hinders the application to the multicomponent ionic materials.

4.3.1 Overview of machine learning interatomic potential

The application of machine learning in computational materials science has experienced a surge in recent years, largely driven by the impressive capacity of these models to predict a variety of material properties [144–146]. Neural network (NN) machine learning interatomic potentials (MLIPs) have emerged as powerful tools that can provide efficient and accurate predictions by learning from high-fidelity data with quantum mechanical accuracies. The first high-dimensional neural network potential was proposed by Behler and Parrinello [147], where the total energy is expressed as a summation of atomic energy $E = \sum_i E_i$ with E_i predicted by a NN. There are many designs of MLIPs that can broadly be categorized into two types: (1) descriptor-based potentials and (2) end-to-end NN potentials [148]. The descriptor-based MLIP typically uses atomic-centered symmetry functions to encode the information of the local chemical environment of atoms, such as two-body terms and three-body terms proposed by Behler and Parrinello [147]:

$$\begin{aligned} G_i^1 &= \sum_{j\neq i} e^{-\eta(R_{ij}-R_s)^2} f_c(R_{ij}) \\ G_i^2 &= 2^{1-\zeta} \sum_{j,k\neq i} (1+\lambda\cos\theta_{ijk})^\zeta \times e^{-\eta(R_{ij}^2+R_{ik}^2+R_{jk}^2)} f_c(R_{ij}) f_c(R_{ik}) f_c(R_{jk}). \end{aligned} \tag{4.5}$$

with $\theta_{ijk} = \boldsymbol{R}_{ij} \cdot \boldsymbol{R}_{ik}/(R_{ij}R_{ik})$ and hyperparameters $\lambda = \pm 1$, η, and ζ. The radical cutoff function reads

$$f_c(R_{ij}) = \begin{cases} 0.5 \times \left[\cos\left(\frac{\pi R_{ij}}{R_c}\right) + 1\right] & \text{for } R_{ij} \leq R_c \\ 0 & \text{for } R_{ij} > R_c \end{cases}, \tag{4.6}$$

which ensures that G_i^1 and G_i^2 vary smoothly at the cutoff radius. The descriptor-based NN potentials such as ænet [149] have provided promising solutions to bridge the gap between expensive electronic structure methods and efficient classical interatomic potentials in energy storage systems [150].

Another type of descriptor-based MLIP is Gaussian process (GP) force fields, also known as Bayesian force fields. The GP force fields have a significant impact on the application of atomistic modeling, such as catalysis [151] and solid-state phase transformation [152]. In GP (or sparse GP) formalism, the local atomic environment ρ_i consists of neighboring atoms within a cutoff radius with a label y_i (e.g., local energy ε_i on atom i. The kernel function $k(\rho_i, \rho_j)$ quantifies the similarity between two atomic environments i and j. For example, the inner product kernel is defined as

$$k(\rho_i, \rho_j) = \sigma^2 \left(\frac{\boldsymbol{d}_1 \cdot \boldsymbol{d}_2}{d_1 d_2}\right)^2, \tag{4.7}$$

where σ^2 is the signal variance which can be optimized by maximizing the log-likelihood of GP, $\boldsymbol{d}_1$ and $\boldsymbol{d}_1$ are descriptors derived from atomic cluster expansion (ACE) [153].

The total energy is a sum of local energies $E = \sum_i \varepsilon(\rho_i)$, where the local energy is evaluated by a weighted sum of kernels between ρ_i and a step of representative environments:

$$\varepsilon(\rho_i) = \sum_{t \in S} k(\boldsymbol{d}_i, \boldsymbol{d}_t)\alpha_t. \tag{4.8}$$

The $\boldsymbol{\alpha}$ is a vector of training coefficients given by

$$\boldsymbol{\alpha} = \boldsymbol{\Sigma} \boldsymbol{K}_{SF} \boldsymbol{y}, \tag{4.9}$$

where $\boldsymbol{\Sigma} = (\boldsymbol{K}_{SF}\boldsymbol{\Lambda}^{-1}\boldsymbol{K}_{FS} + \boldsymbol{K}_{SS})^{-1}$, $\boldsymbol{K}_{SF}$ is the matrix of kernel values between a chosen sparse set S (for efficient evaluation) and the training set F, $\boldsymbol{K}_{SS}$ is the matrix of kernel values between the sparse set S and itself, and $\boldsymbol{\Lambda}$ is a diagonal matrix quantifying the noise of the system. The total potential energy of a structure of N atoms is a sum of all local energies $\varepsilon(\rho_i)$. The most significant feature of GP is that the uncertainty of the prediction can be simultaneously given. For example, the sparse GP predicted variance V_E under deterministic training condition approximation is [154]

$$V_E = k_{EE} - \boldsymbol{k}_{ES}\boldsymbol{K}_{SS}^{-1}\boldsymbol{k}_{ES} + \boldsymbol{k}_{ES}\boldsymbol{\Sigma}\boldsymbol{k}_{SE} \tag{4.10}$$

where $k_{EE} = \sum_{ij} k(\boldsymbol{d}_i, \boldsymbol{d}_j)$ is the GP covariance between E and itself, $\boldsymbol{k}_{ES}$ is a row vector describing the covariance between potential energy E and the local energies of set S. Since GP force fields are uncertainty aware, they have been widely used in autonomous "on-the-fly" training for generating fast and accurate force fields for MD simulations [155].

Nonetheless, one significant drawback of the descriptor-based MLIP is that the number of input dimensions can grow quickly when applying it to multi-component systems. This limits its application in complex materials such as DRXs. In contrast, the end-to-end NN potentials directly learn from the atomic types and positions as inputs for suitable representations via data-driven approaches [148]. For example, the DeepMD model utilized the translational/rotational-invariant coordinates to encode the local environment of atom i given by all neighbors $\{j\}$

$$\{D_{ij}\} = \left\{ \frac{1}{R_{ij}}, \frac{x_{ij}}{R_{ij}}, \frac{y_{ij}}{R_{ij}}, \frac{z_{ij}}{R_{ij}} \right\} \tag{4.11}$$

where (x_{ij}, y_{ij}, z_{ij}) is the local coordinate transformed from the global coordinate to accommodate the rotational invariant [156]. The total potential energy is $E = \sum_i E_i$, where $E_i = \mathrm{DNN}(\{D_{ij}\})$ is the local energy given by a deep NN prediction. The DeepMD has shown various successes in large-scale MD simulations with *ab-initio* accuracy, such as phase diagrams of water [157], solid-state electrolytes [158], and metallic alloys [159].

Furthermore, the development of graph neural networks (GNN) has led to more sophisticated models, such as the message-passing neural network (MPNN) models. Atoms are represented as nodes and bonds as edges. The nodes are initialized as an embedding vector with elemental information, and the edges embody the pair-wise bonding information. The updates of node information are achieved via a message-passing mechanism (graph convolution), which can be written in general as

$$\boldsymbol{x}_i^{(t+1)} = \boldsymbol{x}_i^{(t)} + \mathcal{L}\left[\sum_{j \neq i} \mathcal{F}(\boldsymbol{x}_i^{(t)}, \boldsymbol{x}_j^{(t)}, g(r_{ij})) f_c(r_{ij}) \right], \tag{4.12}$$

where the summation runs over all atoms within a cutoff distance r_c, $\boldsymbol{x}_i^{(t)}$ is the atom feature vector for the i-th atom in the t-th layer of MPNN, $g(r_{ij})$ is the embedded bond feature vector describing the bond information between atom i and j, $f_c(r_{ij})$ is a smooth function and $\mathcal{F}$ is an interaction block which operates the graph convolution. $\mathcal{L}$ is a general linear or identical transformation. The translation, rotation, and permutation invariance are preserved in GNNs [144, 160, 161]. The GNN-based MLIPs such as DimeNet [162], NequIP [163], TeaNet [164], and MACE [165] have been shown to achieve state-of-the-art performance by incorporating invariant/equivariant symmetry constraints.

Most recently, GNN-based MLIPs trained on the periodic table (e.g., M3GNet) have demonstrated the possibility of universal interatomic potentials that may not require chemistry-specific training for each new application [137, 166, 167]. It is critical to acknowledge that the

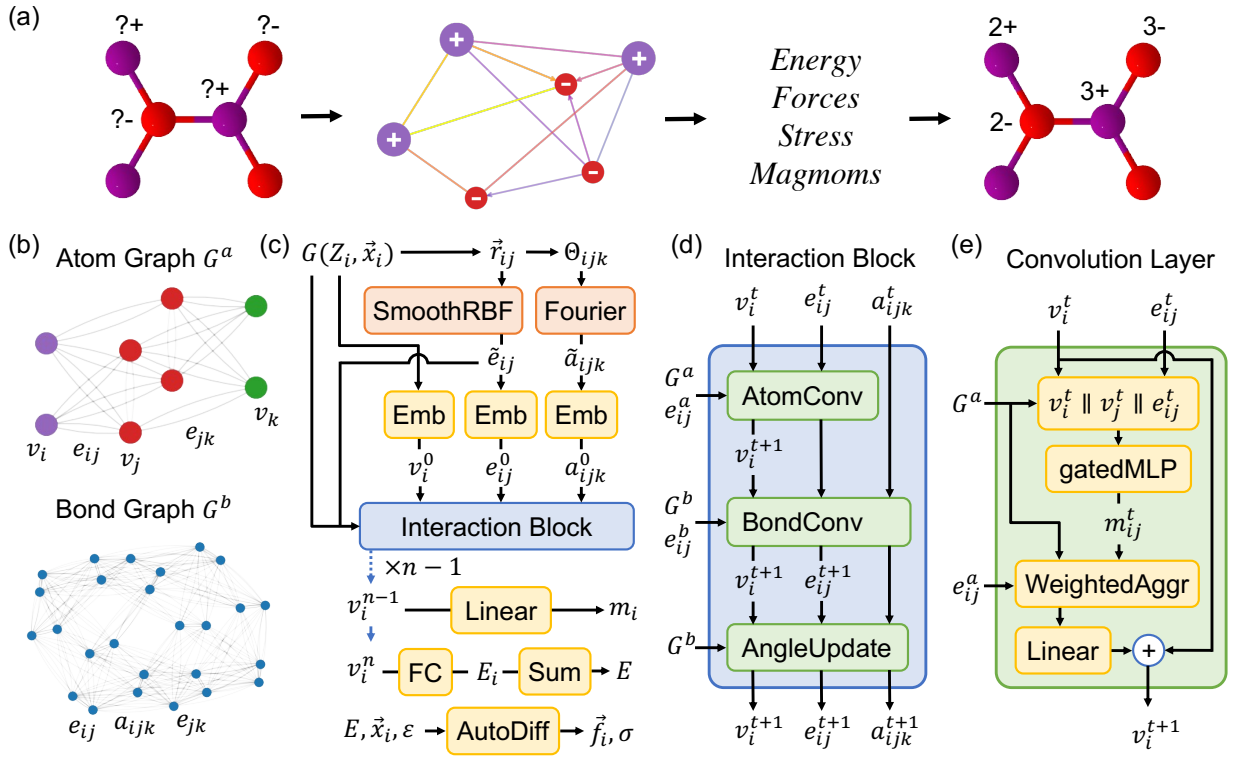

Figure 4.4: (a) CHGNet workflow: a crystal structure with unknown atomic charge is used as input to predict the energy, force, stress, and magnetic moments, resulting in a charge-decorated structure. (b) The model consists of atom graphs and bond graphs. (c) Graphs run through basis expansions and embedding layers to create atom, bond, and angle features. (d) Interaction block in which the atom, bond, and angle share and update information. (e) Atom convolution layer where neighboring atom and bond information is calculated through weighted message passing and aggregates to the atoms. (Ref. [168])

emphasis of past research has primarily been on advancing the state-of-the-art performance of the model itself. The capability to capture the charge information of ions, especially for *d*-orbital transition-metal-containing battery materials, is another crucial aspect that was not well discussed until the introduction of CHGNet [168].

4.3.2 Crystal Hamiltonian Graph Neural Network

Crystal **H**amiltonian **G**raph neural-**Net**work (CHGNet) is another MLIP with charge information. The foundation of CHGNet is a GNN, as shown in Fig. 4.4, where the graph convolution layer is used to propagate atomic information via a set of nodes $\{v_i\}$ connected by edges $\{e_{ij}\}$. Unlike other GNNs, where the updated atom features $\{v_i^n\}$ after n convolution

layers are directly used to predict energies, CHGNet regularizes the node-wise features $\{v_i^{n-1}\}$ at the $n-1$ convolution layer to contain the information about magnetic moments. The regularized features $\{v_i^{n-1}\}$ carry rich information about both local ionic environments and charge distribution. In CHGNet, the energy is calculated by a sum of non-linear projection $\phi_E(\cdot)$ of the site-wise feature vector over all atoms $\{v_i^n\}$. The forces and stress are calculated via auto-differentiation of the energy with respect to the atomic Cartesian coordinates and strain, and the site-wise magnetic moment is calculated by a linear projection $\phi_m(\cdot)$ of the feature vector in the hidden layer $\{v_i^{n-1}\}$.

$$E_{\text{tot}} = \sum_i \phi_E(v_i^n),\ \vec{f}_i = -\frac{\partial E_{\text{tot}}}{\partial \vec{x}_i},\ \boldsymbol{\sigma} = \frac{1}{V}\frac{\partial E_{\text{tot}}}{\partial \boldsymbol{\varepsilon}},\ m_i = \phi_m(v_i^{n-1}). \tag{4.13}$$

Therefore, the atomic charge information can be inferred from the CHGNet predicted magnetic moments, using only the nuclear positions and atomic identities as input. Such an approach allows the study of charge distribution in atomistic modeling. For non-magnetic systems or systems with small magnetic moments, the atomic charge inference may not be adequate enough from the CHGNet prediction. But the interatomic interactions can still be learned and well represented as the model is trained on energy, force, and stress primarily, while the magmom is added as an additional regularization.

Table 4.1: The mean-absolute-errors (MAEs) of pretrained CHGNet on MPtrj test set.

	Energy (meV/atom)	**Force** (meV/Å)	**Stress** (GPa)	**Magmom** (μ_B)
Test Error	30	77	0.348	0.032

The CHGNet was pretrained on the Materials Project Trajecotry (MPtrj) database, consisting of a vast collection of DFT calculations on $\sim 146,000$ inorganic materials composed of 94 elements [118]. Around 1.37 million Materials Project tasks of structure relaxation and static calculations using either the generalized gradient approximation (GGA) or GGA+U exchange-correlation were included. The MPtrj dataset contains 1,580,395 atom configurations, 1,580,395 energies, 7,944,833 magnetic moments, 49,295,660 forces, and 14,223,555 stresses. The GGA/GGA+U mixing compatibility correction was applied to ensure the consistency of energies within the MPtrj dataset, as described by Wang et al. [169]. The pretrained CHGNet demonstrates mean-absolute-errors (MAEs) of 30 meV/atom for energy, 70 meV/Åfor interatomic force, 0.348 GPa for stress, and $0.032\mu_B$ (μ_B is the Bohr magneton) for the magnetic moments.

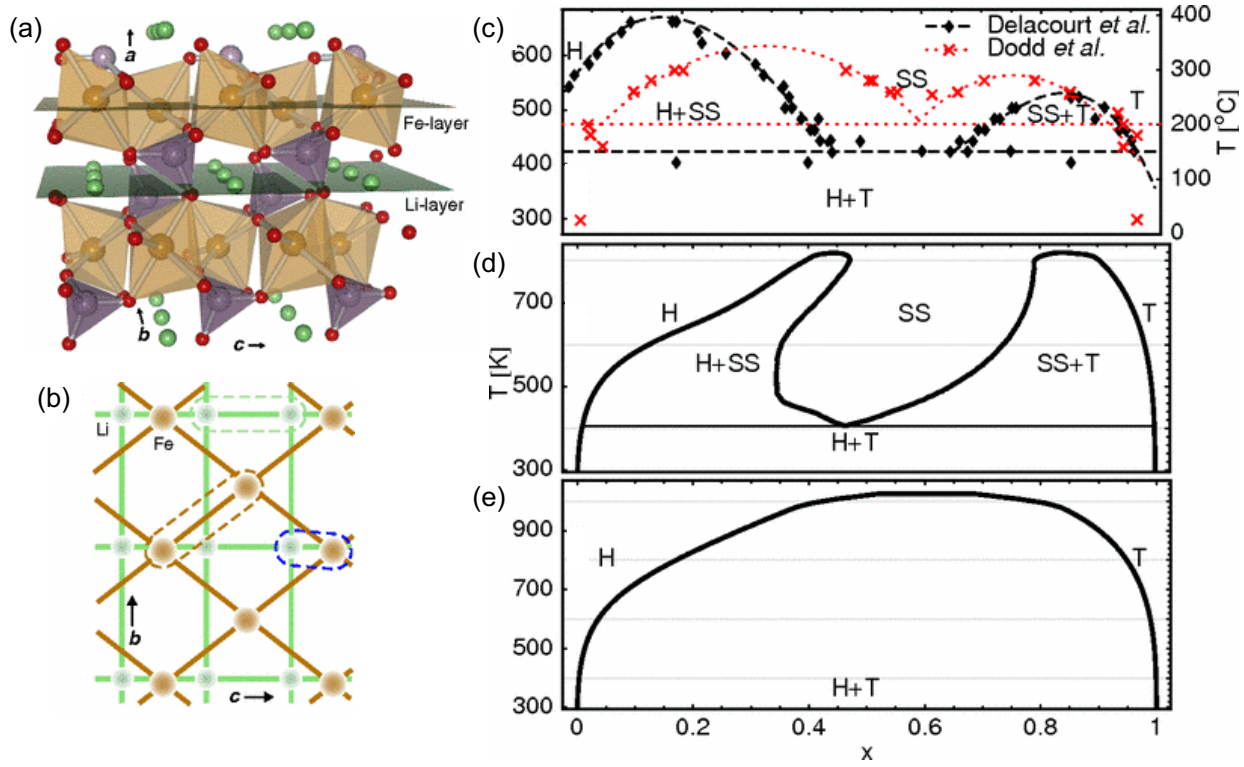

Figure 4.5: (a) The $LiFePO_4$ structure shown with PO_4 (purple) and FeO_6 (brown) polyhedra and Li atoms (green).(b) Illustration of Li and Fe sublattices. (c) Experimental Li_xFePO_4 phase diagram with boundary data from Delacourt et al. [170] and Dodd et al. [171]; (d) Computeed Li_xFePO_4 phase diagram by Zhou et al. [58] with Li/vacancy and electron degrees of freedom and (e) with Li/vacancy degree of freedom only. (Ref. [58])

4.4 Example: Li_xFePO_4 phase diagram

After introducing the background and methodology of atomistic modeling with charge information, the Li_xFePO_4 phase diagram is used as a preliminary example to demonstrate (1) the importance of incorporation of electronic degrees of freedom in materials modeling and (2) how to combine charge-decorated CE and charge-informed MLIP to practically address the charge-correlated thermodynamics.

The configurational electronic entropy has a significant effect on the temperature-dependent phase stability of mixed-valence oxides, and its equilibrium modeling therefore requires an explicit indication of the atomic charge. However, no current MLIPs can provide such information. By using DFT calculations and Monte Carlo simulations with CEs, previous research has shown that the formation of a solid solution in Li_xFePO_4 is mainly driven by electronic entropy rather than by Li^+/vacancy configurational entropy [58] (see Fig. 4.5).

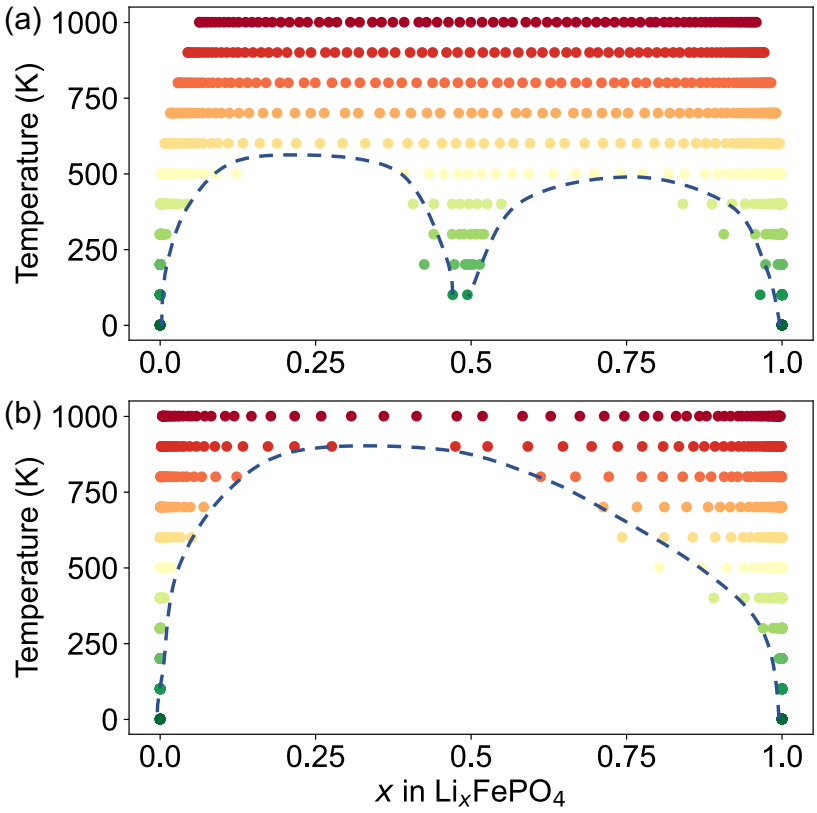

Figure 4.6: The phase diagrams in (a) and (b) are calculated with and without electronic entropy on Fe^{2+} and Fe^{3+}. The colored dots represent the stable phases obtained in semi-grand canonical MC. The dashed lines indicate the two-phase equilibria between solid solution phases. (Ref. [168])

Cluster expansion Monte Carlo with CHGNet

In this example, CHGNet is used as an energy calculator to generate two distinct CEs for MC simulations, followed by the approaches in Ref. [58]. The CEs are constructed with pair interactions up to 11 Å and triplet interactions up to 7 Å based on the relaxed unit cell of $LiFePO_4$. For better energy accuracy, a fine-tuned CHGNet is parameterized with the Materials Project structures in the Li-Fe-P-O chemical space with a `MSE` loss function for 40 epochs, which results in a 12 meV/atom training energy error and 19 meV/atom validation energy error. The fine-tuned CHGNet is used to relax 456 different structures in Li_xFePO_4 ($0 \leq x \leq 1$) and predict the energies and magmoms, where the 456 structures are generated via an automatic workflow including CE fitting, canonical CE Monte Carlo for searching the ground state at varied Li^+ composition and CHGNet relaxation. The charge-decorated CE is defined on coupled sublattices over Li^+/vacancy and Fe^{2+}/Fe^{3+} sites, where Fe^{2+} and Fe^{3+}

are treated as different species. In addition, the non-charge-decorated CE is defined only on Li^+/vacancy sites. In the charge-decorated CE, Fe^{2+}/Fe^{3+} is classified with magmom in $[3\mu_B, 4\mu_B]$ and $[4\mu_B, 5\mu_B]$, respectively.

The semigrand canonical Monte Carlo simulations are implemented using the Metropolis-Hastings algorithm, where 20% of the MC steps are implemented canonically (swapping Li^+/vacancy or Fe^{2+}/Fe^{3+}), and 80% of the MC steps are implemented grand-canonically using the table-exchange method [61, 172]. The simulations are implemented on a $8\times6\times4$ of the unit cell of $LiFePO_4$. In each MC simulation, the chemical potentials in the $[-5.6, -4.8]$ range are scanned with a step of 0.01 and sampled the temperatures from 0 to 1000 K. The boundary for the solid solution stable phases is determined with a difference in the Li concentration < 0.05 by $\Delta\mu = 0.01$ eV.

Discussion

The calculated PD with charge decoration in Fig. 4.6(a) features a miscibility gap between $FePO_4$ and $LiFePO_4$, with a eutectoid-like transition to the solid-solution phase at intermediate Li concentration, qualitatively matching the experiment result [170, 171]. In contrast, the calculated PD without charge decoration in Fig. 4.6(b) features only a single miscibility gap without any eutectoid transitions, in disagreement with experiments. This comparison highlights the importance of explicit inclusion of the electronic degrees of freedom, as failure to do so can result in incorrect physics. The effects of configurational and electronic entropy can be further investigated via

$$S(\mathrm{Li}, e) = S'(\mathrm{Li}) + S'(e) + I(\mathrm{Li}, e), \tag{4.14}$$

where S' represents the conditional entropy $S(X|Y)$ from X (either Li or e) degree of freedom given fixed Y (e or Li), and $I(\mathrm{Li}, e)$ denotes the mutual information of the two degrees of freedom. The acquisition of $S'(e/\mathrm{Li})$ is accomplished by a canonical MC with the frozen configuration of either Li^+/vacancy or Fe^{2+}/Fe^{3+} ordering. This operation can be facilitated by explicitly incorporating the charge decoration within CE, a necessity substantiated by the atomic charge inference derived from CHGNet.

4.5 Conclusion

Chapter 4 presents two computational methodologies incorporating charge information: (1) charge-decorated CE and (2) charge-informed MLIP. The pivotal parameters across these methods are the magnetic moments, serving as the basis for valence state assignment in CE and charge regularization in MLIP.

As a combined application of the two methodologies, the Li_xFePO_4 phase diagram is provided as an introductory example. By comparing phase diagrams calculated with and

without charge degrees of freedom, the example underscores the importance of accommodating heterovalent states in simulations and how practitioners may benefit from CHGNet for equilibrium atomistic modeling. More comprehensive examples of DRX systems are discussed in Chapter 5.

Chapter 5

Atomistic modeling with charge information – Application

5.1 Introduction

Chatper 5 delves into the application of charge-informed atomistic modeling to DRX materials, emphasizing the importance of incorporating charge information for both equilibrium and kinetic modeling.

The first example centers on equilibrium modeling. A charge-decorated cluster expansion is used to model intercalation chemistry involving multi-redox reactions in $Li_{1.3-x}Mn_{0.4}Nb_{0.3}O_{1.6}F_{0.4}$. This involves overcoming challenges posed by a combinatorial increase in configurational degrees of freedom with the growth in species number. The solutions to these challenges are twofold: (1) constructing a robust cluster-expansion Hamiltonian using sparse regression techniques and (2) implementing semigrand-canonical Monte Carlo for sampling charge-balanced ionic configurations.

The second part of this chapter explores kinetic modeling using CHGNet – a charge-informed interatomic potential – for studying the transition metal migration-induced phase transformation in $Li_{0.6}Mn_{0.8}Ti_{0.1}O_{1.9}F_{0.1}$ DRX. Through fine-tuned CHGNet and novel sampling methods, the formation of a partial spinel-like ordering is revealed via MD simulation. A subsequent analysis of the electrochemical properties induced by the structural ordering changes is discussed.

5.2 Equilibrium modeling: intercalation chemistry

The equilibrium voltage is one of the fundamental quantities that help characterize the electrochemical performance of a particular material and is defined by the difference in Li

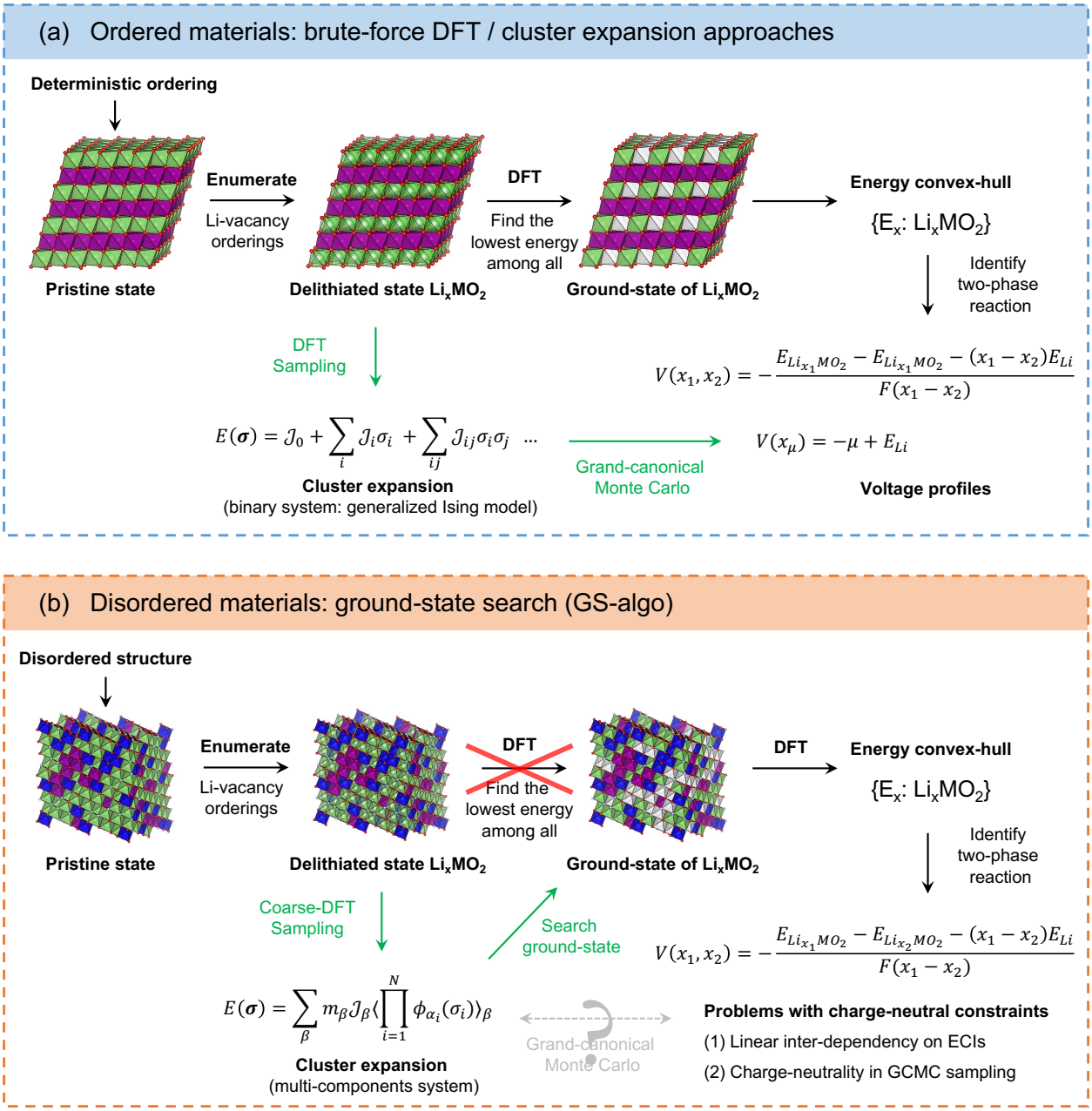

Figure 5.1: Overview of reported methods for computing voltage profiles in (a) ordered and (b) disordered electrode materials. The green arrows represent the configurational samplings that can be accelerated by using cluster expansion as an effective Hamiltonian fitted from DFT calculations.

chemical potentials between the cathode and anode [24, 98, 173]:

$$V = -\frac{\mu_{\mathrm{Li}}^{\mathrm{cathode}} - \mu_{\mathrm{Li}}^{\mathrm{anode}}}{zF}. \tag{5.1}$$

In Eq. (5.1), z is the charge transferred per ion, F is Faraday's constant, and μ_{Li} is the chemical potential of Li. For example, considering a Li transition-metal oxide $\mathrm{Li}_x\mathrm{TMO}_2$ ($x_1 \leq x \leq x_2$) as the cathode and Li metal as the anode with the cell reaction

$$\mathrm{Li}_{x_1}\mathrm{TMO}_2 \longrightarrow \mathrm{Li}_{x_2}\mathrm{TMO}_2 + (x_1 - x_2)\mathrm{Li}, \tag{5.2}$$

the approximated equilibrium voltage can be computed as [174]

$$\bar{V}(x_1, x_2) \approx -\frac{E_{\mathrm{Li}_{x_1}\mathrm{TMO}_2} - E_{\mathrm{Li}_{x_2}\mathrm{TMO}_2} - (x_1 - x_2)E_{\mathrm{Li}}}{F(x_1 - x_2)}. \tag{5.3}$$

The internal energy of the bcc Li metal E_{Li}, the lithiated structure $E_{\mathrm{Li}_{x_1}\mathrm{MO}_2}$, and the delithiated structure ($E_{\mathrm{Li}_{x_2}\mathrm{MO}_2}$) can be obtained from first-principles density functional theory (DFT). In this approach, the entropic effect is assumed to be small at low temperatures, and the change in internal energy is used to approximate the chemical potential change. By computing the formation energy of $\mathrm{Li}_x\mathrm{TMO}_2$ structures with varied Li concentrations x, a convex hull can be constructed from the energy of ground-state structures at each concentration. A piece-wise voltage profile can then be built from Eq. (5.3) via the ground states on the convex hull by using relevant constructive values of x on the hull.

5.2.1 Practical complexity in modeling intercalation chemistry

When the cathode is charged/discharged, Li is removed/inserted into the cathode structure accompanied by oxidation/reduction, resulting in various oxidation states among the redox-active metal M' and oxygen atoms. Different oxidation states of a TM can exhibit very different local chemistry preferences (e.g., Mn^{3+} has a substantial Jahn–Teller effect compared to $\mathrm{Mn}^{2+/4+}$). To capture these chemical differences in simulations, different valence states of the same elements must be treated as distinct species. This treatment is called *charge decoration*, which has been demonstrated to be essential in capturing the electronic entropy effect to construct the correct phase diagram in some compounds [58]. Charge decoration intrinsically increases the number of components and therefore the complexity of modeling the intercalation voltage profiles of DRXs.

Intractability of composition enumeration

To obtain the voltage profile of a DRX material, most previous studies have used the convex-hull construction approach by finding the ground states (GS), which is referred to as the *GS-algo*. In this approach, one tries to find the low-energy structures at varied Li content x using a variety of algorithms [175, 176]. These low-energy configurations are calculated by

DFT to construct the piece-wise voltage profile following Eq. (5.3). The GS-algo has shown reasonable predictions for voltages and redox mechanisms [124, 175–179]. When a high number of components and valence states are present, the GS-algo can become impractical as all possible valence combinations at each stage of delithiation must be enumerated. For example, when evaluating a delithiated supercell of composition $Li_{21}\square_{18}Mn_{12}Nb_9O_{48}F_{12}$, the combination of valence in Mn and O can take $Mn_6^{3+}Mn_6^{4+}$, $Mn_1^{2+}Mn_4^{3+}Mn_7^{4+}$, $Mn_2^{2+}Mn_2^{3+}Mn_8^{4+}$, and even $Mn_7^{3+}Mn_5^{4+}O_1^{-}$, etc. Enumerating all the possible compositions and searching for the possible ground states under each charge-decorated composition are NP-hard problems and become intractable, in particular when the supercell grows. To resolve the enumeration problem, Monte Carlo (MC) sampling is a better choice for studying configurational energetics in a high-dimensional space.

Fast growth of cluster basis caused by charge decoration

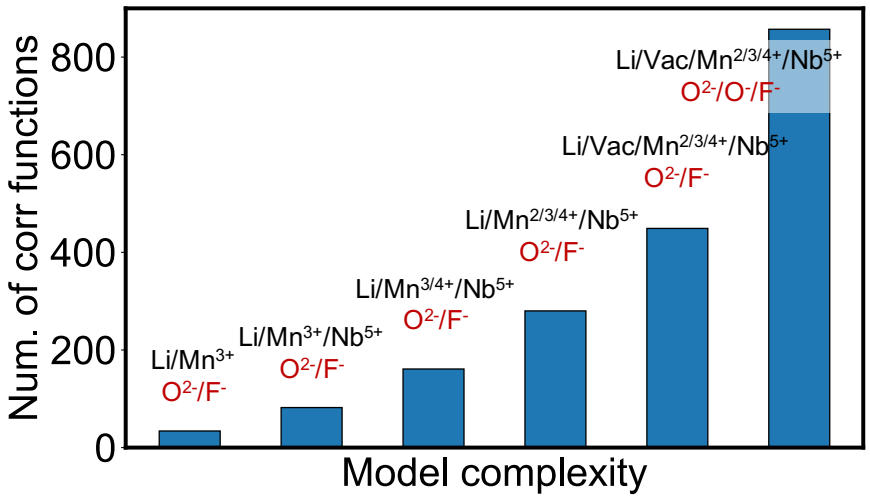

Figure 5.2: An illustration of cluster basis growth: number of correlation functions vs. number of components included in the CE with pair/triplet/quadruplet cutoff radius of 7/4/4 Å based on a rocksalt primitive cell with lattice parameter $a = 3$ Å.

To bridge the gap between 0 K ground states and sampling at finite temperatures, MC simulation with a cluster expansion (CE) as an effective Hamiltonian is typically used for intercalation chemistry in ordered cathode materials [64, 65, 180, 181]. Since the cluster site basis functions are defined by the number of components [72], the charge decoration can significantly increase the model complexity of the CE, resulting in a rapid growth in the number of clusters. Figure 5.2 illustrates how the number of cluster basis functions grows as the number of cation species included in the DRX increases, where the cutoff radius is fixed with pair/triplet/quadruplet interactions up to 7/4/4 Å. For the full description of Mn and O redox, more than 800 ECIs are predefined and need to be fitted, whereas the number of

DFT calculations is typically much smaller than that of predefined ECIs. When building a CE, the ECIs $\boldsymbol{J}^* = \{J_\beta\}$ can be obtained by fitting the DFT energy $\boldsymbol{E}_{\mathrm{DFT},S}$ of training structures S to their correlation functions with (regularized) linear regression:

$$\boldsymbol{J}^* = \arg\min_{\boldsymbol{J}} \ ||\boldsymbol{E}_{\mathrm{DFT},S} - \boldsymbol{\Pi}_S \boldsymbol{J}||_2^2 + \rho(\boldsymbol{J}), \tag{5.4}$$

where $\boldsymbol{\Pi}_S$ is the feature matrix formed by the correlation functions and $\rho(\boldsymbol{J})$ is a regularization term. High-component CE can easily be overfitted as the rank of the feature matrix ($\boldsymbol{\Pi}_S$) is typically smaller than the dimension of ECIs $\dim(\boldsymbol{J})$. The low-rank structure (referred to as *rank deficiency*) of the feature matrix $\boldsymbol{\Pi}_S$ in Eq. (5.4) requires selecting the most physically informative ECIs and avoiding overfitting in CE fitting [75, 182]. The rank deficiency can also arise from other physical constraints in ionic systems. For example, charge balance creates a linear dependency between the number of charge-decorated species and the corresponding correlation functions. And another challenge is that the training structures calculated with DFT are predominantly low in energy, and such low-energy structures often narrow the configurational space that can be represented in the training structures, which in principle, high-energy configurations could be included. DFT tends not to cover such configurations or relax them to lower-energy configurations by moving ions and electrons. The number of non-zero ECIs must be constrained ($||\boldsymbol{J}||_0 \leq \mathrm{rank}(\boldsymbol{\Pi}_S)$) to prevent ECI fitting from being an underdetermined problem. This constraint can be achieved by properly introducing $\mu||\boldsymbol{J}||_0$ as a regularization term in Eq. (5.4) to penalize the number of non-zero ECIs and impose sparsity [83].

Charge-neutrality constraint in MC sampling

After fitting the ECIs, MC simulations can be used to sample the energy of configurations under finite temperatures. Applying semigrand-canonical Monte Carlo (sGCMC) sampling is most suited for calculating voltage profiles [140, 183]. The relation between the Li content x and a Li chemical potential can be obtained by applying the Metropolis–Hastings algorithm with the Boltzmann distribution

$$f(E(\boldsymbol{\sigma}), \mu) \propto \exp\left(-\frac{E(\boldsymbol{\sigma}) - \mu_{\mathrm{Li}} \cdot x_{\mathrm{Li}} N}{k_B T}\right). \tag{5.5}$$

In Eq. (5.5), E is the energy of the configuration $\boldsymbol{\sigma}$ given by the CE Hamiltonian, μ_{Li} is the Li chemical potential, x_{Li} is the Li content in the configuration $\boldsymbol{\sigma}$, N is the total number of Li and vacancy sites, k_B is the Boltzmann constant, and T is the simulation temperature. Computing voltage profiles using sGCMC has been successful in the study of several simple binary electrode materials, such as $LiCoO_2$/$LiNiO_2$ [140, 184, 185], $MgTiS_2$ [186], and disordered $Li_3V_2O_5$ [187].

When charge-decorated CEs are used, the requirement of charge neutrality must be enforced in MC sampling. Because the training set only includes charge-balanced structures

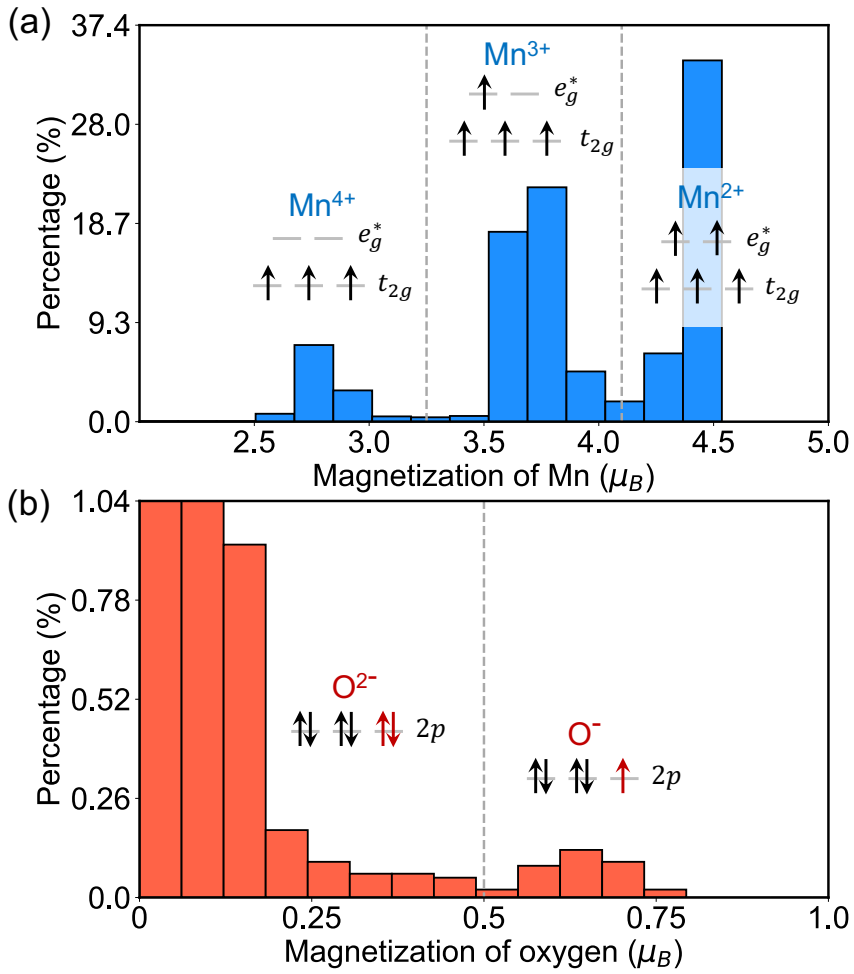

Figure 5.3: Distribution of total on-site magnetizations of (a) Mn and (b) O atoms among all DFT-r^{2}SCAN calculated structures in the chemical space of $Li_{1.3-x}Mn_{0.4}Nb_{0.3}O_{1.6}F_{0.4}$. The valence of each Mn and O atom is determined by the on-site magnetization. From the histogram, the classification boundary between $Mn^{4+/3+}$ and $Mn^{3+/2+}$ is estimated to be $3.25\mu_B$ and $4.1\mu_B$, and the O^- classification is estimated to be $0.5\mu_B$. (As the percentage of O^{2-} with a low magnetization is too large compared to the percentage of O^-, the panel (d) is truncated on the y-axis.)

with no information about the charge-unbalanced structures, the energy predicted by the CE will be unphysical if configurations with non-zero net charge are assessed during sGCMC. Techniques for enforcing strict charge neutrality in sGCMC have been applied to several electrolyte systems [172, 188]; however, few have been demonstrated in a system with complex redox reactions such as DRX [61].

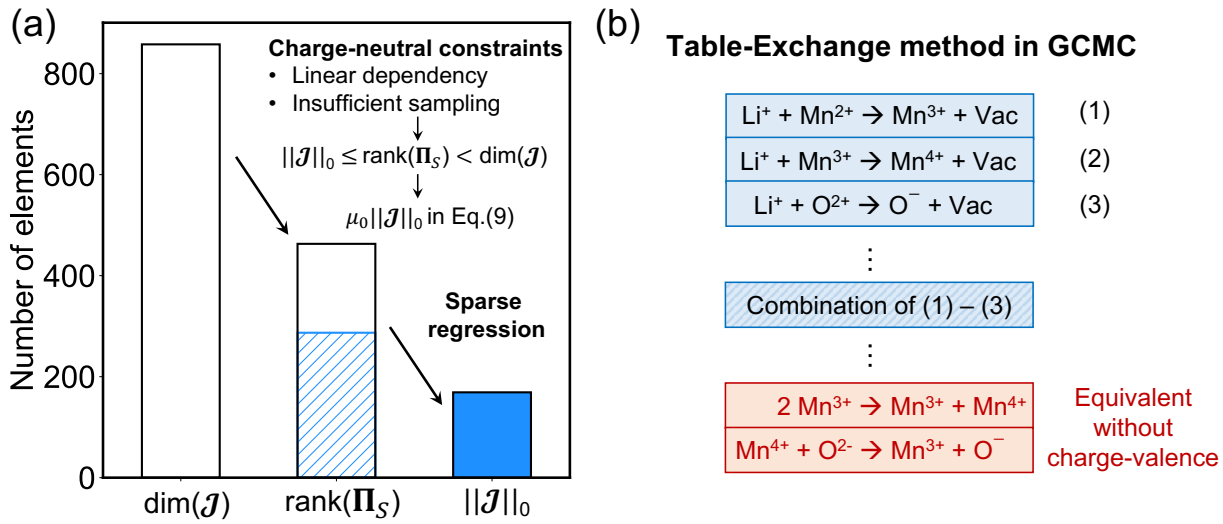

Figure 5.4: (a) An illustration of the rank deficiency in the ECI fitting. The left empty bar represents the dimension of predefined ECIs with $\dim(\boldsymbol{J}) = 858$. The middle empty bar indicates the number of structures sampled in the feature matrix with $\dim(\mathbf{\Pi}_S) = (463 \times 858)$. The blue shaded area overlapping the middle bar indicates a feature matrix of $\text{rank}(\mathbf{\Pi}_S) = 287$. The right solid blue bar represents the number of non-zero ECIs after an $\ell_0\ell_2$-norm regularized sparse regression, giving $||\boldsymbol{J}||_0 = 169$. (b) An illustration of the TEs used in charge-balanced sGCMC.

5.3 Multi-redox reactions in $Li_{1.3-x}Mn_{0.4}Nb_{0.3}O_{1.6}F_{0.4}$

To overcome all the abovementioned issues, a voltage-calculation framework is proposed that combines several state-of-the-art methods in CE-MC. With this framework, it is demonstrated how to correctly model the intercalation voltage profile in DRX and, more generally, any complex ionic systems with redox-active ions and configurational disorder. In the following methodology sections, the chapter will introduce the construction of a robust and predictive cluster-expansion Hamiltonian with $\ell_0\ell_2$-norm regularized sparse regression [83], demonstrate an effective sampling strategy of the intercalation stages with sGCMC under charge balance using the table-exchange (TE) method [61] , and illustrate an ensemble average method over representative structures to handle various chemical environments. In the results section, the equilibrium voltage profile of $Li_{1.3-x}Mn_{0.4}Nb_{0.3}O_{1.6}F_{0.4}$ (LMNOF) is presented and compared with the experiments. To explain the redox mechanism, the proportion of multiple redox-active species at varied Li content is analyzed. It is found that the calculated voltage profile and redox mechanism agree well with experiments and argue that the ability of our method to describe oxygen redox in the Li-excess cathode accurately is particularly noticeable.

5.3.1 Approaches for modeling multi-redox reactions

Training structure generation for DFT

To describe DRX materials well, two configurational degrees of freedom need to be accurately represented: the Li/vacancy interactions and the different local chemical environments (i.e., the SRO of TMs and anions). A two-step procedure for generating the training set is proposed:

(1) *Pristine states*: Generate several fully lithiated structures with different transition-metal and anion configurations in relatively small supercells (e.g., supercell structures with 10× or 20× the formula unit of $Li_{1.3}Mn_{0.4}Nb_{0.3}O_{1.6}F_{0.4}$). These structures can be generated from canonical MC samplings using a pre-fitted cluster expansion as the effective Hamiltonian or using solely the electrostatic energy for simplicity.

(2) *Delithiated states*: Starting from the structures generated in Step 1, fix the TM and O/F orderings and enumerate different Li/vacancy configurations at varied Li contents (e.g., $x = 0.3/0.5/0.7$ in $Li_{1.3-x}$). As the total number of enumerated structures can be large, one can further sort the structures at each Li content by their electrostatic energy and only keep the low-energy ones.

All the sampled structures are in the chemical space of $Li_{1.3-x}Mn_{0.4}Nb_{0.3}O_{1.6}F_{0.4}$, and this two-step procedure covers different Li/vacancy orderings in varied local chemical environments formed by TM and anion SRO to be calculated with DFT. The DFT calculations were performed with the VASP package using the projector-augmented wave method [95, 96], a plane-wave basis set with an energy cutoff of 520 eV, and a reciprocal space discretization of 25 k-points per $Å^{-1}$. The calculations were converged to 10^{-6} eV in total energy for electronic loops and 0.02 eV/Å in interatomic forces for ionic loops. To model the Li–Mn–Nb–O–F oxyfluoride system, we relied on the regularized strongly constrained and appropriately normed meta-GGA exchange-correlation functional (r^2SCAN) [34, 127], which is believed to better capture the cation-anion hybridization and Li coordination preference [48]. r^2SCAN provides better computational efficiency than the earlier version of SCAN [128]. It is noted that the choice of different functionals has an impact on the anionic redox activities [189]. As a proof-of-concept in this study, r^2SCAN is selected for both computational efficiency and accuracy [190].

Sparse regression for charge-decorated CE

To obtain effective valence states of redox-active Mn and O species from a DFT calculated configuration, the on-site magnetization can be used [63, 191]. For example, Figure 5.3(a) and (b) show the distribution of magnetic moments representing $Mn^{2+/3+/4+}$ and $O^{2-/-}$ in our set of 463 DFT-calculated structures. The valence of each Mn and O atom is classified by the site magnetization using $3.25\mu_B$ for distinguishing $Mn^{4+/3+}$, $4.1\mu_B$ for separating $Mn^{3+/2+}$, and $0.5\mu_B$ to indicate O^- [192] (μ_B is the Bohr magneton). For the

sparse regression of ECIs, the $\ell_0\ell_2$-norm regularization with hierarchy constraints is applied [83]. The ECIs are optimized in the following mixed-integer quadratic programming (MIQP) problem:

$$\begin{aligned} \min_{\boldsymbol{J}} \;& \boldsymbol{J}^T \boldsymbol{\Pi}_S^T \boldsymbol{\Pi}_S \boldsymbol{J}^T - 2\boldsymbol{E}_{\mathrm{DFT}}^T \boldsymbol{\Pi}_S \boldsymbol{J} + \mu_0 \sum_{c \in \boldsymbol{C}} z_{0,c} + \mu_2 ||\boldsymbol{J}||_2^2 \\ \textbf{\textit{s.t.}} \quad & M z_{0,c} \geq J_c, \; \forall c \in \boldsymbol{C} \\ & M z_{0,c} \geq -J_c, \; \forall c \in \boldsymbol{C} \\ & z_{0,b} \leq z_{0,a}, \; \forall a \subset b, \; \{a,b\} \in \boldsymbol{C} \\ & z_{0,c} \in \{0,1\}, \; \forall c \in \boldsymbol{C}, \end{aligned} \tag{5.6}$$

where $\boldsymbol{\Pi}_S$ is the feature matrix, $\boldsymbol{J}$ are the ECIs, $z_{0,c}$ is the slack variable representing $J_c = 0, z_{0,c} = 0$, and $J_c \neq 0, z_{0,c} = 1$. $M = 100$ is set to constrain the optimization boundaries, and $||\boldsymbol{J}||_2^2 = \boldsymbol{J}^T\boldsymbol{J}$ is a ridge regression term (ℓ_2-norm). (See Section 2.4 for a detailed description)

The CE Hamiltonian was constructed with pair interactions up to 7 Å, triplet interactions up to 4 Å, and quadruplet interactions up to 4 Å based on a rocksalt primitive cell with lattice parameter $a = 3$ Å leading to a possible 858 ECIs (including the constant term J_0). The ECIs were fitted using 463 training structures, forming a feature matrix of $\mathrm{rank}(\boldsymbol{\Pi}_S) = 287$. The resulting ECIs using the sparse regression in Eq. (5.6) contain 169 non-zero elements ($||\boldsymbol{J}||_0 = 169$). The relationship between dimension, rank, and the number of non-zero elements is illustrated in Fig. 5.4(a).

Charge-balanced Monte Carlo sampling

The sGCMC simulations on the Li/vacancy occupancy and the charge decoration degrees of freedom are used to obtain the voltage curve of $Li_{1.3-x}Mn_{0.4}Nb_{0.3}O_{1.6}F_{0.4}$ composition. The delithiation is achieved by step-wise removal of Li atoms. In each MC step, the Li^+ is removed/inserted, accompanied by the oxidation/reduction of an Mn or O atom. The net charge of each configuration is maintained at zero by only executing a combination of site occupancy changes that are charge neutral. This type of MC step is referred to as table exchange (TE) [61, 188]. In the calculations, three elemental classes of perturbations are considered:

1. $Li^+ + Mn^{2+} \rightarrow Mn^{3+} + \mathrm{Vac.}$
2. $Li^+ + Mn^{3+} \rightarrow Mn^{4+} + \mathrm{Vac.}$
3. $Li^+ + O^{2-} \rightarrow O^- + \mathrm{Vac.}$

Any other charge-conserving MC step can be expressed as a linear combination of these three classes and their inverses. For example, charge transfer such as $2Mn^{3+} \rightarrow Mn^{2+} + Mn^{4+}$ and

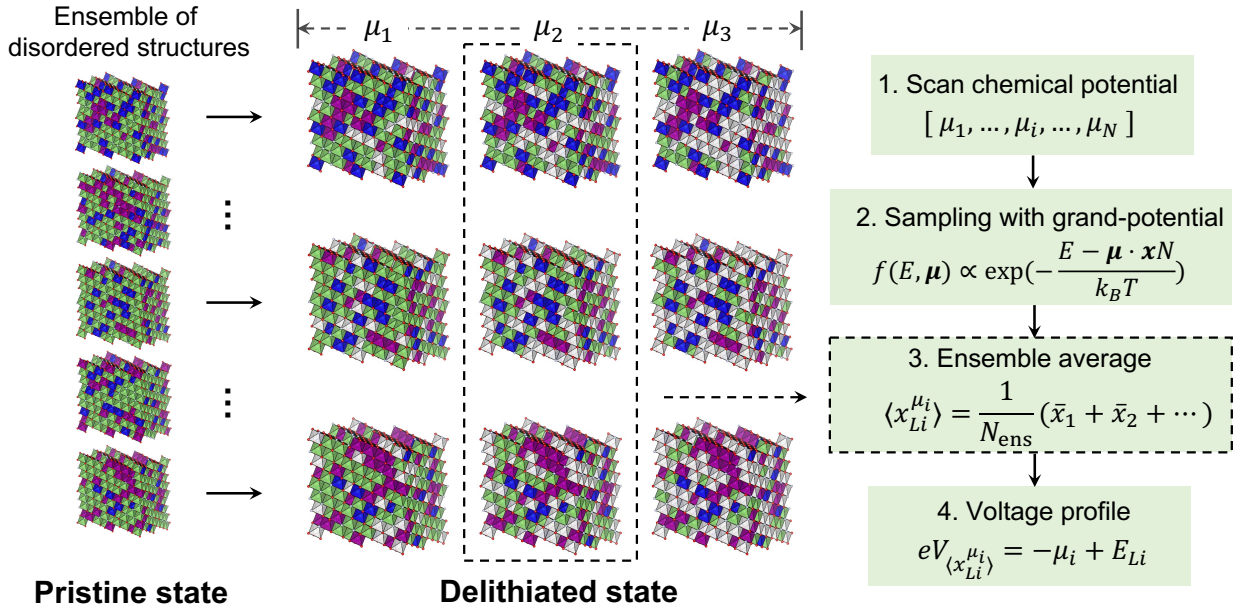

Figure 5.5: An illustration of charge-balanced sGCMC on an ensemble of disordered structures (Green: Li, white: vacancy, other colors: different TM species, anions are not displayed). An ensemble of fully lithiated disordered structures is first generated and referred to as the pristine state. The sGCMC is performed to topotactically delithiate each pristine structure at decreasing Li chemical potentials μ_{Li} (i.e., increasing voltages V). The content of species is averaged over each sGCMC sampling and all the pristine structures.

$\text{Mn}^{4+} + \text{O}^{2-} \rightarrow \text{Mn}^{3+} + \text{O}^{-}$ can be achieved by a combination of elementary perturbations. As the intercalation is assumed to be topotactic, Mn, O, and F ions do not change sites. The acceptance probabilities of each MC step are scaled to ensure detailed balance (see Appendix).

In a series of sGCMC simulations, the chemical potentials are scanned between two limiting values $\mu_{\text{Li}} \in [\mu_{\text{min}}, \mu_{\text{max}}]$ at finite temperature. For each sGCMC simulation with a given Li chemical potential μ, the content of each charge-decorated species is averaged over the sampled MC structures from the equilibrium. The Li chemical potential can be converted into the cathode voltage using $V = -(\mu - E_{\text{Li}})/e$. In this work, the numerical simulations were implemented with the open-source software package `smol` [193], and the ECIs optimization was solved using the `gurobi` package [90].

The ensemble average method

Unlike ordered intercalation compounds which are characterized by a small number of local environments, the configurational disorder in DRX creates an abundance of local chemical environments, leading to a significant variation of Li extraction energy from different sites [194, 195]. This multitude of environments is difficult to capture in a single small unit cell. Instead, the delithiation processes were sampled from multiple distinct structures to obtain the true intercalation curve as the ensemble average of them.

A canonical MC simulation was used to generate an ensemble of fully lithiated (i.e., pristine) configurations $\{\boldsymbol{\sigma}_i\}$, from which multiple representative structures are drawn. The CE model used to generate the canonical MC structures is reported in Ref. [20]. To recover the actual SRO in DRX, it is required that the average of physical quantities in the collection of representative structures be approximately equal to the actual ensemble average, assuming infinitely many structures are drawn from the ensemble ($\langle \boldsymbol{\Pi} \rangle_{\text{ens}} \approx \langle \boldsymbol{\Pi} \rangle_{\infty} = \bar{\boldsymbol{\Pi}}_{\text{SRO}}$). For simplicity, in this work, it is verified that the average energy $\langle E \rangle_{\text{ens}} = \langle \boldsymbol{\Pi} \rangle_{\text{ens}} \cdot \boldsymbol{J} \approx \bar{\boldsymbol{\Pi}}_{\text{SRO}} \cdot \boldsymbol{J}$ converges to the ensemble average with an increasing number of selected structures.

Each simulated fully lithiated structure contains 120 atoms ($Li_{39}Mn_{12}Nb_9O_{48}F_{12}$) with a supercell lattice constant of $\sim$ 10 Å. The choice of such a supercell size is rational because $\sim$ 10 Å is a good cut-off to maintain enough distance between each atom and its periodic images and to encapsulate all cluster-interaction distances. Subsequently, sGCMC simulations are performed for every structure in the ensemble, and for a given chemical potential, the species (e.g., Li) content is computed using the following average

$$\langle x^{\mu}_{\text{Li}} \rangle = \frac{1}{N_{\text{ens}}} (\bar{x}_1 + \bar{x}_2 + ...), \tag{5.7}$$

where $\{\bar{x}_1, \bar{x}_2 ...\}$ are the averaged Li content given by the thermally equilibrated sGCMC sample starting from each structure. In this work, 30 disordered structures were used for the ensemble average.

5.3.2 Simulated intercalation voltage profiles

The procedures presented above demonstrate how to model the intercalation thermodynamics of $Li_{1.3-x}Mn_{0.4}Nb_{0.3}O_{1.6}F_{0.4}$ (LMNOF). Figure 5.6(a) presents the simulated and the experimental voltage profiles [20]. The solid green line is the experimental charging profile under a low current density (20 mA/g) between 1.5 and 5.0 V. The bottom of the discharge state (1.5 V) is aligned to be the fully lithiated state ($Li_{1.3}Mn_{0.4}Nb_{0.3}O_{1.6}F_{0.4}$). The green dots represent the computed voltage profile at T = 300 K. The slope and turning point in the slope are in good agreement with the experimental profile for $0.4 \leq x \leq 1.3$, indicating that the Li/vacancy interaction and redox potentials of Mn and O are well described in our model. In the highly charged region ($x < 0.7$) specifically, the simulation shows remarkably good agreement with the experiment reproducing the fact that the slope of the profile be-

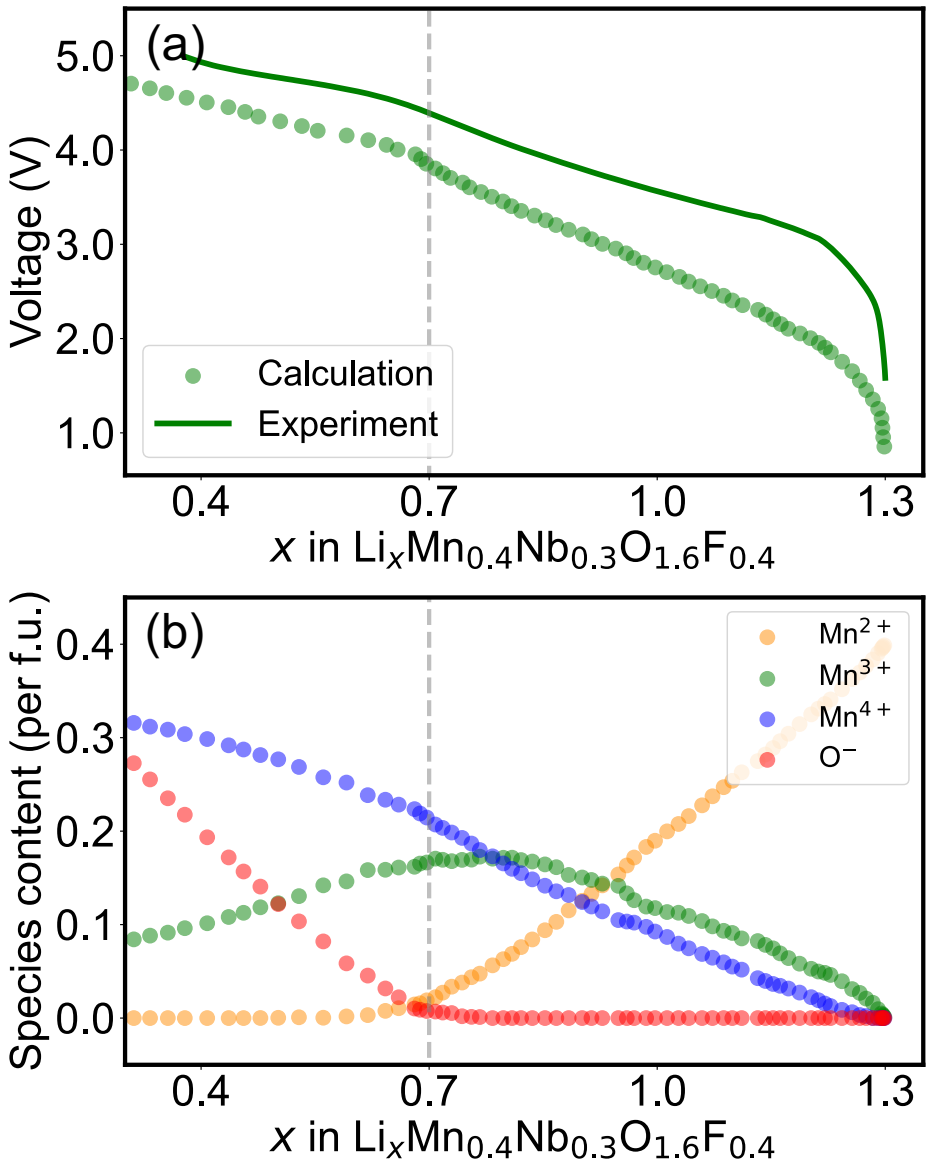

Figure 5.6: (a) Calculated (circle) and experimental (solid line) voltage profiles of ($Li_{1.3-x}Mn_{0.4}Nb_{0.3}O_{1.6}F_{0.4}$). (b) Calculated content of Mn^{2+}, Mn^{3+}, Mn^{4+} and O^{-} per f.u. as a function of Li content (x).

comes flatter at $x \sim 0.7$ (marked by the gray dashed line in Fig. 5.6(a)). The computed voltage profile is systematically lower than the experimental one, which is well-known for most DFT functionals that are not augmented with a Hubbard U correction [41]. Even though the SCAN functional removes more self-interaction than previous LDA and GGA [34], it does not fully remove it and underestimates the intercalation voltage. This could potentially be resolved by using Hubbard U correction to the SCAN functional, which is evidenced to reduce the prediction error on formation energies of transition metal oxides [196, 197].

The fraction of each redox-active species during intercalation is presented in Fig. 5.6(b). $Mn^{2+/3+/4+}$ are represented by orange/green/blue dots, and O^{-} are represented by red dots. Comparing Fig. 5.6(a) and (b) makes it apparent that the Li content where the voltage profile flattens ($x \sim 0.7$) corresponds to the start of the oxidation of O^{2-} to O^{-}. The lowering of the voltage slope as the system changes from TM redox to O redox is consistent with the higher dilution of the oxygen charge compared to TM redox centers. Figure 5.6(b) also reveals several key points about the redox mechanism in LMNOF. The oxidation of Mn does not appear consecutively from Mn^{2+} to Mn^{3+} to Mn^{4+}. The amount of Mn^{3+} and Mn^{4+} increase simultaneously as Mn^{2+} begins to be oxidized. The fact that different oxidation states of Mn co-exist over a wide range of Li content is likely due to the variety of local chemical environments induced by cation disorder. The co-existence is consistent with the marginal stability of Mn^{3+} and its propensity to disproportionate into Mn^{2} and Mn^{4+} when it cannot exist in an environment where it can lower its energy significantly through a Jahn–Teller distortion [132]. O-redox occurs after all the Mn^{2+} has been consumed but before all the Mn atoms are fully oxidized to +4 valence. The hybridized redox mechanism between Mn and O has been confirmed by previous synchrotron characterization experiments [20] and on related materials $Li_{1.2}Mn_{0.4}Ti_{0.4}O_{2.0}$ by mass spectroscopy [198]. Since the cluster expansion method coarse-grains the energetics into lattices (e.g., only considering octahedral occupancies in a rocksalt), the dimerization of oxygen and tetrahedral Li occupancy are not considered.

5.3.3 Discussion

Typical modeling of the intercalation energetics only includes the Li/vacancy degree of freedom, assuming that the electronic degrees of freedom can be integrated out. Integrating out degrees of freedom is based on two key assumptions [51]: (1) One assumes that the degree of freedom that is variationally removed is always optimized in the DFT calculation. More specifically, this would require that for a given Li/vacancy configuration, the DFT calculation can easily find the charge decoration with the lowest energy. While this is a reasonable assumption for systems with a highly delocalized charge such as Li_xCoO_2 [199], it is unlikely to be the case for disordered systems where the variation of local environments and the highly localized charge easily lead to charge metastability in DFT. (2) The second assumption when degrees of freedom are variationally removed is that their entropy contribution can be neglected, as their variational optimization is supposed to find their ground state. The role

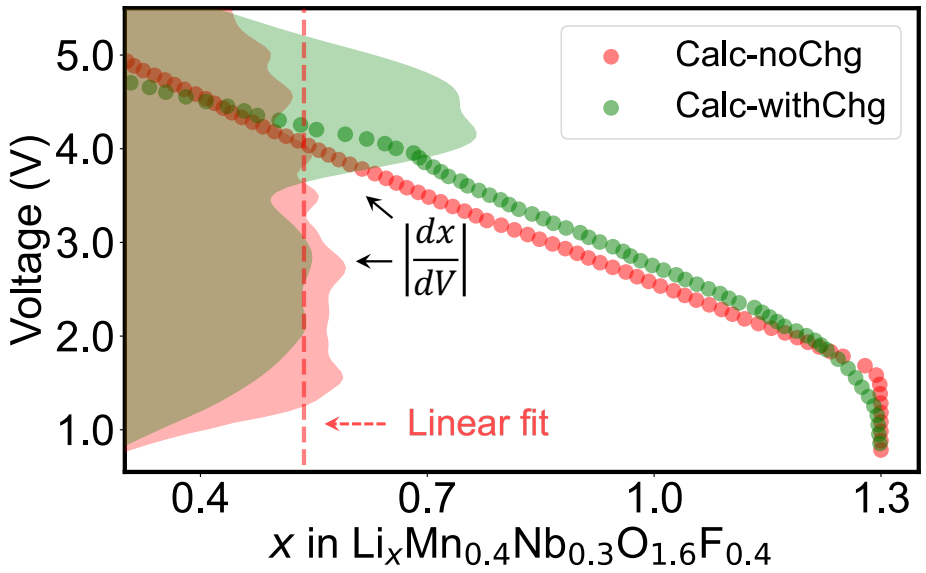

Figure 5.7: Comparison of voltage profiles generated with a charge-decorated CE (green dots) and a CE without charge decoration (red dots). The shaded area represents the distribution of the derivative quantity $|\frac{dx}{dV}|$, which reflects the Li-site energy distribution during the intercalation process.

of electronic entropy in intercalation systems is yet to be fully understood, but at least in Li_xFePO_4 it has been shown to be critical to reproduce the correct intercalation behavior [58]. Both assumptions are unlikely to be valid in DRX cathodes, given their multitude of possible redox couples and large variations of energetic environments.

To illustrate the significance of accurately capturing the electronic degree of freedom in DRX materials, another CE was fitted by parameterizing only the Li/vacancy interactions. Mn and O atoms are considered single charge-less species regardless of their oxidation states in such a CE. The computed voltage profiles with the charge-decorated CE (in green) and the undecorated CE (in red) are compared in Fig. 5.7. The undecorated CE yields a featureless voltage profile and virtually no change of slope as a function of Li content. The mechanism-related details are poorly portrayed in the profile. The shaded areas in Fig. 5.7 are the relative derivative of capacity with respect to voltage (dx/dV). Two distinct peaks are observed in the charge-decorated calculation (green), indicating the contribution from the Mn-redox and O-redox, whereas they cannot be adequately distinguished in the undecorated version (red).

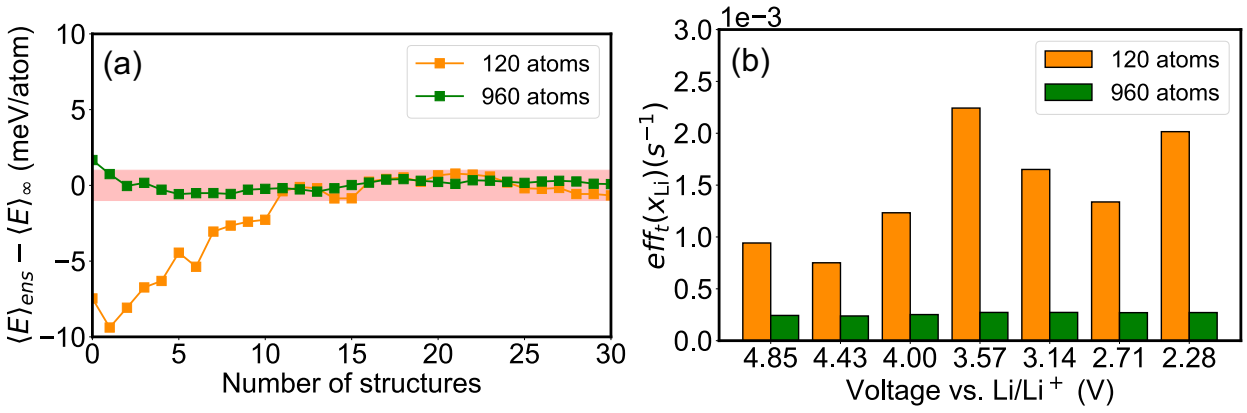

Figure 5.8: (a) Average energy (per atom) among pristine structures as a function of the number of pristine structures selected in an ensemble. The red-shaded region indicates a variation of ±1 meV/atom of $\langle E\rangle_\infty$. The orange/green lines represent the results of the supercell structure with 120/960 atoms, respectively. (b) Comparison of computational efficiency (defined in Eq. (5.8)) between supercells with 120 and 960 atoms, computed and averaged over all the pristine structures in the ensembles.

Necesscity of using ensemble average

The importance of using the ensemble average method to capture the multitude of environments in disordered systems is also highlighted. In principle, one can approach the representation of disordered systems by using a single structure in a very large supercell (e.g., special quasi-random structure (SQS) approach [200]) or by making an ensemble of multiple smaller-sized supercell structures and taking an average of the computed quantities. These two approaches are statistically equivalent, given that enough structures have been used with the smaller-sized supercells. Figure 5.8(a) shows the number of the structures required for the average energy per atom over structures to convergence within ±1 meV/atom of the equilibrium average $\langle E\rangle_\infty$ when choosing from an ensemble of representative structures in canonical MC [20]. The green line represents the results in a supercell of 960 atoms, whereas the orange line represents the results in a supercell of 120 atoms. The smaller-sized supercell requires drawing $\sim$ ten times more structures to converge, with the number of structures required roughly scaling with the supercell size ($960 = 120 \times 8$). A large supercell approaches the actual distribution of SRO with fewer structures. However, a much longer MC sampling time is required in a large supercell, whereas in a smaller supercell, one can easily benefit from parallelizing multiple pristine structures to require much less total time consumption. To illustrate this factor, computational efficiency as a quantitative benchmark for sGCMC is introduced in Note. 1.

Note 1 (Computational efficiency) *At each Metropolis step p in semigrand-canonical*

MC, the Li content (x_{Li}) at the current configuration is recorded as $x_{Li,p}$. $\overline{x_{Li,[p,q]}}$ is denoted as the average of x_{Li} in a block from simulation step p to step q. After thermal equilibration, the block mean-variance *is defined at block length L, Var($\overline{x_{Li}}_L$), as the variance of the* block means $\overline{x_{Li,[p,p+L]}}, \overline{x_{Li,[p+L,p+2L]}}$, ... *for each block containing L samples. The block mean-variance can be used as a measure of uncertainty when estimating $\overline{\theta}$ using a block mean. With the block mean-variance, the* computational efficiency *is further defined,*

$$eff_t(x_{Li}) = \frac{\tau^2}{\overline{T}_L \, Var(\overline{x_{Li}}_L)}, \tag{5.8}$$

where τ^2 is the ensemble variance of Li content x_{Li} approximated by the variance of all MC steps after thermal equilibration, $\overline{T}_L$ is the average CPU time spent in each L-steps block. Given the same set of hardware used in MC simulations, the higher the computational efficiency, the less sampling time required for the uncertainty of the average Li content (i.e., the block mean-variance) to be decreased below the same threshold. In brief, higher sampling efficiency means less sampling time.

Figure 5.8(b) shows the computational efficiency in sGCMC at varied voltages in supercells with 120 (orange) and 960 (green) atoms. Higher efficiency indicates that less computational time is required (see details about the definition in the Appendix). Approximating the computational efficiency, the sampling time required in each pristine structure scales $\sim O(N^1)$ with the supercell size. Therefore, with the help of parallelization, using an ensemble of smaller structures is statistically as accurate but practically more efficient than using fewer large structures. An ensemble of smaller structures is also more tractable in DFT for computing other properties when necessary, such as electronic structure, whereas DFT is computationally prohibitive in large supercells even when the SRO can be well presented.

Finally, it is argued that using enough structure samples is necessary when smaller-sized supercells are used to model disordered systems. Figure 5.9 shows the variance of redox-active species with respect to the averaged Li content. As a result of the disorder, the variance in the content of each species among pristine structures is not negligible. This further discourages the methods based on convex-hull and direct DFT evaluations (e.g., GS-algo) to accurately determine voltage profiles for materials with significant disorder such as DRX. When the size of the supercell in which one enumerates possible Li/vacancy and charge configurations is too small or the number of structure samples is too few, as is often the case in GS-algo, the variance resulting from different local chemical environments cannot be adequately captured.

Summary and Outlook

In DRX materials, the abundance of available redox-active transition metals creates new opportunities for cathode design, such as using the redox reactions between $Cr^{3+}/Cr^{4+}/Cr^{6+}$ [28, 126], $V^{3+}/V^{4+}/V^{5+}$ [201], or even $Fe^{2+}/Fe^{3+}/Fe^{4+}$ [202]. However, the high number of

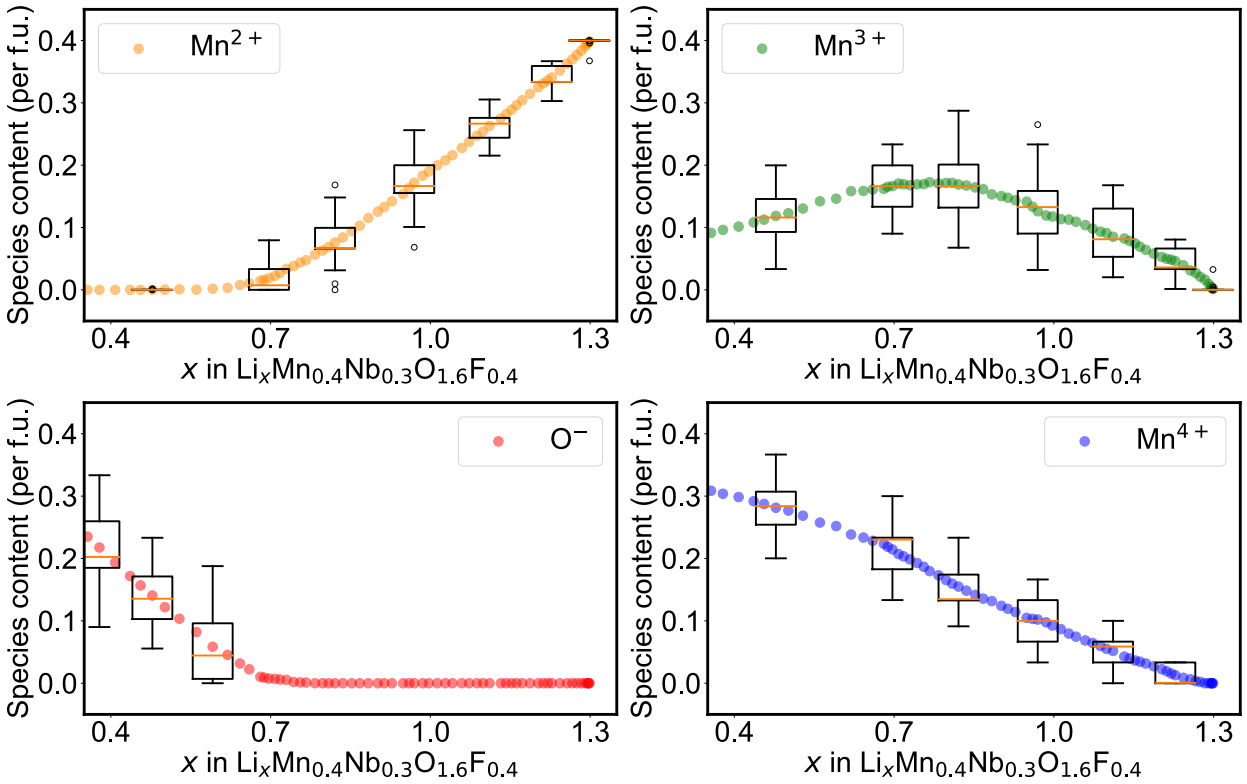

Figure 5.9: Contents of each redox species per formula unit as a function of the Li content x in $Li_xMn_{0.4}Nb_{0.3}O_{1.6}F_{0.4}$ as computed from sGCMC simulations at T = 300 K. The statistics are computed based on an ensemble of disordered structures of in supercells of $Li_{30x}Mn_{12}Nb_9O_{48}F_{12}$. The average values over different disordered structures are marked with colored dots, the median values are marked with orange lines, and the variances are marked with error bars around the medians.

chemical components, distinguished by their valence states in DRX materials, renders the "curse of dimensionality" (CoD) the main simulation obstacle [203]. As the complexity of the energy model grows with the number of components and charge decoration, the computational cost grows exponentially fast. For example, CoD has been an essential impediment for the computational design of high-entropy cathodes [21, 28].

This work proposes the following procedure to obtain accurate intercalation voltage profiles in DRX with multi-redox reactions: (1) build a training set containing different fully lithiated structures and enumerate the Li/vacancy orderings at varied delithiation levels calculated by DFT; (2) construct a charge-decorated CE Hamiltonian and fit the ECIs using the sparse regression technique to address the fast growth of the cluster basis and rank-deficiency issues (e.g., $\ell_0\ell_2$-norm regularized regression); and (3) run sGCMC in an ensemble

of disordered structures under charge balance to obtain physically rational energetics and compute the voltage profiles.

5.4 Kinetic modeling: transition metal migration

Investigating ionic rearrangements is crucial for comprehending ion mobility and interactions among ionic species. Contrasting with the previous section's discussion, the migration of TMs constitutes a kinetic process, necessitating an in-depth description of migrating ion dynamics across various local environments. Traditional MC simulations may be inadequate for this purpose, as MC exchanges between two microstates consider only the energy differences and ignore the dynamics (e.g., energy barriers between the two microstates). While Kinetic Monte Carlo (KMC) addresses this limitation by incorporating migration barriers, the complex environments within DRX (particularly those coupled with charge transfer) challenge the application of KMC with the necessity of calibrating migration barriers. Thus, molecular dynamics (MD) emerges as a suitable approach for investigating TM migrations.

This section starts with the background of an intriguing example, spinel-like phase formation, which has been widely observed in Mn-rich cathode materials during electrochemical cyclings. The mechanism of such a process is explained by charge-informed MD in Li_xMnO_2. The method is further used to explain the formation of spinel-like ordering (δ-phase) in DRX materials and reveal the relation between the structural ordering and electrochemical performance.

5.4.1 Spinel-like phase formation

The $LiMnO_2$ battery cathode demonstrates substantial phase transformations from either layered [204] and orthorhombic ordering [205] to spinel ordering during battery cycling ($0 \leq x \leq 1$ in Li_xMnO_2) because of the TM migrations [205, 206]. Figure 5.10 presents the spinel ordering, which can be represented by the cation occupancy in AB_2O_4 of a FCC anion framework with $8a$, $16c$ and $16d$ sites. Cation A occupying on the tetrahedral $8a$ sites with four face-sharing $16c$ octahedral sites. The four $16c$ sites ($8a$ tetrahedron) form a 0-TM channel. Cation B occupying on the octahedral $16d$ sites. The intercalation of spinel Li_xMnO_2 is characterized by varying the Li occupancy on $8a$ and $16c$ sites. For example, the intercalation process between $LiMn_2O_4$ and $Li_2Mn_2O_4$ is the conversion of $16c$ octahedral Li into $8a$ tetrahedral Li occupancy, and the intercalation process between $LiMn_2O_4$ and Mn_2O_4 is the insert/removal of $8a$ Li.

Figure 5.10(a) presents the characteristic voltage profile of spinel Li_xMnO_2 displays a strong two-phase reaction with a sharp voltage decrease from 4 V to 3 V. Due to the substantial collective Jahn-Teller distortion of Mn^{3+} in spinel $LiMnO_2$, the large octahedral distortion results in lattice incompatibility and a first-order phase transformation. Because of this, the strong compositional inhomogeneity and large stresses in cathode particles lead

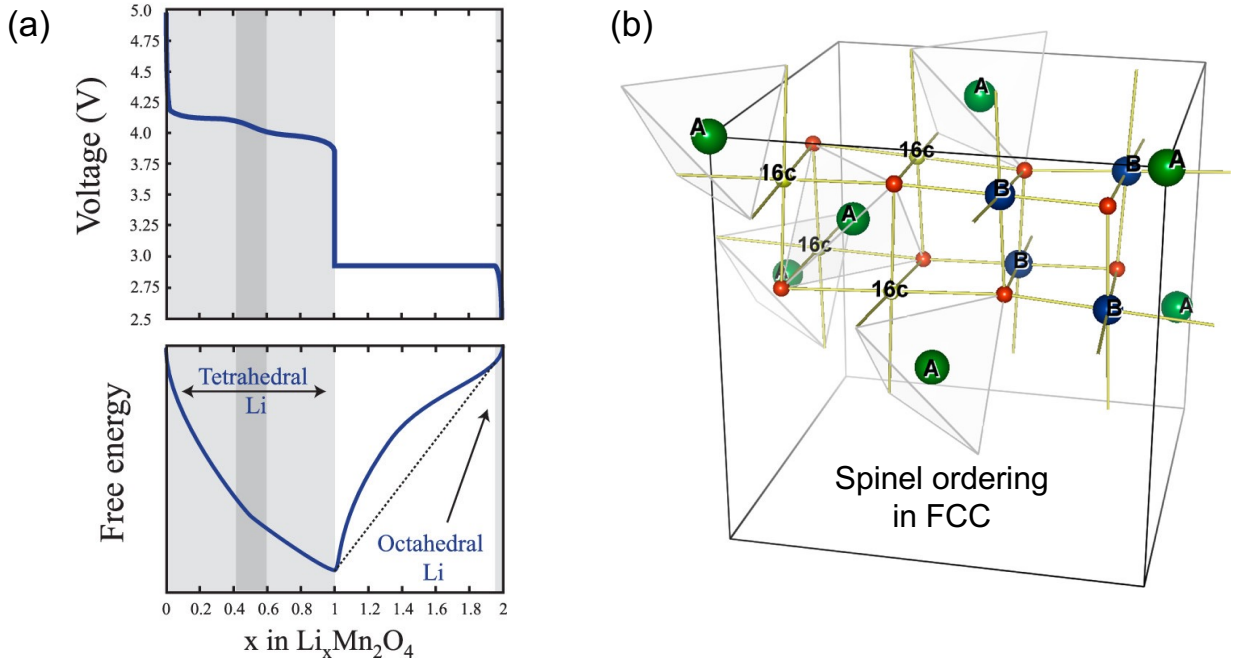

Figure 5.10: (a) The intercalation voltage profile and free energy of spinel $Li_xMn_2O_4$ (Ref. [24]). (b) An AB_2O_4 spinel structure showing tetrahedral 8*a* sites (atom A) with neighboring octahedral 16*c* (vacancy) and octahedral 16*d* sites (atom B). (Ref. [6])

to capacity loss and battery degradation. For practical use of spinel Li_xMnO_2, Li cycling is confined to the 4 V range between MnO_2 and $Li_{0.5}MnO_2$, exploiting merely half of the theoretical capacity. It is essential to assess how the intercalation chemistry around the 3 V voltage could extend the capacity.

Ji et al. [26] and Cai et al. [27] have proposed that creating a partially disordered spinel could resolve the two-phase reaction issue by successfully synthesizing several ball-milled cathode materials in a series of compositions $Li_{1+x+y}Mn_{2-y}(O,F)_4$. The mechanism to unlock the Li capacity in partially disordered spinel is explained by Chen et al. [207]. It is found that introducing approximately 25% cation disorder can remove the two-phase reaction by increasing the solubility (decreasing the defect energy) of cation vacancy in spinel $LiMnO_2$. Moreover, the spinel-like ordering formation is more commonly observed across several DRX systems via electrochemical cyclings, including $Li_{1.2}Mn_{0.6}Nb_{0.2}O_2$ [208], $Li_{1.2}Ti_{0.2}Mn_{0.6}O_{1.8}F_{0.2}$ [30], and $Li_{1.1}Mn_{0.8}Ti_{0.1}O_{1.9}F_{0.1}$ [209]. These Mn-rich DRX compounds exhibit a gradual phase transition towards spinel-like ordering. No two-phase reaction has been observed for the Li intercalation of the transformed materials.

The phase transformation is believed to be related to the mobile Mn ion when cation

vacancies are created. The mechanism of Mn migration has been under debate and investigation. It is typically concluded that Mn migration is strongly coupled with its charge state, Mn^{4+} is generally considered immobile, while Mn^{3+} and Mn^{2+} are considered more mobile [210–212]. However, revealing the charge-coupled dynamics of Mn ion migration has been challenging over the past decades, as the time scale and computational cost of observing such phenomena are far beyond any possible *ab-initio* methods.

5.4.2 Transition metal migration in Li_xMnO_2

In early quasi-static *ab-initio* investigations, Reed et al. [204] rationalized the remarkably rapid phase transformation observed at room temperature via a charge disproportion mechanism: $2Mn^{3+}_{oct} \rightarrow Mn^{2+}_{tet} + Mn^{4+}_{oct}$. Here, the subscript refers to a location in either the tetrahedral or octahedral site of face-centered cubic anion packing (see Fig. 5.13). The hypothesis proposed that Mn^{2+} presented a lower energy barrier for migration between tetrahedral and octahedral sites, showing a preference for the tetrahedral site. However, a subsequent magnetic characterization experiment by Jang et al. [210] demonstrated that the electrochemically transformed spinel $LiMnO_2$ hosts lower-spin (high-valence) Mn ions at the tetrahedral sites. This finding suggested the potential for higher-valence Mn to stabilize at tetrahedral sites during phase transformation.

In a recent study, Deng et al. [168] applied the pre-trained CHGNet to thoroughly describe this process via a charge-informed MD simulation. The simulation started from a partially delithiated supercell structure featuring orthorhombic ordering, characterized by peaks at 15°, 26°, and 40°in the X-ray diffraction (XRD) pattern (see the bottom line in Fig. 5.11(b)). A phase transition from orthorhombic to spinel-like ordering was observed as the simulation proceeded. Figure 5.11(b) showcases the simulated XRD patterns of MD structures at various time intervals ranging from 0 to 1.5 ns. These patterns exhibit a discernible increase in characteristic spinel peaks (18°, 35°) and a decrease in the orthorhombic peak, which agree well with the experimental in-situ XRD results [206, 210].

The advantage of CHGNet is illustrated in its capacity to predict charge-coupled physics, as demonstrated in Fig. 5.11. The figure shows the CHGNet-predicted energy of the LMO supercell structure as a function of simulation time, coupled with the peak strength of $2\theta = 15°$ and 18°. A clear correlation between the structural transformation and energy landscape is observed. In the early stage of the simulation, the magnetic moments of Mn ions predominantly range between $3\mu_B$ and $4\mu_B$, corresponding to Mn^{4+} and Mn^{3+}. Approximately at 0.8 ns, there is a substantial increase in Mn^{2+} quantity, which is accompanied by a decrease in the potential energy and changes in the XRD peaks. Following this major transition point, Mn^{3+} ions undergo charge disproportionation, resulting in the coexistence of Mn^{2+}, Mn^{3+}, and Mn^{4+} in the transformed spinel-like structure.

Another key observation made by Deng et al. [168] is the correlation between ionic rearrangements and the charge-state evolution. In particular, the timescale of charge dispropor-

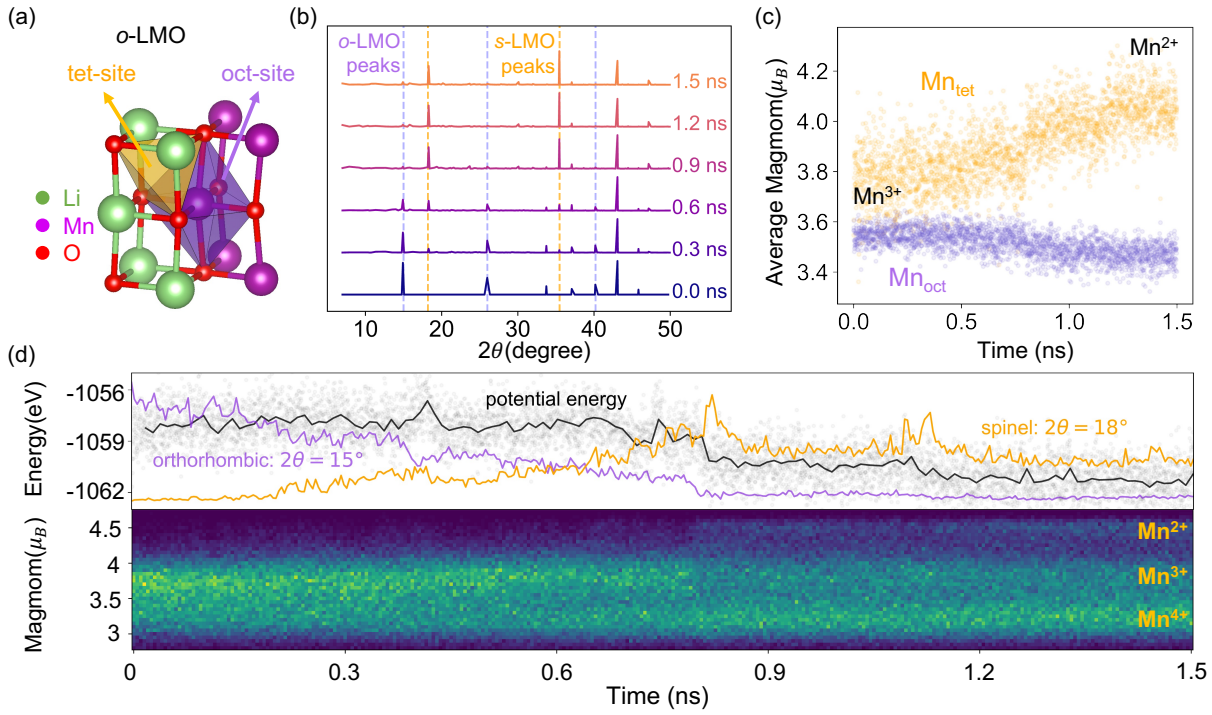

Figure 5.11: (a) orthorhombic $LiMnO_2$ (*o*-LMO) unit cell plotted with the tetrahedral site and the octahedral site. (b) Simulated XRD pattern of CHGNet MD structures as the system transforms from the *o*-LMO phase to the *s*-LMO. (c) Average magmoms of tetrahedral and octahedral Mn ions *vs.* time. (d) Top: total potential energy and the relative intensity of *o*-LMO and *s*-LMO characteristic peaks *vs.* time. Bottom: the histogram of magmoms on all Mn ions *vs.* time. The brighter color indicates more Mn ions distributed at the magmom.

tionation, with a notable emergence of Mn^{2+} occurring at $\sim$ ns scale, is considerably longer than the timescale of ion hops, with the manifestation of Mn_{tet} at $\sim$ ps scale. This implies that the migration of Mn to the tetrahedral coordination is less likely associated with the emergence of Mn^{2+}. Instead, the emergence of Mn^{2+}tet is correlated with the formation of long-range spinel-like ordering, as evidenced in Fig. 5.11(c).

5.5 Molecular dynamics of $Li_{1.1-x}Mn_{0.8}Ti_{0.1}O_{1.9}F_{0.1}$

Inspired by the success of using CHGNet to simulate Mn migration in $Li_{0.5}MnO_2$ for the formation of spinel ordering, the studies in this section have extended to more complex scenarios, i.e., understanding how phase transformation happens from DRX compounds using MD simulations.

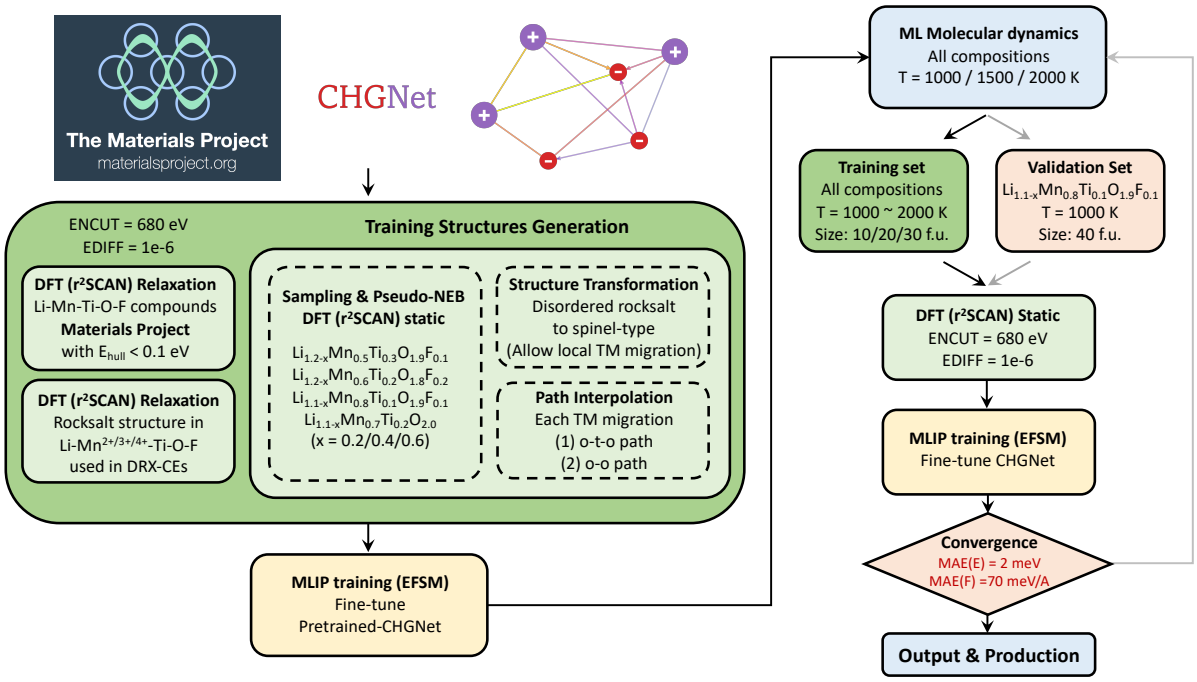

Figure 5.12: The fine-tuning workflow of CHGNet in Li-Mn-Ti-O-F chemical space with r^{2}SCAN-DFT, including relaxation of existing datasets (Materials Project and DRX), passive sampling of TM migration and MD simulations.

5.5.1 Sampling the Potential Energy Surface

To tackle this challenge, it is crucial to parameterize an effective machine learning interatomic potential (MLIP) within the desired chemical space with high-fidelity DFT data. The crux of this task lies in creating an effective training dataset for model parameterization, which essentially involves sampling the potential energy surface (PES) in the Li–Mn–Ti–O–F chemical space. The PES sampling needs to address three primary aspects: (1) compositional space, incorporating various pristine compositions and Li concentrations; (2) cation ordering space, spanning from ordered phases (e.g., orthorhombic, layered, and spinel) to disordered ones; and (3) migration paths, indispensable for assessing the energy of rare events. The following procedures outline our approach to PES sampling.

Initial sampling from pre-existing datasets

For the initial sampling, the compounds on Materials Project within the Li–Mn–Ti–O–F chemical space that has a decomposition energy (energy above the convex hull, E_{hull}) lower than 0.1 eV/atom [118] are selected. To sample the configurational space of disordered phases, a training dataset for DRX cluster expansion models containing Mn^{2+}/Mn^{3+} is used,

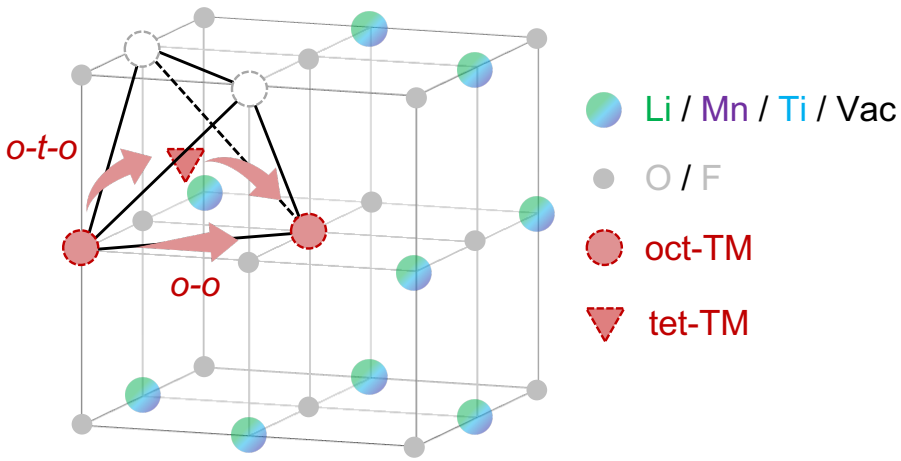

Figure 5.13: Illustration of TM migration in various local environments in DRX compounds. The gradient color ball represents partial occupancy of cation (Li/Mn/Ti). The gray ball represents an anion (O/F). Two types of migration are demonstrated: (1) *o-t-o* migration through an intermediate tetrahedral site and (2) *o-o* migration directly connected by two octahedral sites.

as reported in Refs. [17, 116]. The structures obtained from pre-existing datasets are relaxed using r^{2}SCAN-DFT (see Fig. 5.12). Upon initial sampling and DFT calculations, the relaxed structures were used to fit a trial CHGNet and a CE Hamiltonian in Li–Mn^{3+}–Ti–O–F space.

The DFT calculations were performed with the VASP package using the projector-augmented wave method [95, 96], a plane-wave basis set with an energy cutoff of 680 eV, and a reciprocal space discretization of 25 k-points per Å^{-1}. The calculations were converged to 10^{-6} eV in total energy for electronic loops and 0.02 eV/Å in interatomic forces for ionic loops. The regularized strongly constrained and appropriately normed meta-GGA exchange-correlation functional (r^{2}SCAN) [34, 127] was used with consistent computational settings as `MPScanRelaxSet` [128].

Sampling of TM migration paths

The TM migration is a rare event with high energy in MD simulations, as the diffusivity of TM is considerably slower than that of Li [179]. To augment the sampling of the migration pathway of TM, TM migration events are generated across varying local environments, taking into account different TM compositions, Li concentrations, and cation ordering.

A CE Hamiltonian fitted in Li–Mn^{3+}–Ti–O–F space is used to generate pristine (lithiated) DRX structures via MC simulations at T = 1273 K for representing solid-state synthesis conditions and capturing the underlying SRO. Next, for varying Li concentrations

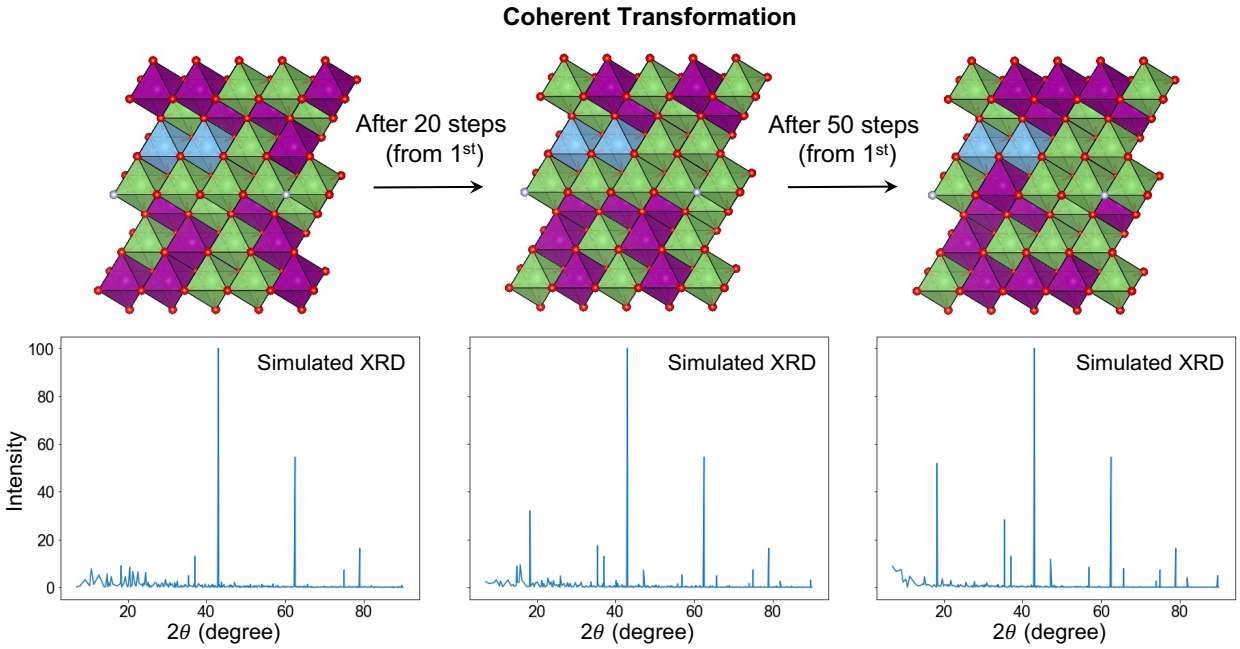

Figure 5.14: Coherent transformation: a structure ordering change that only allows TM local migration, whereas the anion framework and non-neighboring cation orderings are fixed. The coherent transformation can be implemented several times to transform the disordered phase to a spinel-like phase.

($x = 0.2/0.4/0.6$), delithiated structures are generated by removing Li from octahedral sites based on the pristine structures. The two procedures covered the compositional sampling of such as $Li_{1.2-x}Mn_{0.5}Ti_{0.3}O_{1.9}F_{0.1}$, $Li_{1.2-x}Mn_{0.6}Ti_{0.2}O_{1.8}F_{0.2}$, $Li_{1.1-x}Mn_{0.8}Ti_{0.1}O_{1.9}F_{0.1}$, $Li_{1.1-x}Mn_{0.7}Ti_{0.2}O_{2.0}$, etc. To scrutinize local migration in these delithiated structures, a heuristic approach is proposed for inducing cation ordering changes from disordered to different degrees of spinel orderings, which includes:

- Classifying and labeling all transition metals based on their occupancy in the $16c/16d$ sites within the spinel structure.
- Initiating a possible local octahedral hop, either through an exchange between $16d$ TM and another $16d$ cation or between $16c$ TM and $16d$ Li.
- Removing extraneous octahedral cations that face-share with the tetrahedral site along the *o-t-o* migration path, thereby constructing three distinct structures: initial (prior to TM exchange), intermediate (with TM occupying an intermediate tetrahedral site), and final (post TM exchange). Such a local migration is called a *coherent transformation* step, where the ordering of other atoms not associated with the migration is fixed.

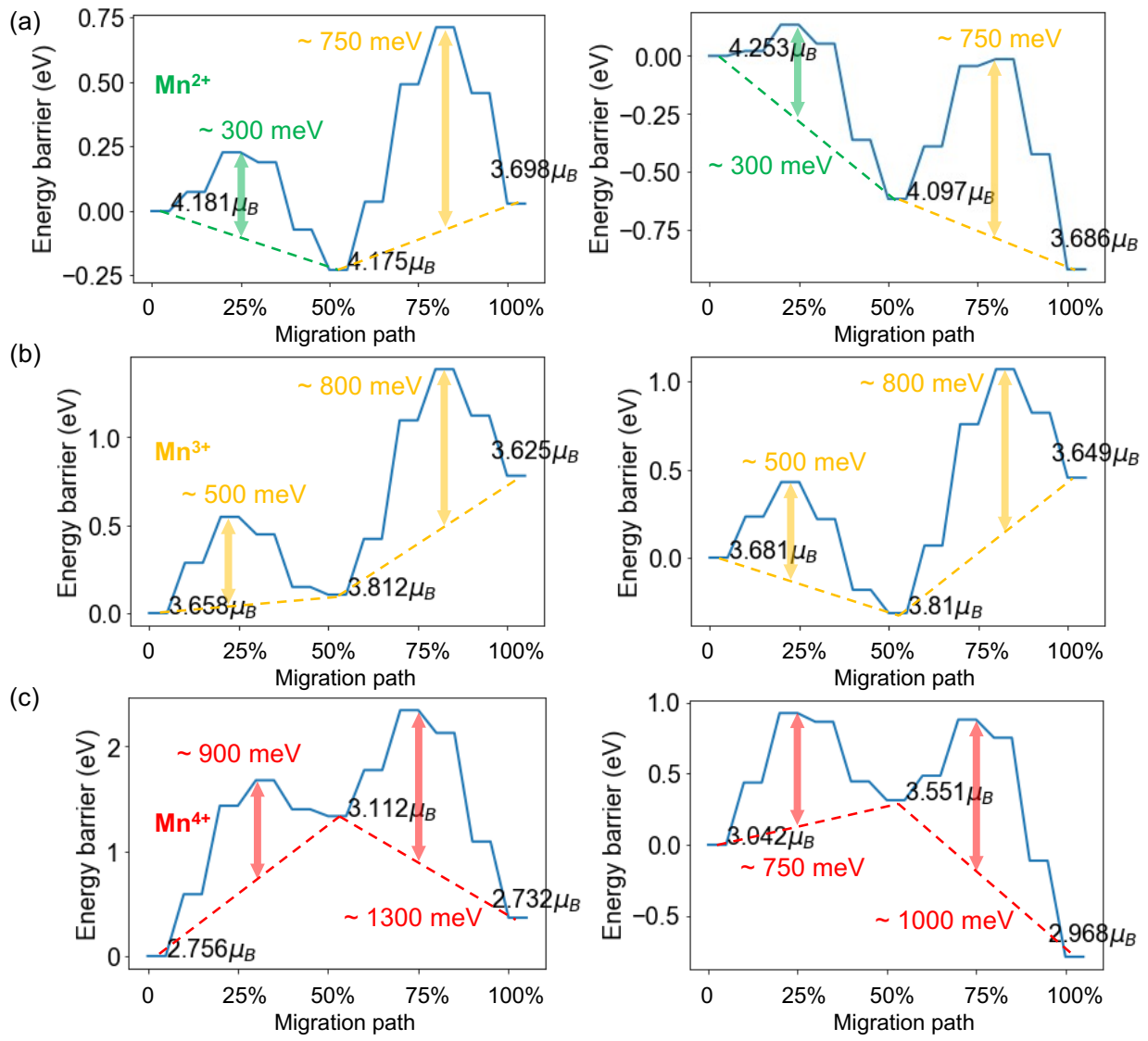

Figure 5.15: The calculated "migration barrier" of Mn in different local environments of host structure $Li_{14}Mn_{13}Ti_2O_{32}$ in a dilute vacancy concentration. The barrier is estimated from the static DFT calculations of interpolated images along the migration pathway. The different valences of Mn are shown, which are determined by the calculated magnetic moments (Mn^{2+} in green, Mn^{3+} in yellow, Mn^{4+} in red).

- Implementing coherent transformation many times until there is no 16*c* Mn occupancy.
- Employing the trial CHGNet to relax these structures (initial, intermediate, and final) in each coherent transform step and linearly interpolating between migration pathways based on the relaxed structures.
- Computing the energies, forces, stress, and magnetic moments of these interpolated structures using static calculations via r^{2}SCAN-DFT.

Figure 5.15 displays the calculated energy landscape as an approximated "migration barrier" of Mn in different local environments, which is estimated from the static DFT calculations of interpolated images along the migration pathway.

Molecular dynamics trajectory

Following the passive sampling of local migration paths and DFT-relaxed structure from pre-existing datasets, a new CHGNet model is parameterized. This model is further used for MD simulations of the delithiated structures of various compositions as described above. The MD simulations are conducted using supercells ranging from 10 to 40 formula units (f.u.) under various temperature conditions (T = 1000/1500/2000 K) with a time step of $\Delta t = 2$ fs. The resulting MD trajectories are uniformly sampled for DFT evaluations and further partitioned into training and test datasets. Specifically, the test dataset is constructed by the MD trajectories of the $Li_{0.6}Mn_{0.8}Ti_{0.1}O_{1.9}F_{0.1}$ composition at T = 1000 K with a supercell size of 40 f.u. (including 80 anions), which is the composition of interest to simulate.

Table 5.1: The model errors of pretrained CHGNet and fine-tuned CHGNet.

	Energy (meV/atom)	**Force** (meV/Å)	**Stress** (GPa)	**Magmom** (μ_B)
Pretrained	30	77	0.348	0.032
Fine-tuned	2	68	0.086	0.019

As depicted in Fig. 5.12, the model was subjected to iterative refinement until convergence criteria were met. In practice, we reached the convergence after two iterations. The first fit only takes the MD trajectories under T = 1000 K. And the second fit takes the MD trajectories under T = 1000/1500/2000 K. Finally, all the training data within the Li–Mn–Ti–O–F chemical space (including 88,852 structures) is used to fine-tune the pretrained CHGNet to achieve a MAE of 2 meV/atom for energy and 68 meV/Å for interatomic forces on the validation set as shown in Table. 5.1 (The training errors are 3 meV/atom for energy and 31 meV/Å for interatomic forces).

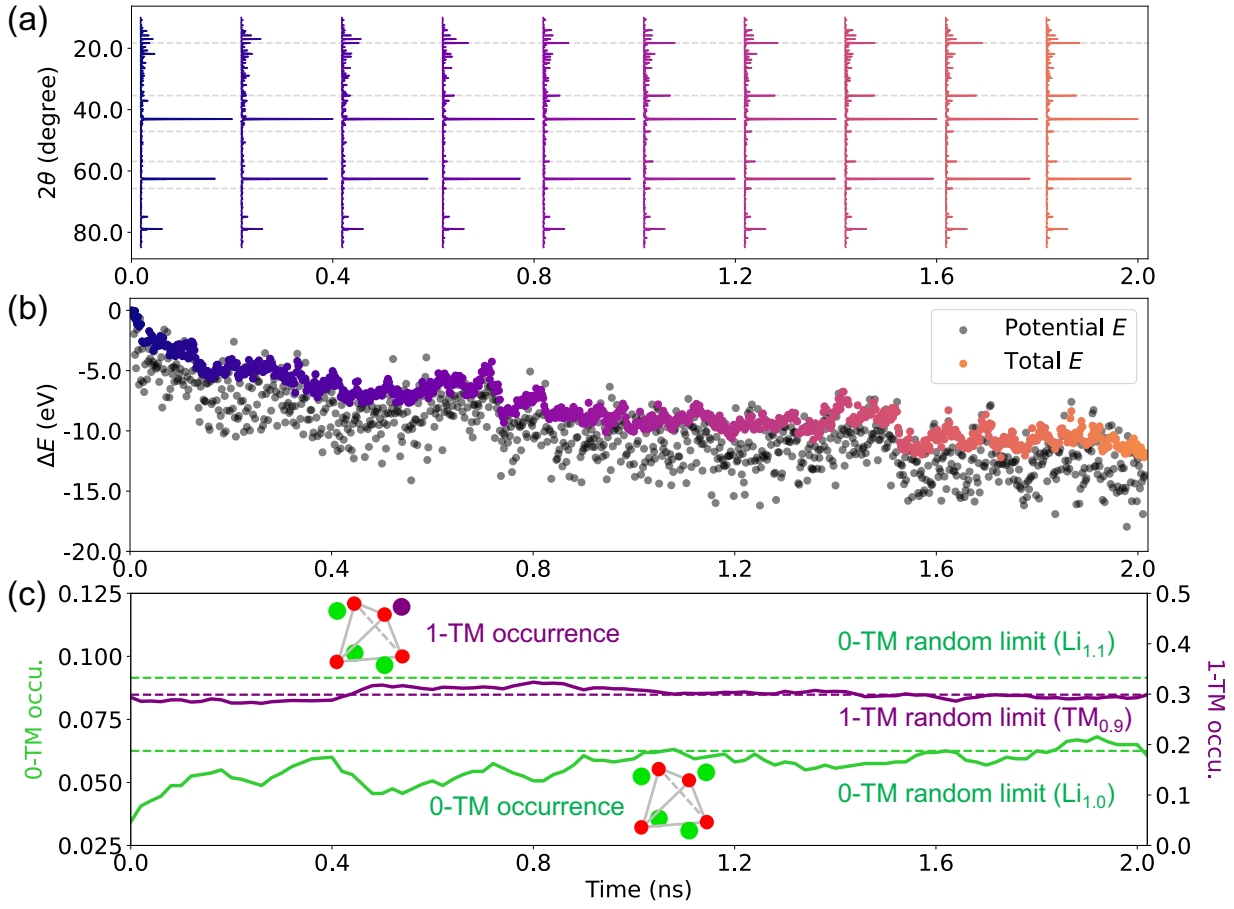

Figure 5.16: Simulated XRD, potential energy, charge distribution on Mn ions, and SRO analysis of the LMTOF MD trajectories

5.5.2 DRX to partially disordered spinel-like transformation

The fine-tuned CHGNet is used for MD production to study the structure change from DRX to the spinel-like ordering of $Li_{1.1-x}Mn_{0.8}Ti_{0.1}O_{1.9}F_{0.1}$. The structure with partial disorder and spinel-like ordering is denoted as δ-phase. The initial structure ($Li_{88}Mn_{64}Ti_8O_{152}F_8$) is derived from a canonical CEMC simulation at T = 1273 K. The Li ions are randomly removed from the MC structure to create the delithiated structure ($Li_{48}\square_{40}Mn_{64}Ti_8O_{152}F_8$). The delithiated structure is relaxed by CHGNet with a force convergence to < 0.1 eV/Å and then used for MD simulation at T = 1273 K for $t = 2$ ns with a time step of $\Delta t = 2$ fs under the NVT ensemble.

Structure ordering analysis

Figure 5.16(a) presents the simulated XRD patterns observed within the time interval of $t = 0$ to $t = 2$ ns. The minor diffraction peaks, noticeable in the low-angle region, are primarily due to artifacts originating from finite-sized structures ($Li_{48}\square_{40}Mn_{64}Ti_8O_{152}F_8$). The characteristic peaks of spinel ordering (18°, 35°, etc.) within the FCC rocksalt framework become increasingly significant as MD proceeds. Figure 5.16(b) illustrates the energy landscape across the simulated MD trajectories. The black data points denote the potential energies, while the colored ones represent the total energies. The energies are depicted relative to their values at the initial state. A notable decrease in energy is observed for the δ-phase (approximately 60 meV/anion) following a $t = 2$ ns of MD simulation, implying that the spinel-like cation ordering is thermodynamically favorable for the $Li_{0.6}Mn_{0.8}Ti_{0.1}O_{1.9}F_{0.1}$ composition in the presence of cation deficiencies.

Figure 5.16(c) provides an analysis of short-range order variations as a function of time. To obtain this, the cations in the MD structures are coarse-grained to their nearest octahedral sites (occupying the Wyckoff positions $16c/d$) to evaluate the occurrence of the 0/1-TM channel. The solid green line indicates the occurrence of the 0-TM channel, with the dashed green line signifying its random limit for two Li contents ($Li_{1.0}$ and $Li_{1.1}$). The purple line corresponds to the occurrence of 1-TM channel, which remains relatively stable and akin to the random limit for $TM_{0.9}$ throughout the MD trajectories. At the onset ($t = 0$ ns), the occurrence of the 0-TM channel is approximately 0.03, which increases to around 0.06 after $t = 2$ ns. The rise in the number of 0-TM channels explains the enhanced rate performance of the δ-phase compared to the DRX phases, which is ascribed to its spinel-like ordering formation.

Charge distribution with ion rearrangement

A key feature of CHGNet lies in its ability to simultaneously predict atomic charge (inferred from magnetic moments) along with energetics. This attribute proves particularly significant for the phase transition from DRX to δ, as the Mn migration is correlated with its heterovalent state. Figure 5.17(a) illustrates the site-wise distribution of magnetic moments for Mn ions. Heterovalent states of Mn are categorized as follows: $Mn^{2+} \in [4.1\mu_B, 5.0\mu_B]$, $Mn^{3+} \in [3.25\mu_B, 4.1\mu_B]$, and $Mn^{4+} \in [2.5\mu_B, 3.25\mu_B]$. At the onset of the MD simulation, Mn predominantly exists in valence states of +3 and +4. As the simulation proceeds, the content of Mn^{2+} gradually increases, as highlighted by the yellow circles in Fig. 5.17(a). Figure 5.17(b) details the per formula unit content of Mn^{2+} and Mn^{2+} on both octahedral and tetrahedral sites.

The atomic charges predicted by CHGNet reveal the emergence of Mn^{3+}_{tet} in the early stages of the simulation. The crystal field theory suggests that Mn^{2+} exhibits no site preference between octahedral and tetrahedral positions, and the low migration barrier energy makes Mn^{2+} as an ideal candidate to contribute to the TM migration [132]. The results

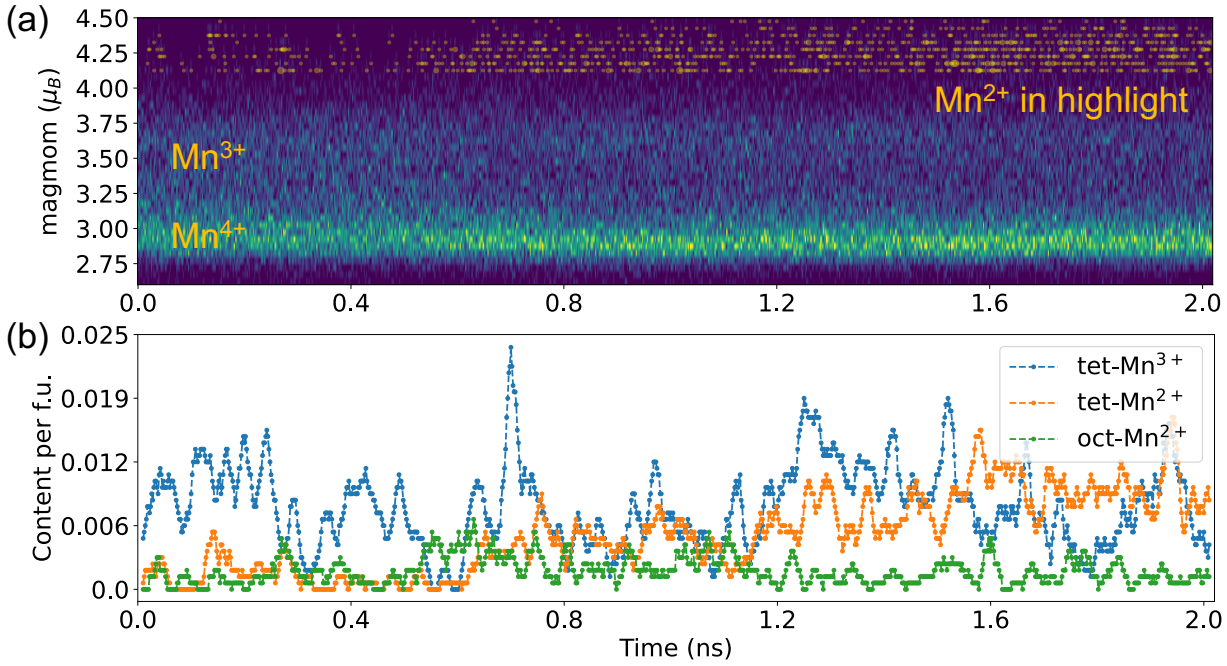

Figure 5.17: Simulated charge distribution of Mn ions along the MD trajectories

carried out by CHGNet simulation clearly indicate that a significant amount of Mn^{3+} starts to migrate and emerges on the tetrahedral sites almost at the beginning of the simulation.

The emergence of Mn^{2+}_{tet} is more likely to correlate with the formation of long-range order rather than the phenomenon of local migration in the phase transformation from DRX. The small quantity of Mn^{2+}_{oct} can be attributed to the variety of local chemical environments in DRX as compared to the ordered structure. Within these diverse environments, Mn^{3+} with marginal stability can disproportionate into Mn^{2+} and Mn^{4+}. The simulation result also agrees with the phase transformation simulation from orthorhombic to spinel-like $Li_{0.5}MnO_2$ as revealed by pretrained CHGNet simulation in Ref. [168], whereas this simulation addresses a more complex compound with significant configurational disorder and substantial SRO of TMs and anions.

5.5.3 Intercalation voltage profile of δ-phase

To assess the impacts of structural disorder and partial spinel-like ordering on the electrochemical performance of the transformed structure (δ-phase), the fine-tuned CHGNet is used as an energy calculator to examine the equilibrium voltage profile.

According to experimental results, the spinel-like structure transformed after electro-

chemical cyclings manifests a pronounced 3 V plateau in both charge and discharge voltage profiles [209]. The 3 V voltage plateau is a characteristic feature of the intercalation of spinel with 0-TM to Li_{tet} conversion reaction (see Fig. 5.18), which is defined as

$$4Li_{oct} \rightarrow 3\square_{oct} + 1Li_{tet}. \tag{5.9}$$

To compare the computed intercalation voltage profiles of the δ-phase with those of the DRX and spinel, the delithiation process involves the 0-TM to Li_{tet} conversion is primarily assessed. The energy preferences associated with other types of delithiation processes after such the 0-TM conversion is assessed subsequently.

Given that the intercalation problem involves identifying ground-state related energetics and considering that the partially disordered δ-phase possesses a high-dimensional configurational space, constructing a comprehensive CE model that includes both tetrahedral and octahedral cation occupancy is significantly more complex than for normal DRX with only octahedral occupancy. Therefore, a simplified voltage profile using a beam search algorithm is resorted:

1. Select an initial structure with composition $Li_{x_1}TMO_2$, relax the structure by the fine-tuned CHGNet and get the internal energy E_1.
2. Generate 20 different delithiated structures, each with a different vacancy occupancy and composition $Li_{x_2^i}TMO_2$ (x_2^i may not be equal for all $\{i\}$ structures. This generation process is referred to as an *intercalation step*.
3. Relax these 20 structures and obtain their corresponding internal energies E_2^i (i denotes the index of each structure).
4. The proposed next delithiated structure is chosen based on the minimum (maximum for lithiation process) voltage calculated using Eq. (5.3) with respect to the initial structure $Li_{x_1}TMO_2$.
5. Repeat Step 1 until all possible intercalation steps are used.

It is noted that different 0-TM channels may share the same Li atoms in a FCC framework. The conversion of different 0-TM to Li_{tet} may result in delithiated structures of varying Li concentrations in Step 2. Therefore it is rational to use the minimum voltage as a selecting criterion in the beam search algorithm.

Computed voltage profile of δ-phase

Figure 5.18(a) illustrates the formation energy convex hull constructed using all the relaxed structures. In the range of $0.5 \leq x \leq 1.1$, only 0-TM to Li_{tet} conversion reactions are evaluated. The voltage profile exhibits a plateau around 3 V, with a minor slope. Upon

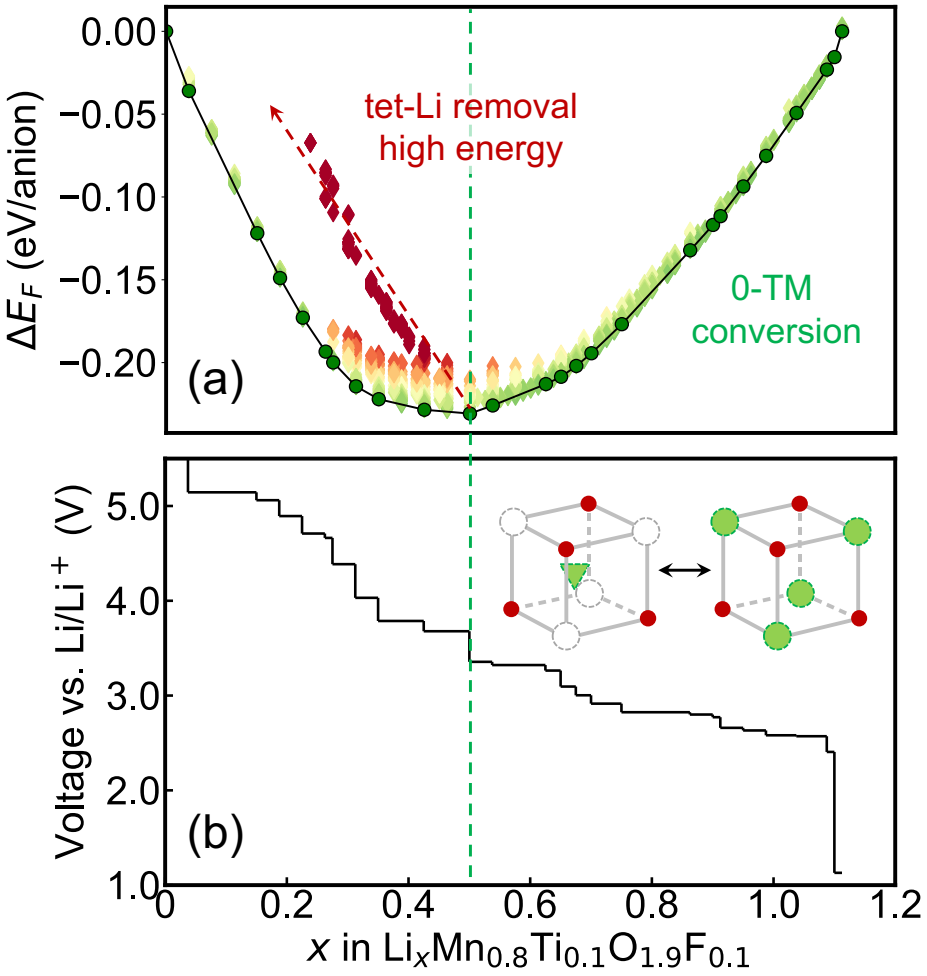

Figure 5.18: Computed formation energy convex hull and voltage profile of $Li_{1.1-x}Mn_{0.8}Ti_{0.1}O_{1.9}F_{0.1}$ of the δ-phase. Voltage profiles constructed from the GS of energy convex hull. The inset illustrates the 0-TM to tet-Li conversion in the intercalation process.

reaching $x = 0.5$, all 0-TM channels have been converted into tetrahedral lithium (Litet) occupancy, marking the start of another type of delithiation process, which involves the removal of either Li_{tet} or (Li_{oct}). Although a slight increase of voltage is observed at $x = 0.5$ after the consumption of all 0-TM conversions, the quantity is much reduced compared to the two-phase reaction as shown in Fig. 5.10(a) and Fig. 5.19(d). For $0 \leq x \leq 0.5$, delithiation of both Li_{oct} and Li_{tet} is considered using the aforementioned method.

The low-energy configurations near the convex hull within the range $0.25 \leq x \leq 0.5$ correspond to the removal of Li_{oct}. In contrast, the high-energy configurations, represented in dark red, correspond to the removal of Li_{tet}. Notably, the removal of Li_{tet} is characterized by a high defect energy in the formation energy convex hull, identified by a steep slope that almost parallels the delithiation process for $x < 0.25$. For $x < 0.25$, all Li-ions are located at the tetrahedral site, and the delithiation process entails the removal of Li_{tet}.

The intercalation voltage profiles constructed using Eq. 5.3 are displayed in Fig. 5.18. The 0-TM conversion reaction contributes to approximately 0.6 Li capacity ($\sim$ 181 mAh/g) within the voltage window centered around 3 V. This 0-TM capacity contribution arises from an increased spinel-like characteristic and the presence of 0-TM channels, as indicated by the statistics of the MD trajectories from the CHGNet simulation. Although the δ-phase (from the MD simulation) does not reach the highest amount of 0-TM compared to the ordinary $LiMnO_2$ spinel, the capacity contributed by 0-TM conversion does not necessarily decrease. This is because the correlations between 0-TM channels are less frequent than ordinary $LiMnO_2$ spinel. For instance,

1. An independent 0-TM conversion results in 3 Li capacity per 0-TM

$$4Li_{oct} \rightarrow 3\square_{oct} + 1Li_{tet}$$

2. Two correlated 0-TM with two point-sharing Li-ion (7 Li_{oct} in total) results in 2.5 Li capacity per 0-TM:

$$7Li_{oct} \rightarrow 5\square_{oct} + 2Li_{tet}.$$

It is noted that, for spinel $LiMnO_2$, all Li resides on the 16*c* sites and is shared by two 0-TM tetrahedra. Therefore, the Li capacity is shared by two 0-TM channels, resulting in 2 Li capacity per 0-TM. These findings clarify why the δ-phase, despite having a lower number of 0-TM channels, can still yield a comparable (or even greater) Li capacity around 3 V through the 0-TM conversion.

Comparision to DRX and spinel phase

To further elucidate the variations in intercalation voltage profiles between the DRX and spinel phases, we conducted additional evaluations for comparison. The DRX structure is selected as the initial structure derived from the CEMC simulations (the configuration at

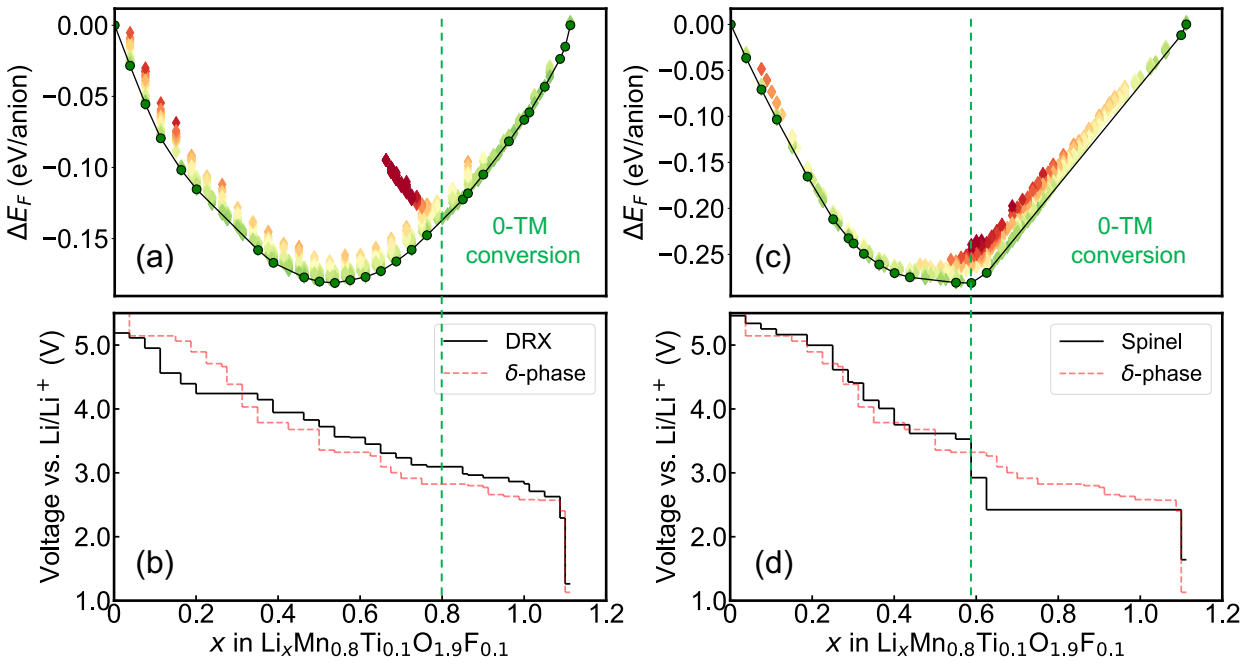

Figure 5.19: Computed formation energy convex hull of $Li_{1.1-x}Mn_{0.8}Ti_{0.1}O_{1.9}F_{0.1}$ of (a) DRX and (b) spinel phase. Voltage profiles constructed from the GS of energy convex hull of (c) DRX and (d) spinel phase. The voltage profiles of partially transformed δ-phase are shown in red dashed lines for comparison.

$t = 0$ s in MD simulation). The spinel $Li_{1.1}Mn_{0.8}Ti_{0.1}O_{1.9}F_{0.1}$ is generated through another CEMC simulation by fixing the 16*d* occupancy of Mn and Ti and the 16*c* occupancy of Li, which could capture the underlying SRO of anions and cations (e.g., Li-F SRO).

Figure 5.19(a) illustrates the formation energy convex hull and voltage profile of the DRX phase, where the δ-phase is plotted in the red dashed line for comparison. Due to the absence of 0-TM channels in the DRX structure, a relatively limited amount of 0-TM conversion Li capacity (approximately 0.3 per f.u.) can be achieved. The absence of spinel-like ordering results in a profile marked by a mildly steep increase as delithiation progresses. Notably, the overall voltage profile for $x > 0.25$ of the DRX phase is higher than that of the δ-phase. This restricts the accessible capacity within an operational voltage window, as previously reported in experimental studies [209].

Figure 5.19(b) depicts the calculated results for spinel $Li_{1.1-x}Mn_{0.8}Ti_{0.1}O_{1.9}F_{0.1}$. The voltage profile clearly displays a two-phase reaction between $Li_{1.1}$ and $Li_{0.6}$. Due to the absence of disorder, the spinel phase manifests a lower average voltage for the 0-TM conversion reaction, which is in full agreement with the previous finding by Chen et al. [207] in cation disorder effect in $LiMnO_2$ spinel.

In summary, two conclusions can be drawn from the simulation results: (1) The presence of partial cation disorder in the δ-phase effectively removes the two-phase reaction, as demonstrated in Fig. 5.19(d). (2) The introduction of partial spinel-like ordering increases the 0-TM occurrence and thus expands the available Li capacity around the 3 V. The 0-TM in a partially disordered spinel-like structure is less inter-correlated compared to ordinary spinel, providing enough Li capacity. The two characteristics of δ-phase $Li_{1.1-x}Mn_{0.8}Ti_{0.1}O_{1.9}F_{0.1}$ make it a promising candidate for the next-generation of cathodes with earth-abundant cathode materials.

5.6 Conclusion

In this chapter, the thesis has addressed the computational challenges associated with modeling the complex oxides embedded with charge information for modern battery materials applications, including disordered rocksalt cathodes and their derivatives. Charge degrees of freedom or charge information play a pivotal role in modeling battery materials and understanding atomistic-scale reaction mechanisms. This aspect is typically coarse-grained as a degree of freedom that can be variationally removed in many previous pieces of research. However, the examples presented in this chapter underscore the importance of incorporating charge information, as well as elucidate how to apply it to complex, multi-component systems effectively.

The first example showcases the equilibrium modeling using a charge-decorated cluster expansion for intercalation chemistry with multi-redox reactions in $Li_{1.3-x}Mn_{0.4}Nb_{0.3}O_{1.6}F_{0.4}$. The application of commonly used cluster expansion techniques to model the intercalation thermodynamics is challenged by the combinatorial increase in configurational degrees of freedom as the number of species grows, which necessitates the efficient generation of lattice models without over-fitting and proper sampling of the configurational space under the requirement of charge balance in ionic systems. In this work, we introduce a combined approach that addresses these challenges by (1) constructing a robust cluster-expansion Hamiltonian using the sparse regression technique, including $\ell_0\ell_2$-norm regularization and structural hierarchy; and (2) implementing semigrand-canonical Monte Carlo to sample charge-balanced ionic configurations using the table-exchange method and an ensemble-average approach. The simulated voltage profile is found to be in good agreement with experimental data and particularly provides a clear demonstration of the Mn and oxygen contribution to the redox potential as a function of Li content.

The second example presents the kinetic modeling using CHGNet as a charge-informed interatomic potential to study the transition metal migration-induced phase transformation in $Li_{0.6}Mn_{0.8}Ti_{0.1}O_{1.9}F_{0.1}$ DRX. A fine-tuned CHGNet with high-fidelity quantum accuracy of r^{2}SCAN-DFT is built. For this purpose, structures from the existing dataset are initially computed. A unique sampling method is developed to span the configurational space from disordered to spinel phases with coherent structure transformation. Throughout this trans-

formation, interpolated structures are generated along various migration pathways for DFT evaluations. The structures produced via MD simulations are further evaluated and included for data augmentation. A fine-tuned MLIP is constructed from the pretrained CHGNet and such a comprehensive dataset in the Li–Mn–Ti–O–F chemical space. And the MLIP is further applied to diverse applications, such as structure relaxation and MD simulations.

The studies reveal that a partial spinel-like ordering (referred to as the δ-phase) can be attained via MD simulation of the disordered $Li_{0.6}Mn_{0.8}Ti_{0.1}O_{1.9}F_{0.1}$. Analysis of structural ordering changes (e.g., simulated XRD and SRO) is conducted on the MD structures. Particularly, the charge information on Mn ions revealed a correlation between charge disproportionation and the formation of spinel-like long-range order. It is found that Mn^{3+} contributes significantly to the migration, starting almost immediately at the onset of the MD simulation. Moreover, it is identified that these structural characteristics profoundly influence the electrochemical properties of the material, especially its intercalation voltage profile. When compared to the spinel phase, the simplified voltage profile derived from the MD-simulated δ-phase demonstrates that partial cation disorder can effectively remove the two-phase reaction. In contrast to the DRX phase, the introduction of partial spinel-like ordering in the δ-phase extends the available Li capacity around the 3V plateau, which is facilitated by the increased number of 0-TM channels with reduced inter-correlation.

Looking forward, the recently developed universal MLIP (or fine-tuned version of such universal MLIP) provides new opportunities to accelerate the training structure generation process by accurately approximating DFT calculations [166, 168]. The CE Hamiltonian demonstrated in the first case can be further obtained by coarse-graining the MLIP predicted configurational energy, especially using the charge-informed MLIP to include the heterovalent states of transition metals [168, 213]. It is believed such an approach has the potential to bridge up first-principles calculations, force fields, and cluster expansions and give a higher accuracy sampling at a lower computational cost to study the thermodynamic and kinetic properties of energy storage materials.

Chapter 6

Deep learning of experimental cathode electrochemistry

6.1 Introduction

In previous chapters, the thesis discusses atomistic modeling approaches derived from *ab-initio*, such as the cluster expansion Monte Carlo and molecular dynamics. While these methodologies are powerful tools for comprehending the structure-property relationships in materials science, their computational demands present a significant challenge when applied to disordered systems. Additionally, many experimentally measured quantities (e.g., high-rate reactions) are far from the equilibrium, while the *ab-initio* modeling struggles with these representations due to both temporal and spatial scale challenges. Furthermore, virtual high-throughput screening for materials optimization demands an approach that is accurate and versatile yet also cost-efficient. An alternative approach to well represent and predict the electrochemistry of cathode materials is desired beyond *ab-initio* modeling.

Artificial intelligence (AI) has emerged as a powerful tool in discovering and optimizing novel battery materials [214]. By leveraging vast amounts of experimental and computational data, AI-assisted techniques can accelerate the battery design process by identifying promising candidates within large chemical spaces [215], predicting battery remaining lifespan [216–218], and optimizing the fast charge/discharge protocol [219]. These efforts significantly reduce the time and cost required for conventional trial-and-error approaches. Most recently, the battery data genome initiative has been proposed to use AI assistance to accelerate the discovery and optimization of battery materials [220].

Despite these advancements, current machine-learning efforts in battery research primarily focus on predicting the lifespan within one battery system in a rather simple chemical space, such as NMC (Ni–Mn–Co). The development of exploratory machine learning for representing chemical effects in a more complicated multi-dimensional chemical space remains underdeveloped due to the challenges associated with simultaneously optimizing multiple

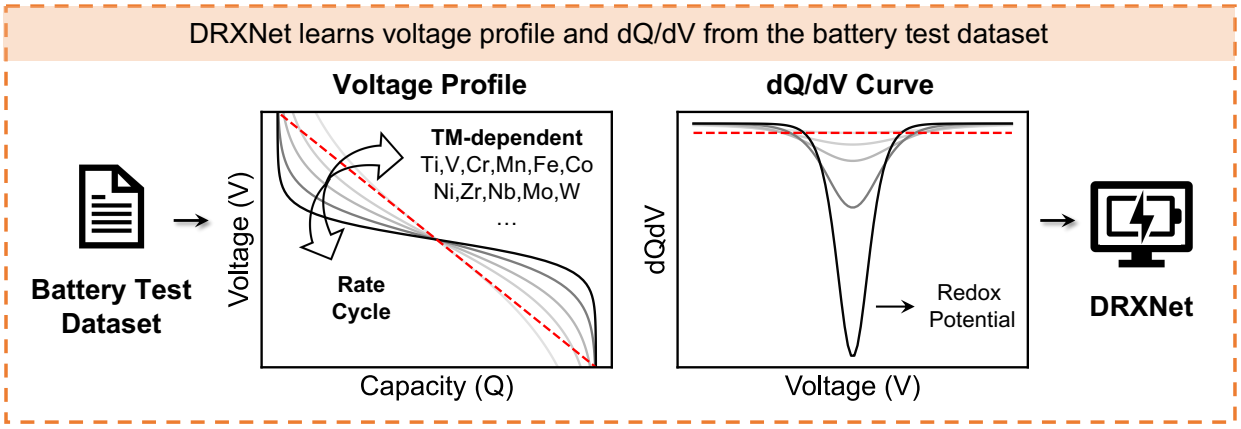

Figure 6.1: The voltage profile illustrates the relationship between capacity (Q) and voltage (V), which is strongly correlated with the composition of transition metal (TM) species. The derivative quantity dQ/dV peaks at the redox potential of TM, where a pronounced peak indicates a flat plateau in the voltage profile. (Ref. [222])

electrochemical properties (e.g., rate capability, cyclability, and various test voltage windows) and capturing the complex chemistry among different transition metal (TM) species [221]. Moreover, the scarcity of high-fidelity data further hinders the progress of AI in the battery field.

Owing to the nearly unlimited compositional design space and considerably more complex structure-property relationship of DRX cathodes compared with conventional layered cathodes, their rational design requires the extensive involvement of advanced characterization techniques as well as complicated computational tools under a conventional frame of investigation. Data-driven methods offer alternative means of compositional design and optimization of high-dimensional DRX cathodes without having to fully construct their structure-property relationships. Instead of computing from *ab-initio*, this chapter presents an exploratory deep-learning model (DRXNet) for the discovery and optimization of battery cathode materials.

As shown in Fig. 6.1, the discharge-voltage profile presents a negative voltage slope against capacity. This profile shape is tied to various factors, such as the DRX composition, applied current density rate, and degradation that may have occurred in various cycles. In experiments, the capacity Q is measured by determining the cumulative charge transfer using galvanostatic tests. Another relevant quantity of the voltage profile, dQ/dV, is obtained by taking the derivative of Q with respect to V. The dQ/dV curve is a crucial physical quantity for analyzing characteristic redox potentials from different TMs.

6.2 Data collection from electrochemical test

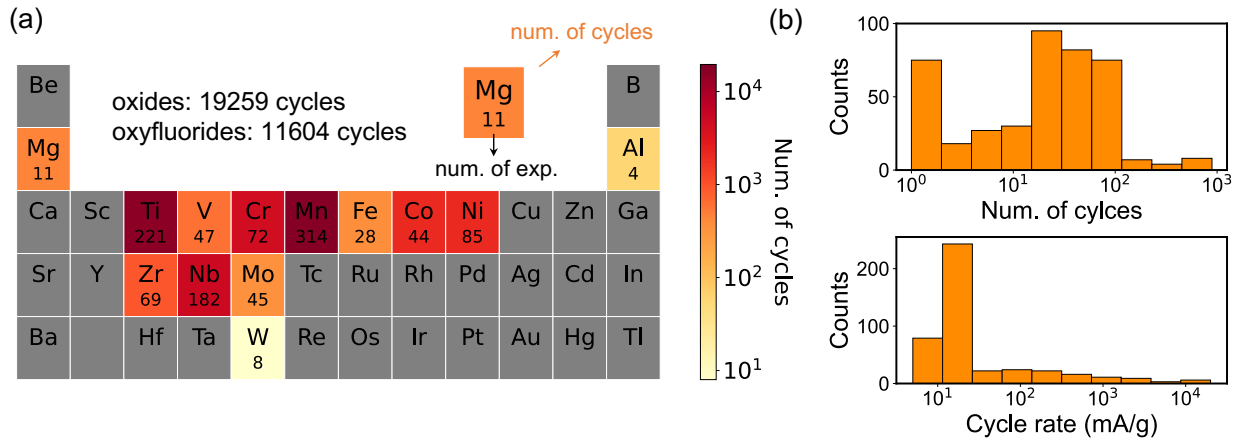

Figure 6.2: (a) The elemental distribution of collected experimental electrochemistry data. In total, the dataset contains 19,259 discharge profiles collected from DRX oxides and 11,604 discharge profiles from oxyfluorides. The color-coded boxes indicate the number of discharge profiles (cycles) on compounds that contain that specific element. The number within each elemental box represents the count of individual experiments conducted. (b) A histogram of the number of cycles (N_{cycle}) and current density (rate) for all the individual electrochemical tests.

Unlike conventional NMC-based layered cathodes, DRX materials exhibit much more diverse electrochemical performance due to their significantly larger chemical existence and the more complex structure-property relationship involving not only long-range ordering but also short-range ordering [17]. For instance, Mg doping in Mn-based oxyfluoride DRX can increase the discharge capacity while retaining similar voltage-profile shapes [114]; Cr doping in $Li_{1.2}Mn_{0.4}Ti_{0.4}O_{2.0}$ results in comparable low-rate capacity but significantly improves the high-rate performance due to the non-topotactic TM migration [126]. These non-linear effects arising from compositional changes make both material design and machine-learning modeling challenging, thereby necessitating a comprehensive, high-fidelity dataset to address such issues.

To address these issues, the electrochemical test data related to DRX compounds over the past five years have been compiled by mining electronic experimental notebooks in CEDER Group to construct the DRX Test Dataset (DRX-TD). The dataset contains not only the successful materials using galvanostatic charge/discharge tests in several papers but also less well-performing DRX compounds. This endeavor yielded a comprehensive dataset containing 30,000 discharge profiles across 16 elements (14 metal species) from lab experiments and published literature.

Coin-cell electrochemical test data from the lab starting in 2016 were collected and converted into a digital format (`.json`). Each `.json` file contains information on one individual electrochemical test, including the electrode composition, electrode mass (g), active mass (g), test current rate (mA/g), low and high voltage value of the working window (V), and charge/discharge profiles of N_{cycle} collected cycles.

An individual electrochemical test is defined as a group of N_{cycle} discharge profiles with a fixed current density rate, where N_{cycle} is the number of cycles conducted in such a test, corresponding to the results obtained from one coin-cell in experiments. The distribution of elements in the DRX-TD is shown in Fig. 6.2(a), where the number in each element's box represents the number of times that element is presented in a compound for which an electrochemical test is present. The box's color indicates the number of times that element is presented in a discharge profile. Comprising 19,259 discharge profiles of DRX oxides and 11,604 discharge profiles of oxyfluorides, the dataset offers extensive coverage of major redox-active TMs. Figure 6.2(b) displays the histograms of the N_{cycle} and the loading current rates. Most of the electrochemical tests were conducted at a low current rate (20 mA/g).

The `UnivariateSpline` and average convolution were used to denoise the experimental profile and compute the dQ/dV curve. One hundred points were uniformly sampled to form the voltage series $\boldsymbol{V} = [V_1, V_2, ..., V_i, ...]$ and a capacity series $\boldsymbol{Q} = [Q_1, Q_2, ..., Q_i, ...]$ for each discharge profile. As dQ/dV is a more intrinsic property for battery materials representing the redox information, including this value in the modeling allows for a more representative analysis of the electrochemical performance of DRX compounds under various conditions. The dQ/dV series were calculated accordingly based on $\boldsymbol{V}$.

Dataset from lab experiments

For the in-house battery tests, the CR2032 coin cells were assembled using commercial 1 M $LiPF_6$ in an ethylene carbonate and dimethyl carbonate solution (volume ratio 1:1) as the electrolyte, glass microfiber filters (Whatman) as separators, and Li-metal foil (FMC) as the anode. The coin cells were tested on an Arbin battery cycler at room temperature. The cathode consisted of a mixture of active material (DRX), Super C65 carbon black, and polytetrafluoroethylene (PTFE). The capacity signal, collected in units of Ah from the Arbin battery cycler, was normalized to mAh/g using the mass of the active material (active mass). The data from the failed tests (e.g., Arbin cycler breakdown, electrolyte failure, strong signal fluctuations ...) were removed from the dataset. Figure 6.3 demonstrates the typical examples of failed data collection during experimental electrochemical testing.

Dataset augmentation from published literature

To enhance the generalization and expressibility of DRXNet, the dataset was expanded by figure mining published voltage profiles in related systems not covered by the lab tests, which

Table 6.1: This table presents supplementary electrochemical cycling data extracted from previously published literature, which has been used to augment the training dataset.

Composition	Voltage window	Rate	Reference
$Li_{1.333}V_{0.667}O_{2.0}$	1.3 – 4.1 V	C/20	Chen et al. [110]
$Li_{1.333}V_{0.667}O_{1.333}F_{0.667}$	1.3 – 4.1 V	C/20	
$Li_{1.211}Mo_{0.467}Cr_{0.3}O_2$	1.5 – 4.3 V	C/20	Lee et al. [25]
$Li_{1.2}Mo_{0.6}Fe_{0.2}O_2$	2 – 4.4 V	0.1C	Liu et al. [223]
$Li_{1.2}Ni_{0.333}Ti_{0.333}Mo_{0.133}O_2$	1.5 – 4.5 V	20 – 400 mA/g	Lee et al. [103]
$Li_{1.15}Ni_{0.375}Ti_{0.375}Mo_{0.1}O_2$	1.5 – 4.5 V	20 mA/g	
$Li_{1.1}Ni_{0.416}Ti_{0.416}Mo_{0.06}O_2$	1.5 – 4.5 V	20 mA/g	
$Li_{1.05}Ni_{0.458}Ti_{0.458}Mo_{0.03}O_2$	1.5 – 4.5 V	20 mA/g	
$LiNi_{0.5}Ti_{0.5}O_2$	1.5 – 4.5 V	20 – 400 mA/g	
$Li_{1.15}Ni_{0.375}Ti_{0.375}Mo_{0.1}O_2$	1.5 – 4.6 V	20 mA/g	Lee et al. [111]
$Li_{1.2}Ni_{0.333}Ti_{0.333}Mo_{0.133}O_2$	1.5 – 4.6 V	20 mA/g	
$Li_{1.15}Ni_{0.45}Ti_{0.3}Mo_{0.1}O_{1.85}F_{0.15}$	1.5 – 4.6 V	20 mA/g	
$Li_{1.333}Mo_{0.667}O_2$	1 – 4 V	10 mA/g	Hoshino et al. [224]
$Li_{1.286}Mo_{0.428}Nb_{0.286}O_2$	1 – 4 V	10 mA/g	
$Li_{1.2}Mo_{0.4}Ti_{0.4}O_2$	1 – 4 V	10 mA/g	
$Li_{1.4}Mo_{0.4667}Ti_{0.1333}O_{1.333}F_{0.667}$	1.2 – 4 V	10 mA/g	
$Li_{1.333}Mo_{0.667}O_{1.333}F_{0.667}$	1.2 – 4 V	10 mA/g	
$Li_{1.33}Nb_{0.3}Mn_{0.4}O_2$	1.5 – 4.8 V	10 – 1600 mA/g	Yabuuchi et al. [104]
$Li_{1.25}Nb_{0.25}Mn_{0.5}O_2$	1.5 – 4.8 V	10 mA/g	Wang et al. [225]
$Li_{1.3}Nb_{0.3}V_{0.4}O_2$	1.5 – 4.2 V	10 mA/g	Nakajima and Yabuuchi [201]
$Li_{1.25}Nb_{0.25}V_{0.5}O_2$	1.5 – 4.8 V	10 mA/g	
$Li_{1.3}Nb_{0.3}V_{0.4}O_2$	1.5 – 4.8 V	10 mA/g	
$Li_{1.2}Ti_{0.4}Fe_{0.4}O_2$	2.5 – 4.8 V	7.5 mA/g	Tabuchi et al. [226]
$Li_{1.273}Ti_{0.546}Fe_{0.18}O_2$	2.5 – 4.8 V	7.5 mA/g	
$Li_{1.111}Ti_{0.222}Fe_{0.667}O_2$	2.5 – 4.8 V	7.5 mA/g	
$Li_{1.333}Cr_{0.667}O_{1.333}F_{0.667}$	1.3 – 4.8 V	13 mA/g	Ren et al. [227]
$Li_{1.333}Cr_{0.533}V_{0.133}O_{1.333}F_{0.667}$	1.3 – 4.7 V	13 mA/g	
$Li_{1.333}Cr_{0.333}V_{0.333}O_{1.333}F_{0.667}$	1.3 – 4.1/4.5/4.7 V	13 mA/g	
$Li_{1.333}Cr_{0.133}V_{0.533}O_{1.333}F_{0.667}$	1.3 – 4.1/4.3/4.5/4.7 V	13 mA/g	
$Li_{1.0}Ni_{0.5}Ti_{0.5}O_{2.0}$	1.3 – 4.5 V	20 mA/g	Cambaz et al. [228]
$Li_{1.05}Ni_{0.458}Ti_{0.458}W_{0.033}O_{2.0}$	1.3 – 4.5 V	20 mA/g	
$Li_{1.10}Ni_{0.416}Ti_{0.416}W_{0.066}O_{2.0}$	1.3 – 4.5 V	20 mA/g	
$Li_{1.15}Ni_{0.375}Ti_{0.375}W_{0.10}O_{2.0}$	1.3 – 4.5 V	20 mA/g	
$Li_{1.20}Ni_{0.333}Ti_{0.333}W_{0.133}O_{2.0}$	1.3 – 4.5 V	20 – 400 mA/g	

was accomplished using the `WebPlotDigitizer` [229]. The information of the augmented dataset from published literature is summarized in Table. 6.1.

6.3 Model design of DRXNet

DRXNet aims to draw a connection between chemistry and cathode performance by establishing a mapping between $\boldsymbol{V}$ and $\boldsymbol{Q}$ for arbitrary cathode compositions under various test conditions. This idea is conceptualized as identifying a function $\mathcal{F}$ that maps cathode parameters and the voltage state V_i to produce the capacity state Q_i as an output. The function $\mathcal{F}$ is conditionally defined by the parameters $\mathcal{O}$, which consider the electrode composition, current rate, and cycle number

$$Q_i = \mathcal{F}(V_i|\mathcal{O}). \tag{6.1}$$

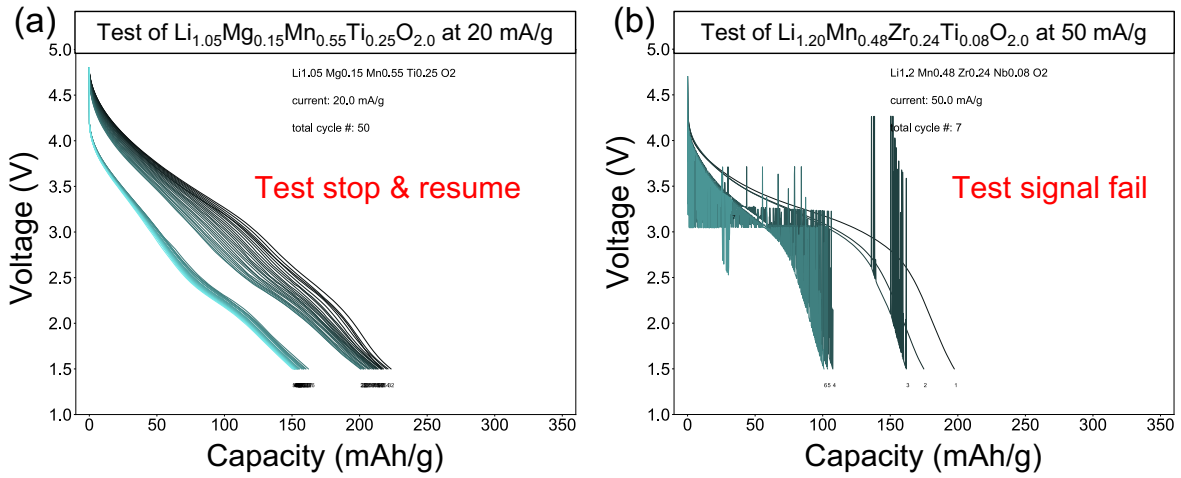

Figure 6.3: Two examples of failed data collection during experimental electrochemical testing. (a) The Arbin cycler accidentally stopped, and the test resumed later. Discharge cycles after the stoppage were excluded from the dataset. (b) The electrochemical test experienced a complete breakdown with significant signal fluctuations. Only the first and second cycles were retained, while the remaining cycles were discarded.

With this intuition, the DRXNet is designed with two main components, as shown in Fig. 6.4(a) and Fig. 6.4(b): (1) an electrochemical condition network that generates a feature vector $\vec{X}_{\mathcal{O}}$ based on the compound composition and additional features of the electrochemical test information; (2) a state prediction network to approximate the discharge state of the cathode as a function of the voltage state, $Q_i = \mathcal{F}(V_i|\mathcal{O})$, given the electrochemical conditional encoding of $\mathcal{O}$.

Preliminaries

Define a linear layer with trainable weight $\boldsymbol{W}$ and bias $\boldsymbol{b}$ as

$$L(\vec{X}) = \vec{X}\boldsymbol{W} + \boldsymbol{b}. \tag{6.2}$$

A multi-layer perceptron (MLP) is denoted as

$$\phi(\vec{X}) = \sigma\left(L(\vec{X})\right) = \sigma \circ L(\vec{X}), \tag{6.3}$$

where σ is a non-linear activation function. In this thesis, σ_s represents the `Sigmoid` activation function

$$\sigma_s(x) = \text{Sigmoid}(x) = \frac{1}{1+\exp(-x)}, \tag{6.4}$$

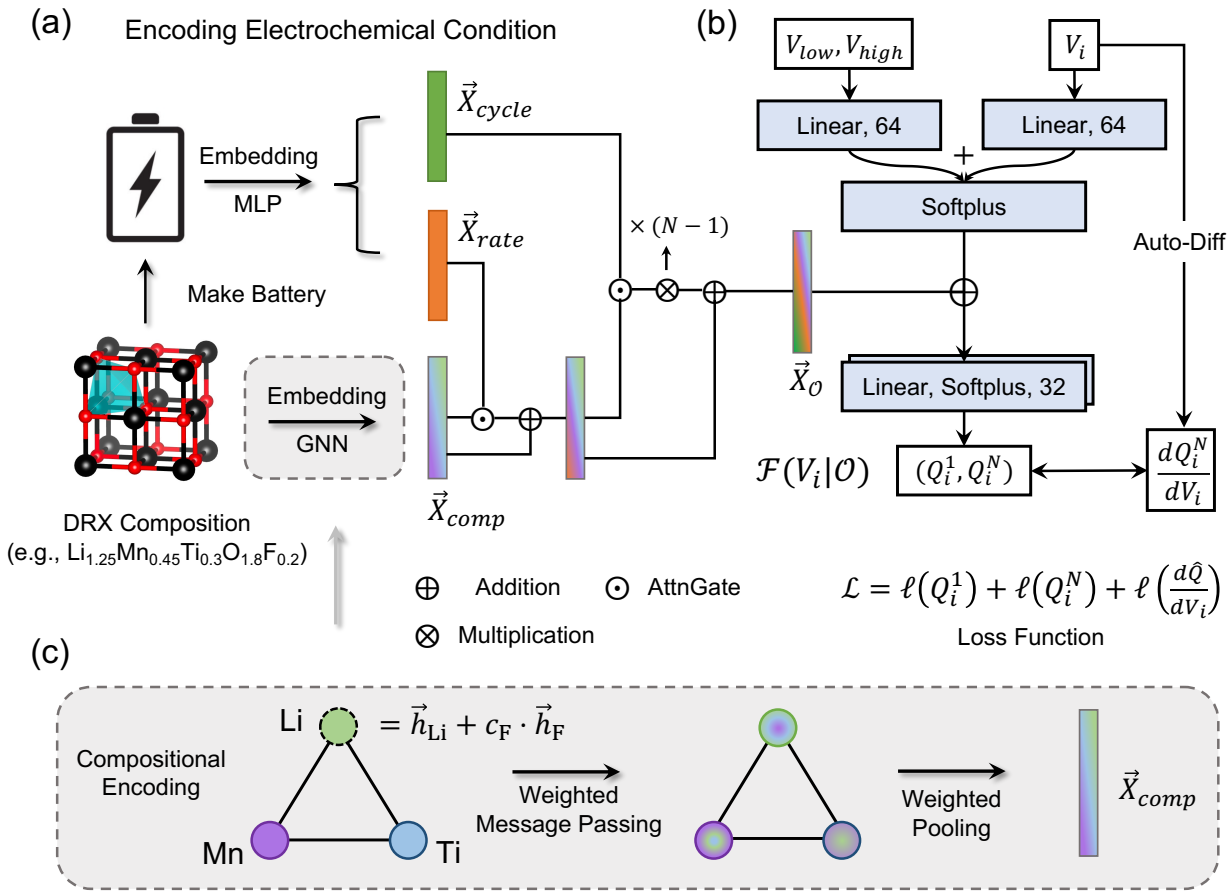

Figure 6.4: An end-to-end pipeline that maps $Q_i = \mathcal{F}(V_i|\mathcal{O})$, which consists of the electrochemical condition network $\mathcal{O}$ and the state prediction network $\mathcal{F}$. (A) The electrochemical condition network encodes the DRX composition, current density rate, and cycle information. The three encoded vectors are synthesized through gated-MLPs with soft attention to obtain the condition vector $\vec{X}_{\mathcal{O}}$ [144]. (B) The state prediction is approximated as a forward deep neural network that takes the voltage state V_i and cycling voltage window $V_{\text{low}}, V_{\text{high}}$ as inputs. The encoded condition vector $\vec{X}_{\mathcal{O}}$ is element-wise added in the hidden layer of $\mathcal{F}$. The circled symbols are all element-wise operations. (C) The message-passing graph neural network (GNN) is used for compositional encoding of DRX, adapted from the Roost model [230].

σ_g represents the `SiLu` activation function

$$\sigma_g(x) = \mathrm{SiLu}(x) = x \cdot \sigma_s(x), \tag{6.5}$$

and $\sigma_{\mathcal{F}}$ represents the `Softplus` activation function

$$\sigma_{\mathcal{F}}(x) = \mathrm{Softplus}(x) = \log(1 + \exp(x)). \tag{6.6}$$

Compositional encoding

`Roost` (Representation Learning from Stoichiometry) model is used for compositional encoding [230]. `Roost` takes elements as graph nodes and updates the correlation between elements through weighted message passing based on each element's fractional concentration (see Fig. 6.4(c)). For elemental information, each element is embedded into a 200-dimensional vector using `mat2vec` to capture as much prior chemical information as possible through text mining of previously published literature [231]. The node information is updated by message passings as follows:

$$\begin{aligned} \vec{h}_i^{t+1} &= \vec{h}_i^t + \sum_{j,m} a_{i,j}^{t,m} \cdot \sigma_g \circ L_c \left(\vec{h}_i^t || \vec{h}_j^t \right), \\ a_{i,j}^{t,m} &= \frac{w_j \exp(e_{i,j}^{t,m})}{\sum_k w_k \exp(e_{i,k}^{t,m})}, \; e_{i,k}^{t,m} = \sigma_g \circ L_a \left(\vec{h}_i^t || \vec{h}_j^t \right). \end{aligned} \tag{6.7}$$

In these equations, $\vec{h}_i^t$ represents the t-th hidden layer for the i-th element; $||$ denotes the concatenation operation; and the soft-attention coefficient $a_{i,j}^{t,m}$ describes the interaction between elements i and j, with m as the index of multi-head attention. L_c and L_a denote the linear layer for the core and attention layer, respectively. The fractional concentration w_j of element j depends on the specific compound (e.g., $w_j = 0.6/0.2/0.2$ for Li/Mn/Ti in $Li_{1.2}Mn_{0.4}Ti_{0.4}O_{2.0}$). σ_g is the `SiLu` activation function. After n graph convolution layers, the encoded composition vector $\vec{X}_{\mathrm{comp}}$ is obtained by average pooling over the elements with weighted attention

$$\vec{X}_{\mathrm{comp}} = \mathrm{Pooling} \left[\frac{w_i \exp\left(\sigma_g \circ L_a(\vec{h}_i^n) \right)}{\sum_k \exp\left(\sigma_g \circ L_a(\vec{h}_i^n) \right)} \cdot \left(\sigma_g \circ L_c(\vec{h}_i^n) \right) \right] \tag{6.8}$$

Secifically, only the cation species are considered as independent nodes in `Roost`, treating the anion-species information (fluorine) as a mean-field background, i.e., $\vec{h}'_{\mathrm{Li}} = \vec{h}_{\mathrm{Li}} + c_{\mathrm{F}} \cdot \vec{h}_{\mathrm{F}}$, where c_{F} is the fractional concentration of fluorine and $\vec{h}_{\mathrm{Li/F}}$ is the embedded vector of Li/F.

Electrochemical condition encoding

The electrochemical test primarily involves two pieces of information: the current density rate and cycle number. Rate and cycle information is encoded using multi-layer perceptrons (MLPs). MLPs are used to encode the rate and cycle number:

$$\vec{X}_{\text{rate}} = \sigma_g \circ L(\text{rate}),\ \vec{X}_{\text{cycle}} = \sigma_g \circ L(\text{cycle}). \tag{6.9}$$

As the actual rate and cycle performance are strongly correlated with cathode materials, the relationship between the composition, rate, and cycle is synthesized using gated-MLPs with soft attention [144, 232]:

$$\begin{aligned} \vec{X}_{\mathcal{O}_1} &= \vec{X}_{\text{comp}} + \sigma_{f_1}(\vec{X}_{\text{comp}}||\vec{X}_{\text{rate}}) \cdot f_1(\vec{X}_{\text{comp}}||\vec{X}_{\text{rate}}) \\ \vec{X}_{\mathcal{O}_N} &= \vec{X}_{\mathcal{O}_1} + \sigma_{f_2}(\vec{X}_{\mathcal{O}_1}||\vec{X}_{\text{cycle}}) \cdot f_2(\vec{X}_{\mathcal{O}_1}||\vec{X}_{\text{cycle}}) \cdot \boldsymbol{W}_n(N-1) \end{aligned} \tag{6.10}$$

where $\sigma_f = \sigma_s \circ B \circ L$ is an MLP, σ_s is the `Sigmoid` activation function, and $f = \sigma_g \circ B \circ L$ is an MLP with `SiLu` activation function σ_g. The `BatchNormalization` layer B is added before the activation function. In this equation, $\vec{X}_{\mathcal{O}_1}$ is a feature vector jointly determined by the composition and rate information, which is used to predict the first cycle property. $\vec{X}_{\mathcal{O}_N}$ is a feature vector jointly determined by the composition, rate, and cycle information, which is used to predict the N-th cycle property. The difference between $\vec{X}_{\mathcal{O}_1}$ and $\vec{X}_{\mathcal{O}_N}$ is linearly dependent on the number of cycles with a trainable weight $\boldsymbol{W}_n$, allowing the model to learn cycle performance contrastively.

State prediction network

The state prediction network $\mathcal{F}$ is constructed with several MLPs (see Fig. 6.4(b)), which takes the inputs of voltage state (V_i) and outputs the discharge-capacity state (Q_i) $Q_i = \mathcal{F}(V_i|\mathcal{O})$. In practice, the voltage profile is measured within the applied voltage window $[V_{\text{low}}, V_{\text{high}}]$. To accommodate the voltage window in the discharge state prediction, the first layer in $\mathcal{F}$ is encoded via an MLP:

$$\vec{Z}_i^0 = \sigma_{\mathcal{F}}\left([V_{\text{low}}, V_{\text{high}}]^T \boldsymbol{W}_1 + [V_i]^T \boldsymbol{W}_2\right), \tag{6.11}$$

where $\sigma_{\mathcal{F}}(\cdot)$ is the `Softplus` activation function and $\boldsymbol{W}_{1/2}$ is the trainable weight. A ResNet-like structure is used to incorporate the test-condition information from $\vec{X}_{\mathcal{O}}$ [233]

$$\begin{aligned} \vec{Z}_i^1 &= \sigma_{\mathcal{F}} \circ L_0\left(\vec{Z}_i^0 + \vec{X}_{\mathcal{O}_1}\right) \\ \vec{Z}_i^N &= \sigma_{\mathcal{F}} \circ L_0\left(\vec{Z}_i^0 + \vec{X}_{\mathcal{O}_N}\right) \end{aligned} \tag{6.12}$$

The state of capacity is obtained by

$$\begin{aligned} Q_i^1 &= \sigma_{\mathcal{F}} \circ L_2 \circ \sigma_{\mathcal{F}} \circ L_1(\vec{Z}_i^1) \\ Q_i^N &= \sigma_{\mathcal{F}} \circ L_2 \circ \sigma_{\mathcal{F}} \circ L_1(\vec{Z}_i^N) \end{aligned} \tag{6.13}$$

Algorithm 1: The workflow of DRXNet with an example of $Li_{1.2}Mn_{0.4}Ti_{0.4}O_2$

Condition Inputs:

$$\mathcal{O} = \begin{cases} \textbf{composition} = Li_{1.2}Mn_{0.4}Ti_{0.4}O_2 \\ \textbf{rate} = 20 \text{ mA/g}, \\ \textbf{cycle} = 1 \end{cases}$$

Condition Outputs:

$$\vec{X}_{\mathcal{O}_1} = \vec{X}_{\text{comp}} + \sigma_{f_1}(\vec{X}_{\text{comp}}||\vec{X}_{\text{rate}}) \cdot f_1(\vec{X}_{\text{comp}}||\vec{X}_{\text{rate}})$$
$$\vec{X}_{\mathcal{O}_N} = \vec{X}_{\mathcal{O}_1} + \sigma_{f_2}(\vec{X}_{\mathcal{O}_1}||\vec{X}_{\text{cycle}}) \cdot f_2(\vec{X}_{\mathcal{O}_1}||\vec{X}_{\text{cycle}}) \cdot \boldsymbol{W}_n(N-1)$$

Inputs: $\boldsymbol{V} = [1.5, ..., V_i, ..., 4.8] \rightarrow N$ series

for $i = 1$ **to** N **do**
  Compute $Q_i = \mathcal{F}(V_i|\vec{X}_{\mathcal{O}}) \rightarrow \mathcal{F}$ is an NN
 end

Outputs: $\boldsymbol{Q} = [Q_1, ..., Q_i, ..., Q_N] \rightarrow N$ series

where Q_i^1 is the capacity for the first cycle and Q_i^N is the capacity for the N-th cycle. Because the discharge capacity is always positive, $\sigma_{\mathcal{F}}$ is added to constrain the predicted capacity to be positive and accelerate the training process. dQ/dV for the redox potential can be obtained via `PyTorch` auto-differentiation [234]

$$\left.\frac{dQ}{dV}\right|_i = \text{AutoDiff}(Q_i, V_i). \tag{6.14}$$

For instance, Algo. 1 demonstrates how DRXNet predicts the first-cycle discharge profile of $Li_{1.2}Mn_{0.4}Ti_{0.4}O_2$ at a current rate of 20 mA/g between 1.5 and 4.8 V by using electrochemical condition and state prediction network.

Model training

The model is trained to minimize the sum of multi-task losses for the capacity of the first cycle, the n-th cycle, and dQ/dV:

$$\mathcal{L} = w_Q \ell(Q_i^N) + w_{dQ} \ell(\frac{dQ^N}{dV_i}) + w_{Q_1} \ell(Q_i^1) + \mathcal{R}. \tag{6.15}$$

The `MSE` loss function is used for $\ell(Q_i^N)$ and $\ell(\frac{dQ^N}{dV_i})$, whereas the `MAE` loss function is employed for the first cycle as a contrastive term $\ell(Q_i^1)$. The weights for Q_i^N, dQ/dV, and Q_i^1 are

set to $w_Q = 1$, $w_{dQ} = 1$, and $w_{Q_1} = 5$. The combination of loss functions performs well empirically according to the tests (e.g., correct prediction of redox potential). The term $\mathcal{R}$ represents regularization, which consists of two parts: (1) an ℓ_2-norm regularization of the network's parameters $||\boldsymbol{\theta}||_2$ and (2) a smoothing term $||dQ/d\mathbf{c}||_2$ to avoid large, unphysical performance fluctuations ($\mathbf{c}$ denotes the fractional concentration of elements). The weight of regularization is 10^{-4}.

To make predictions, an ensemble of five independent models was trained to make predictions. Each model was trained with a batch size of 1024 within 30 epochs. The `Adam` optimizer was used with 10^{-3} as the initial learning rate. The `ExponentialLR` scheduler was used to adjust the learning rate with a decay of 0.9 per epoch.

6.4 Applicability domain of DRXNet

In this section, the scope of DRXNet's applicability in the realm of composition space is explored. Determination of the applicability domain in battery machine-learning models can be challenging due to the unavailability of a sufficient test dataset, as generating new data necessitates the synthesis of new solid-state materials or conducting battery cycling tests for weeks to months [221, 235]. For example, simply separating the sequence of voltage and capacity signals $\{V_i, Q_i\}$ into training and test sets can result in data-leakage issues and a failure to represent the expected error in real applications. To evaluate the expressibility and generalization of DRXNet, several experiments are designed by partitioning the dataset based on compositions. The electrochemical tests with no more than two metal species (2TM, excluding Li) were designated as the training set, whereas the tests with three metal species (3TM) and higher numbers of TM components (high-entropy, HE) were assigned as test sets. An ensemble of five independent models was trained for each test to enhance the overall prediction accuracy and robustness and quantify the model variance. Predictions were generated by averaging the predicted capacities of each DRXNet model.

Figure 6.5(a) and (b) present the performance of the DRXNet models trained on the 2TM dataset and tested on the 3TM and HE datasets. Mean absolute errors (MAEs) of 0.1/0.13 V for the average voltage ($\bar{V} = \sum_i V_i \Delta Q_i / \sum_i \Delta Q_i$) and 23.38/29.97 mAh/g for the capacity were obtained for the 3TM/HE test datasets, respectively, by comparing the prediction to the experimental Q–V curve within the voltage range of 2.0 – 4.4 V. As a baseline, the mean absolute deviation (MAD) of average voltage is 0.16/0.21 V for 3TM/HE and the MAD of discharge capacity is 36.59/38.54 mAh/g for 3TM/HE for comparisons. It is found that large prediction errors already occurred at the first cycle and propagated into the subsequent cycles. Notably, a systematic underestimation of capacity is observed for HE (see Fig. 6.5(b)), which can be rationalized by the fact that 2TM represents low-entropy DRX and cannot capture the improved performance arising from the novel high-entropy physics [28].

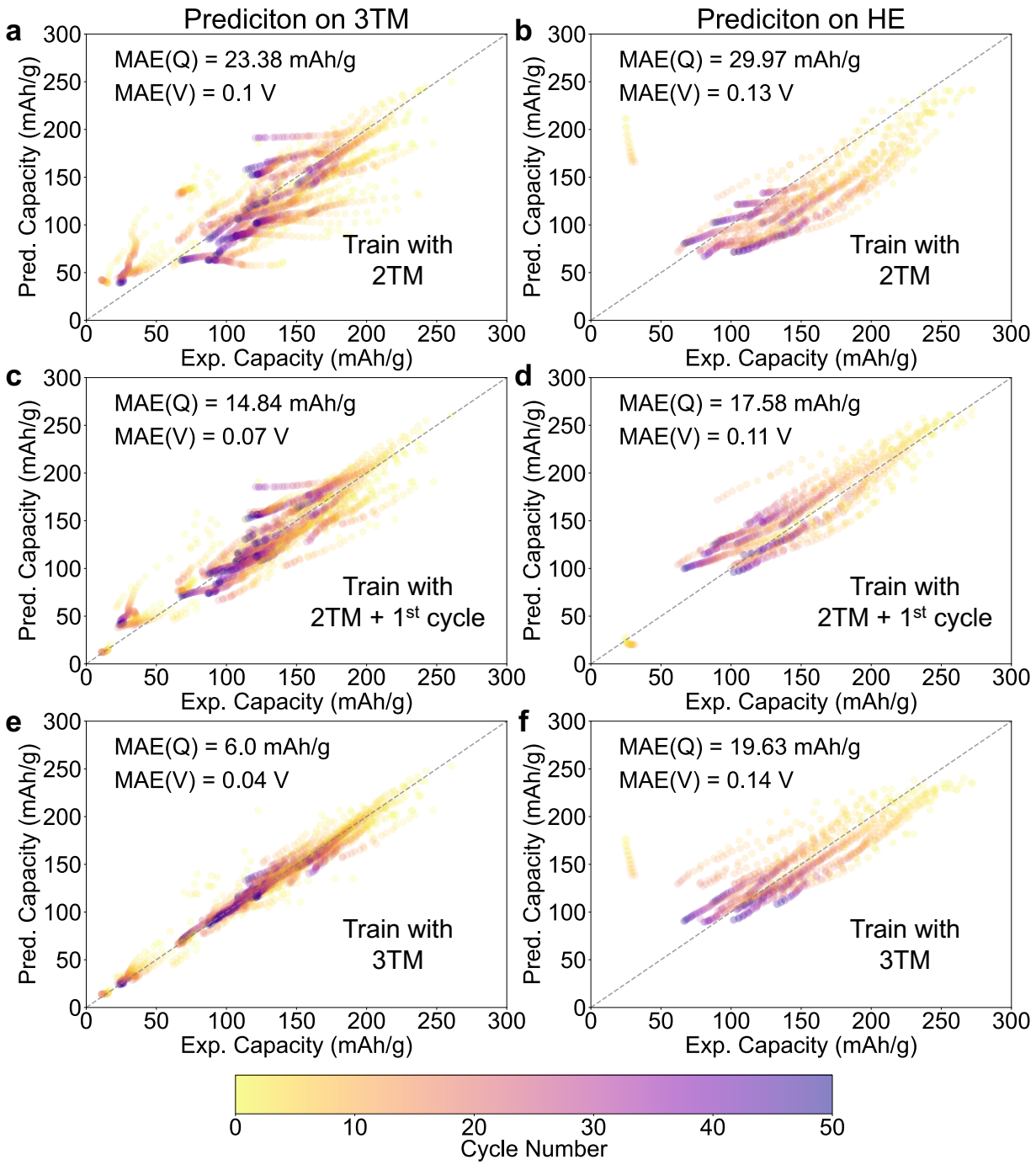

Figure 6.5: (a)–(b) Models are trained on DRX compositions with only two TM species (denoted as 2TM). The models are tested on predicting the delivered capacity between 2.0 and 4.4 V for DRXs composed of three metal species (denoted as 3TM) and higher components (denoted HE for high entropy). (c)–(d) Models are trained on a 2TM dataset along with the first cycles of 3TM and HE as corrected models. The corrected models are tested for subsequent cycles on 3TM and HE to assess the prediction error. (e)–(f) Models are trained on a 3TM dataset and tested on 3TM and HE dataset.

For practical applications, there are two approaches to improving the model's accuracy and enhancing its predictive capabilities: (1) new data points can be continuously collected as experiments progress, enabling on-the-fly training with in-situ data to improve predictive performance in data-scarce chemical space; and (2) incorporating a diverse range of information from chemical space and test conditions to deliver well-pretrained models. Regarding (1), this concept was tested by evaluating the improvement when DRXNet was trained on a dataset containing all 2TM data and was provided with the first cycle data from 3TM/HE materials. The knowledge of just the first cycle data reduced the capacity MAE from 23.38/29.97 mAh/g to 14.84/17.58 mAh/g for 3TM/HE. The enhanced performance achieved by explicitly training with the first cycle indicates that the model can better generalize cycling performance, even when experiments for a specific composition are not extensively sampled. This capability has the potential to significantly reduce the month-long timeframe typically required for electrochemical testing. Regarding (2), the results for models trained on the 3TM dataset are, where Fig. 6.5(e) displays the training errors (6.0 mAh/g), and the test error on the HE data is 19.63 mAh/g, reduced by 10 mAh/g from those trained on 2TM data.

To rationalize the improvement and assess the expressibility for extrapolation in untrained domains, the prediction error and model variance is examined as a function of cycle number (see Fig. 6.6). The standard deviation of the prediction from the ensemble of five DRXNet models (σ_Q) was used to represent the model variance as an approximation of how uncertain the predictions are. The 2TM model exhibited moderate model variance for 3TM predictions and high model variance for HE predictions (> 50 mAh/g) as shown in Fig. 6.6(a) and (b). Training the model with first-cycle data led to a substantial decrease in both the prediction error and model variance for the initial few cycles, although the model variance increased subsequently with the cycle number for untrained domains (see Fig. 6.6(c) and (d)).

It is important to note that the models trained on 3TM data show a significantly reduced prediction error and model variance for the HE prediction compared to those obtained when training the 2TM model (see Fig. 6.6(f)). This finding suggests that the 2TM dataset is inadequate for extracting relevant information and generalizing to other compositions. The scaling to high-component electrodes necessitates capturing more than 2TM correlations or interactions in training the graph neural network. Failure to do so may lead to systematic prediction errors, as demonstrated in Fig. 6.5(b). When the model is able to acquire sufficient chemical domain knowledge (e.g., 3TM-model), it becomes feasible to extrapolate the electrochemical properties of high-component electrodes.

6.5 Exploratory predictions in electrochemical spaces

The following sections will present several examples to illustrate how DRXNet learns the underlying cathode chemistry and assists in designing new materials. The models used for these applications are pretrained on all discharge profiles.

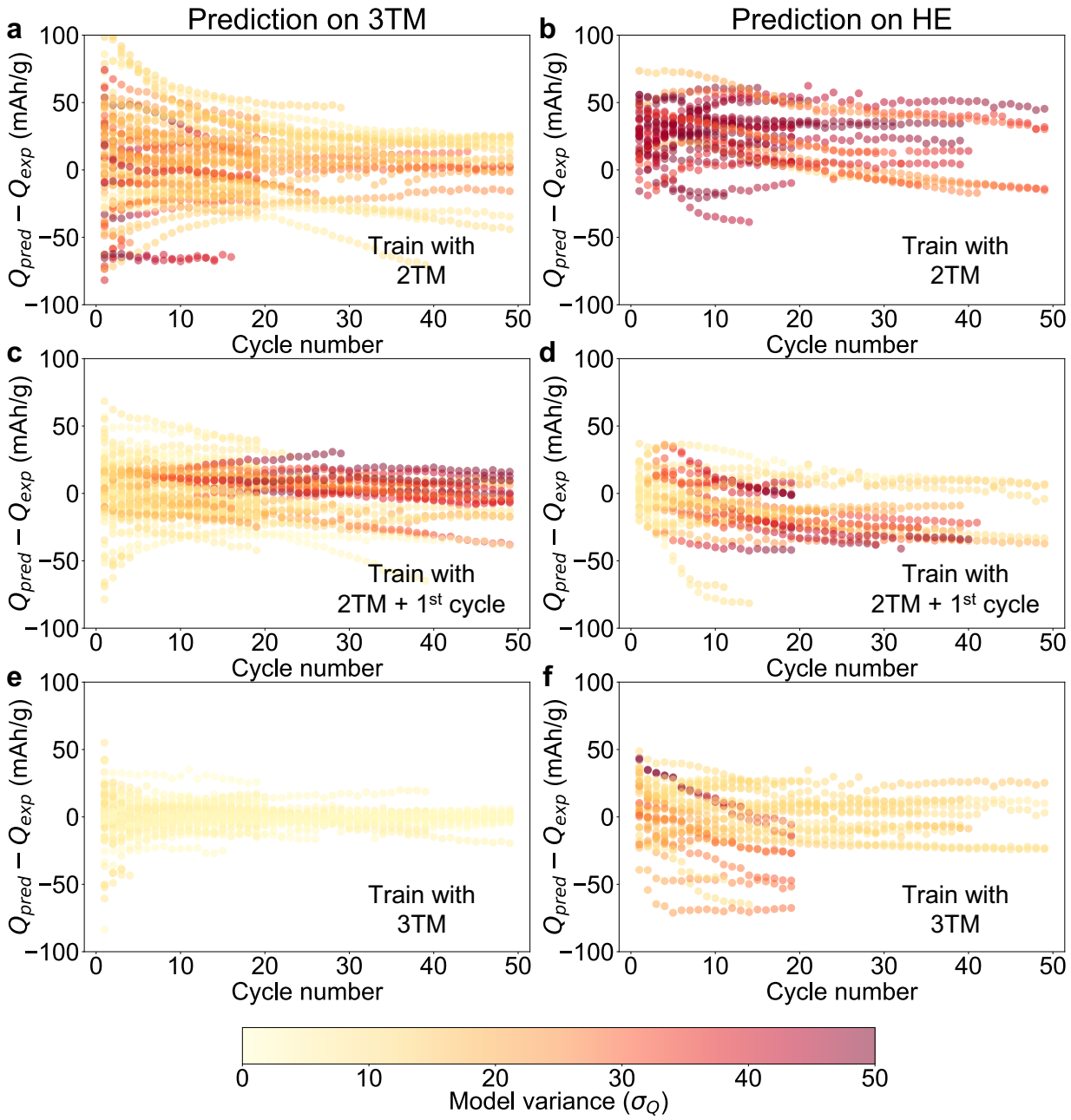

Figure 6.6: The prediction error of discharge capacity between 2.0 and 4.4 V (y-axis) *vs.* cycle number (x-axis). The model variance is represented by σ_Q, a standard deviation of the ensemble of the models' prediction, which is plotted as scaled colored dots. (a)–(b): Predictions on 3TM/HE using models trained on the 2TM dataset. (c)–(d): Predictions on 3TM/HE using models trained on both the 2TM dataset and the first cycles of the 3TM/HE dataset. (e)–(f): Predictions on 3TM/HE using models trained on the 3TM dataset.

6.5.1 Synergistic prediction in Li-Mn-O-F

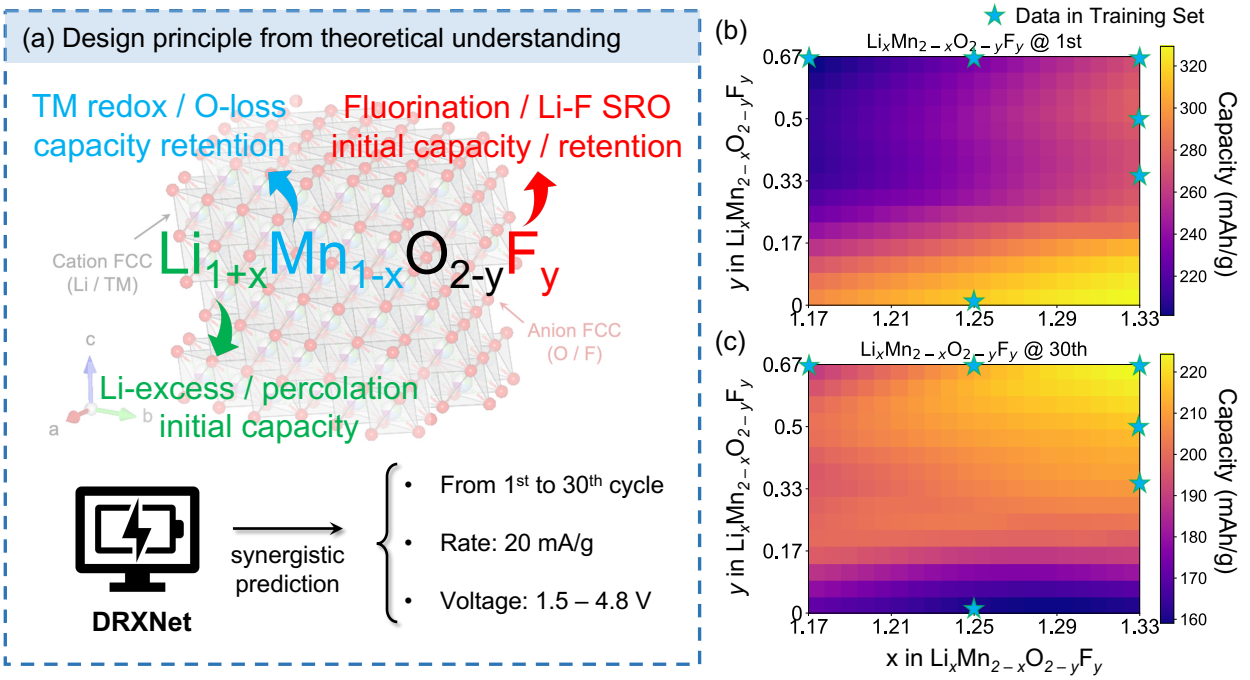

Figure 6.7: (A) Design principle from theory, where the Li/Mn/F content jointly determines the performance of battery materials (see Ref. [113]). (B) Prediction of discharge capacity for the 1st and 30th cycle in Li–Mn–O–F chemical space between 1.5 – 4.8 V at a current density rate of 20 mA/g, with the blue stars indicating the compositions included in the training set.

Manganese is an attractive earth-abundant, non-precious TM for next-generation cathode design [107]. Lun et al. [113] proposed three primary design degrees of freedom for Mn-based DRX (see Fig. 6.7(a)): (1) the Li-excess content, which controls the presence of a percolating network creating facile Li diffusion; (2) the Mn content, as low amounts of Mn can lead to severe oxygen redox and poor cyclability; and (3) the fluorine content, which lowers the total cation valence and provides greater freedom to optimize the Li and Mn content. Fluorine modifies cation short-range order through the strong Li–F attraction and lowers the initial capacity [114, 116]. These theoretical principles are highly correlated and exert non-linear effects on performance, making it challenging to predict.

DRXNet is used to predict the discharge capacity between 1.5 and 4.8 V at a current rate of 20 mA/g for the 1st and 30th cycles as a function of Li and F content, which is illustrated in Fig. 6.7(b). The amount and valence of Mn follow directly from the Li and F content. The critical feature of fluorine that has been extensively characterized experimentally is well

captured by the model. A higher F content (y in $O_{2-y}F_y$) results in a lower discharge capacity for the 1st cycle but a higher capacity for the 30th cycle. In particular, $Li_{1.333}Mn_{0.667}O_2$ is predicted to have the highest capacity ($>$ 320 mAh/g) for the first cycle but the lowest capacity for the 30th cycle. This prediction is consistent with the understanding the capacity originates from oxygen as the valence of Mn is 4+. Such a large amount of O-redox leads to rapid capacity fade and aligns with the experimental observations of disordered Li_2MnO_3 reported in Ref. [123].

To rationalize the extrapolation ability of DRXNet, Fig. 6.7(b) displays the compositions in the training dataset using blue stars. It is evident that despite the sparse distribution of training points across the composition map, DRXNet delivers accurate predictions that align with the experimental observations beyond the scope of the training points. As DRXNet is trained on various compositions beyond the Li–Mn–O–F chemical space, the ability to extrapolate to other domains can be attributed to the transfer learning from other F- and non-F-containing compounds. The example in this section demonstrates how practitioners can generalize the design principles from a data-driven perspective purely starting from experiments.

6.5.2 Exploratory search for high-entropy cathodes

High-entropy DRXs are composed of many species and present a vast chemical space to explore for battery materials discovery. To demonstrate the power of DRXNet, virtual high-throughput screening is conducted in the system with composition $Li_{1.2}A_{0.2}B_{0.3}Ti_{0.2}Nb_{0.1}O_{1.8}F_{0.2}$ (see Fig. 6.8), where A^{2+}/B^{3+} represent divalent/trivalent redox-active transition metals. Particularly, two compounds with both good discharge capacities and rate performances are selected:

- HE-1: $Li_{1.2}Mn_{0.1}Mg_{0.1}Cr_{0.3}Ti_{0.2}Nb_{0.1}O_{1.8}F_{0.2}$
- HE-2: $Li_{1.2}Mn_{0.1}Mg_{0.1}Cr_{0.15}V_{0.15}Ti_{0.2}Nb_{0.1}O_{1.8}F_{0.2}$

The predicted discharge profiles of HE-1/2 under various current densities are shown in Fig. 6.9.

For HE-1, DRXNet predicts a discharge capacity of 276 mAh/g at a low current rate of 20 mA/g. The discharge voltage profile shows a clear transition from a flat curve to a slopy curve after at around 3 V, which has been widely observed in Mn redox and/or Cr redox-based DRXs [28, 126, 227]. A capacity of 196 mAh/g is predicted at 1000 mA/g, retaining 71% of that delivered at a slow rate of 20 mA/g. From previous studies, multi-elemental substitution (i.e., high-entropy strategy) frustrates unfavorable SRO that leads to sluggish kinetics; Cr incorporation and Cr^{6+}-migration at high voltage upon delithiation opens up a better-extended 0-TM network for Li transport, both of which can improve the Li diffusion

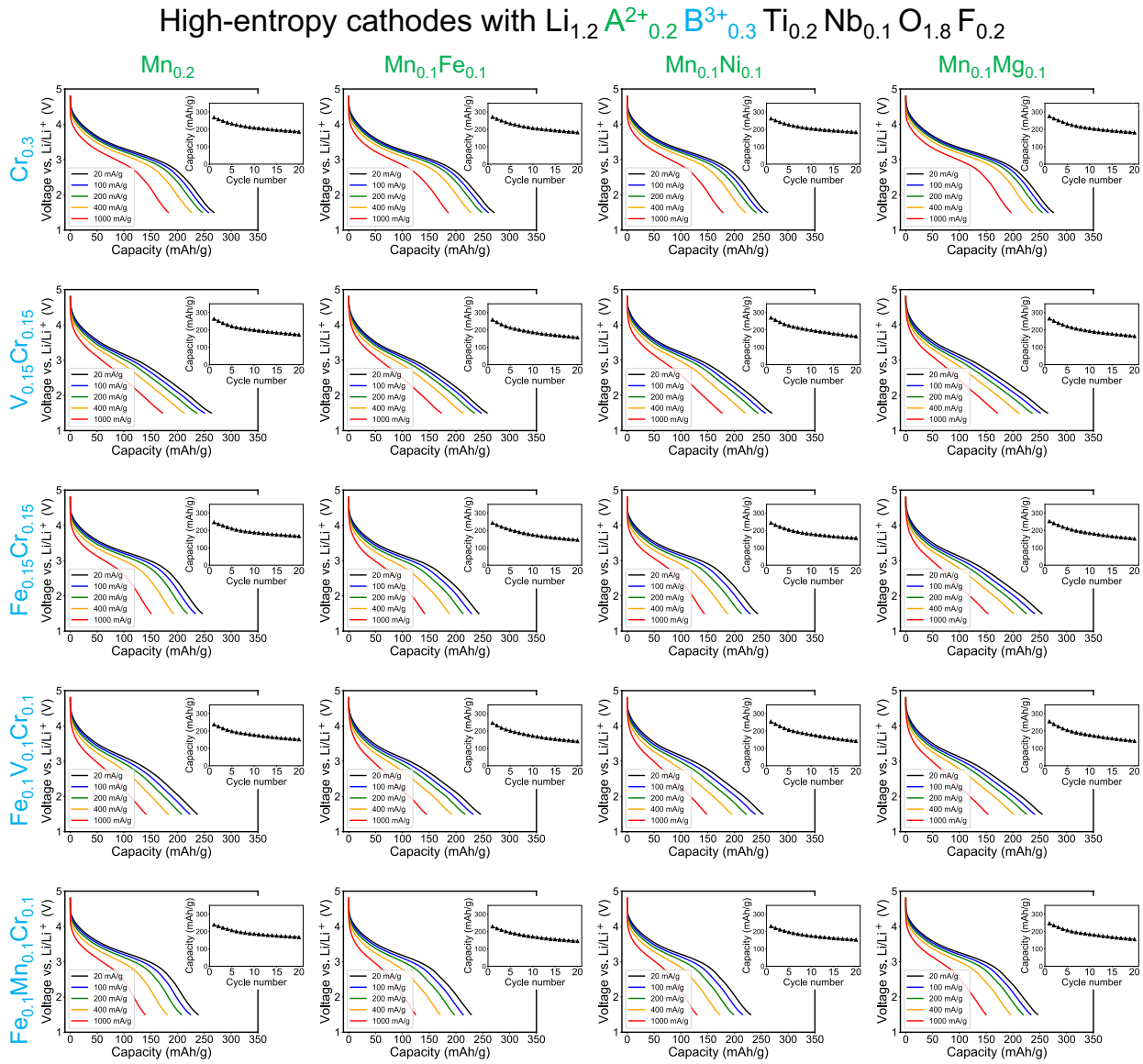

Figure 6.8: Design map for high-entropy DRX with composition in formula of $Li_{1.2}A_{0.2}B_{0.3}Ti_{0.2}Nb_{0.1}O_{1.8}F_{0.2}$ with the predicted electrochemical performance. The A^{2+}/B^{3+} represent divalent/trivalent redox-active transition metals. All compositions contain some Cr^{3+} and Mn^{2+}. The discharge profiles at various current density rates are displayed in distinct colors. Each profile plot's inset shows the cyclability performance, depicting capacity versus cycle number.

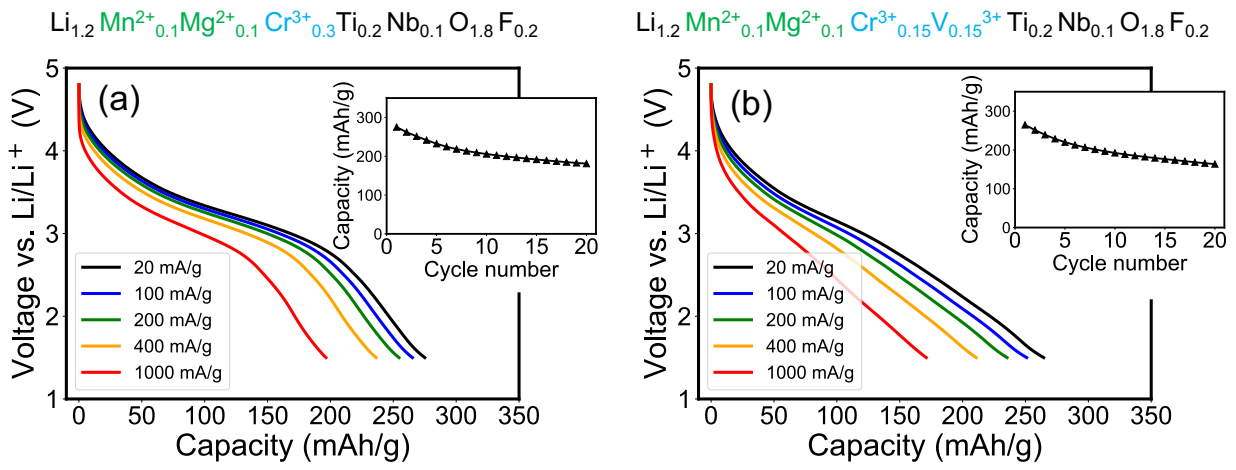

Figure 6.9: Predicted discharge profiles of two high-entropy DRX materials with various current density rates (from 20 mA/g to 1000 mA/g). (A) $Li_{1.2}Mn_{0.1}Mg_{0.1}Cr_{0.3}Ti_{0.2}Nb_{0.1}O_{1.8}F_{0.2}$ (HE-1) and (B) $Li_{1.2}Mn_{0.1}Mg_{0.1}Cr_{0.15}V_{0.15}Ti_{0.2}Nb_{0.1}O_{1.8}F_{0.2}$ (HE-2). The inset displays the cycled discharge capacity at a current density rate of 20 mA/g.

kinetics [28, 126]. DRXNet clearly learns those benefits and extrapolates rationally into electrochemistry prediction of the high-entropy compositions.

As a comparison, partial V^{3+} to Cr^{3+} substitution in HE-1, yielding HE-2 is expected to change the shape of the voltage curves dramatically due to the low potential of V^{5+}/V^{3+} reduction, which is also predicted using DRXNet as shown in Fig. 6.9(b). It is clearly demonstrated that with V^{3+} incorporation, a nearly constant slope can be observed down to the low-voltage region, which is characteristic for V-based DRX cathodes reported previously [110, 201]. Nevertheless, V^{5+} has a similar migration mechanism to enhance Li transport as Cr and is likely to be beneficial for the rate capability [201]. Consistently, although a slightly lower discharge capacity is predicted (266 mAh/g) for HE-2, it retains 171 mAh/g capacity at 1000 mA/g (64% of the capacity at 20 mA/g), which is better than the majority of the DRX cathodes reported to date.

In terms of cyclability, the inset plot shows the predicted discharge capacity of DRX materials within 20 cycles for both materials. A more dramatic capacity drop from the first 5 cycles is predicted, which slows down upon further cycling. This result is in full agreement with experimental findings, which indicate that some of the irreversibility in the initial cycles, such as surface carbonate decomposition [236] or cathode–electrolyte interface formation [237]. These examples illustrate how practitioners can effectively use DRXNet to navigate the extensive chemical space of high-entropy DRXs and identify promising candidates for cathode design and optimization.

Discussion on experimental conditions

The pursuit of carbon neutralization by optimizing the discovery and application of energy-storage materials using AI has long captivated materials scientists. Numerous efforts have been made in this area, and the Battery Data Genome is proposed as a potential breakthrough along with the fast development of AI technologies [217–220]. With this endeavor, it is proposed a deep learning approach for battery electrochemistry representation and learning from the experimental data. A machine-learning model (DRXNet) trained on over 30,000 experimental discharge voltage profiles is developed, encompassing diverse compositional chemistry in DRX cathodes. This was achieved through a novel model design consisting of an electrochemical condition network ($\mathcal{O}$) and a state prediction network ($\mathcal{F}$).

The design of the two networks promotes modularity in the architecture, streamlining the optimization and interpretation of each network individually and their learned features. For instance, the hierarchical network structure in $\mathcal{O}$ properly synthesizes the information from composition, rate, and cycle via soft attention. The feature of the N-th cycle is intrinsically embedded with the difference between the first cycle to learn the capacity change (see Eq. (6.10)). As highlighted in model training, the loss function is designed for multi-task learning. The first and N-th cycle capacities are trained simultaneously in each update, constructing contrastive terms to make the model informative of the cyclability rather than learning an average (see Eq. (6.15)).

In addition, the electrochemical condition network design provides flexibility in terms of model application. It is recognized that most training datasets are derived from the lab experimental results, which do not encompass critical testing parameters such as particle size, electrolyte type, electrode fabrication methods, etc. These factors have been coarsely integrated into the compositional model in the dataset. In principle, researchers can choose to include any factors to design the electrochemical feature vector, depending on the specific problem they are addressing. Given the vast amount and complexity of these properties, a synthetic data collection approach is necessary. Data-mining techniques, such as text mining and figure mining, can automatically retrieve valuable experimental information from decades of published literature [238, 239]. This has the potential to enhance the model's generalizability and incorporate extensive prior domain knowledge in electrochemical fields.

The depth and transferability of DRXNet's predictive capabilities for exploration are also discussed, especially for the state prediction network $\mathcal{F}$. The electrochemical performance of HE-2 is further tested by varying the voltage window and cycling rate, which are the parameters that typically require multiple individual electrochemical tests in experiments. Figure 6.10(a) displays the discharge profiles between 2.0 – 4.4 V, with two additional rates tested (10 mA/g for a low rate and 10^4 mA/g for an extremely high rate). These conditions are infrequently incorporated into the training data. The low rate exhibits a discharge profile very similar to 20 mA/g, which is entirely consistent with experimental findings, as the discharge process at a low rate exhibits a reduced overpotential. The 10 A/g rate discharge

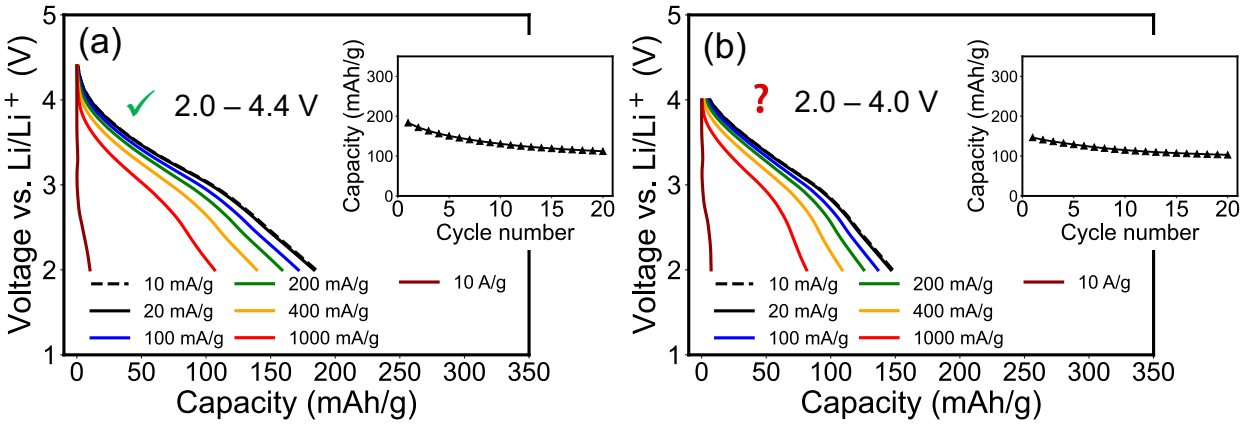

Figure 6.10: Predicted discharge profiles with various current density rates (from 10 mA/g to 10 A/g) of $Li_{1.2}Mn_{0.1}Mg_{0.1}Cr_{0.15}V_{0.15}Ti_{0.2}Nb_{0.1}O_{1.8}F_{0.2}$ (HE-2) between (a) 2.0 – 4.4 V and (b) 2.0 – 4.0 V. The inset displays the cycled discharge capacity at a current density rate of 20 mA/g.

profile demonstrates a sharp drop in voltage, reasonably indicating poor performance at an extremely high rate. In contrast, Fig. 6.10(b) presents the discharge profiles between 2.0 – 4.0 V, which starts to show some unphysical predictions. Small offsets appear at the beginning of discharge for the low rate profiles, resulting in a non-zero discharge capacity at 4.0 V. This discrepancy can be attributed to (1) the connection between voltage state V_i and window $[V_{\text{low}}, V_{\text{high}}]$ being achieved by linear combinations in the hidden layer (see Fig. 6.4(b)), which is a data-driven encoding and requires training; and (2) a limited number of experiments being conducted with V_{high} lower than 4.0 V, which leads to data scarcity in such voltage range. These two reasons may rationalize why the predictions for 2.0 – 4.4 V show better accuracy (no offsets) while the ones for 2.0 – 4.0 V deviate higher.

Based on the tests, the primary conclusion is that DRXNet exhibits a reasonable ability to learn chemical interactions and generalize to test conditions included in the dataset among different chemical compositions. However, for test conditions that the model has not encountered (e.g., experiments with $V_{\text{high}} < 4.0$ V), discrepancies or unphysical profiles may arise (e.g., non-zero capacity at the beginning). This highlights the data scarcity issue, which arises from human bias and outliers in experimental setups or poorly performing systems, as researchers may discontinue their discovery efforts when faced with unfavorable results [240]. In the future, automated labs can address this scarcity issue by enabling more extensive exploration of the experimental space (e.g., various voltage windows to find the optimal trade-off between energy density and cyclability, along with a combination of different current density rates), even for "failed" experiments [241]. This approach can result in a more comprehensive dataset for building machine-learning models and understanding the

electrochemical properties of battery materials.

6.6 Conclusion

This chapter describes a notable shift from the atomistic modeling discussed in previous chapters, presenting a significant step forward in applying artificial intelligence for battery materials research with the introduction of DRXNet. The core strength of DRXNet lies in its ability to extract and represent critical features (e.g., rate capability and cyclability) that are typically non-equilibrium and cannot be well derived from *ab-initio* modeling. Training on a substantial dataset of over 30,000 discharge voltage profiles across 14 different metal species, collected from experimental findings over the past five years, has empowered DRXNet with the capability to directly predict the electrochemical performance upon cycling under various conditions.

The first case study demonstrates how DRXNet can provide rational predictions of the discharge capacity for a wide range of compositions in the Li–Mn–O–F chemical space under cycled conditions. The direct prediction of the cycled discharge performance unveils the design principles of DRX in such chemical space, aligning well with reported literature informed by *ab-initio* calculations [113]. The second example underscores the power of DRXNet in its ability to conduct exploratory searches for high-entropy compositions under various rate and cycling conditions. Enabled by a universal training scheme across diverse chemistries, DRXNet proposes two high-entropy compounds as viable candidates for experimental validation. It is believed that the approach provides a data-driven solution for the fast identification of novel cathode materials, thereby accelerating the development of next-generation batteries for carbon neutrality. By continuously refining the model and incorporating additional data and parameters, such a machine-learning framework will play an increasingly critical role in the discovery and optimization of next-generation battery materials.

Chapter 7

Concluding remarks

7.1 Summary

The computational modeling of multicomponent disordered rocksalt cathodes (DRX) is a subject of great interest given the increasing need for efficient and sustainable energy storage applications. This thesis has addressed this timely topic through a combination of advanced computational techniques that cover a range of scales, from first-principles calculations to deep learning.

- Chapter 2 of this thesis explores the broad methodology for modeling thermodynamics in lattices from first principles. It demonstrates an effective use of density functional theory (DFT) and statistical mechanics to investigate complex oxides with substantial configurational disorder, such as disordered rocksalt cathodes. It introduces cluster expansion (CE) methods as effective Hamiltonians to approximate DFT for sampling equilibrium states via Monte Carlo (MC) simulation. Significantly contributing to this modeling methodology is incorporating $\ell_0\ell_2$-norm regularization and structural hierarchy constraints into linear regression for robust cluster expansion.
- Chapter 3 advances the understanding of DRX materials through the use of *ab-initio* calculation and CEMC for simulating short-range order (SRO). It discusses two approaches to optimize the SRO in DRX: (1) using Mg-doping to reduce the Li-F locking effect to improve Li capacity and (2) introducing partial Li deficiency to modify the overall cation-SRO to improve the Li transport kinetics. The examples highlight the importance of understanding the relationship between local structural orderings and electrochemical performance and demonstrate that CEMC is a natural way to simulate configurational thermodynamics, which is crucial in guiding the design of DRX materials and optimizing performance.
- Chapter 4 and 5 shift the discussion towards atomistic modeling incorporating charge information. Chapter 4 first introduces the background and foundation of two advanced

computational methodologies: (1) charge-decorated CE and (2) charge-informed machine learning interatomic potentials (MLIP). The importance of including charge information in the modeling process is highlighted, specifically for ionic materials.

- Chapter 5 discusses the application of the two methods to DRX systems. The equilibrium modeling sample showcases the application of charge-decorated CE for intercalation chemistry with multi-redox reactions in $Li_{1.3-x}Mn_{0.4}Nb_{0.3}O_{1.6}F_{0.4}$. It is demonstrated that using a sparse lattice model with $\ell_0\ell_2$-norm regularized regression and charge-neutral semigrand-canonical MC can adequately resolve the issue and sample the equilibrium states. Using CHGNet as a charge-informed interatomic potential, the second example illustrates how to approach the modeling o transition metal migration-induced phase transformation in $Li_{0.6}Mn_{0.8}Ti_{0.1}O_{1.9}F_{0.1}$. The insights obtained showcase the effects of structural ordering change on the electrochemical properties (e.g., the intercalation voltage profiles) and reveal the TM migration mechanism that is correlated with atomic charge states.

- Chapter 6 introduces another novel approach for modeling DRX materials via deep learning, where the electrochemical performance properties (discharge profiles) are directly represented and learned from experiments. The introduction of our comprehensive machine-learning model, DRXNet, demonstrates the power of artificial intelligence in extracting and representing critical features of battery materials. DRXNet can predict electrochemical performance under various cycling conditions, enabled through training on an extensive dataset of discharge voltage profiles from diverse metal species collected over five years. The examples in this chapter showcase the highlights of conducting exploratory searches for an extensive range of chemical spaces under various test conditions. The work with DRXNet ultimately provides a data-driven solution to identify novel cathode materials for next-generation battery applications.

7.2 Outlook on future directions

This thesis represents a concerted effort to advance simulation and learning methodologies for compositionally complex oxides, particularly on disordered rocksalt cathode materials. The works leverage the *ab-initio* calculations and statistical learning tools such as the cluster expansion method and machine learning to successfully model the thermodynamic and kinetic properties.

Future endeavors will undoubtedly continue to drive the development of computational methodologies to contribute to designing and optimizing energy materials. Here I present several directions, aiming to achieve comprehensive, efficient, and accurate computational modeling of energy materials at scale, which are posited as potentially fruitful avenues for exploration:

- While DFT-based modeling has demonstrated significant success for ground-state calculations in energy storage materials, the excited-state-related physics (e.g., optical absorption) of these materials remains less understood in modeling complex oxides. Techniques such as X-ray absorption spectroscopy (XAS) and resonant inelastic X-ray absorption spectroscopy (RIXS) play pivotal roles in characterizing and quantifying the oxidation states of elements, crucial to understanding charge transfer effects in cathodes [242]. Although there are several advanced electronic structure methods, such as the OCEAN package based on the Bethe-Salpeter-Equation (BSE) [243, 244], which have shown success in calculating these quantities of several battery cathode materials [245, 246], it is still not well known how to properly apply it to multicomponent oxides, as DRX materials typically require a large number of atoms to well represent the configurational disorder but the computational cost of GW-BSE can scale up to $\mathcal{O}(N^4)$ to $\mathcal{O}(N^6)$ depending on the computational task [247].

- The relevance of electronically excited states extends to their incorporation in statistical learning or machine learning models [248, 249]. Although the works presented in this thesis demonstrate that charge-decoration of species can represent charge states, this approach is typically effective when the electronic states are localized [58]. For a comprehensive description of interatomic potentials with electronic degrees of freedom, the charge information should serve as an input rather than an output regularization. Several studies have successfully addressed this issue by including charge or spin states from *ab-initio* calculations [250–252]. However, obstacles remain in the form of computational costs and a lack of large-scale datasets for training universal potentials for general materials design.

- Rethinking the approach to designing new functional materials for energy applications represents another fundamental trajectory. The design of energy materials has predominantly been property or phenomenologically guided to date, i.e., applying computational modeling to elucidate emergent phenomena and understand underlying mechanisms based on experimental observations. This process, which can often be implemented in a high-throughput way (termed forward design), has seen considerable success over the past decade [118]. However, there are vast structural, chemical, and configurational spaces that remain unexplored. Forward design is inherently an NP-hard approach, as enumeration-based algorithms are required to search the designing space. In contrast, inverse design, especially the score-based diffusion generative model [253], has emerged as a novel and essential tool for generating protein structures [254], molecules [255, 256], and crystal materials [257] via property-guided design [258]. The prospect of integrating the universal interatomic potential, statistical mechanics model (e.g., cluster expansion), and generative model to establish a closed-loop materials discovery framework [259] presents an intriguing avenue for exploration.

- Automated experiments and laboratories promise to revolutionize experimental discoveries within materials science [260, 261], which is particularly relevant to the future

evolution of DRXNet. As a performance-based prediction model, DRXNet may be influenced by human biases and discrepancies in experimental conditions, which can occur when researchers may halt discovery processes or neglect to record suboptimal results. Automated laboratories, however, can document nearly all aspects of experimentation, offering a comprehensive view of experimental conditions. This expanded perspective and design space can significantly enhance the representation and expressibility of future versions of DRXNet. The integration of an automated electrochemical laboratory could herald the arrival of a truly universal battery model.

To conclude, I hope the demonstrated progress in this thesis and the outlook on future directions benefit the computational modeling and materials science community for developing energy and sustainability technologies. I will continuously pursue solving the abovementioned challenges in my future career. Fiat Lux!

Bibliography

[1] N. S. Kardashev, "Transmission of information by extraterrestrial civilizations.", Soviet Astronomy **8**, 217 (1964).

[2] C Sagan, *The Cosmic Connection: An Extraterrestrial Perspective* (1973).

[3] "BP Statistical Review of World Energy 2023", 72$^{\text{st}}$ edition (2023).

[4] G. E. Blomgren, "The Development and Future of Lithium Ion Batteries", Journal of The Electrochemical Society **164**, A5019–A5025 (2017).

[5] J. B. Goodenough, "How we made the Li-ion rechargeable battery", Nature Electronics **1**, 204–204 (2018).

[6] J. B. Goodenough and K.-S. Park, "The Li-Ion Rechargeable Battery: A Perspective", Journal of the American Chemical Society **135**, 1167–1176 (2013).

[7] R. Fong and U. Von Sacken, "Studies of lithium intercalation into carbons using nonaqueous electrochemical cells", Journal of The Electrochemical Society **137**, 2009 (1990).

[8] M. T. McDowell, S. W. Lee, W. D. Nix, and Y. Cui, "25th anniversary article: understanding the lithiation of silicon and other alloying anodes for lithium-ion batteries", Advanced materials **25**, 4966–4985 (2013).

[9] T. R. Jow, K. Xu, O. Borodin, and M. Ue, *Electrolytes for lithium and lithium-ion batteries*, Vol. 58 (Springer, 2014).

[10] K. Mizushima, P. Jones, P. Wiseman, and J. Goodenough, "Li_xCoO_2 ($0 < x < 1$): A new cathode material for batteries of high energy density", Materials Research Bulletin **15**, 783–789 (1980).

[11] M. Thackeray, P. Johnson, L. de Picciotto, P. Bruce, and J. Goodenough, "Electrochemical extraction of lithium from $LiMn_2O_4$", Materials Research Bulletin **19**, 179–187 (1984).

[12] A. K. Padhi, K. S. Nanjundaswamy, and J. B. Goodenough, "Phospho-olivines as Positive-Electrode Materials for Rechargeable Lithium Batteries", Journal of The Electrochemical Society **144**, 1188–1194 (1997).

[13] E. A. Olivetti, G. Ceder, G. G. Gaustad, and X. Fu, "Lithium-Ion Battery Supply Chain Considerations: Analysis of Potential Bottlenecks in Critical Metals", Joule **1**, 229–243 (2017).

[14] R. J. Clément, Z. Lun, and G. Ceder, "Cation-disordered rocksalt transition metal oxides and oxyfluorides for high energy lithium-ion cathodes", Energy & Environmental Science **13**, 345–373 (2020).

[15] A. Urban, A. Abdellahi, S. Dacek, N. Artrith, and G. Ceder, "Electronic-Structure Origin of Cation Disorder in Transition-Metal Oxides", Physical Review Letters **119**, 1–6 (2017).

[16] W. D. Richards, S. T. Dacek, D. A. Kitchaev, and G. Ceder, "Fluorination of Lithium-Excess Transition Metal Oxide Cathode Materials", Advanced Energy Materials **8**, 1701533 (2018).

[17] H. Ji, A. Urban, D. A. Kitchaev, D.-H. Kwon, N. Artrith, C. Ophus, W. Huang, Z. Cai, T. Shi, J. C. Kim, H. Kim, and G. Ceder, "Hidden structural and chemical order controls lithium transport in cation-disordered oxides for rechargeable batteries", Nature Communications **10**, 592 (2019).

[18] Z. Lun, B. Ouyang, D. A. Kitchaev, R. J. Clément, J. K. Papp, M. Balasubramanian, Y. Tian, T. Lei, T. Shi, B. D. McCloskey, J. Lee, and G. Ceder, "Improved Cycling Performance of Li-Excess Cation-Disordered Cathode Materials upon Fluorine Substitution", Advanced Energy Materials **9**, 1802959 (2019).

[19] J. Huang, P. Zhong, Y. Ha, Z. Lun, Y. Tian, M. Balasubramanian, W. Yang, and G. Ceder, "Oxygen Vacancy Introduction to Increase the Capacity and Voltage Retention in Li-Excess Cathode Materials", Small Structures **4**, 2200343 (2023).

[20] L. Huang, P. Zhong, Y. Ha, Z. Cai, Y. Byeon, T. Huang, Y. Sun, F. Xie, H. Hau, H. Kim, M. Balasubramanian, B. D. McCloskey, W. Yang, and G. Ceder, "Optimizing Li-Excess Cation-Disordered Rocksalt Cathode Design Through Partial Li Deficiency", Advanced Energy Materials **13**, 2202345 (2023).

[21] R. Zhang, C. Wang, P. Zou, R. Lin, L. Ma, L. Yin, T. Li, W. Xu, H. Jia, Q. Li, S. Sainio, K. Kisslinger, S. E. Trask, S. N. Ehrlich, Y. Yang, A. M. Kiss, M. Ge, B. J. Polzin, S. J. Lee, W. Xu, Y. Ren, and H. L. Xin, "Compositionally complex doping for zero-strain zero-cobalt layered cathodes", Nature **610**, 67–73 (2022).

[22] K. Zhou, Y. Li, Y. Ha, M. Zhang, W. Dachraoui, H. Liu, C. Zhang, X. Liu, F. Liu, C. Battaglia, W. Yang, J. Liu, and Y. Yang, "A Nearly Zero-Strain Li-Rich Rock-Salt Oxide with Multielectron Redox Reactions as a Cathode for Li-Ion Batteries", Chemistry of Materials **34**, 9711–9721 (2022).

[23] X. Zhao, Y. Tian, Z. Lun, Z. Cai, T. Chen, B. Ouyang, and G. Ceder, "Design principles for zero-strain Li-ion cathodes", Joule **6**, 1654–1671 (2022).

[24] A. Van der Ven, Z. Deng, S. Banerjee, and S. P. Ong, "Rechargeable Alkali-Ion Battery Materials: Theory and Computation", Chemical Reviews **120**, 6977–7019 (2020).

[25] J. Lee, A. Urban, X. Li, D. Su, G. Hautier, and G. Ceder, "Unlocking the Potential of Cation-Disordered Oxides for Rechargeable Lithium Batteries", Science **343**, 519–522 (2014).

[26] H. Ji, J. Wu, Z. Cai, J. Liu, D. H. Kwon, H. Kim, A. Urban, J. K. Papp, E. Foley, Y. Tian, M. Balasubramanian, H. Kim, R. J. Clément, B. D. McCloskey, W. Yang, and G. Ceder, "Ultrahigh power and energy density in partially ordered lithium-ion cathode materials", Nature Energy **5**, 213–221 (2020).

[27] Z. Cai, H. Ji, Y. Ha, J. Liu, D.-H. Kwon, Y. Zhang, A. Urban, E. E. Foley, R. Giovine, H. Kim, Z. Lun, T.-Y. Huang, G. Zeng, Y. Chen, J. Wang, B. D. McCloskey, M. Balasubramanian, R. J. Clément, W. Yang, and G. Ceder, "Realizing continuous cation order-to-disorder tuning in a class of high-energy spinel-type Li-ion cathodes", Matter **4**, 3897–3916 (2021).

[28] Z. Lun, B. Ouyang, D.-h. Kwon, Y. Ha, E. E. Foley, T.-Y. Huang, Z. Cai, H. Kim, M. Balasubramanian, Y. Sun, J. Huang, Y. Tian, H. Kim, B. D. McCloskey, W. Yang, R. J. Clément, H. Ji, and G. Ceder, "Cation-disordered rocksalt-type high-entropy cathodes for Li-ion batteries", Nature Materials **20**, 214–221 (2021).

[29] B. Key, M. Morcrette, J.-M. Tarascon, and C. P. Grey, "Pair Distribution Function Analysis and Solid State NMR Studies of Silicon Electrodes for Lithium Ion Batteries: Understanding the (De)lithiation Mechanisms", Journal of the American Chemical Society **133**, 503–512 (2011).

[30] L. Li, Z. Lun, D. Chen, Y. Yue, W. Tong, G. Chen, G. Ceder, and C. Wang, "Fluorination-Enhanced Surface Stability of Cation-Disordered Rocksalt Cathodes for Li-Ion Batteries", Advanced Functional Materials **31**, 2101888 (2021).

[31] R. J. Clément, D. Kitchaev, J. Lee, and Gerbrand Ceder, "Short-Range Order and Unusual Modes of Nickel Redox in a Fluorine-Substituted Disordered Rocksalt Oxide Lithium-Ion Cathode", Chemistry of Materials **30**, 6945–6956 (2018).

[32] A. Ferrari, F. Körmann, M. Asta, and J. Neugebauer, "Simulating short-range order in compositionally complex materials", Nature Computational Science **3**, 221–229 (2023).

[33] L. Wang, T. Maxisch, and G. Ceder, "Oxidation energies of transition metal oxides within the GGA+U framework", Physical Review B **73**, 195107 (2006).

[34] J. Sun, A. Ruzsinszky, and J. P. Perdew, "Strongly Constrained and Appropriately Normed Semilocal Density Functional", Physical Review Letters **115**, 036402 (2015).

[35] B. Deng, "Application and challenges of computational simulation in lithium battery materials research and development – a perspective from the industry", Online presentation (in Chinese).

[36] R. M. Martin, *Electronic structure: basic theory and practical methods* (Cambridge University Press, 2020).

[37] J. P. Perdew, A. Ruzsinszky, L. A. Constantin, J. Sun, and G. I. Csonka, "Some Fundamental Issues in Ground-State Density Functional Theory: A Guide for the Perplexed", Journal of Chemical Theory and Computation **5**, 902–908 (2009).

[38] W. Kohn and L. J. Sham, "Self-Consistent Equations Including Exchange and Correlation Effects", Physical Review **140**, A1133–A1138 (1965).

[39] J. P. Perdew, K. Burke, and M. Ernzerhof, "Generalized Gradient Approximation Made Simple", Physical Review Letters **77**, 3865–3868 (1996).

[40] V. L. Chevrier, S. P. Ong, R. Armiento, M. K. Y. Chan, and G. Ceder, "Hybrid density functional calculations of redox potentials and formation energies of transition metal compounds", Physical Review B **82**, 075122 (2010).

[41] F. Zhou, M. Cococcioni, C. A. Marianetti, D. Morgan, and G. Ceder, "First-principles prediction of redox potentials in transition-metal compounds with LDA+U", Physical Review B **70**, 235121 (2004).

[42] M. Cococcioni and S. de Gironcoli, "Linear response approach to the calculation of the effective interaction parameters in the LDA+U method", Physical Review B **71**, 035105 (2005).

[43] A. Jain, G. Hautier, S. P. Ong, C. J. Moore, C. C. Fischer, K. A. Persson, and G. Ceder, "Formation enthalpies by mixing GGA and GGA+U calculations", Physical Review B **84**, 045115 (2011).

[44] I. Timrov, F. Aquilante, M. Cococcioni, and N. Marzari, "Accurate Electronic Properties and Intercalation Voltages of Olivine-Type Li-Ion Cathode Materials from Extended Hubbard Functionals", PRX Energy **1**, 033003 (2022).

[45] G. C. Moore, M. K. Horton, A. M. Ganose, M. Siron, E. Linscott, D. D. O'Regan, and K. A. Persson, "High-throughput determination of hubbard u and hund j values for transition metal oxides via linear response formalism", arXiv preprint arXiv:2201.04213 (2022).

[46] J. Paier, M. Marsman, K. Hummer, G. Kresse, I. C. Gerber, and J. G. Ángyán, "Screened hybrid density functionals applied to solids", The Journal of Chemical Physics **124**, 154709 (2006).

[47] M. Kothakonda, A. D. Kaplan, E. B. Isaacs, C. J. Bartel, J. W. Furness, J. Ning, C. Wolverton, J. P. Perdew, and J. Sun, "Testing the r^{2}SCAN Density Functional for the Thermodynamic Stability of Solids with and without a van der Waals Correction", ACS Materials Au **3**, 102–111 (2023).

[48] Y. Zhang, D. A. Kitchaev, J. Yang, T. Chen, S. T. Dacek, R. A. Sarmiento-Pérez, M. A. L. Marques, H. Peng, G. Ceder, J. P. Perdew, and J. Sun, "Efficient first-principles prediction of solid stability: Towards chemical accuracy", npj Computational Materials **4**, 9 (2018).

[49] J. H. Yang, D. A. Kitchaev, and G. Ceder, "Rationalizing accurate structure prediction in the meta-GGA SCAN functional", Physical Review B **100**, 035132 (2019).

[50] D. Chandler, *Introduction to modern statistical mechanics* (1987).

[51] G. Ceder, "A derivation of the Ising model for the computation of phase diagrams", Computational Materials Science **1**, 144–150 (1993).

[52] G. D. Garbulsky and G. Ceder, "Effect of lattice vibrations on the ordering tendencies in substitutional binary alloys", Physical Review B **49**, 6327–6330 (1994).

[53] G. D. Garbulsky, "Ground-state structure and vibrational free energy in first-principles models of subsitutional-alloy thermodynamics", PhD thesis (Massachusetts Institute of Technology, 1996).

[54] A. Van der Ven, "First Principles Investigation of the Thermodynamic and Kinetic Properties of Lithium Transition Metal Oxides", PhD thesis (Massachusetts Institute of Technology, 2000).

[55] V. Ozoliņš, C Wolverton, and A. Zunger, "Cu-Au, Ag-Au, Cu-Ag, and Ni-Au intermetallics: First-principles study of temperature-composition phase diagrams and structures", Physical Review B **57**, 6427–6443 (1998).

[56] G. D. Garbulsky and G. Ceder, "Effect of lattice vibrations on the ordering tendencies in substitutional binary alloys", Physical Review B **49**, 6327–6330 (1994).

[57] G. Ceder and A. Van Der Ven, "Phase diagrams of lithium transition metal oxides: investigations from first principles", Electrochimica Acta **45**, 131–150 (1999).

[58] F. Zhou, T. Maxisch, and G. Ceder, "Configurational Electronic Entropy and the Phase Diagram of Mixed-Valence Oxides: The Case of Li_xFePO_4", Physical Review Letters **97**, 155704 (2006).

[59] N. Metropolis, A. W. Rosenbluth, M. N. Rosenbluth, A. H. Teller, and E. Teller, "Equation of state calculations by fast computing machines", The Journal of Chemical Physics **21**, 1087–1092 (1953).

[60] W. K. Hastings, "Monte carlo sampling methods using markov chains and their applications", (1970).

[61] F. Xie, P. Zhong, L. Barroso-Luque, B. Ouyang, and G. Ceder, "Semigrand-canonical Monte-Carlo simulation methods for charge-decorated cluster expansions", Computational Materials Science **218**, 112000 (2023).

[62] Z. Deng, T. P. Mishra, W. Xie, D. A. Saeed, G. S. Gautam, and P. Canepa, "Kmcpy: a python package to simulate transport properties in solids with kinetic monte carlo", chemRxiv (2022).

[63] L. Barroso-Luque, P. Zhong, J. H. Yang, F. Xie, T. Chen, B. Ouyang, and G. Ceder, "Cluster expansions of multicomponent ionic materials: Formalism and methodology", Physical Review B **106**, 144202 (2022).

[64] J.-Z. Xie, X.-Y. Zhou, and H. Jiang, "Perspective on optimal strategies of building cluster expansion models for configurationally disordered materials", The Journal of Chemical Physics **157**, 200901 (2022).

[65] M. Ångqvist, W. A. Muñoz, J. M. Rahm, E. Fransson, C. Durniak, P. Rozyczko, T. H. Rod, and P. Erhart, "ICET – A Python Library for Constructing and Sampling Alloy Cluster Expansions", Advanced Theory and Simulations **2**, 1900015 (2019).

[66] J. Sanchez, F. Ducastelle, and D. Gratias, "Generalized cluster description of multicomponent systems", Physica A: Statistical Mechanics and its Applications **128**, 334–350 (1984).

[67] J. M. Sanchez, "Renormalized interactions in truncated cluster expansions", Physical Review B **99**, 134206 (2019).

[68] P. D. Tepesch, G. D. Garbulsky, and G. Ceder, "Model for Configurational Thermodynamics in Ionic Systems", Physical Review Letters **74**, 2272–2275 (1995).

[69] A. Seko, Y. Koyama, and I. Tanaka, "Cluster expansion method for multicomponent systems based on optimal selection of structures for density-functional theory calculations", Physical Review B **80**, 165122 (2009).

[70] X. Zhang and M. H. F. Sluiter, "Cluster Expansions for Thermodynamics and Kinetics of Multicomponent Alloys", Journal of Phase Equilibria and Diffusion **37**, 44–52 (2016).

[71] L. Barroso-Luque, J. H. Yang, and G. Ceder, "Sparse expansions of multicomponent oxide configuration energy using coherency and redundancy", Physical Review B **104**, 224203 (2021).

[72] A. van de Walle, "Multicomponent multisublattice alloys, nonconfigurational entropy and other additions to the Alloy Theoretic Automated Toolkit", Calphad **33**, 266–278 (2009).

[73] W. Huang, D. A. Kitchaev, S. T. Dacek, Z. Rong, A. Urban, S. Cao, C. Luo, and G. Ceder, "Finding and proving the exact ground state of a generalized Ising model by convex optimization and MAX-SAT", Physical Review B **94**, 1–12 (2016).

[74] S. P. Ong, W. D. Richards, A. Jain, G. Hautier, M. Kocher, S. Cholia, D. Gunter, V. L. Chevrier, K. A. Persson, and G. Ceder, "Python Materials Genomics (pymatgen): A robust, open-source python library for materials analysis", Computational Materials Science **68**, 314–319 (2013).

[75] L. J. Nelson, G. L. W. Hart, F. Zhou, and V. Ozoliņš, "Compressive sensing as a paradigm for building physics models", Physical Review B **87**, 035125 (2013).

[76] A. Walle and G. Ceder, "Automating first-principles phase diagram calculations", Journal of Phase Equilibria **23**, 348–359 (2002).

[77] T. Mueller and G. Ceder, "Exact expressions for structure selection in cluster expansions", Physical Review B **82**, 184107 (2010).

[78] T. Mueller and G. Ceder, "Bayesian approach to cluster expansions", Physical Review B **80**, 024103 (2009).

[79] J. J. Faraway, *Linear Models with Python* (CRC Press, Jan. 2021).

[80] P. Drineas, M. Magdon-Ismail, M. W. Mahoney, and D. P. Woodruff, "Fast approximation of matrix coherence and statistical leverage", The Journal of Machine Learning Research **13**, 3475–3506 (2012).

[81] E. J. Candes and M. B. Wakin, "An introduction to compressive sampling: A sensing/sampling paradigm that goes against the common knowledge in data acquisition", IEEE Signal Processing Magazine **25**, 21–30 (2008).

[82] Z. Leong and T. L. Tan, "Robust cluster expansion of multicomponent systems using structured sparsity", Physical Review B **100**, 1–8 (2019).

[83] P. Zhong, T. Chen, L. Barroso-Luque, F. Xie, and G. Ceder, "An $\ell_0\ell_2$-norm regularized regression model for construction of robust cluster expansions in multicomponent systems", Physical Review B **106**, 024203 (2022).

[84] D. B. Laks, L. G. Ferreira, S. Froyen, and A. Zunger, "Efficient cluster expansion for substitutional systems", Physical Review B **46**, 12587–12605 (1992).

[85] V. Blum and A. Zunger, "Mixed-basis cluster expansion for thermodynamics of bcc alloys", Physical Review B **70**, 155108 (2004).

[86] L. J. Nelson, V. Ozoliņš, C. S. Reese, F. Zhou, and G. L. W. Hart, "Cluster expansion made easy with Bayesian compressive sensing", Physical Review B **88**, 155105 (2013).

[87] E. Cockayne and A. van de Walle, "Building effective models from sparse but precise data: application to an alloy cluster expansion model", Physical Review B **81**, 012104 (2010).

[88] M. Elad, "Pursuit Algorithms – Practice", in *Sparse and Redundant Representations: From Theory to Applications in Signal and Image Processing*, edited by M. Elad (Springer, New York, NY, 2010), pages 35–54.

[89] W. Huang, A. Urban, P. Xiao, Z. Rong, H. Das, T. Chen, N. Artrith, A. Toumar, and G. Ceder, "An L_0L_1-norm compressive sensing paradigm for the construction of sparse predictive lattice models using mixed integer quadratic programming", arXiv:1807.10753 (2018).

[90] Gurobi Optimization, LLC, *Gurobi Optimizer Reference Manual*, 2021.

[91] M. H. F. Sluiter and Y. Kawazoe, "Invariance of truncated cluster expansions for first-principles alloy thermodynamics", Physical Review B **71**, 212201 (2005).

[92] N. A. Zarkevich and D. D. Johnson, "Reliable first-principles alloy thermodynamics via truncated cluster expansions", Physical Review Letters **92**, 255702 (2004).

[93] R. Tibshirani, "Regression Shrinkage and Selection Via the Lasso", Journal of the Royal Statistical Society: Series B (Methodological) **58**, 267–288 (1996).

[94] A. Seko and I. Tanaka, "Cluster expansion of multicomponent ionic systems with controlled accuracy: importance of long-range interactions in heterovalent ionic systems", Journal of Physics: Condensed Matter **26**, 115403 (2014).

[95] G. Kresse and J. Furthmüller, "Efficiency of ab-initio total energy calculations for metals and semiconductors using a plane-wave basis set", Computational Materials Science **6**, 15–50 (1996).

[96] G. Kresse and D. Joubert, "From ultrasoft pseudopotentials to the projector augmented-wave method", Physical Review B **59**, 1758–1775 (1999).

[97] C. J. Bartel, A. Trewartha, Q. Wang, A. Dunn, A. Jain, and G. Ceder, "A critical examination of compound stability predictions from machine-learned formation energies", npj Computational Materials **6**, 97 (2020).

[98] A. Urban, D.-H. Seo, and G. Ceder, "Computational understanding of Li-ion batteries", npj Computational Materials **2**, 16002 (2016).

[99] W. Huang, A. Urban, Z. Rong, Z. Ding, C. Luo, and G. Ceder, "Construction of ground-state preserving sparse lattice models for predictive materials simulations", npj Computational Materials **3**, 30 (2017).

[100] A. Van der Ven, J. Bhattacharya, and A. A. Belak, "Understanding Li Diffusion in Li-Intercalation Compounds", Accounts of Chemical Research **46**, 1216–1225 (2013).

[101] M Obrovac, "Structure and electrochemistry of $LiMO_2$ (M=Ti, Mn, Fe, Co, Ni) prepared by mechanochemical synthesis", Solid State Ionics **112**, 9–19 (1998).

[102] A. Urban, J. Lee, and G. Ceder, "The configurational space of rocksalt-type oxides for high-capacity lithium battery electrodes", Advanced Energy Materials **4**, 1–9 (2014).

[103] J. Lee, D.-H. H. Seo, M. Balasubramanian, N. Twu, X. Li, and G. Ceder, "A new class of high capacity cation-disordered oxides for rechargeable lithium batteries: Li-Ni-Ti-Mo oxides", Energy & Environmental Science **8**, 3255–3265 (2015).

[104] N. Yabuuchi, M. Takeuchi, M. Nakayama, H. Shiiba, M. Ogawa, K. Nakayama, T. Ohta, D. Endo, T. Ozaki, T. Inamasu, K. Sato, and S. Komaba, "High-capacity electrode materials for rechargeable lithium batteries: Li_3NbO_4-based system with cation-disordered rocksalt structure", Proceedings of the National Academy of Sciences **112**, 7650–7655 (2015).

[105] N. Yabuuchi, M. Nakayama, M. Takeuchi, S. Komaba, Y. Hashimoto, T. Mukai, H. Shiiba, K. Sato, Y. Kobayashi, A. Nakao, M. Yonemura, K. Yamanaka, K. Mitsuhara, and T. Ohta, "Origin of stabilization and destabilization in solid-state redox reaction of oxide ions for lithium-ion batteries", Nature Communications **7**, 1–10 (2016).

[106] D. Chen, W. H. Kan, and G. Chen, "Understanding Performance Degradation in Cation-Disordered Rock-Salt Oxide Cathodes", Advanced Energy Materials **9**, 1–15 (2019).

[107] J. Lee, D. A. Kitchaev, D.-H. Kwon, C.-W. Lee, J. K. Papp, Y.-S. Liu, Z. Lun, R. J. Clément, T. Shi, B. D. McCloskey, J. Guo, M. Balasubramanian, and G. Ceder, "Reversible Mn^{2+}/Mn^{4+} double redox in lithium-excess cathode materials", Nature **556**, 185–190 (2018).

[108] S. Ren, R. Chen, E. Maawad, O. Dolotko, A. A. Guda, V. Shapovalov, D. Wang, H. Hahn, and M. Fichtner, "Improved Voltage and Cycling for Li^+ Intercalation in High-Capacity Disordered Oxyfluoride Cathodes", Advanced Science **2**, 1500128 (2015).

[109] C. Baur, I. Källquist, J. Chable, J. H. Chang, R. E. Johnsen, F. Ruiz-Zepeda, J.-M. Ateba Mba, A. J. Naylor, J. M. Garcia-Lastra, T. Vegge, F. Klein, A. R. Schür, P. Norby, K. Edström, M. Hahlin, and M. Fichtner, "Improved cycling stability in high-capacity Li-rich vanadium containing disordered rock salt oxyfluoride cathodes", Journal of Materials Chemistry A **7**, 21244–21253 (2019).

[110] R. Chen, S. Ren, M. Knapp, D. Wang, R. Witter, M. Fichtner, and H. Hahn, "Disordered Lithium-Rich Oxyfluoride as a Stable Host for Enhanced Li + Intercalation Storage", Advanced Energy Materials **5**, 1401814 (2015).

[111] J. Lee, J. K. Papp, R. J. Clément, S. Sallis, D.-H. Kwon, T. Shi, W. Yang, B. D. McCloskey, and G. Ceder, "Mitigating oxygen loss to improve the cycling performance of high capacity cation-disordered cathode materials", Nature Communications **8**, 981 (2017).

[112] R. A. House, L. Jin, U. Maitra, K. Tsuruta, J. W. Somerville, D. P. Förstermann, F. Massel, L. Duda, M. R. Roberts, and P. G. Bruce, "Lithium manganese oxyfluoride as a new cathode material exhibiting oxygen redox", Energy & Environmental Science **11**, 926–932 (2018).

[113] Z. Lun, B. Ouyang, Z. Cai, R. J. Clément, D.-H. Kwon, J. Huang, J. K. Papp, M. Balasubramanian, Y. Tian, B. D. McCloskey, H. Ji, H. Kim, D. A. Kitchaev, and G. Ceder, "Design Principles for High-Capacity Mn-Based Cation-Disordered Rocksalt Cathodes", Chem **6**, 153–168 (2020).

[114] P. Zhong, Z. Cai, Y. Zhang, R. Giovine, B. Ouyang, G. Zeng, Y. Chen, R. Clément, Z. Lun, and G. Ceder, "Increasing Capacity in Disordered Rocksalt Cathodes by Mg Doping", Chemistry of Materials **32**, 10728–10736 (2020).

[115] N. Mozhzhukhina, J. Kullgren, C. Baur, O. Gustafsson, W. R. Brant, M. Fichtner, and D. Brandell, "Short-range ordering in the Li-rich disordered rock salt cathode material Li_2VO2F revealed by Raman spectroscopy", Journal of Raman Spectroscopy **51**, 2095–2101 (2020).

[116] B. Ouyang, N. Artrith, Z. Lun, Z. Jadidi, D. A. Kitchaev, H. Ji, A. Urban, and G. Ceder, "Effect of Fluorination on Lithium Transport and Short-Range Order in Disordered-Rocksalt-Type Lithium-Ion Battery Cathodes", Advanced Energy Materials **10**, 1903240 (2020).

[117] D. A. Kitchaev, Z. Lun, W. D. Richards, H. Ji, R. J. Clément, M. Balasubramanian, D. H. Kwon, K. Dai, J. K. Papp, T. Lei, B. D. McCloskey, W. Yang, J. Lee, and G. Ceder, "Design principles for high transition metal capacity in disordered rocksalt Li-ion cathodes", Energy and Environmental Science **11**, 2159–2171 (2018).

[118] A. Jain, S. P. Ong, G. Hautier, W. Chen, W. D. Richards, S. Dacek, S. Cholia, D. Gunter, D. Skinner, G. Ceder, and K. A. Persson, "Commentary: The Materials Project: A materials genome approach to accelerating materials innovation", APL Materials **1**, 011002 (2013).

[119] "On the Theory of Super-Lattice Structures in Alloys", Zeitschrift für Kristallographie - Crystalline Materials **91**, 23–47 (1935).

[120] R. D. Shannon, "Revised effective ionic radii and systematic studies of interatomic distances in halides and chalcogenides", Acta Crystallographica Section A **32**, 751–767 (1976).

[121] A. Urban, "Modeling ionic transport and disorder in crystalline electrodes using percolation theory", arXiv:2302.06759 (2023).

[122] D. Chen, J. Wu, J. K. Papp, B. D. McCloskey, W. Yang, and G. Chen, "Role of Redox-Inactive Transition-Metals in the Behavior of Cation-Disordered Rocksalt Cathodes", Small **16**, 2000656 (2020).

[123] R. Kataoka, T. Kojima, and N. Takeichi, "Electrochemical Property of Li-Mn Cation Disordered Li-Rich Li_2MnO_3 with NaCl Type Structure", Journal of The Electrochemical Society **165**, A291–A296 (2018).

[124] H. Ji, D. A. Kitchaev, Z. Lun, H. Kim, E. Foley, D.-H. Kwon, Y. Tian, M. Balasubramanian, M. Bianchini, Z. Cai, R. J. Clément, J. C. Kim, and G. Ceder, "Computational Investigation and Experimental Realization of Disordered High-Capacity Li-Ion Cathodes Based on Ni Redox", Chemistry of Materials **31**, 2431–2442 (2019).

[125] Z. Cai, Y. Zhang, Z. Lun, B. Ouyang, L. C. Gallington, Y. Sun, H. Hau, Y. Chen, M. C. Scott, and G. Ceder, "Thermodynamically Driven Synthetic Optimization for Cation-Disordered Rock Salt Cathodes", Advanced Energy Materials **12**, 2103923 (2022).

[126] J. Huang, P. Zhong, Y. Ha, D.-H. Kwon, M. J. Crafton, Y. Tian, M. Balasubramanian, B. D. McCloskey, W. Yang, and G. Ceder, "Non-topotactic reactions enable high rate capability in Li-rich cathode materials", Nature Energy **6**, 706–714 (2021).

[127] J. W. Furness, A. D. Kaplan, J. Ning, J. P. Perdew, and J. Sun, "Accurate and Numerically Efficient r^2SCAN Meta-Generalized Gradient Approximation", The Journal of Physical Chemistry Letters **11**, 8208–8215 (2020).

[128] R. Kingsbury, A. S. Gupta, C. J. Bartel, J. M. Munro, S. Dwaraknath, M. Horton, and K. A. Persson, "Performance comparison of r^2SCAN and SCAN metaGGA density functionals for solid materials via an automated, high-throughput computational workflow", Physical Review Materials **6**, 013801 (2022).

[129] A. Y. Toukmaji and J. A. Board, "Ewald summation techniques in perspective: a survey", Computer Physics Communications **95**, 73–92 (1996).

[130] L. Greengard and V. Rokhlin, "A Fast Algorithm for Particle Simulations", Journal of Computational Physics **135**, 280–292 (1997).

[131] G. Ceder, G. D. Garbulsky, and P. D. Tepesch, "Convergent real-space cluster expansion for configurational disorder in ionic systems", Physical Review B **51**, 11257–11261 (1995).

[132] J. Reed and G. Ceder, "Role of Electronic Structure in the Susceptibility of Metastable Transition-Metal Oxide Structures to Transformation", Chemical Reviews **104**, 4513–4534 (2004).

[133] A. Walsh, A. A. Sokol, J. Buckeridge, D. O. Scanlon, and C. R. A. Catlow, "Oxidation states and ionicity", Nature Materials **17**, 958–964 (2018).

[134] R. F. Bader, "Atoms in molecules", Accounts of Chemical Research **18**, 9–15 (1985).

[135] B. Silvi and A. Savin, "Classification of chemical bonds based on topological analysis of electron localization functions", Nature **371**, 683–686 (1994).

[136] N. Marzari, A. A. Mostofi, J. R. Yates, I. Souza, and D. Vanderbilt, "Maximally localized Wannier functions: Theory and applications", Reviews of Modern Physics **84**, 1419–1475 (2012).

[137] S. Takamoto, C. Shinagawa, D. Motoki, K. Nakago, W. Li, I. Kurata, T. Watanabe, Y. Yayama, H. Iriguchi, Y. Asano, T. Onodera, T. Ishii, T. Kudo, H. Ono, R. Sawada, R. Ishitani, M. Ong, T. Yamaguchi, T. Kataoka, A. Hayashi, N. Charoenphakdee, and T. Ibuka, "Towards universal neural network potential for material discovery applicable to arbitrary combination of 45 elements", Nature Communications **13**, 1–6 (2022).

[138] L. Zhang, H. Wang, M. C. Muniz, A. Z. Panagiotopoulos, R. Car, and W. E, "A deep potential model with long-range electrostatic interactions", The Journal of Chemical Physics **156**, 124107 (2022).

[139] A. Krishnamoorthy, K. I. Nomura, N. Baradwaj, K. Shimamura, P. Rajak, A. Mishra, S. Fukushima, F. Shimojo, R. Kalia, A. Nakano, and P. Vashishta, "Dielectric Constant of Liquid Water Determined with Neural Network Quantum Molecular Dynamics", Physical Review Letters **126**, 216403 (2021).

[140] C. Wolverton and A. Zunger, "First-principles prediction of vacancy order-disorder and intercalation battery voltages in Li_xCoO_2", Physical Review Letters **81**, 606–609 (1998).

[141] A. Zunger, "Electronic structure of 3d transition-atom impurities in semiconductors", in *Solid state physics*, Vol. 39 (Elsevier, 1986), pages 275–464.

[142] F. Haldane and P. Anderson, "Simple model of multiple charge states of transition-metal impurities in semiconductors", Physical Review B **13**, 2553 (1976).

[143] D. Frenkel and B. Smit, *Understanding molecular simulation: from algorithms to applications*, Vol. 1 (Elsevier, 2001).

[144] T. Xie and J. C. Grossman, "Crystal Graph Convolutional Neural Networks for an Accurate and Interpretable Prediction of Material Properties", Physical Review Letters **120**, 145301 (2018).

[145] C. Chen, W. Ye, Y. Zuo, C. Zheng, and S. P. Ong, "Graph Networks as a Universal Machine Learning Framework for Molecules and Crystals", Chemistry of Materials **31**, 3564–3572 (2019).

[146] K. Choudhary, B. DeCost, C. Chen, A. Jain, F. Tavazza, R. Cohn, C. W. Park, A. Choudhary, A. Agrawal, S. J. Billinge, E. Holm, S. P. Ong, and C. Wolverton, "Recent advances and applications of deep learning methods in materials science", npj Computational Materials **8**, 10.1038/s41524-022-00734-6 (2022).

[147] J. Behler and M. Parrinello, "Generalized neural-network representation of high-dimensional potential-energy surfaces", Physical Review Letters **98** (2007).

[148] O. T. Unke, S. Chmiela, H. E. Sauceda, M. Gastegger, I. Poltavsky, K. T. Schütt, A. Tkatchenko, and K.-R. Müller, "Machine Learning Force Fields", Chemical Reviews **121**, 10142–10186 (2021).

[149] N. Artrith, T. Morawietz, and J. Behler, "High-dimensional neural-network potentials for multicomponent systems: Applications to zinc oxide", Physical Review B **83**, 153101 (2011).

[150] N. Artrith, A. Urban, and G. Ceder, "Constructing first-principles phase diagrams of amorphous lixsi using machine-learning-assisted sampling with an evolutionary algorithm", The Journal of Chemical Physics **148** (2018).

[151] J. Vandermause, Y. Xie, J. S. Lim, C. J. Owen, and B. Kozinsky, "Active learning of reactive Bayesian force fields applied to heterogeneous catalysis dynamics of H/Pt", Nature Communications **13**, 5183 (2022).

[152] Y. Xie, J. Vandermause, S. Ramakers, N. H. Protik, A. Johansson, and B. Kozinsky, "Uncertainty-aware molecular dynamics from Bayesian active learning for phase transformations and thermal transport in SiC", npj Computational Materials **9** (2023).

[153] R. Drautz, "Atomic cluster expansion for accurate and transferable interatomic potentials", Physical Review B **99**, 014104 (2019).

[154] J. Quinonero-Candela and C. E. Rasmussen, "A unifying view of sparse approximate gaussian process regression", The Journal of Machine Learning Research **6**, 1939–1959 (2005).

[155] J. Vandermause, S. B. Torrisi, S. Batzner, Y. Xie, L. Sun, A. M. Kolpak, and B. Kozinsky, "On-the-fly active learning of interpretable Bayesian force fields for atomistic rare events", npj Computational Materials **6**, 1–11 (2020).

[156] H. Wang, L. Zhang, J. Han, and W. E, "DeePMD-kit: A deep learning package for many-body potential energy representation and molecular dynamics", Computer Physics Communications **228**, 178–184 (2018).

[157] L. Zhang, H. Wang, R. Car, and W. E, "Phase Diagram of a Deep Potential Water Model", Physical Review Letters **126**, 236001 (2021).

[158] S. Wang, Y. Liu, and Y. Mo, "Frustration in Super-Ionic Conductors Unraveled by the Density of Atomistic States", Angewandte Chemie **135**, 10.1002/ange.202215544 (2023).

[159] W. Jiang, Y. Zhang, L. Zhang, and H. Wang, "Accurate deep potential model for the al–cu–mg alloy in the full concentration space", Chinese Physics B **30**, 050706 (2021).

[160] J. Bruna, W. Zaremba, A. Szlam, and Y. LeCun, "Spectral networks and locally connected networks on graphs", arXiv:1312.6203 (2013).

[161] M. Geiger and T. Smidt, "e3nn: Euclidean neural networks", arXiv:2207.09453 (2022).

[162] J. Gasteiger, J. Groß, and S. Günnemann, "Directional message passing for molecular graphs", in International Conference on Learning Representations (ICLR) (2020).

[163] S. Batzner, A. Musaelian, L. Sun, M. Geiger, J. P. Mailoa, M. Kornbluth, N. Molinari, T. E. Smidt, and B. Kozinsky, "E(3)-equivariant graph neural networks for data-efficient and accurate interatomic potentials", Nature Communications **13**, 2453 (2022).

[164] S. Takamoto, S. Izumi, and J. Li, "Teanet: universal neural network interatomic potential inspired by iterative electronic relaxations", Computational Materials Science **207**, 111280 (2022).

[165] I. Batatia, D. P. Kovacs, G. N. C. Simm, C. Ortner, and G. Csanyi, "MACE: Higher Order Equivariant Message Passing Neural Networks for Fast and Accurate Force Fields", in Advances in Neural Information Processing Systems (2022).

[166] C. Chen and S. P. Ong, "A universal graph deep learning interatomic potential for the periodic table", Nature Computational Science **2**, 718–728 (2022).

[167] K. Choudhary, B. DeCost, L. Major, K. Butler, J. Thiyagalingam, and F. Tavazza, "Unified graph neural network force-field for the periodic table: solid state applications", Digital Discovery (2023).

[168] B. Deng, P. Zhong, K. Jun, J. Riebesell, K. Han, C. J. Bartel, and G. Ceder, "CHGNet: Pretrained universal neural network potential for charge-informed atomistic modeling", arXiv:2302.14231 (2023).

[169] A. Wang, R. Kingsbury, M. McDermott, M. Horton, A. Jain, S. P. Ong, S. Dwaraknath, and K. A. Persson, "A framework for quantifying uncertainty in DFT energy corrections", Scientific Reports **11**, 15496 (2021).

[170] C. Delacourt, P. Poizot, J.-M. Tarascon, and C. Masquelier, "The existence of a temperature-driven solid solution in Li_xFePO_4 for $0 \leq x \leq 1$", Nature Materials **4**, 254–260 (2005).

[171] J. L. Dodd, R Yazami, and B Fultz, "Phase Diagram of Li_xFePO_4", Electrochemical and Solid-State Letters **9**, A151 (2006).

[172] Z. Deng, G. Sai Gautam, S. K. Kolli, J. N. Chotard, A. K. Cheetham, C. Masquelier, and P. Canepa, "Phase Behavior in Rhombohedral NaSiCON Electrolytes and Electrodes", Chemistry of Materials **32**, 7908–7920 (2020).

[173] Y. S. Meng and M. E. Arroyo-De Dompablo, "First principles computational materials design for energy storage materials in lithium ion batteries", Energy and Environmental Science **2**, 589–609 (2009).

[174] M. K. Aydinol, A. F. Kohan, G. Ceder, K. Cho, and J. Joannopoulos, "Ab initio study of lithium intercalation in metal oxides and metal dichalcogenides", Physical Review B **56**, 1354–1365 (1997).

[175] J. Lee, C. Wang, R. Malik, Y. Dong, Y. Huang, D. Seo, and J. Li, "Determining the Criticality of Li-Excess for Disordered-Rocksalt Li-Ion Battery Cathodes", Advanced Energy Materials **11**, 2100204 (2021).

[176] B. Li, M. T. Sougrati, G. Rousse, A. V. Morozov, R. Dedryvère, A. Iadecola, A. Senyshyn, L. Zhang, A. M. Abakumov, M.-L. Doublet, and J.-M. Tarascon, "Correlating ligand-to-metal charge transfer with voltage hysteresis in a Li-rich rock-salt compound exhibiting anionic redox", Nature Chemistry **13**, 1070–1080 (2021).

[177] Z. Yao, S. Kim, J. He, V. I. Hegde, and C. Wolverton, "Interplay of cation and anion redox in Li_4 Mn_2O_5 cathode material and prediction of improved $Li_4(Mn,M)_2O_5$ electrodes for Li-ion batteries", Science Advances **4**, eaao6754 (2018).

[178] Q. Li, J. Wu, Z. Yao, Y. Xu, M. M. Thackeray, C. Wolverton, and V. P. Dravid, "Dynamic imaging of metastable reaction pathways in lithiated cobalt oxide electrodes", Nano Energy **44**, 15–22 (2018).

[179] K. McColl, R. A. House, G. J. Rees, A. G. Squires, S. W. Coles, P. G. Bruce, B. J. Morgan, and M. S. Islam, "Transition metal migration and O2 formation underpin voltage hysteresis in oxygen-redox disordered rocksalt cathodes", Nature Communications **13**, 5275 (2022).

[180] Q. Wu, B. He, T. Song, J. Gao, and S. Shi, "Cluster expansion method and its application in computational materials science", Computational Materials Science **125**, 243–254 (2016).

[181] A. van de Walle, M. Asta, and G. Ceder, "The alloy theoretic automated toolkit: A user guide", Calphad **26**, 539–553 (2002).

[182] A. Seko, A. Takahashi, and I. Tanaka, "Sparse representation for a potential energy surface", Phys. Rev. B **90**, 024101 (2014).

[183] B. Puchala, J. C. Thomas, A. R. Natarajan, J. G. Goiri, S. S. Behara, J. L. Kaufman, and A. Van der Ven, "CASM — A software package for first-principles based study of multicomponent crystalline solids", Computational Materials Science **217**, 111897 (2023).

[184] A. Van der Ven, M. K. Aydinol, G. Ceder, G. Kresse, and J. Hafner, "First-principles investigation of phase stability in Li_xCoO_2", Physical Review B **58**, 2975–2987 (1998).

[185] G. Houchins and V. Viswanathan, "An accurate machine-learning calculator for optimization of Li-ion battery cathodes", The Journal of Chemical Physics **153**, 054124 (2020).

[186] S. K. Kolli and A. Van Der Ven, "First-Principles Study of Spinel $MgTiS_2$ as a Cathode Material", Chemistry of Materials **30**, 2436–2442 (2018).

[187] X. Guo, C. Chen, and S. P. Ong, "Intercalation Chemistry of the Disordered Rocksalt $Li_3V_2O_5$ Anode from Cluster Expansions and Machine Learning Interatomic Potentials", Chemistry of Materials **35**, 1537–1546 (2023).

[188] J. P. Valleau and L. K. Cohen, "Primitive model electrolytes. I. Grand canonical Monte Carlo computations", The Journal of Chemical Physics **72**, 5935–5941 (1980).

[189] A. S. Tygesen, J. H. Chang, T. Vegge, and J. M. García-Lastra, "Computational framework for a systematic investigation of anionic redox process in Li-rich compounds", npj Computational Materials **6**, 65 (2020).

[190] J. Vinckeviciute, D. A. Kitchaev, and A. Van der Ven, "A Two-Step Oxidation Mechanism Controlled by Mn Migration Explains the First-Cycle Activation Behavior of Li2MnO3-Based Li-Excess Materials", Chemistry of Materials **33**, 1625–1636 (2021).

[191] J. H. Yang, T. Chen, L. Barroso-Luque, Z. Jadidi, and G. Ceder, "Approaches for handling high-dimensional cluster expansions of ionic systems", npj Computational Materials **8**, 133 (2022).

[192] D.-H. Seo, J. Lee, A. Urban, R. Malik, S. Kang, and G. Ceder, "The structural and chemical origin of the oxygen redox activity in layered and cation-disordered Li-excess cathode materials", Nature Chemistry **8**, 692–697 (2016).

[193] L. Barroso-Luque, J. H. Yang, F. Xie, T. Chen, R. L. Kam, Z. Jadidi, P. Zhong, and G. Ceder, "smol: A Python package for cluster expansions and beyond", Journal of Open Source Software **7**, 4504 (2022).

[194] A. Abdellahi, A. Urban, S. Dacek, and G. Ceder, "The Effect of Cation Disorder on the Average Li Intercalation Voltage of Transition-Metal Oxides", Chemistry of Materials **28**, 3659–3665 (2016).

[195] A. G. Squires and D. O. Scanlon, "Understanding the limits to short-range order suppression in many-component disordered rock salt lithium-ion cathode materials", Journal of Materials Chemistry A **11**, 13765–13773 (2023).

[196] N. Artrith, J. A. Garrido Torres, A. Urban, and M. S. Hybertsen, "Data-driven approach to parameterize SCAN+U for an accurate description of $3d$ transition metal oxide thermochemistry", Physical Review Materials **6**, 035003 (2022).

[197] S. Swathilakshmi, R. Devi, and G. Sai Gautam, "Performance of the r 2 SCAN Functional in Transition Metal Oxides", Journal of Chemical Theory and Computation **19**, 4202–4215 (2023).

[198] T. Y. Huang, Z. Cai, M. J. Crafton, L. A. Kaufman, Z. M. Konz, H. K. Bergstrom, E. A. Kedzie, H. M. Hao, G. Ceder, and B. D. McCloskey, "Quantitative Decoupling of Oxygen-Redox and Manganese-Redox Voltage Hysteresis in a Cation-Disordered Rock Salt Cathode", Advanced Energy Materials **2300241**, 1–14 (2023).

[199] M. Ménétrier, I. Saadoune, S. Levasseur, and C. Delmas, "The insulator-metal transition upon lithium deintercalation from $LiCoO_2$: electronic properties and ^{7}Li NMR study", Journal of Materials Chemistry **9**, 1135–1140 (1999).

[200] A. Zunger, S.-H. Wei, L. G. Ferreira, and J. E. Bernard, "Special quasirandom structures", Physical Review Letters **65**, 353–356 (1990).

[201] M. Nakajima and N. Yabuuchi, "Lithium-Excess Cation-Disordered Rocksalt-Type Oxide with Nanoscale Phase Segregation: $Li_{1.25}Nb_{0.25}V_{0.5}O_2$", Chemistry of Materials **29**, 6927–6935 (2017).

[202] Z. Lebens-Higgins, H. Chung, I. Temprano, M. Zuba, J. Wu, J. Rana, C. Mejia, M. A. Jones, L. Wang, C. P. Grey, et al., "Electrochemical Utilization of Iron IV in the $Li_{1.3}Fe_{0.4}Nb_{0.3}O_2$ Disordered Rocksalt Cathode", Batteries & Supercaps **4**, 771–777 (2021).

[203] E Weinan, "Machine learning and computational mathematics", arXiv preprint arXiv:2009.14596 (2020).

[204] J Reed, G Ceder, and A. V. D. Ven, "Layered-to-Spinel Phase Transition in Li_xMnO_2", Electrochemical and Solid-State Letters **4**, A78 (2001).

[205] I. Koetschau, M. N. Richard, J. R. Dahn, J. B. Soupart, and J. C. Rousche, "Orthorhombic LiMnO2 as a High Capacity Cathode for Li-Ion Cells", Journal of The Electrochemical Society **142**, 2906–2910 (1995).

[206] J. N. Reimers, E. W. Fuller, E. Rossen, and J. R. Dahn, "Synthesis and Electrochemical Studies of LiMnO2 Prepared at Low Temperatures", Journal of The Electrochemical Society **140**, 3396–3401 (1993).

[207] T. Chen, J. Yang, L. Barroso-Luque, and G. Ceder, "Removing the Two-Phase Transition in Spinel $LiMn_2O_4$ through Cation Disorder", ACS Energy Letters **8**, 314–319 (2023).

[208] D.-H. Kwon, J. Lee, N. Artrith, H. Kim, L. Wu, Z. Lun, Y. Tian, Y. Zhu, and G. Ceder, "The Impact of Surface Structure Transformations on the Performance of Li-Excess Cation-Disordered Rocksalt Cathodes", Cell Reports Physical Science **1**, 100187 (2020).

[209] J. Ahn, R. Giovine, V. C. Wu, K. P. Koirala, C. Wang, R. J. Clément, and G. Chen, "Ultrahigh-Capacity Rocksalt Cathodes Enabled by Cycling-Activated Structural Changes", Advanced Energy Materials **13**, 1–14 (2023).

[210] Y.-I. Jang, F. Chou, B. Huang, D. R. Sadoway, and Y.-M. Chiang, "Magnetic characterization of orthorhombic $LiMnO_2$ and electrochemically transformed spinel Li_xMnO_2 ($x < 1$)", Journal of Physics and Chemistry of Solids **64**, 2525–2533 (2003).

[211] M. R. Jo, Y. Kim, J. Yang, M. Jeong, K. Song, Y.-I. Kim, J.-M. Lim, M. Cho, J.-H. Shim, Y.-M. Kim, W.-S. Yoon, and Y.-M. Kang, "Triggered reversible phase transformation between layered and spinel structure in manganese-based layered compounds", Nature Communications **10**, 3385 (2019).

[212] M. D. Radin, J. Vinckeviciute, R. Seshadri, and A. Van der Ven, "Manganese oxidation as the origin of the anomalous capacity of Mn-containing Li-excess cathode materials", Nature Energy **4**, 639–646 (2019).

[213] J. Z. Xie, X. Y. Zhou, D. Luan, and H. Jiang, "Machine Learning Force Field Aided Cluster Expansion Approach to Configurationally Disordered Materials: Critical Assessment of Training Set Selection and Size Convergence", Journal of Chemical Theory and Computation **18**, 3795–3804 (2022).

[214] C. Lv, X. Zhou, L. Zhong, C. Yan, M. Srinivasan, Z. W. Seh, C. Liu, H. Pan, S. Li, Y. Wen, and Q. Yan, "Machine Learning: An Advanced Platform for Materials Development and State Prediction in Lithium-Ion Batteries", Advanced Materials **34**, 2101474 (2022).

[215] Z. Ahmad, T. Xie, C. Maheshwari, J. C. Grossman, and V. Viswanathan, "Machine Learning Enabled Computational Screening of Inorganic Solid Electrolytes for Suppression of Dendrite Formation in Lithium Metal Anodes", ACS Central Science **4**, 996–1006 (2018).

[216] K. A. Severson, P. M. Attia, N. Jin, N. Perkins, B. Jiang, Z. Yang, M. H. Chen, M. Aykol, P. K. Herring, D. Fraggedakis, M. Z. Bazant, S. J. Harris, W. C. Chueh, and R. D. Braatz, "Data-driven prediction of battery cycle life before capacity degradation", Nature Energy **4**, 383–391 (2019).

[217] P. K. Jones, U. Stimming, and A. A. Lee, "Impedance-based forecasting of lithium-ion battery performance amid uneven usage", Nature Communications **13**, 1–9 (2022).

[218] M. Aykol, C. B. Gopal, A. Anapolsky, P. K. Herring, B. van Vlijmen, M. D. Berliner, M. Z. Bazant, R. D. Braatz, W. C. Chueh, and B. D. Storey, "Perspective–Combining Physics and Machine Learning to Predict Battery Lifetime", Journal of The Electrochemical Society **168**, 030525 (2021).

[219] P. M. Attia, A. Grover, N. Jin, K. A. Severson, T. M. Markov, Y.-H. Liao, M. H. Chen, B. Cheong, N. Perkins, Z. Yang, P. K. Herring, M. Aykol, S. J. Harris, R. D. Braatz, S. Ermon, and W. C. Chueh, "Closed-loop optimization of fast-charging protocols for batteries with machine learning", Nature **578**, 397–402 (2020).

[220] L. Ward, S. Babinec, E. J. Dufek, D. A. Howey, V. Viswanathan, M. Aykol, D. A. Beck, B. Blaiszik, B.-R. Chen, G. Crabtree, S. Clark, V. De Angelis, P. Dechent, M. Dubarry, E. E. Eggleton, D. P. Finegan, I. Foster, C. B. Gopal, P. K. Herring, V. W. Hu, N. H. Paulson, Y. Preger, D. Uwe-Sauer, K. Smith, S. W. Snyder, S. Sripad, T. R. Tanim, and L. Teo, "Principles of the Battery Data Genome", Joule **6**, 2253–2271 (2022).

[221] A. D. Sendek, B. Ransom, E. D. Cubuk, L. A. Pellouchoud, J. Nanda, and E. J. Reed, "Machine Learning Modeling for Accelerated Battery Materials Design in the Small Data Regime", Advanced Energy Materials **12**, 2200553 (2022).

[222] P. Zhong, B. Deng, T. He, Z. Lun, and G. Ceder, "Deep learning of experimental electrochemistry for battery cathodes across diverse compositions", arXiv 2304.04986 (2023).

[223] S. Liu, X. Feng, X. Wang, X. Shen, E. Hu, R. Xiao, R. Yu, H. Yang, N. Song, Z. Wang, X. Yang, and L. Chen, "Another strategy, detouring potential decay by fast completion of cation mixing", Advanced Energy Materials **8**, 1703092 (2018).

[224] S. Hoshino, A. M. Glushenkov, S. Ichikawa, T. Ozaki, T. Inamasu, and N. Yabuuchi, "Reversible Three-Electron Redox Reaction of Mo^{3+}/Mo^{6+} for Rechargeable Lithium Batteries", ACS Energy Letters **2**, 733–738 (2017).

[225] R. Wang, X. Li, L. Liu, J. Lee, D.-H. Seo, S.-H. Bo, A. Urban, and G. Ceder, "A disordered rock-salt Li-excess cathode material with high capacity and substantial oxygen redox activity: $Li_{1.25}Nb_{0.25}Mn_{0.5}O_2$", Electrochemistry Communications **60**, 70–73 (2015).

[226] M. Tabuchi, A. Nakashima, H. Shigemura, K. Ado, H. Kobayashi, H. Sakaebe, K. Tatsumi, H. Kageyama, T. Nakamura, and R. Kanno, "Fine $Li_{(4-x)/3}Ti_{(2-2x)/3}Fe_xO_2$ ($0.18 < x < 0.67$) powder with cubic rock-salt structure as a positive electrode material for rechargeable lithium batteries", Journal of Materials Chemistry **13**, 1747 (2003).

[227] S. Ren, R. Chen, E. Maawad, O. Dolotko, A. A. Guda, V. Shapovalov, D. Wang, H. Hahn, and M. Fichtner, "Improved Voltage and Cycling for Li^+ Intercalation in High-Capacity Disordered Oxyfluoride Cathodes", Advanced Science **2**, 1500128 (2015).

[228] M. A. Cambaz, A. Urban, S. A. Pervez, H. Geßwein, A. Schiele, A. A. Guda, A. L. Bugaev, A. Mazilkin, T. Diemant, R. J. Behm, T. Brezesinski, and M. Fichtner, "Understanding the Origin of Higher Capacity for Ni-Based Disordered Rock-Salt Cathodes", Chemistry of Materials **32**, 3447–3461 (2020).

[229] A. Rohatgi, *Webplotdigitizer: version 4.6*, 2022.

[230] R. E. A. Goodall and A. A. Lee, "Predicting materials properties without crystal structure: deep representation learning from stoichiometry", Nature Communications **11**, 6280 (2020).

[231] V. Tshitoyan, J. Dagdelen, L. Weston, A. Dunn, Z. Rong, O. Kononova, K. A. Persson, G. Ceder, and A. Jain, "Unsupervised word embeddings capture latent knowledge from materials science literature", Nature **571**, 95–98 (2019).

[232] T. Xie, A. France-Lanord, Y. Wang, Y. Shao-Horn, and J. C. Grossman, "Graph dynamical networks for unsupervised learning of atomic scale dynamics in materials", Nature Communications **10**, 2667 (2019).

[233] K. He, X. Zhang, S. Ren, and J. Sun, "Deep Residual Learning for Image Recognition", in IEEE Conference on Computer Vision and Pattern Recognition (CVPR) (2016).

[234] A. Paszke, S. Gross, F. Massa, A. Lerer, J. Bradbury, G. Chanan, T. Killeen, Z. Lin, N. Gimelshein, L. Antiga, et al., "Pytorch: an imperative style, high-performance deep learning library", Advances in neural information processing systems **32** (2019).

[235] C. Sutton, M. Boley, L. M. Ghiringhelli, M. Rupp, J. Vreeken, and M. Scheffler, "Identifying domains of applicability of machine learning models for materials science", Nature Communications **11**, 4428 (2020).

[236] L. A. Kaufman and B. D. McCloskey, "Surface Lithium Carbonate Influences Electrolyte Degradation via Reactive Oxygen Attack in Lithium-Excess Cathode Materials", Chemistry of Materials **33**, 4170–4176 (2021).

[237] K. Edström, T. Gustafsson, and J. Thomas, "The cathode–electrolyte interface in the Li-ion battery", Electrochimica Acta **50**, 397–403 (20).

[238] O. Kononova, T. He, H. Huo, A. Trewartha, E. A. Olivetti, and G. Ceder, "Opportunities and challenges of text mining in materials research", iScience **24**, 102155 (2021).

[239] V. Baibakova, M. Elzouka, S. Lubner, R. Prasher, and A. Jain, "Optical emissivity dataset of multi-material heterogeneous designs generated with automated figure extraction", Scientific Data **9**, 589 (2022).

[240] P. Raccuglia, K. C. Elbert, P. D. F. Adler, C. Falk, M. B. Wenny, A. Mollo, M. Zeller, S. A. Friedler, J. Schrier, and A. J. Norquist, "Machine-learning-assisted materials discovery using failed experiments", Nature **533**, 73–76 (2016).

[241] N. J. Szymanski, Y. Zeng, H. Huo, C. J. Bartel, H. Kim, and G. Ceder, "Toward autonomous design and synthesis of novel inorganic materials", Materials Horizons **8**, 2169–2198 (2021).

[242] A. Firouzi, R. Qiao, S. Motallebi, C. W. Valencia, H. S. Israel, M. Fujimoto, L. A. Wray, Y. D. Chuang, W. Yang, and C. D. Wessells, "Monovalent manganese based anodes and co-solvent electrolyte for stable low-cost high-rate sodium-ion batteries", Nature Communications **9** (2018).

[243] J. Vinson, J. J. Rehr, J. J. Kas, and E. L. Shirley, "Bethe-Salpeter equation calculations of core excitation spectra", Physical Review B **83**, 115106 (2011).

[244] J. Vinson, "Advances in the ocean-3 spectroscopy package", Physical Chemistry Chemical Physics **24**, 12787–12803 (2022).

[245] I. I. Abate, C. D. Pemmaraju, S. Y. Kim, K. H. Hsu, S. Sainio, B. Moritz, J. Vinson, M. F. Toney, W. Yang, W. E. Gent, T. P. Devereaux, L. F. Nazar, and W. C. Chueh, "Coulombically-stabilized oxygen hole polarons enable fully reversible oxygen redox", Energy & Environmental Science **14**, 4858–4867 (2021).

[246] Z. Zhuo, C. D. Pemmaraju, J. Vinson, C. Jia, B. Moritz, I. Lee, S. Sallies, Q. Li, J. Wu, K. Dai, Y.-d. Chuang, Z. Hussain, F. Pan, T. P. Devereaux, and W. Yang, "Spectroscopic Signature of Oxidized Oxygen States in Peroxides", The Journal of Physical Chemistry Letters **9**, 6378–6384 (2018).

[247] J. Deslippe, G. Samsonidze, D. A. Strubbe, M. Jain, M. L. Cohen, and S. G. Louie, "BerkeleyGW: A massively parallel computer package for the calculation of the quasiparticle and optical properties of materials and nanostructures", Computer Physics Communications **183**, 1269–1289 (2012).

[248] R. Drautz, "Atomic cluster expansion of scalar, vectorial, and tensorial properties including magnetism and charge transfer", Physical Review B **102**, 024104 (2020).

[249] J. Westermayr and P. Marquetand, "Machine Learning for Electronically Excited States of Molecules", Chemical Reviews **121**, 9873–9926 (2021).

[250] O. T. Unke, S. Chmiela, M. Gastegger, K. T. Schütt, H. E. Sauceda, and K.-R. Müller, "Spookynet: learning force fields with electronic degrees of freedom and nonlocal effects", Nature Communications **12**, 7273 (2021).

[251] T. W. Ko, J. A. Finkler, S. Goedecker, and J. Behler, "A fourth-generation high-dimensional neural network potential with accurate electrostatics including non-local charge transfer", Nature Communications **12**, 398 (2021).

[252] J. Westermayr, M. Gastegger, and P. Marquetand, "Combining SchNet and SHARC: The SchNarc Machine Learning Approach for Excited-State Dynamics", Journal of Physical Chemistry Letters **11**, 3828–3834 (2020).

[253] Y. Song, J. Sohl-Dickstein, D. P. Kingma, A. Kumar, S. Ermon, and B. Poole, "Score-based generative modeling through stochastic differential equations", arXiv preprint arXiv:2011.13456 (2020).

[254] J. Ingraham, V. Garg, R. Barzilay, and T. Jaakkola, "Generative models for graph-based protein design", Advances in neural information processing systems **32** (2019).

[255] M. Xu, L. Yu, Y. Song, C. Shi, S. Ermon, and J. Tang, "Geodiff: a geometric diffusion model for molecular conformation generation", arXiv preprint arXiv:2203.02923 (2022).

[256] G. Corso, H. Stärk, B. Jing, R. Barzilay, and T. Jaakkola, "Diffdock: diffusion steps, twists, and turns for molecular docking", arXiv preprint arXiv:2210.01776 (2022).

[257] T. Xie, X. Fu, O.-E. Ganea, R. Barzilay, and T. Jaakkola, "Crystal diffusion variational autoencoder for periodic material generation", arXiv preprint arXiv:2110.06197 (2021).

[258] S. Zheng, J. He, C. Liu, Y. Shi, Z. Lu, W. Feng, F. Ju, J. Wang, J. Zhu, Y. Min, et al., "Towards predicting equilibrium distributions for molecular systems with deep learning", arXiv preprint arXiv:2306.05445 (2023).

[259] Y. Du, Y. Wang, Y. Huang, J. C. Li, Y. Zhu, T. Xie, C. Duan, J. M. Gregoire, and C. P. Gomes, "M^2hub: unlocking the potential of machine learning for materials discovery", arXiv preprint arXiv:2307.05378 (2023).

[260] J. Chen, S. R. Cross, L. J. Miara, J.-J. Cho, Y. Wang, and W. Sun, "Navigating phase diagram complexity to guide robotic inorganic materials synthesis", arXiv preprint arXiv:2304.00743 (2023).

[261] N. Szymanski, B. Rendy, Y. Fei, R. Kumar, T. He, D. Milsted, M. McDermott, M. Gallant, D. Cubuk, A. Merchant, H. Kim, A. Jain, C. Bartel, K. Persson, Y. Zeng, and G. Ceder, "An autonomous laboratory for inorganic materials discovery", *Under review.*